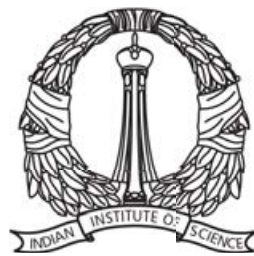


Fermi Bubbles and galactic outflows in circumgalactic medium

A THESIS
SUBMITTED FOR THE DEGREE OF
Doctor of Philosophy
IN THE FACULTY OF SCIENCE

by
Kartick Chandra Sarkar

Under the supervision of
Prof. Biman B. Nath (Raman Research Institute)
Prof. Prateek Sharma (Indian Institute of Science)



Joint Astronomy Program
Department of Physics
Indian Institute of Science
Bengaluru - 560012

July, 2017

©Kartick Chandra Sarkar
July, 2017
All rights reserved.

To
My parents,
Shri Subhash Chandra Sarkar
&
Smt. Bishaka Sarkar

Declaration

I, Kartick Chandra Sarkar, hereby declare that the work presented in this thesis titled ‘Fermi Bubbles and galactic outflows in circumgalactic medium’ is entirely original. This work has been carried out by me under the supervision of Prof. Biman B. Nath (Raman Research Institute) and Prof. Prateek Sharma (Indian Institute of Science) at the Department of Astronomy and Astrophysics, Raman Research Institute under the Joint Astronomy Program hosted by the Department of Physics, Indian Institute of Science.

I further declare that the subject matter presented in this thesis has not previously formed the basis for the award of any degree, diploma, membership, associateship or any other similar title of any university or institution.

Department of Physics
Indian Institute of Science
Bengaluru, 560012
India

Kartick Chandra Sarkar
Date:

Acknowledgement

It would be a lie if I say that I was determined all along to do research in Astronomy and Astrophysics. But, a deep curiosity to learn about the existence of the universe and objects far beyond our own little Earth was always present in my mind. After all, who does not want to know what is beyond our limited visible world?

My journey to learn astronomy started with looking at countless stars in the night sky and wondering about the mystery that the universe holds. However, I never thought that I will be pursuing a research carrier in astrophysics. After taking admission to MSc, I was slowly moving towards the experimental condensed matter field. But things changed when Prof. Somnath Bhardwaj gave a beautiful course on Astronomy and Astrophysics. Since then I am following my curiosity to know about the objects that are far far away from us. I am grateful to my Supervisors Prof Biman Nath and Prof Prateek Sharma, who have been very supportive of my tendency to learn even completely unrelated topics. They have been excellent mentors to guide me through the complex trajectory of a PhD life and enhanced my curiosity to learn even more. Their compassionate way to answer even my stupid questions is what makes them wonderful supervisors. Other than science, Prof Biman Nath's vast knowledge in the field of history, music and philosophy led to many inspiring and memorable discussions. Prof Shiv Sethi is another person who has been a source of knowledge for my random questions in astrophysics. His friendly approach towards the students made him a great teacher to ask any academic question without a fear. I enjoyed working with Prof Yuri Shchekinov, who has provided insightful understanding of my research topic as well as on other lighter subjects.

I am thankful to the Chairman of the department of Physics for providing me a chance to pursue a research carrier in astrophysics in that department. I am grateful to Prof Ravi Subrahmanyan, the director of the Raman Research Institute (RRI) for providing me an wonderful research environment. I also thank the current and previous Administrative Officers C. S. R. Murthy and K. Krishnamaraju for making the official processes so easy. A simple thank to the previous Astronomy and Astrophysics group secretary Vidyamani ma'm is not enough for how much she has contributed to my PhD as well as my personal life. Apart from being a very strict and disciplined administrator, she has also been a local guardian for me and ready to help in any kind of issues. I also thank the current Astronomy group secretary Harini for the helps to process the official works. I want to thank RRI library staffs for maintaining important books and journals, moreover, for arranging the books or journals if they are not present in the library. I am thankful to all the academic staffs in RRI astrophysics and IISc physics department for discussing various aspects of science at various periods of my life here

in RRI.

I thank all my friends in RRI, IISc and IIA for converting otherwise a hectic research life into five enjoyable years. I have enjoyed spending time with my friends Abir, Deovrat, Gopal, Mohan, Prasun, Soumavo and Srihari in IISc. Srihari has been an wonderful friend and a source of inspiration for my philosophical thoughts as well as extracurricular activities. My friends at RRI have been a large part of my PhD life. I want to thank Arpita Di, Karamveer, Varun and Sourabh Da for many memorable discussions and activities inside and outside RRI. A special thanks to Karamveer who has been a very supportive friend at different stages of the RRI as well as personal life. I thank Amit and Santanu for creating interest in sports and also teaching me table tennis and football. My sincere thanks to Soumya (kaka) and Chandan who have been excellent sources of my intellectual as well as spiritual knowledge.

I also thank Prof Lars Bildsten, the director of Kavli Institute for Theoretical Physics, Santa Barbara, for providing me an opportunity to be in KITP for several months during which I could interact with the pioneers of science and learn how science takes its next step. My thanks to the extended family of apartment 106, specially Sourabh Da, Soupitak Da and Chandi Da who made my stay at Santa Barbara a memorable event in my life.

The acknowledgement is truly not complete without mentioning my parents who have struggled through a very poor economic condition to support my education. I am lucky to have them. During my entire educational life, starting from the admission to a higher secondary school, my education has been built by the kind supports from various people at various times. Among them, I thank Mr. Subir Dey, Mr. Samrat Dey, Dr. Rabiul Islam, Dr Ganesh Mandal and Mrs Chhaya Mandal for making my education a reality. Lastly, I want to thank my friends Biplab and Subhajit who are with me at every single step of my life.

Synopsis

Galactic outflows play an important role in the formation and evolution of galaxies by regulating the star formation rate (SFR) within them and by throwing out metals into the intergalactic medium (IGM). They are key to understand the relation between the stellar and the dark matter halo mass, mass-metallicity relation of galaxies, intergalactic metal enrichment, formation of high velocity clouds and much more. Galactic outflows have been observed to be present in galaxies at all redshifts either in emission or in absorption of the stellar continuum. Outflows have been also detected in the immediate vicinity of galaxies by probing absorption lines in the spectrum of background Active Galactic Nuclei. In this thesis we explore the interactions between supernovae (SNe) driven outflows and the circumgalactic medium (CGM), an extended hot gas atmosphere believed to be present in the haloes of massive (stellar mass, $M_* \gtrsim 10^{10} M_\odot$) galaxies. Given the complexity of geometry and multiphase nature of outflows, we use numerical simulations to study gas interactions. Our results shine light on many interesting aspects of the galactic outflows, such as, i) the effect of the circumgalactic medium on the mass outflow rate and velocity of the outflowing gas on large scales, ii) origin of high velocity cold ($\sim 10^4$ K) gas in outflows iii) origin of X-ray emission in different scenarios. We connect our numerical and analytical work with the X-ray data. We also use our numerical set up to understand the origin and nature of two giant γ -ray bubbles, called the Fermi Bubbles, at the centre of our Galaxy. We compare our synthetic emission models to the observed γ -rays, X-rays, radio and UV absorption data and constrain the energetics and age of these bubbles. Below we outline the investigations undertaken in this thesis and point out our main results.

Interaction of circumgalactic medium and outflows

In a standard SNe driven outflow scenario, SNe ejected gas is considered to be a continuous outflow that expands freely with or without the gravity of the galaxy (Chevalier & Clegg 1985; Sharma & Nath 2013). The multiphase nature of the outflowing gas and the resistance provided by the CGM is often neglected while estimating the total mass outflow rate from galaxies (Arribas et al. 2014; Heckman et al. 2015). In the presence of a CGM, this scenario can change completely as the wind does not remain in a steady state any more and involves far more complexities than typically considered, such as mixing with the hot CGM. The dynamics of the cold gas is expected to be different in such a non-steady state compared to the calculations in which the cold clumps move under the effect of a steady state wind.

To study these effects, we perform hydrodynamical simulations of SNe driven out-

flows in a Milky-Way type galaxy that includes a CGM. We assess the effects of the CGM on the outflow by varying the star formation rate. We find that the total mass outflow rate is divided almost equally in two phases that peak at $\sim 10^5$ K (warm) and at $\sim 3 \times 10^6$ K (hot). This means that observations in optical/UV or X-ray only probe a fraction of the outflowing mass. We also find that the mass loading factor (η), defined as the ratio between mass outflow rate to the star formation rate, at outer radii (~ 100 kpc) of a galaxy can be much higher than the rate observed in warm gas ($\eta \approx 0.3-0.5$). We present simple scaling relations between the mass loading factor in warm gas and the total mass loading factor at the virial radius (η_v) that can be used to estimate the total mass outflow rate from such galaxies. We also find that warm gas can be entrained by ~ 1000 km s $^{-1}$ free wind to reach velocities as large as ~ 700 km s $^{-1}$. Cold clouds also form at the interaction zone between the outflow and the CGM. Some of these clouds keep moving outwards while some of them fall back to the stellar disc due to gravity. This galactic fountain gas which falls back can lead to further star formation in the disc.

X-rays from galaxies

Diffuse X-ray emission in case of a standard SNe driven outflow is dominated by the central part of the wind where temperature is $\sim 10^7$ K and density is $\gtrsim 0.1 m_p \text{ cm}^{-3}$. Since density at the centre of a standard SNe driven outflow is simply proportional to the star formation rate (SFR), the X-ray luminosity (L_X) is expected to be proportional to the SFR 2 . Observations, however, indicate a linear, or even a sub linear relation between L_X and SFR (Mineo et al. 2012b; Wang et al. 2016).

We used analytical results and numerical simulations to understand the origin of the X-ray emission from the star forming galaxies. We find that for highly star forming galaxies with no CGM, the diffuse X-ray mainly comes from the centre of the SNe wind as expected. However, for massive galaxies with low star formation rate ($\lesssim 1 M_\odot \text{ yr}^{-1}$), the emission is dominated by the contribution from the CGM. This contamination results in a flatter L_X -SFR relation than typically expected from a pure SNe driven outflow. Even after we increased the contribution from the outflowing wind by enhancing the mass loading factor to its maximum value, the CGM contamination could not be ignored. We further argue that these high L_X values of low star forming, massive galaxies could be inverted to study the properties of the CGM itself.

Multi-wavelength properties of outflow and Fermi Bubbles in our Galaxy

Observations reveal two giant ($\approx 50^\circ$) gamma-ray bubbles, called the Fermi Bubbles (FBs) toward the centre of our Galaxy (Su et al., 2010; Ackermann et al., 2014) the origin of which is still a mystery. Observations in other wavebands such as X-ray, radio and UV (absorption lines) also revealed many other interesting features associated with the FBs. There have been a number of attempts to explain the gamma-ray brightness and spectrum by considering feedback from the Galactic centre black hole (GCBH) and cosmic ray diffusion (Guo et al., 2012; Yang et al., 2012; Zubovas & Nayakshin, 2012).

The required mechanical luminosity in these models exceeds the value that is achievable with the current accretion rate by a few orders of magnitude. Star formation driven wind models have been, however, under-investigated so far with much less attention to explain the multi-wavelength features related to the FBs.

To understand the origin and nature of these bubbles, we simulate SNe driven wind scenario appropriate for the Milky-Way. By using the information about morphology and X-ray emission, we find that the required star formation rate at the centre of our Galaxy is $\approx 0.5 M_{\odot} \text{ yr}^{-1}$. After comparing the synthetic microwave surface brightness from our simulation with the observed data, we constrain the magnetic field inside the bubbles to be $\sim 4\mu\text{G}$. We also find that the gamma-ray morphology and spectral signatures in our simulated bubbles closely resemble the observed ones. The cold gas ($< 10^5 \text{ K}$) kinematics in our simulations also have a similar behaviour, to some extent, as observed in UV absorption lines through the northern bubbles.

O VIII and O VII line ratio through Fermi Bubbles

Most of the models of the Fermi Bubbles focus on getting a reasonable gamma-ray morphology and spectrum by varying the mechanical luminosity of the central source. Other ways to determine the origin of the FBs include probing the bubbles in X-rays to obtain information about the strength of the explosion at the Galactic centre. X-ray spectral analysis by [Kataoka et al. \(2013\)](#) suggests that the shock velocity is $\sim 300 \text{ km s}^{-1}$ with an age of $\sim 20 \text{ Myr}$ for the bubble, whereas, by analysing the O VIII and O VII line ratio [Miller & Bregman \(2016\)](#) obtained a shock speed of $\sim 500 \text{ km s}^{-1}$, indicating an age of $\sim 4 \text{ Myr}$.

We simulate both star formation driven and GCBH driven wind scenarios in our Galaxy with varying strength of star formation and accretion rate. We consider a self consistent gas distribution for the Milky-Way CGM that is close to the observations. We compare the synthetic O VIII and O VII lines from our simulations with the observations of [Miller & Bregman \(2016\)](#) and find that the data indicates a shock velocity of $\sim 300 \text{ km s}^{-1}$ and a corresponding age of the bubbles to be 15-25 Myr. After considering possible electron-proton non-equilibrium in the shocked gas that can affect the observability of the X-ray lines, we rule out mechanical luminosities $\gtrsim 10^{41} \text{ erg s}^{-1}$ as the possible driver of the Fermi Bubbles.

Contents

1	Thesis objectives	1
1.1	Motivation	1
1.2	Review of structure formation	1
1.2.1	Formation of dark matter haloes	2
1.2.2	Formation of gaseous haloes	3
1.2.3	Observations of gaseous halos	5
1.2.4	Hot and cold mode accretion	6
1.2.5	Stellar to halo mass relation	7
1.2.6	Requirement of outflow	8
1.3	Description of galactic outflow	10
1.3.1	Supernovae (SNe) driven outflows	10
1.3.1.1	Energetics	11
1.3.1.2	Condition for a wind	12
1.3.1.3	A spherical cow	13
1.3.1.4	Structure of wind	13
1.3.1.5	Simulations	16
1.3.2	Active Galactic Nuclei (AGN) driven	17
1.3.2.1	Energetics	17
1.4	Observations of outflows in external galaxies	18
1.4.1	Observed phases of outflow	21
1.4.1.1	Hot phase	21
1.4.1.2	Warm phase	21
1.4.1.3	Cold/molecular phase	22
1.4.2	Observed properties of outflow	22
1.4.2.1	Mass loading factor (MLF; η)	22
1.4.2.2	Velocity of outflow	23
1.5	Outflow in our Galaxy: the Fermi Bubbles	24
1.5.1	HI shells	24
1.5.2	Galactic centre lobe (GCL)	25
1.5.3	Microwave Haze	25
1.5.4	North Polar Spur (NPS)	25
1.5.4.1	Proposed origin	26
1.5.4.2	Physical parameters	27
1.5.5	Energetics at the Galactic centre	28
1.5.5.1	Star formation	28

1.5.5.2	Black hole accretion rate	28
1.5.6	Fermi Bubbles (FBs)	29
1.5.6.1	Morphology and Spectra	29
1.5.6.2	Kinematics	31
1.5.6.3	Models so far	31
1.6	Motivations for this thesis	33
1.7	Tools	35
1.7.1	Equations used	36
1.7.2	Code used	36
1.8	Structure of the thesis	37
2	Outflow in circumgalactic medium	39
2.1	Introduction	41
2.2	Mass model of the Galaxy	42
2.2.1	Gravitational potentials	42
2.2.2	Setting the initial density distribution	44
2.3	Simulation set-up	45
2.3.1	Injection parameters	46
2.3.2	The code settings	46
2.4	Results	50
2.4.1	Mass loading factor	51
2.4.2	Effect of multiple bursts and injection time	54
2.4.3	Comparison with observed mass loading factor	57
2.4.4	Velocity structure	60
2.4.5	Mass inventory	64
2.5	Discussion	65
2.5.1	Definition of mass loading factor	65
2.5.2	Dust in clouds	66
2.5.3	Absorption study of clouds	66
2.5.4	Redshift dependence	66
2.5.5	IGM enrichment	67
2.6	Summary	67
3	Diffuse X-ray emission	69
3.1	Introduction	71
3.2	Mass loading of outflows	72
3.3	Simulation details	74
3.4	Results	74
3.5	Discussion	76
4	Fermi Bubbles as Galactic wind	79
4.1	Introduction	81
4.2	Simulation	82
4.2.1	Initial set up	82
4.2.2	Code settings	83
4.2.3	Injection parameters	84
4.3	Results: wind & bubble morphology	85

4.4	Results: emission in different wavebands	88
4.4.1	X-ray	88
4.4.2	Microwave Haze	91
4.4.3	γ -ray	93
4.4.3.1	Hadronic emission	93
4.4.3.2	Leptonic	94
4.5	Results: kinematics	95
4.6	Discussion	99
4.6.1	Diffusion of CRs	99
4.6.2	Note on Loop-I	99
4.6.3	Kinematics of the cold/warm gas	99
4.6.4	Effects of the injection geometry and CGM rotation	100
4.6.5	Effects of CR and magnetic pressure	100
4.7	Summary	100
5	Fermi Bubbles: clues from O VIII/O VII	103
5.1	Introduction	105
5.2	Galactic halo distribution	106
5.3	Simulation details	109
5.3.1	Star formation driven wind (SFW)	110
5.3.2	Accretion wind (AGNW)	111
5.4	Analysis Tools	111
5.4.1	Projection tool	111
5.4.2	Oxygen emission lines	112
5.5	Results	112
5.6	Discussion	118
5.6.1	Effects of cosmic ray and magnetic pressure	118
5.6.2	Enhanced emission beyond FBs	118
5.6.3	Effects of conduction	118
5.6.4	Electron-proton energy equilibration	119
5.6.5	AGNW vs. SFW	120
5.7	Summary	121
6	Summary and Conclusion	123
A		129
A.1	Rotation curve and gravitational acceleration	129
A.2	Modified NFW profile	131
A.3	Initial density setup	131
B		135
B.1	Projection effects	135
C		139
C.1	Injection radius for SNe driven winds	139
C.2	Electron temperature for high luminosity winds	139

Chapter 1

Thesis objectives

1.1 Motivation

Galaxies trace the large scale structure of the Universe as they are frozen in the co-moving space. Studying the structure and dynamics of the Universe, therefore, essentially entails the study of the galaxies. While the position of galaxies traces large scale structure, the physical conditions such as the baryonic density and the flow of matter at any point of the Universe are determined by the evolution of galaxies. For example, a larger number of elliptical galaxies at the centre of galaxy clusters than the outskirts implies the merging of smaller structures to form larger objects, which indicates a hierarchical formation scenario. The number of galaxies at different mass range also indicates characteristic matter perturbations in the primordial Universe. However, such tracers are also affected by the internal evolution of galaxies. For example, variation of star formation due to local interstellar conditions could affect the stellar mass of a galaxy and may not represent the actual characteristic matter fluctuations of the Universe. It is, therefore, important to understand the internal evolution of galaxies.

However, given the current breadth and width of this field which requires accurate knowledge of atomic physics to large scale dynamics of the galaxies, it is impossible to grasp all aspects in a single study. Consequently, this thesis contains only a narrow aspect of the evolution of galaxies.

1.2 Review of structure formation

The idea of dark matter in its present context was first put forward by [Zwicky](#) in 1937. He found that the luminous mass contained in galaxies in the Coma cluster was insufficient to explain the velocity dispersion of the member galaxies. The corresponding mass to light ratio needed to explain the velocity dispersion was ~ 500 . However, it was only in 1960s when [Rubin & Ford](#) studied the rotation curves of nearby galaxies and showed the need for such unseen matter even in those galaxies. Cosmologists, who were struggling to explain structure formation with baryonic-only models so far, realised immediately that the incorporation of a gravitationally dominating component, such as

the dark matter, simplifies the problems greatly. It was noticed that the fluctuations in the number of galaxies within randomly chosen 10 Mpc volumes is almost 100% (Davis & Peebles, 1983), whereas the cosmic microwave background (CMB) anisotropies show a temperature fluctuation $\delta T/T \lesssim 10^{-4}$ (Uson & Wilkinson, 1982). If the baryons were the only constituents of the universe, then the temperature fluctuation of the CMB should match the fluctuations in the galaxy numbers. The only way to solve this problem was to assume another component of matter that gravitationally dominates the baryonic matter but does not have electromagnetic interactions. Fluctuations of such matter could form and grow even before the radiation-baryon equality, and therefore, can enhance the baryonic fluctuations to form more clustered galaxies than expected from the CMB anisotropy (Peebles, 2017). Since then, the idea of a dark matter dominated universe has flourished to explain more and more observations and has prevailed in terms of its predicting power. It was not, however, clear what the composition of the dark matter is. The current understanding of the structure formation process favours dark matter particles that have low velocity dispersion (or famously ‘cold’). An excellent discussion on the nature of dark matter and the structure formation can be found in Blumenthal et al. (1984) and Narlikar & Padmanabhan (2001). To put my thesis work in context, I provide a very brief introduction of the structure formation in this section.

1.2.1 Formation of dark matter haloes

It is understood that galaxies reside inside the potential wells of dark matter haloes. The formation of such haloes was initiated by random tiny fluctuations of dark matter after $\sim 40,000$ years of the ‘Big Bang’ when the matter energy density became greater than the radiation energy density. Initially, these small fluctuations grew linearly, but with time, non-linear processes took over to determine the fate of the collapsed objects. Press & Schechter (1974) realised that currently collapsed haloes could be the peaks of the primordial Gaussian random density fluctuation field and the condensation of individual haloes can be described as a self-similar evolution of this field. This led them to formulate a simple mass distribution function of these collapsed objects that is a power law at small mass scales but falls off exponentially at large masses. It has been seen in more recent numerical simulations (viz. Somerville & Primack, 1999; Springel et al., 2005)) that the form of this function holds true despite the simplicity of its derivation.

Once virialised, i.e., when the kinetic energy of the inflowing matter converts into random motion of the dark matter particles, further gravitational collapse of the object is prevented. Such haloes, therefore, can be characterised by a radius within which the virial theorem holds. The virial radius (r_{vir}) for a halo of mass M can be written as

$$r_{\text{vir}} = \left(\frac{3M}{4\pi\bar{\rho}\Delta} \right)^{1/3}, \quad (1.1)$$

where, Δ represents the average overdensity inside the halo compared to the mean density of the Universe. The dark matter profile inside such a halo can be described as (Navarro et al., 1997)

$$\rho(r) = \frac{4\rho_s}{(r/r_s)(1+r/r_s)^2}, \quad (1.2)$$

where, ρ_s is the dark matter density at $r = r_s$, $r_s = r_{\text{vir}}/c$ and c is the compactness parameter of the dark matter distribution. Although, recent simulations agree more with the Einasto profile (Prada et al., 2006), NFW profile is still preferred in many calculations due to its simple analytical form. This density distribution will be used as a background dark matter potential in next chapters.

1.2.2 Formation of gaseous haloes

Since the baryonic matter decoupled from radiation field in the Universe much after the matter-radiation equality, the dark matter fluctuations could grow to large amplitudes by this time while the baryons were still coupled to the radiation. Since the pressure of the radiation-baryon fluid was too large to form any structures, it is, therefore, fair to assume that the baryons were initially distributed more uniformly on top of the larger dark matter fluctuations. The baryons, with only a sixth of the matter density¹ and hence gravitationally sub-dominant, fell into the gravitational potential of dark matter overdensities. The gravitational energy of the infalling baryon, thereafter, got converted into its thermal energy via accretion shocks. The temperature of such a gaseous halo (*aka*, virial temperature) can be roughly estimated as

$$T_{\text{vir}} \sim \frac{\mu m_p}{k_B} \frac{GM_{\text{vir}}}{r_{\text{vir}}}, \quad (1.3)$$

where, for convenience, we have used M_{vir} to represent the total mass of the halo. Unlike the collisionless violent relaxation which randomised the dark matter, this thermal energy can be radiated away by the gas. This makes the problem somewhat more complicated but leads to interesting manifestations of observed galaxies. We can in fact, arrive at some basic conclusions about the nature of this radiating gaseous halo just from simple considerations.

Let us assume a simple flat universe with $\Omega_{m0} = 0.3$ (ratio of matter density to critical density), Hubble constant $H_0 = 100 h \text{ km s}^{-1} \text{ Mpc}^{-1}$, $h = 0.7$ and the dark matter halo overdensity $\Delta = 200$ at present (Bullock et al., 2001). Note that these values are only indicative and will be updated with proper values in exact calculations. The virial radius and virial temperature can be then written as (see Eq. 1.1 and 1.3)

$$\begin{aligned} r_{\text{vir}} &= 310 M_{\text{vir},12}^{1/3} (1+z)^{-1} \text{ kpc}, \\ T_{\text{vir}} &\sim 1.5 \times 10^6 M_{\text{vir},12}^{2/3} (1+z) \text{ K}, \end{aligned} \quad (1.4)$$

where, $M_{\text{vir},12} = M_{\text{vir}}/10^{12} M_{\odot}$ and z is the redshift at which the halo has virialised. Now, if we assume that the total virialised gas mass is $M_{\text{gas}} = f_{\text{gas}} M_{\text{vir}}$, then the average gas density is

$$n_{\text{gas}} = \frac{3 M_{\text{gas}}}{4\pi \mu m_p r_{\text{vir}}^3} = 5.5 \times 10^{-5} f_{\text{gas},0.1} (1+z)^3 \text{ cm}^{-3}, \quad (1.5)$$

where, $f_{\text{gas},0.1} = f_{\text{gas}}/0.1$. The radiative cooling time for this gas can be estimated as

$$t_{\text{cool}} \sim \frac{\frac{3}{2} k_B T_{\text{vir}}}{n_{\text{gas}} \Lambda(T)} = 12 M_{\text{vir},12}^{2/3} f_{\text{gas},0.1}^{-1} (1+z)^{-2} \Lambda(T)_{-23}^{-1} \text{ Gyr}. \quad (1.6)$$

¹According to the energy budget (*WMAP* results) in the Universe, matter forms only $\approx 28\%$ of the Universe and out of which only $\approx 16\%$ is baryonic. This is represented by the universal baryonic fraction f_b .

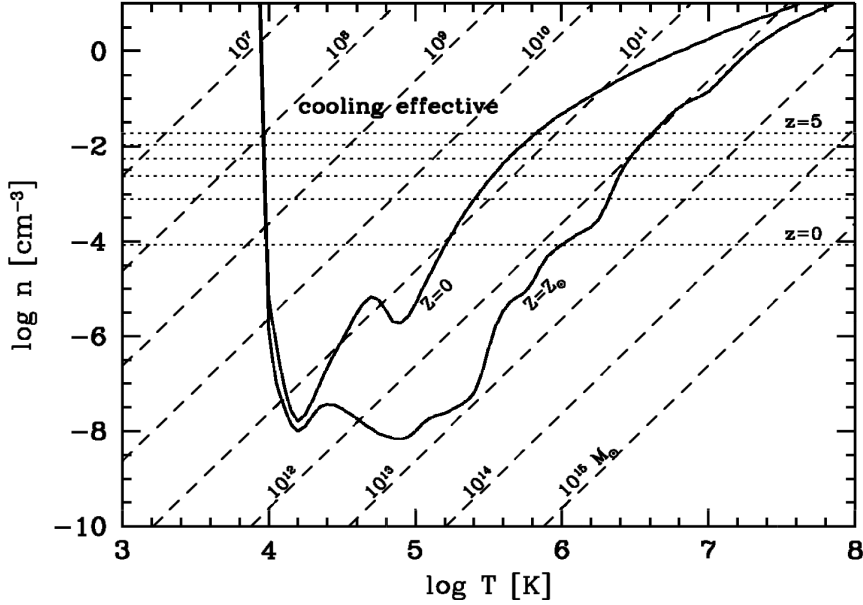


Figure 1.1: $n_{\text{gas}} - T_{\text{vir}}$ parameter space showing the effectiveness of gas cooling in gaseous haloes at different gaseous mass (M_{gas} ; dashed lines) and redshift (dotted lines). The solid lines represent $t_{\text{cool}} = t_{\text{ff}}$ for primordial gas metallicity ($Z = 0$) and Solar metallicity ($Z = Z_{\odot}$). Image credit [Mo et al. \(2010\)](#).

Here, $\Lambda(T) = 10^{-23} \Lambda(T)_{-23} \text{ erg s}^{-1} \text{ cm}^3$ is the cooling function. The free-fall time for this gas under the influence of dark matter potential is

$$t_{\text{ff}} \sim \sqrt{\frac{3\pi}{32 \rho_{\text{DM}} G}} = 2.8 (1+z)^{-3/2} \text{ Gyr}, \quad (1.7)$$

which produces

$$\frac{t_{\text{cool}}}{t_{\text{ff}}} \sim 1.3 M_{\text{vir},12}^{2/3} f_{\text{gas},0.1}^{-1} (1+z)^{-1/2} \Lambda(T)_{-23}^{-1}, \quad (1.8)$$

where, we have used the dark matter density, $\rho_{\text{DM}} = 3M_{\text{vir}}/4\pi r_{\text{vir}}^3$.

Eq. 1.8 shows that for a galaxy with total mass $\gtrsim 10^{12} M_{\odot}$, virialised at $z = 0$, can not radiate away the thermal energy content of its gaseous halo and will therefore retain a hot ($\gtrsim 10^6$ K) and low density ($\sim 10^{-4} m_{\text{p}} \text{ cm}^{-3}$) halo. A better representation of the above discussion containing a more appropriate treatment of the cooling function has been shown in Figure 1.1. It is interesting to notice that for primordial metallicities, galaxies with $M_{\text{gas}} \lesssim 10^{11} M_{\odot}$ ($M_{\text{vir}} \lesssim 10^{12} M_{\odot}$ for $f_{\text{gas}} = 0.1$) are able to radiate away the gaseous thermal energy at all redshifts. This is the reason that galaxy clusters and massive galaxies $M_{\text{vir}} \gtrsim 10^{12} M_{\odot}$ are expected to contain their gaseous halo ([Rees & Ostriker, 1977](#); [White & Rees, 1978](#)). It is however difficult for a halo with $M_{\text{gas}} \sim 10^8 M_{\odot}$ virialised at $z = 5$ to lose its thermal energy content and collapse. This is because of the photo-heating of the stars that keeps the gaseous halo warm at 10^4 K. Note that in above calculation, we have used the fact that all gaseous haloes initially reach virial temperature (T_{vir}) before cooling takes place. In actual situations for low mass galaxies, cooling takes place much earlier than the gaseous halo to reach its virial temperature.

Therefore, the accretion is expected to be primarily in the form of cold streams than via accretion shocks (Birnboim & Dekel, 2003; Dekel & Birnboim, 2006).

1.2.3 Observations of gaseous halos

The observational evidence of X-ray emitting, hot ($T \sim 10^7$ K) intra-cluster medium of galaxy clusters ($M_{\text{vir}} \sim 10^{15} M_{\odot}$) confirms the validity of the above simple argument and indicates that such halo gases should also be found around massive galaxies like our own Milky Way (MW). Numerical simulations of galaxy formation also showed the existence of hot ($T \sim 10^6$ K) circumgalactic medium (CGM) around massive galaxies (Toft et al., 2002; Crain et al., 2010; Crain et al., 2013). However, the first attempts to detect such gaseous halo in galaxies using x-ray emission have been futile. It was partly because of the low emission measure ($EM \sim n_{\text{gas}}^2 r_{\text{vir}} = 10^{-3} f_{\text{gas},0.1}^2 M_{\text{vir}}^{1/3} (1+z)^5 \text{ cm}^{-6} \text{ pc}$) of the CGM and partly due to the virial temperature falling in the soft X-ray emission band (0.3–2.0 keV) where the sky is dominated by foreground contamination, such as the emission from the local bubble.

The first indirect clues that MW has an extended low density medium came from the head-tail structure of high latitude HI clouds (Peek et al., 2007; Putman et al., 2011) and lack of HI in satellite galaxies (Blitz & Robishaw, 2000). These were attributed to the effect of ram pressure arising from the motion of HI clouds and satellite galaxies through a low density ($\sim 10^{-4} \text{ cm}^{-3}$) medium at a height of $\sim 50 - 100$ kpc. Detection of two giant (~ 10 kpc) γ -ray bubbles, called the Fermi Bubbles (to be discussed later in detail) towards the centre of our galaxy (Su et al., 2010) also provides clues that hot gas is being sent into the extended gaseous halo. It was only recently that the CGM of MW has been observed in both absorption and emission of highly ionised Oxygen *viz.*, O VII and O VIII lines (Gatto et al., 2013; Fang & Jiang, 2014; Miller et al., 2016; Nicastro et al., 2016). The temperature of the MW halo gas has also been estimated to be $\approx 2 \times 10^6$ K which is very close to the expected virial temperature (T_{vir}) of MW.

Detection of halo gas around other massive galaxies has also been claimed (O’Sullivan et al., 2001; Strickland et al., 2004b; Li & Wang, 2007). However, the sample galaxies are either surrounded by a dense environment (like intra-cluster medium) where a separate CGM is not very clear or they are associated with star formation activities in those galaxies. The first evidence of a hot CGM came from the X-ray observations of field galaxies NGC1961 and NGC12591 (Anderson & Bregman, 2010; Dai et al., 2012). Bogdán et al. (2013) found that the amount hot halo gas in NGC1961 and NGC6753 is comparable to the stellar mass in those galaxies. The total baryonic fraction in those galaxies was found to be ~ 0.1 which is very close the universal baryonic fraction $f_b \approx 0.16$. This raised hope that the ‘missing baryons’ in massive galaxies are in the form of hot halo gas. However, the observational evidence for a baryonically closed halo is far from being certain.

Interestingly, more recent observations of extended, ionised, warm ($\sim 10^4$ - 10^5 K) gas around galaxies have given a boost to find the missing baryons (Tumlinson et al., 2011; Werk et al., 2013, 2014). Simple estimates show that this warm gas, together with the stars, can make up most of the missing baryons in these galaxies (Werk et al., 2014). The estimates, however, depend on the exact nature of such warm gas (i.e. density, volume filling factor etc.) which is still being investigated (Stern et al., 2016; McCourt et al., 2016).

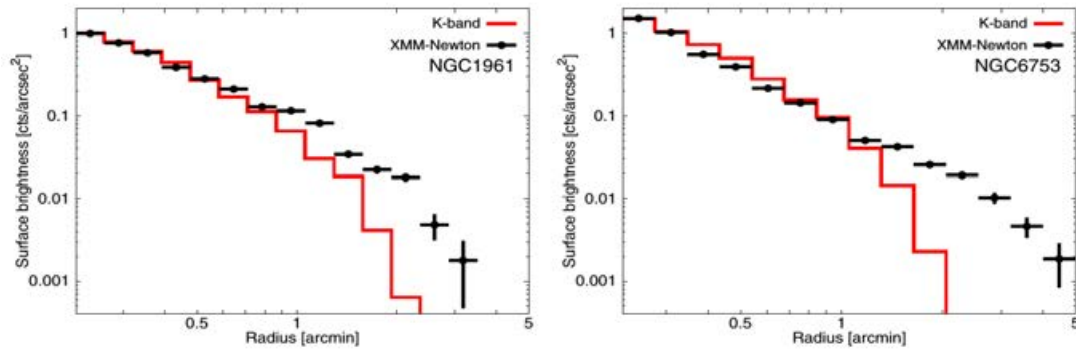


Figure 1.2: Angle averaged surface brightness profiles of NGC1961 (left panel) and NGC6753 (right panel). The red line shows normalised K-band light profile (representation of stars) and the black line shows 0.3 – 2.0 keV surface brightness profile. An excess of x-ray emission profile clearly indicates presence of diffuse-hot gas corresponding to halo gas or CGM. In these figures, $1'$ corresponds to ≈ 16.2 kpc for NGC1961 and ≈ 12.7 kpc for NGC 6753. This figure has been reproduced from [Bogdán et al. \(2013\)](#)

1.2.4 Hot and cold mode accretion

The above discussion suggests that for galaxies with $M_{\text{vir}} \gtrsim 10^{12} M_{\odot}$, the halo gas, heated by the accretion shock, is not able to cool within a dynamical time-scale. However, for dark matter haloes with $10^{10} \lesssim M_{\text{vir}} \lesssim 10^{12} M_{\odot}$, the accretion shocked gas is able to radiate away a good fraction of its thermal energy (see Eq. 1.8) so that it loses its pressure support. This gas, thereafter, falls down to the centre of the dark matter gravitational potential where it fragments and forms stars. This form of gas accretion is called the ‘hot-mode accretion’ ([Bertschinger, 1985](#)).

Although it is particularly true that the average cooling time of the halo gas for massive galaxies ($\gtrsim 10^{12} M_{\odot}$) is insufficient to radiate away most of the thermal energy, it is possible that the central part of the halo gas has a higher density compared to the outskirts and therefore cools efficiently. Such strong cooling would lead to fragmentation of the halo gas and, therefore, it would settle down at the bottom of potential. This is termed as the ‘cooling flow’. The situation is very probable in galaxy clusters where the central density can be high enough. Observations of the galaxy clusters however reveals negligible amount of cooling compared to expectations. This issue is termed as the ‘cooling flow problem’. Most arguments to solve this problem involves additional heating from Active Galactic Nuclei (AGN) in the central massive galaxy.

Another effective way to accrete more material into the galaxy is to accrete via ‘cold-mode’. If the infalling material is cold, dense and clumpy or filamentary, it does not undergo any accretion shock. Therefore, this gas can almost free-fall all the way to the bottom of the gravitational well without facing any pressure barrier even if there is a hot halo gas already present ([Birnboim & Dekel, 2003](#); [Kereš et al., 2005](#)). This is the process by which massive galaxies are thought to have accreted most of their mass at $z \gtrsim 2$ ([Dekel & Birnboim, 2006](#)). Observationally, there are a number of examples where signatures of cold mode accretion into galaxies have been found ([Kacprzak et al., 2015](#)). One problem with the cold-mode is that the cold clumps or filaments may

suffer from hydrodynamic instabilities while moving through a low density hot gas which can lead to disruption of the cold gas. The tension between the theoretical expectation and observational facts is now being actively investigated by performing idealised simulations of motion of a cold cloud through hot halo gas (Cooper et al., 2009; Armillotta et al., 2016).

1.2.5 Stellar to halo mass relation

It is believed that the accreted cold gas after settling down at the bottom of the gravitational potential would become Jeans unstable due to its own gravity and collapse to even denser clumps where they finally start forming stars (Kennicutt, Jr., 1998; Mo et al., 2010). Naively, one would expect that the amount of stars formed (M_\star) is a constant fraction of the total gas mass (M_{gas}) available to the galaxy i.e. $M_\star = \epsilon M_{\text{gas}}$, where ϵ is the star formation efficiency. Extending it to another simple assumption that the total gas available to the galaxy (f_b) is the universal baryonic fraction (≈ 0.16) of the total dark matter mass (M_{vir}), one can write

$$M_\star = \epsilon M_{\text{gas}} \approx \epsilon f_b M_{\text{vir}}. \quad (1.9)$$

This tells us that the stellar to dark matter ratio should be a constant value across different galaxies. The exact relation however depends of the values of ϵ and somewhat on f_b which are difficult to estimate as they depend on the sub-parsec scale physics of star formation and cosmological infall. Some basic conclusions about the formation of stars in galaxies can still be obtained from the statistical properties of galaxies before going into the details of complex star formation process. For example, estimation of M_\star/M_{vir} from the observed galaxies can give us useful information about the product of ϵ and f_b .

Observationally it is, however, challenging to estimate the dark matter mass M_{vir} of a galaxy for a given M_\star . There is, however, one way in which the ratio of these two quantities can be found in a statistical sense. It is known as the *abundance matching* technique. The idea is simple but effective. It is assumed that a virialised dark matter halo (which may contain sub-haloes) contains one central galaxy. One can, then, compare the dark matter halo distribution Φ_{dm} (density of haloes per unit mass bin) obtained either by analytical calculations (Press & Schechter, 1974) or by simulations (Springel et al., 2005) at any mass M_{vir} to the stellar mass distribution Φ_\star of the observed galaxies at that mass to solve for the stellar to dark matter mass ratio (Moster et al., 2010; Behroozi et al., 2010).

An example of such a technique has been shown in Fig. 1.3, where $M_h = M_{\text{vir}}$ represents the dark matter halo mass. It shows that the $M_\star/M_{\text{vir}} = \epsilon f_b$ is not a constant value; rather it initially rises with the dark matter mass, peaks at $M_{\text{vir}} \sim 10^{12} M_\odot$ (known as L_\star galaxies) and then decreases for heavier haloes. In an ideal situation, where the total baryon content in the halo is equal to the universal baryon fraction ($f_b = 0.16$) and all the baryons are converted to the stars, $\log_{10}(M_\star/M_{\text{vir}}) = -0.8$. It is clear that even galaxies with most efficient star formation ($M_{\text{vir}} \sim 10^{12} M_\odot$) are not able to convert all of their baryons to stars. Moreover, the star formation efficiency is poorer on the either side of the peak. A similar conclusion can also be obtained by studying the stellar luminosity function (Somerville & Primack, 1999).

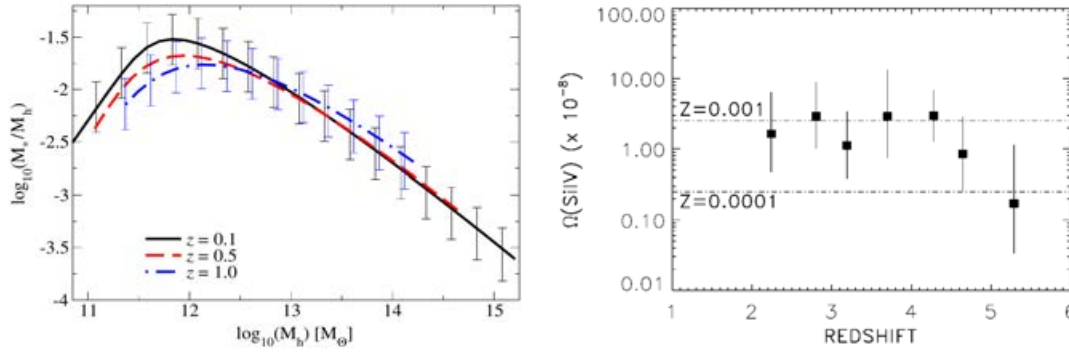


Figure 1.3: *Left panel:* stellar mass to halo relation (SMHR) obtained by using abundance matching technique at different redshifts. Points with error bars are observed data and lines represent corresponding best fit values indicating that the star formation efficiency depends on the galaxy mass. M_h represents the dark matter halo mass and same as M_{vir} adopted in the text. *Right panel:* fraction of Si IV ion, a tracer of metallicity, in the IGM compared to critical density at that redshift. Standard values for this quantity for different metallicities (in units of Z_\odot) have been shown by the dashed lines. The data points are of clear indication of the presence of metals in IGM even at high redshifts. Figures have been reproduced from Behroozi et al. (2010) and Songaila (2001).

1.2.6 Requirement of outflow

While massive galaxies ($\gtrsim 10^{12} M_\odot$) can contain a large fraction of their baryons in hot-gaseous halo form (though it may not account for all the baryons; see section 1.2.2), low mass galaxies are not expected to form such haloes as they accrete via ‘cold mode’ and, therefore, can keep their baryonic fraction. This is clearly not the case, given that the luminous mass in most of the low mass galaxies do not contribute much to the baryonic fraction. There are, therefore, two ways that this issue can be resolved.

- **Preventive**, in which the gas is either prevented from falling into the galaxy by resistance provided by the halo gas or removed from the galaxy by ram pressure stripping due to the motion through dense environments thus suppressing star formation.
- **Ejective**, in which the gas is ejected out of the galaxy or heated up by some form of energy source at the centre of the galaxies to suppress star formation. This might be due to energy injection by supernovae or AGN activity at the centre.

While the preventive method has been shown to be the main reason behind shutting down star formation massive red galaxies and dwarf satellite galaxies (Peng et al., 2015; Feldmann et al., 2016), it is not able to explain the presence of metals in IGM. The ejective method, on the other hand, can easily explain this feature of the IGM. The reason is simple to understand. In an ideal situation where galaxies evolve separately and do not interact with outside (other than infalling material), the IGM would contain only pristine gas. The detection of metal lines in Ly- α forest, however, showed that the galaxies do interact with the IGM and throw metal enriched gas into it (Cowie et al., 1995; Nath & Trentham, 1997; Songaila, 2001). Since metals come from stars and supernovae

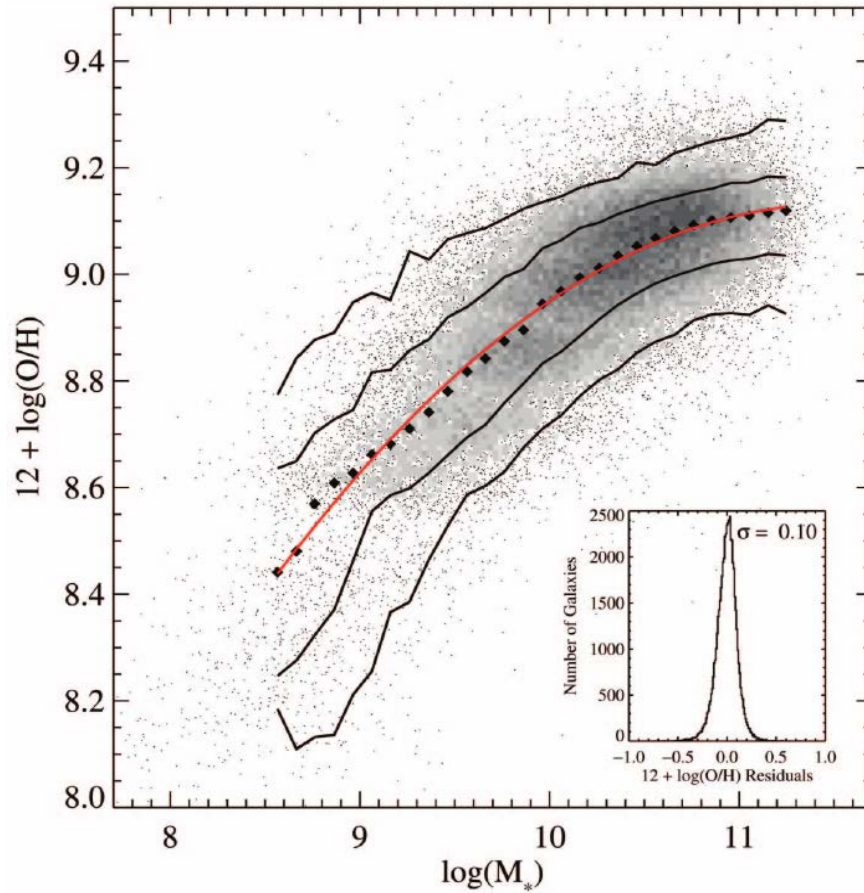


Figure 1.4: Relation between stellar mass (M_* , in units of M_\odot) and gas-phase metallicity of $\sim 53,000$ ($z \lesssim 0.3$) star forming galaxies. The gas-phase metallicity is represented by the oxygen abundance of that galaxy. In case of a Solar metallicity, $12 + \log[O/H] = 8.69$ (Asplund et al., 2009). The filled squares represent median value of the data points (black dots) at that mass bin (width = 0.05 dex). The black solid lines encloses 68% and 95% of the data. The red line is a polynomial fit to the. Inset shows the residual of the fit. Figure credit- Tremonti et al. (2004)

shocks, and supernovae activity can also drive mass away from galaxy, a supernovae-driven ejective method (outflow) seemed very likely and has been explored by early semi-analytical calculations (Kauffmann et al., 1993; Cole et al., 1994; Somerville & Primack, 1999). In fact, these were not the first instances when an ejective mechanism has been incorporated in the context of structure formation. Mathews & Baker (1971); Larson (1974) also used this idea of supernovae driven ejective mechanism, known as ‘galactic outflow’ or ‘galactic wind’, to explain the lack of gas in elliptical galaxies.

Another fact that fuelled the idea of supernovae driven galactic outflow is the discovery of mass metallicity relation (Tremonti et al., 2004, see figure 1.4). It shows that the gas-phase metallicity increases with stellar mass for low mass galaxies, but remains flat for massive galaxies. It means that low mass galaxies tend to lose more metals (and therefore, mass) compared to higher mass galaxies. This, together with previous arguments, makes galactic outflow ubiquitous in the field of formation and evolution of galaxies. Since, this thesis is directly related to studying the outflows, let us go into the details of the description of galactic outflows in the next section.

Note that the supernovae driven outflow seem to work well only for low mass galaxies ($M_{\text{vir}} \lesssim 10^{12} M_{\odot}$). The problem with massive galaxies, however, is that the deep gravitational potential of massive galaxies do not allow ‘galactic wind’ to escape the galaxy and requires an alternative source of large amount of energy to explain the discrepancy in stellar mass to halo relation. Observations of super-massive black holes ($M \sim 10^6 - 10^{10} M_{\odot}$) at the centre of almost every massive galaxy gave rise to the hope that these black holes can supply required amount of energy to drive gas out of galaxies or heat up the material to suppress star formation. Though the inclusion of energy from black holes has been successful in explaining the stellar mass function at higher mass end, the prescription to include such an energy source is arbitrary and still being investigated.

1.3 Description of galactic outflow

It follows from the previous discussion that the phenomenon of outflow, be it to eject or heat up the interstellar medium (ISM), is required to explain observations of galaxies on both lower and higher side of the L_{\star} galaxies. The driving engine is believed to be supernovae in low mass galaxies and AGN in massive galaxies. Let us, therefore, discuss different sources and driving mechanisms of outflows in this section for an overview of the topic.

1.3.1 Supernovae (SNe) driven outflows

The first observational clue that gas can be driven out from galaxies came from van Woerden et al. in 1957 when they found two expanding arms at the centre of our Galaxy. The firm evidence that supernovae can drive large scale galactic outflows, however, came from the observation of a nearby galaxy M82 when a remarkable similarity between the radio and optical spectra of the central few kpc of M82 and the crab nebula was found (Lynds & Sandage, 1963; Burbidge et al., 1964). It was also found that the optical emitting filaments are expanding on both sides of the centre with a velocity of $\sim 10^3$ km s⁻¹. This led theorists to consider supernovae driven wind (SNW) as an important

mechanism in galaxy formation and evolution. Though initial applications of the SNW was to explain the lack of ISM in dwarf elliptical galaxies (Mathews & Baker, 1971; Larson, 1974), it was quickly incorporated into the galaxy formation and evolution models as an important mechanism. In order to understand the impact of a SNW, let us look at the energetics and other conditions that can drive a successful supernovae driven wind.

1.3.1.1 Energetics

Recent stellar population synthesis models have been able to accurately predict the energetics of stellar wind and supernovae as well as the evolution of spectra from such a population either for an instantaneous burst of star formation or for a continuous star formation (Leitherer et al. 1999; *starburst99*). Generally, the properties of the population is more or less determined by the stellar winds from Wolf-Rayet and O/B-type stars and other massive stars for first ~ 3 -4 Myrs of the evolution, after which core collapse supernovae take over (Figure 114 in *starburst99*). For an instantaneous star-burst case, the mechanical energy output drops after ~ 30 Myr when almost all the massive stars ($\gtrsim 8 M_{\odot}$) have undergone core-collapse. However, for continuous star formation, the mechanical energy output becomes almost constant and remains so after ~ 10 Myrs. For a stellar population, that is characterised by Salpeter initial mass function (IMF) with a low mass limit of $M_{\text{low}} = 1 M_{\odot}$ and maximum stellar mass of $M_{\text{high}} = 100 M_{\odot}$, the mechanical energy and mass output via both stellar wind and SNe in case of continuous star formation (star formation rate = SFR) are given as

$$\begin{aligned} \mathcal{L}_{\star} &\approx 7 \times 10^{41} \times \frac{\text{SFR}}{M_{\odot} \text{ yr}^{-1}} \text{ erg s}^{-1} \\ \dot{M}_{\star} &\approx 0.3 \frac{\text{SFR}}{M_{\odot} \text{ yr}^{-1}} M_{\odot} \text{ yr}^{-1} , \end{aligned} \quad (1.10)$$

for a population of age $\gtrsim 5$ Myr. For a population with $M_{\text{low}} = 0.1 M_{\odot}$, as observed in M82, the above values have to be multiplied by a factor of 0.4. Note that, all of this mechanical energy does not necessarily contribute towards driving a wind; most of it gets radiated away in the ISM itself as will be discussed later.

Apart from generating the mechanical energy, the stars also produce photons that can contribute to a radiation driven wind. The rate at which the stellar population injects momentum via radiation is $\dot{P}_{\text{rad}} = \tau L_{\text{bol}}/c$, where, τ is the optical depth of the ISM surrounding the stars, $L_{\text{bol}} \sim 7 \times 10^{43} \text{ SFR}/M_{\odot} \text{ yr}^{-1}$ is the bolometric luminosity and c is the speed of light in vacuum. In an optical thick case ($\tau \gtrsim 1$), the momentum injection rate is, therefore, given as

$$\dot{P}_{\text{rad}} \sim 2 \times 10^{33} \frac{\text{SFR}}{M_{\odot} \text{ yr}^{-1}} \text{ dyne} . \quad (1.11)$$

Now, for comparison, the rate of mechanical momentum injection is

$$\dot{P}_{\text{mech}} \sim \sqrt{2\dot{M}_{\star}L_{\star}} \approx 5 \times 10^{33} \frac{\text{SFR}}{M_{\odot} \text{ yr}^{-1}} \text{ dyne} . \quad (1.12)$$

This implies that radiation pressure can also be important while driving wind. However, the effect of radiation highly depends on whether the wind is optically thick or not.

Moreover, it has been shown that the radiation pressure drops several factors below the thermal pressure for $t \gtrsim 4$ Myr when the first SNe start to go off (Gupta et al., 2016). A study of radiation driven galactic winds is not a part of this thesis work. See papers by Murray et al. (2005); Chattopadhyay et al. (2012); Zhang & Thompson (2012) for details on the radiation driven winds.

1.3.1.2 Condition for a wind

We must, however, remember that not all of the mechanical energy that is generated by the stellar population is useful in driving a wind. Most of this energy gets radiated away over a radiation time-scale t_{cool} once the shock starts travelling through the ISM. A fraction of the energy can still be retained in the form of dilute and hot gas behind the cooled shell of supernova remnants. This fraction is almost (few-10)% of the total SN energy i.e. 10^{51} erg (Larson, 1974; Dekel & Silk, 1986; Sharma et al., 2014b; Gupta et al., 2016). The retained fraction of the energy can be even larger if the subsequent SNe heat up previous supernovae remnants by merging together thus minimising the radiative loss. Larson (1974) defined a time-scale, t_{snr} , after which this effect will be important to scale up the retained heat by the hot-bubble. This time-scale, therefore, depends on the the SN rate density for a medium. By assuming that the radiative loss will be important only if $t_{\text{cool}} < t_{\text{snr}}$, he estimated a critical star formation rate density

$$S_{\text{crit}} \approx 2 \times 10^{-8} n^{1.76} \text{ M}_{\odot} \text{ yr}^{-1} \text{ pc}^{-3} \quad (1.13)$$

below which the radiative cooling will take away most of the energy and above which the radiation loss can be neglected. He also showed that for $\text{SFR} > S_{\text{crit}}$, the retained energy can be even $> 20\%$ of the SN energy. Note that this calculation is for a constant background density of $n \times m_p \text{ g cm}^{-3}$. For a porous medium with a porosity f_p , the above equation can be modified roughly by simply changing n to $n(1 - f_p)$ which represents the average density of the medium. The above equation can be turned into a star formation rate surface density as

$$\Sigma_{\text{crit}} \sim 0.2 n^{1.76} \text{ M}_{\odot} \text{ yr}^{-1} \text{ kpc}^{-2}, \quad (1.14)$$

where we have assumed $f_p \approx 0.8$ following Mckee & Ostriker (1977) and a typical gas-disc thickness of 200 pc. This value is surprisingly close to the observed threshold

$$\Sigma_{\text{th}} \approx 0.1 \text{ M}_{\odot} \text{ yr}^{-1} \text{ kpc}^{-2} \quad (1.15)$$

for the presence of a galactic wind in disc galaxies (Heckman, 2002). Given the simplicity of the model, the outcome is rather surprisingly close to the observed value.

We can now easily estimate if a galaxy is likely to have a wind or not. For example, our galaxy has a total $\text{SFR} \approx 2 - 3 \text{ M}_{\odot} \text{ yr}^{-1}$ within a radius of $\sim 10 \text{ kpc}$ which means $\Sigma \sim 10^{-2} \text{ M}_{\odot} \text{ yr}^{-1} \text{ kpc}^{-2}$ much less than the threshold value. However, if we consider the central region of our galaxy where the star formation rate is $\approx 0.1 \text{ M}_{\odot} \text{ yr}^{-1}$ within a region of $\sim 100 \text{ pc}$ radius (Yusef-Zadeh et al., 2009), the star formation rate density $\Sigma \sim 3 \text{ M}_{\odot} \text{ yr}^{-1} \text{ kpc}^{-2}$ much higher than the threshold value for producing a wind. Therefore, we can expect a galactic wind from the centre of our Galaxy but not from the whole disc. For star-burst galaxies, this threshold is easily exceeded for the whole galaxy, therefore, giving rise to galaxy-wide outflows.

1.3.1.3 A spherical cow

Now that we have an understanding of the SNe energetics, and the radiation loss in the ISM, we can try to estimate the extent to which galactic winds can be important. The following picture is a very simplified picture of a galactic wind and has been adapted from [Larson \(1974\)](#).

Let us consider a spherically symmetric galaxy with a very simple configuration that its total baryonic mass ($\approx 1/6 M_{\text{tot}}$) is divided equally into stellar and gaseous form i.e. $M_{\star} = M_{\text{gas}} \approx M_{\text{tot}}/12$. Now, if we consider that there is one supernova (SN) for every $100 M_{\odot}$ of stars formed (for a typical mass function) and each SN produces roughly 10^{51} erg energy, then the total SNe energy that the galaxy has produced while building up its stellar stock is $\approx 10^{49}(M_{\star}/M_{\odot})$ erg. Let us assume that $\approx 10\%$ of this energy survives the radiation loss and is trapped within the galaxy unless the hot gas is mechanically thrown away by outflows ([Dekel & Silk, 1986](#); [Sharma et al., 2014b](#); [Mukherjee et al., 2017](#)). Therefore, the total amount of SNe energy stocked up in the galaxy is $E_{sn} \approx 10^{48}(M_{\star}/M_{\odot})$ erg. Now, if this energy is coupled to the gas and drives a wind, the wind velocity is

$$v_w = \sqrt{\frac{2E_{sn}}{M_{\text{gas}}}} \approx 220 \left(\frac{M_{\star}}{M_{\text{gas}}} \right)^{1/2} \text{ km s}^{-1} . \quad (1.16)$$

Whether, this wind is able to escape the galaxy is determined by the escape velocity $v_e = \sqrt{2GM/R}$, where, M is the total mass (including dark matter) within a radius R . For a typical elliptical galaxy, $M = M_{\text{tot}} \sim 10^{11} M_{\odot}$ for $R \sim 10$ kpc, the escape velocity is then

$$v_e \sim 300 \left(\frac{M_{\text{tot}}}{10^{11} M_{\odot}} \right)^{2/3} \text{ km s}^{-1} , \quad (1.17)$$

where, we have used the fact that $v_e \propto M_{\text{tot}}^{2/3}$ for a constant stellar density in elliptical galaxies. The wind will be able to escape if $v_w > v_e$, which leads to an upper limit on the total mass, below which the galaxy is severely affected by SNW,

$$M_{\text{tot}} \lesssim 7 \times 10^{10} M_{\odot} . \quad (1.18)$$

Despite the simplicity in arriving at the results, we notice that this upper limit is within an order of magnitude close to L_{\star} galaxies as well as matches with the knee of the mass-metallicity relation ([Tremonti et al., 2004](#)). In a more realistic situation, the galaxy initially starts only with gas and then converts it to stars. However, it can be understood simply that the effect of galactic wind is at its onset and most effective when $M_{\star} \approx M_{\text{gas}}$ (see [Larson, 1974](#)).

1.3.1.4 Structure of wind

It is clear that merging of SNe bubbles can reduce ISM radiation loss and a large fraction of the stellar energy (given by Eq. 1.10 and section 1.3.1.2) can be used to drive a wind. For a continuous star formation process, much higher than the threshold value Σ_{th} , the wind can be considered a steady feature. Such a case has been discussed by [Chevalier & Clegg \(1985\)](#) in the context of the wind observed in M82.

Let us consider a situation where star formation (rate = SFR) occurs within a radius R and that a fraction (α) of the mechanical energy output from stellar population (\mathcal{L}_\star) has survived the radiation loss in the ISM. We also assume that some material from the ISM has been evaporated and has become a part of the stellar ejected material (McKee & Ostriker, 1977). With this addition of the material, the thermalised mass and energy can be written as

$$\begin{aligned}\mathcal{L} &= \alpha \mathcal{L}_\star \approx 7\alpha \times 10^{41} \frac{\text{SFR}}{\text{M}_\odot \text{ yr}^{-1}} \text{ erg s}^{-1} \\ \dot{M} &= \eta \frac{\text{SFR}}{\text{M}_\odot \text{ yr}^{-1}} \text{ M}_\odot \text{ yr}^{-1},\end{aligned}\tag{1.19}$$

where, the mass loading factor (MLF) η takes into account for the mixing of ISM mass into the hot bubble. Note that $\eta = 0.3$ means that no additional mass has been added to the SNe ejected mass (see section 1.3.1.1). Now let us also assume that the ejected energy is too large to experience any resistance from the background or that the ISM was swept away by initial phases of the bubble evolution. The hot material therefore will expand adiabatically and convert all of its thermal energy into kinetic energy at a distance $r \gg R$. The terminal velocity of the wind or the ‘free wind’ velocity will be

$$v_{\text{fw}} = \sqrt{\frac{2\mathcal{L}}{\dot{M}}} \approx 1000 \sqrt{\frac{\alpha}{\eta}} \text{ km s}^{-1}.\tag{1.20}$$

For typical values of $\alpha = \eta \approx 0.3$, the wind speed is much larger than the escape velocity of most of the galaxies ($\lesssim 300 \text{ km s}^{-1}$). Therefore, gravity can be neglected in such cases. A full solution of such a wind in steady state has been shown in the left panel of Fig. 1.5 (Chevalier & Clegg, 1985). Two important properties of this wind is that the density, pressure and velocities are almost constant for $r \lesssim R$ and behaves like a power law for $r \gtrsim R$ corresponding to adiabatic expansion. By construction, the wind is transonic ($v = c_s$) at $r = R$. Typical values of R can range from few pc for star clusters to ~ 500 pc for ULIRGs.

Although the free wind solution is good for $r > R$, it ceases to be valid in more realistic situation where the ISM is not yet swept out at larger scales. For example, the ejected mass (\dot{M}) for a SFR of $1 \text{ M}_\odot \text{ yr}^{-1}$ inside an ISM density of $n = 1 \text{ m}_p \text{ cm}^{-3}$ extended over 200 pc will take at least ~ 2 Myr to become comparable to the ISM mass. This time-scale will be at least ~ 300 Myr for a medium of $n = 10^{-3} \text{ m}_p \text{ cm}^{-3}$ over a region of 10 kpc (suitable for halo gas). Clearly, the wind will not be able to completely clear out the background material within a dynamical time-scale ($\sim r/v_{\text{fw}}$, where r is the size of the region). Therefore, a dynamical evolution, rather than a steady state solution, of the wind is needed to be considered for a full understanding of the wind structure.

A simplified dynamical picture of the evolution of such a wind in the presence of a uniform background medium has been portrayed in the right panel of Fig. 1.5. Although, in the original paper by Weaver et al. (1977), the central source has been considered to be a stellar wind with constant velocity v_w and mechanical luminosity $\mathcal{L}_w = (1/2)M_w v_w^2$, the model can be extended to work with a steady wind originating from continuous SNe explosion where a similar situation appears at the free wind region. Since the free wind velocity ($\approx 1000 \text{ km s}^{-1}$) is much larger than the sound speeds

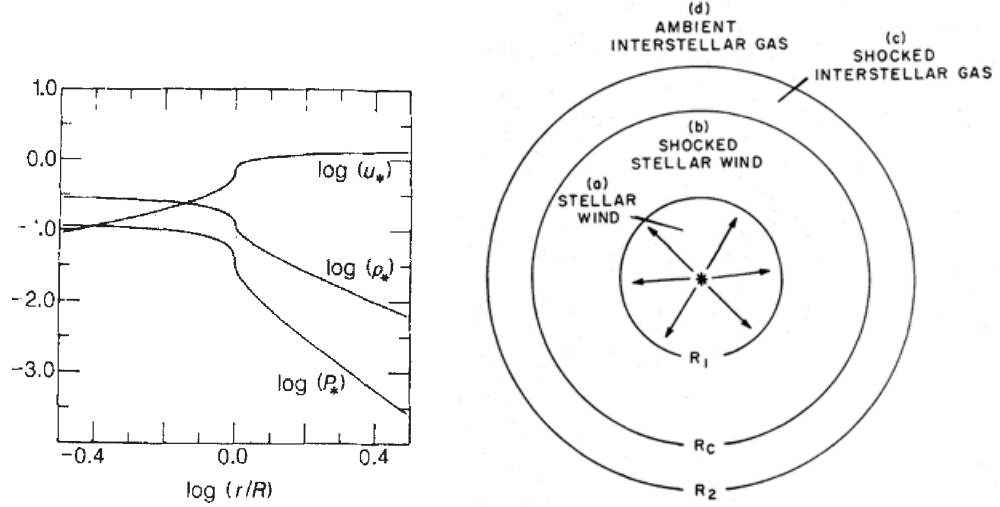


Figure 1.5: *Left panel:* Steady state profile of density $\rho = \rho_* \dot{M}^{3/2} \mathcal{L}^{-1/2} R^{-2}$, velocity $v = v_* (\mathcal{L}/\dot{M})^{1/2}$ and thermal pressure $P = P_* \dot{M}^{1/2} \mathcal{L}^{1/2} R^{-2}$ of a SNe driven wind. Two important features of the profiles are that they are almost constant for $r \lesssim R$ and following adiabatic power laws for $r \gtrsim R$ when it becomes a ‘free wind’. *Right panel:* Structure of a wind bubble when interacting with the background ISM. Figures have been reproduced from [Chevalier & Clegg \(1985\)](#) and [Weaver et al. \(1977\)](#).

(c_s) in the ISM ($c_s \sim 20 \text{ km s}^{-1}$) or in the halo gas ($c_s \sim 200 \text{ km s}^{-1}$), it will drive a strong shock through the background medium. The shock radius in this case is given as $R_2 \approx (\mathcal{L}t^3/\rho_0)^{1/5}$ and the shock velocity is $v_s = (3/5)R_2/t$, where, ρ_0 is the constant background density. For a typical case, where the wind is expanding in a gaseous halo medium, these quantities can be written as

$$\begin{aligned} R_2 &\approx 4 \mathcal{L}_{40}^{1/5} n_{-3}^{-1/5} t_{10\text{Myr}}^{3/5} \text{ kpc} \\ v_s &\approx 400 \mathcal{L}_{40}^{1/5} n_{-3}^{-1/5} t_{10\text{Myr}}^{-2/5} \text{ km s}^{-1} , \end{aligned} \quad (1.21)$$

where, \mathcal{L}_{40} is the mechanical luminosity in units of $10^{40} \text{ erg s}^{-1}$, n_{-3} is the background density in units of $10^{-3} \text{ particles cm}^{-3}$ and $t_{10\text{Myr}}$ is the time in units of 10 Myr. Clearly, the outer shock velocity and, hence, the velocity of the downstream material ($\approx (3/4)v_s$) is lower than the wind velocity. The situation is similar when a heavy shell of gas is moving slowly in front of the fast moving light wind. The obvious outcome of this situation is another shock which travels backwards with respect to the wind frame. This secondary shock is known as the reverse shock and has been marked as R_1 in the diagram. This shock marks the end of the free wind where most of the wind energy is converted back to thermal energy. Between the ‘outer shock’ (R_2) and the reverse shock (R_1), there is a boundary that separates the reverse-shocked wind material and outer-shocked background material at $\approx 0.8R_2$. A complete solution of the density, velocity and pressure behind the outer shock shows that the pressure remains constant across this boundary but the density falls rapidly. This boundary is, therefore, known as the contact discontinuity, marked by R_c in the diagram. Since the pressure remains constant across R_c but the density is very low for $r < R_c$, the temperature of the interior to R_c can become very high ($\sim 10^7 \text{ K}$). Energetically, almost 45% of the wind energy

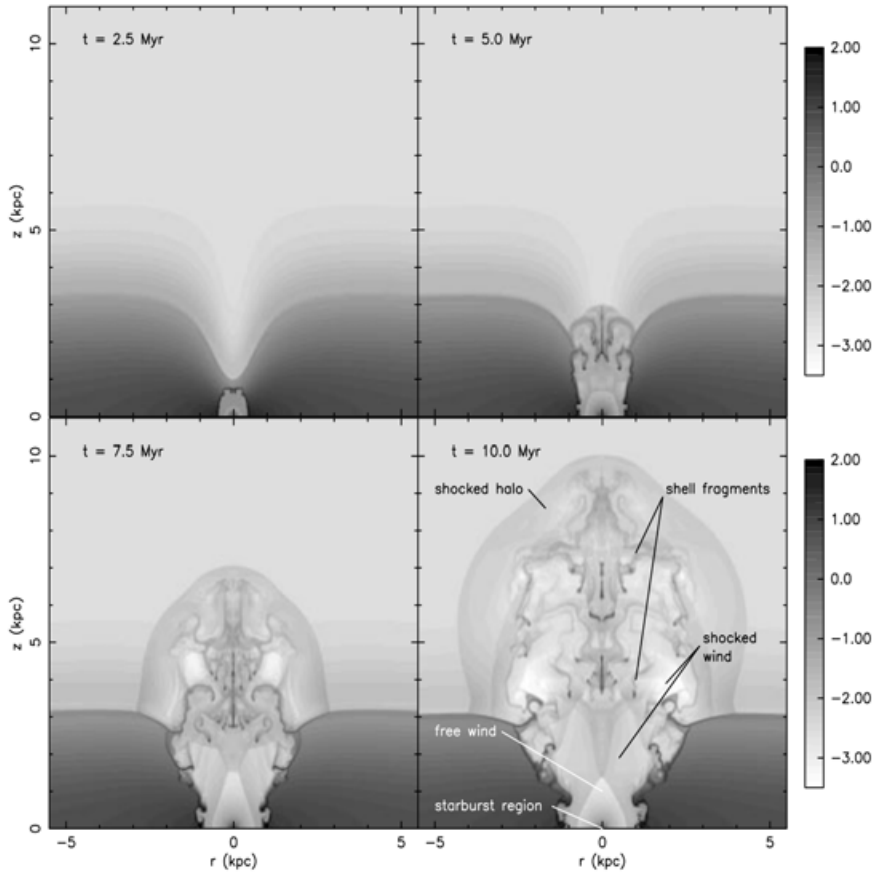


Figure 1.6: Evolution of a SNW placed within a gaseous disc. The grey-scale contours represent logarithmic density in units of $m_p \text{ cm}^{-3}$. A bipolar wind structure arises due to the presence of the stratified disc gas. Other features of a bubble are identifiable except the contact discontinuity which has fragmented into cold-dense gas due to hydrodynamical instabilities. Image credit [Strickland & Stevens \(2000\)](#).

can be in the form of this low density and hot bubble region between R_1 and R_c (see [Weaver et al. \(1977\)](#) for further details).

1.3.1.5 Simulations

More realistic analysis of the evolution of the wind structure in a variety of stratified discs have also been done ([Kompaneets, 1960](#); [Olano, 2009](#)). However, the actual gas distribution in a galactic disc is rather arbitrary depending on its stellar gravity, rotation etc. The situation gets complicated when radiative cooling or other heating terms are included. Moreover, hydrodynamical instabilities like Rayleigh-Taylor or Kelvin-Helmholtz can not be considered in full details by simple analytical methods. Numerical simulations have helped us to overcome these limitations.

Simulations have been performed where a constant mechanical luminosity source has been considered to be the driver of SNW at the centre of a rotating disc ([Heckman et al., 1990](#); [Suchkov et al., 1994](#); [Strickland & Stevens, 2000](#)). An example of such a simulation has been shown in Figure 1.6. A bipolar structure is easily understandable due to the

presence of a disc. One interesting aspect to be noticed here is the fragmentation of the contact discontinuity due to thermal and Rayleigh-Taylor instability. Simulations with varying SNe activity depending on the local star formation rate have also been performed and they portray a more complex picture of the multiphase outflow (Cooper et al., 2008). No doubt that the nature and morphology of the wind and bubble is quite different than a simple spherically symmetric model as discussed above and, therefore, requires numerical simulations in order to understand the complex nature of the galactic wind.

Simplistic wind simulations have been used to understand the disruption of dwarf galaxies, mass and metal ejection into the halo gas by the SNW (Mac low & Ferrara, 1999), X-ray emission from star-burst galaxies (Strickland & Stevens, 2000) and generation of cold gas (Cooper et al., 2008). In the recent past, these simulations have been enabled to include self-gravity, radiation pressure, random distribution of SNe in the disc, ion transport and much more (Girichidis et al., 2016; Zhang & Davis, 2017; Kim et al., 2017). Many basic analysis of the simple systems, however, remain to be done in different contexts. This thesis contains few such analysis of simple disc winds and will be discussed in later chapters.

1.3.2 Active Galactic Nuclei (AGN) driven

Similar to the Supernovae activity in the galaxies, AGNs also produce a large amount of energy. The main source of the AGN energy comes from the release of gravitational energy either in the form of radiation from the accretion disc or mechanical energy in the form of highly collimated jets or widespread disc winds. After the discovery of a very strong relation between the black hole mass and bulge velocity dispersion, $M_{\text{BH}} \propto \sigma^{4.8}$ (Ferrarese & Merritt, 2000), it was clear that the central black holes have crucial importance in the evolution of the galaxy (King, 2003, 2010). Though there are only a handful of direct evidences of the central black holes, a very strong $M_{\text{BH}} - \sigma$ relation has made it clear that almost every galaxy may contain a central black hole and, thereafter, this relation has been inverted to estimate the central back hole mass in distant galaxies.

1.3.2.1 Energetics

The energy of an AGN depends on the rate of mass accretion (\dot{M}_{acc}) onto the black hole. The total energy efficiency (ξ) is thought to be $\sim 10\%$, i.e.

$$L = \xi \dot{M}_{\text{acc}} c^2 \sim 0.1 \dot{M}_{\text{acc}} c^2 . \quad (1.22)$$

However, not all of this energy goes into mechanical energy. For $\dot{M}_{\text{acc}} \lesssim 10^{-2}$ of the Eddington accretion rate, $\dot{M}_{\text{edd}} = 4\pi G m_p M_{\text{BH}} / \eta c \sigma_T$, most of the energy goes into driving mechanical outflow from the black hole, whereas, for $\dot{M}_{\text{acc}} / \dot{M}_{\text{edd}} \gtrsim 10^{-2}$, most of the output energy is in the form of radiation (Churazov et al., 2005). However, this radiation energy can also be turned into mechanical energy as the wind is Compton-thick to the radiation (King, 2003). For an Eddington limited black hole, it can be showed that the mechanical energy output is almost 5% of the Eddington luminosity $L_{\text{edd}} = 4\pi G M_{\text{BH}} m_p c / \sigma_T \approx 1.3 \times 10^{38} (M_{\text{BH}} / M_{\odot}) \text{ erg s}^{-1}$, where, σ_T is the Thompson

scattering cross section of electrons and the velocity of such a wind is $\approx 0.1 c$ (King, 2010).

Although it was believed that only the radiative phase (high accretion rate) of the black hole could heat up the ISM of elliptical galaxies to stop the cooling flow, Churazov et al. (2002) showed that heating from a jet or accretion wind (low accretion rate) from the black holes can also be highly efficient in heating up the gas. For example, our Galaxy has a black hole mass $\approx 4 \times 10^6 M_{\odot}$ and an accretion rate as low as $\sim 10^{-8} M_{\odot} \text{ yr}^{-1}$, i.e. $\dot{M}_{\text{acc}}/\dot{M}_{\text{edd}} \sim 10^{-7}$, and therefore, it is more probable to heat up the halo gas mechanically than any radiation driven heating. On the other hand, quasars which have accretion rates close to the Eddington limit are supposed to heat up the surroundings more by radiation than any mechanical outflow.

The exact mechanism to drive a jet or an outflow from an accretion disc of a black hole is still an unsolved problem. There have been attempts to explain the origin of jets and winds in black holes by invoking the idea of frame-dragging of magnetic field lines around black holes or magnetically driven wind from the disc. A more detailed discussion of these mechanisms is out of the scope of this thesis and can be found in Semenov et al. (2004); Tchekhovskoy (2015); Fukumura et al. (2017).

1.4 Observations of outflows in external galaxies

Progress in astrophysics is often driven by observations. For example, it was the observation of SNe activities in M82 that kick-started the whole new field of galactic wind in structure formation. Although, there were ideas that such processes can contribute to the galaxy formation, it was not taken very seriously until 1963 when Lynds & Sandage found similarity between the radio and optical spectra of M82 and the crab nebulae. Since then, M82 has been the most popular galaxy to study galactic winds, partly because it is only ≈ 3 Mpc away from us and it has a high star formation rate (SFR $\approx 10 M_{\odot} \text{ yr}^{-1}$). The star formation in M82 is confined within a region of 300 pc implying a SFR density of $\sim 30 M_{\odot} \text{ yr}^{-1} \text{ kpc}^{-2}$, much higher than the wind launching threshold (see Eq. 1.15). Over time, more and more observational facts have been gathered to support the idea that M82 indeed hosts a large scale SNe driven wind. While studying far-infrared galaxies (FIRG), Heckman et al. (1990) noticed that the bright nebulae at the centre of the galaxies are highly over-pressurised compared to the ISM of our Galaxy. They also noticed that optical lines ([N II], [O III], $H\alpha$) at \sim kpc away from the centre shows double peaked emission profile. This means that these lines originate from the wall of a conically outflowing wind. Observations of limb brightened $H\alpha$ emission in many star forming galaxies also supported that warm ionised ($T \sim 10^4\text{K}$) gas resides on the conical wall of the wind. Moreover, the ionisation state of this warm gas is a mixture of both photo-ionisation and shock-ionisation. Interestingly, a flux averaged velocity of this warm gas was found to be $\sim 300 \text{ km s}^{-1}$, which is comparable to or larger than the escape velocities of the host galaxies (Heckman et al., 1990; Shopbell & Bland-Hawthorn, 1998).

Observations of X-ray emission from M82 provided further evidences supporting galactic outflow in that galaxy. Lehnert et al. (1999) found that the X-ray emitting gas in M82 is highly ionised representing a temperature of $\sim 8 \times 10^6 \text{ K}$. The corresponding outflow velocity is $\sim 800 \text{ km s}^{-1}$, close to the theoretical understanding of a steady

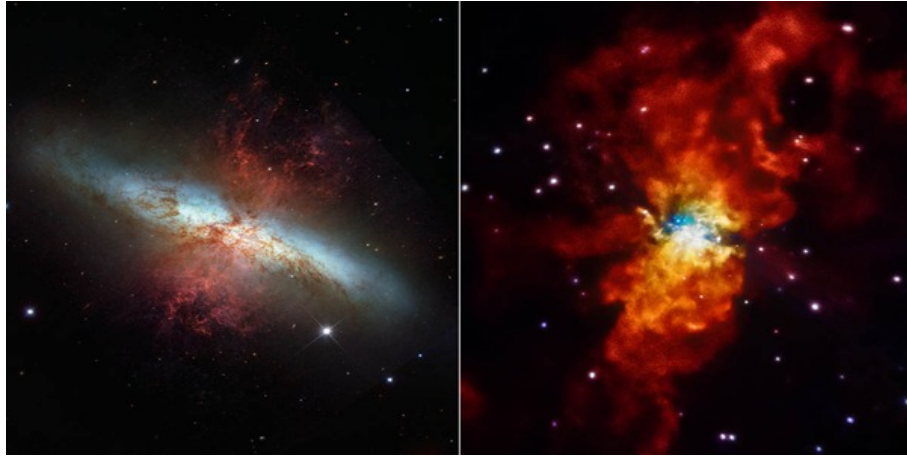


Figure 1.7: Multiphase view of M82. Left panel shows the optical emission seen by HST representing the warm ionised ($\sim 10^4$ K) gas and right panel shows the X-ray emission representing $\sim 10^7$ K gas seen by the Chandra observatory. The bluish patch at the centre of the left panel represents the stellar disc. Presence of the multi-phase extra-planer gas indicates outflow in this galaxy. The image is ≈ 4 kpc across. Image credit-NASA/STScI/SAO.

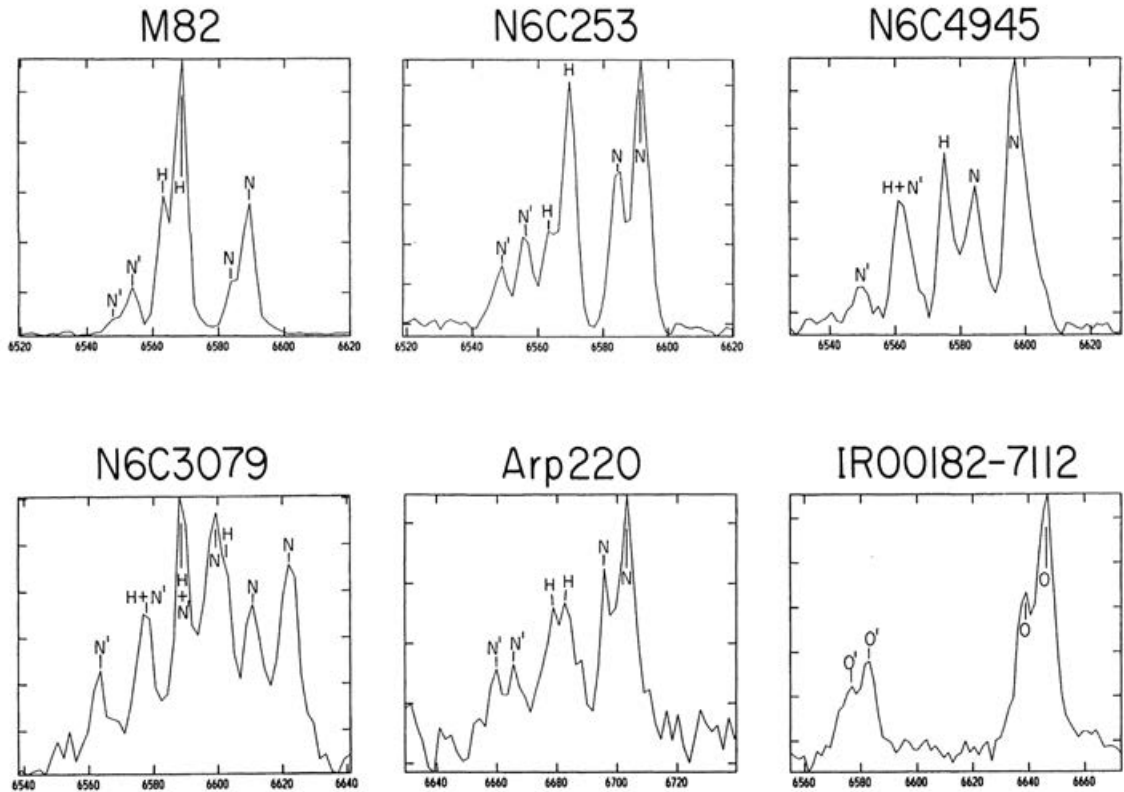


Figure 1.8: Observed double/triple peaked emission profile in external galaxies. The symbols are as follows. O' and O represent $[\text{O III}]\lambda\lambda 4959, 5007\text{\AA}$ doublet. N' and N represent $[\text{N II}]\lambda\lambda 6548, 6584\text{\AA}$, and H represents $\text{H}\alpha$. The spectra are redshift uncorrected. Image credit- [Heckman et al. \(1990\)](#).

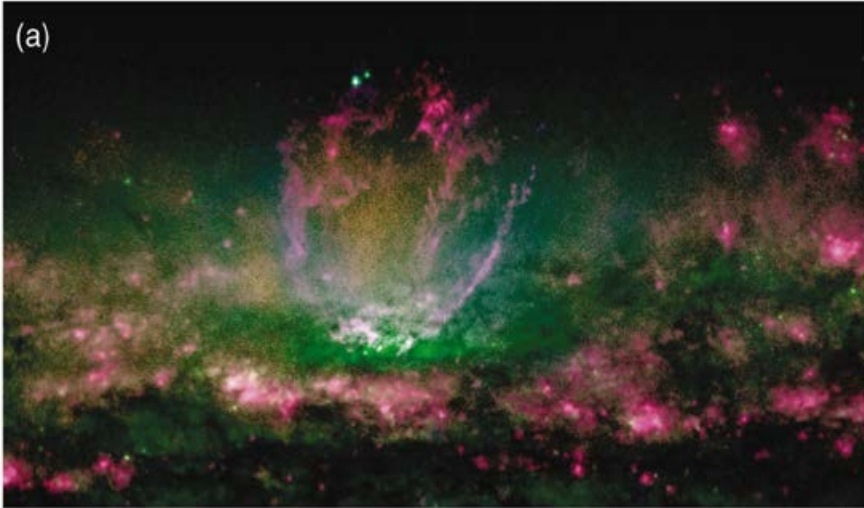


Figure 1.9: Composite image of the central $\approx 4 \times 2 \text{ kpc}^2$ of NGC 3079 showing the presence of a bowl representing an outflow activity. The green, red and blue colors represent the I -band star light, $\text{H}\alpha$ and $[\text{N II}]$ emission line, respectively. The absence of $\text{H}\alpha$ emission across $\sim 2 \text{ kpc}$ region at the base of the bowl indicates absence of HII in that region. Signatures of outflowing material surrounding the $\text{H}\alpha$ emitting bowl can also be noticed. Image credit - Cecil et al. (2001).

wind (see 1.3.1.4). They also found of a strong spatial correlation between the X-ray emission and the $\text{H}\alpha$ emission indicating that the warm gas could have been entrained by the high velocity hot wind (Strickland et al., 2004a). Strickland & Heckman (2009) found that the thermalisation efficiency in M82 could be from 30% to as high as 100%. This estimate validates the discussion in section 1.3.1.2 that SNe remnants in a high star formation region can minimise their radiation losses in the ISM and use most of the energy to drive a galactic wind.

Gas kinematics in high redshifted galaxies that are not directly observable in emission, have been probed using rest frame UV absorption lines (Heckman et al., 2000; Martin, 2005; Heckman et al., 2015; Steidel et al., 2010). The idea is that the UV light originating from massive stars in the galaxy gets absorbed by some material (preferably atomic Na or weakly ionised C, O, N, Si, Mg or Fe) that may be present between the observer and the galaxy. The motion of the intervening material, i.e. outflowing/inflowing, is accurately captured by the blueshift/redshift of the absorption lines with respect to the galaxy. For example, observed blueshift in Na D lines (5890, 5896 Å) in far-infrared galaxies indicated velocities ranging from +400 to +600 km s^{-1} (Heckman et al., 2000) which is much larger than velocities arising due to any ISM turbulence and, therefore, indicates outflow from the galaxies. Observations of dwarf star forming galaxies, however, revealed much smaller outflow velocities ($\sim 30 \text{ km s}^{-1}$; Schwartz & Martin 2004).

1.4.1 Observed phases of outflow

Clearly, observations of different phases of the interstellar matter or outflowing matter indicate different characteristics of the medium and probably contain information regarding the physics of the outflow itself. For example, observations of X-ray emitting gas in M82 has been interpreted to have a velocity of $\sim 800 \text{ km s}^{-1}$ (Lehnert et al., 1999), but H α emitting gas is moving only at $\sim 200 - 300 \text{ km s}^{-1}$ (Shopbell & Bland-Hawthorn, 1998). It is, therefore, important to understand the multiphase nature of the outflowing gas. Following the notion of a three phase medium (Mckee & Ostriker, 1977), the outflowing gas can be grouped in the following phases.

1.4.1.1 Hot phase

The hot, ionised phase is characterised by temperature $T \gtrsim 10^6 \text{ K}$. It is expected that the base of the outflowing gas will have a temperature $\sim 10^7 \text{ K}$ (Chevalier & Clegg, 1985) arising from high energy deposition rate from SNe. In a simple model of galactic wind, the temperature of the wind decreases as the hot gas expands adiabatically ($T \propto r^{-4/3}$, for adiabatic index $\gamma = 5/3$) and falls below the X-ray observable limit of $\sim 10^6 \text{ K}$ at some distance. This sets the maximum extent of the X-ray emission for such cases. As an example, for a star forming galaxy that injects its SNe energy within a radius of $R = 300 \text{ pc}$ (see Section 1.3.1.4), the X-ray emission will be visible till $\sim 1.5 \text{ kpc}$. This value is roughly consistent with the observations of M82 where the X-ray emission extends few kpc on the both sides of the galactic centre (Strickland et al., 2002, 2004b). Note that this radius can be even larger in case of a non-spherical wind or smaller in case the wind is highly mass loaded. X-ray emission can also arise from the shock heating of a pre-existing CGM or the CGM itself (for massive galaxies; see Section 1.2.2). It can be, therefore, tricky to distinguish between the X-ray emission from wind and the CGM, a topic we will come back in a later chapter.

1.4.1.2 Warm phase

Gas with temperature $10^4 \lesssim T \lesssim 10^5 \text{ K}$ is categorised as the warm phase. At the lower end of this range both weakly ionised *viz.*, C II, [N II], Si II, [O III], Fe II etc and neutral *viz.*, Na gas can be observed in emission or absorption (Heckman et al., 1990, 2015; Heckman & Borthakur, 2016; Rupke et al., 2002; Tremonti et al., 2007). HI gas at this temperature can also be photo-ionised by the UV light produced by massive stars formed at the starburst location and can be visible in H α emission (Strickland et al., 2004a; Cecil et al., 2001). The gas in this phase can originate as a result of thermal and Kelvin-Helmholtz instability at the interaction zone of the wind and CGM (Cecil et al., 2001; Sharma et al., 2014a; Sarkar et al., 2015a) or, be entrained from the disc by radiation pressure (Murray et al., 2005; Sharma & Nath, 2012) or ram pressure of the high velocity wind (Martin, 2005). It is also possible that this gas originates *in-situ* at the wind due to thermal instability of a highly mass loaded wind (Thompson et al., 2016; Scannapieco, 2017).

At the upper end of the temperature range ($\sim 10^5 \text{ K}$), highly ionised gas like Si IV, O VI, N V, Ne VIII can be observed via quasar absorption lines (Tumlinson et al., 2011; Werk et al., 2013, 2014; Bordoloi et al., 2014). Interestingly, the extent of this phase of the gas can be from ~ 10 to $\sim 100 \text{ kpc}$ and, therefore, it is not clear if this phase of

the gas is related to outflow or infall or a static CGM medium. Detection of HI 21cm absorption lines along with the highly ionised gas indicates this phase as a boundary layer between the hot ($\sim 10^6$ K) and cold (10^4 K) phase (Werk et al., 2013; Stern et al., 2016). This can also be a transitioning phase when hot gas cools via radiation losses (Bordoloi et al., 2016). With recent estimations of the warm mass in the CGM, it has also been claimed that the galaxies can be baryonically closed (Werk et al., 2014, 2016).

1.4.1.3 Cold/molecular phase

The cold/molecular phase of the outflow is characterised by a temperature of $10 - 10^3$ K. Since molecules start forming at such low temperatures, this phase of the outflow is regularly observed in molecular emission via radio observations. For example, observations of blueshifted CO($1 \rightarrow 0$) transition in M82, NGC253 and NGC3628 in the inner few kpc of the starburst active region clearly indicate the presence of a molecular outflow phase (Walter et al., 2002; Tsai et al., 2012; Bolatto et al., 2013). Not only CO, but signatures of other molecules like HCN, CN, HCO+ and CS have also been found in NGC253 (Walter et al., 2017). Observations of ULIRGs also provided evidence for the molecular phase of the outflow (Cicone et al., 2014). The formation of such molecules in the presence of such high level of ionising photons from star forming region is still under investigation. These molecules could be formed *in-situ* in a thermally unstable wind (Scannapieco, 2017) or could be entrained from the disc gas where the ionising radiation has been screened out due to large column density (see Roy et al. 2016 for a detailed discussion).

1.4.2 Observed properties of outflow

1.4.2.1 Mass loading factor (MLF; η)

The most crucial importance of galactic outflow, in the cosmological context, is to suppress star formation in galaxies. Cosmological semi-analytical models (Somerville & Primack, 1999) or numerical simulations (Springel & Hernquist, 2003; Oppenheimer & Davé, 2006; Oppenheimer & Davé, 2008) reduce this effect of mass outflow into a single parameter called the mass loading factor (MLF; η) which is the ratio between the amount of outflowing mass to the amount of mass that gets locked in stars per unit time.

Theoretically, the outflowing gas can be either driven by momentum from radiation or ram pressure of the hot wind, or can be driven by the SNe deposited energy (in case of an adiabatic expansion of the outflow). The total momentum deposited to the ISM in case of a pure SNe driven wind is \propto SFR (see Eq. 1.3.1.1), which means, in a ‘momentum-driven’ outflow $\dot{M}v_{\text{out}} \propto \epsilon_m$ SFR or

$$\eta = \frac{\dot{M}}{\text{SFR}} \propto \frac{\epsilon_m}{v_{\text{out}}}. \quad (1.23)$$

Here, \dot{M} is the mass outflow rate, v_{out} is the outflow velocity and ϵ_m is the fraction of injected momentum used to drive the outflow. Similarly, in an ‘energy-driven’ outflow

$$\eta \propto \frac{\epsilon_e}{v_{\text{out}}^2}, \quad (1.24)$$

where, ϵ_e is the fraction of energy that has been used to drive the outflow. Note that, ϵ_e may not be always equal to α (section 1.3.1.4) as there may be radiation losses in the wind itself (Thompson et al., 2016). These relations have been widely used in semi analytical models as well as state-of-the-art numerical simulations by assuming that $v_{\text{out}} \propto v_{\text{circ}}$ (Springel & Hernquist, 2003; Oppenheimer & Davé, 2008; Baugh, 2006; Dutton et al., 2010). Here, $v_{\text{circ}} \approx \sqrt{GM_{\star}/r_{\text{vir}}}$. Although, new generation simulations contain more realistic sub-grid physics to implement galactic outflows (Vogelsberger et al., 2013; Schaye et al., 2015), the lack of resolution limits the understanding of such outflows at smaller scales.

Observational values of the mass loading factor vary from 0.1 to 100 depending on the phase of the outflow probed and the driving engine, i.e. SNe or AGN. For example, observations of molecular gas (mostly CO($J = 1 \rightarrow 0$)) in M82, NGC253 and in other starburst dominated ULIRGs indicate $\eta \sim 1-5$ (Walter et al., 2002; Bolatto et al., 2013; Cicone et al., 2014). It is easy to understand that the value of MLF can be even higher (~ 100) in case an AGN is working along with the SNe as the normalisation is only with respect to SFR and not AGN luminosity (Cicone et al., 2014). In the warm phase of the outflow, this value range from 0.1-10 with slight anti correlation with the SFR of the galaxy ($\eta \sim \text{SFR}^{-0.3}$; Rupke et al. 2005; Heckman et al. 2015; Heckman & Borthakur 2016). The anti-correlation with the stellar mass of the galaxy is, however, steeper ($\eta \sim M_{\star}^{-0.5}$; Arribas et al. 2014; Chisholm et al. 2016). Estimation of the MLF in the hot phase for a large number of galaxy samples, however, has been difficult due to the lack of observations in the X-rays. Observations combined with numerical simulations of galactic wind has been used to estimate the value of MLF only for a limited number of samples indicating $\eta \sim 0.3 - 5$ in the hot phase (Suchkov et al., 1996; Grimes et al., 2007; Strickland & Heckman, 2009).

1.4.2.2 Velocity of outflow

One critical assumption in the theoretical models in the above discussion is that $v_{\text{out}} \propto v_{\text{circ}}$ that neglects the detailed dynamics of the multiphase gas. While, the observations of molecular or ionised gas reveal an outflow velocity ranging from few 100 to 2000 km s⁻¹ (Rupke et al., 2005; Tremonti et al., 2007; Arribas et al., 2014; Cicone et al., 2014; Sell et al., 2014), temperature of the X-ray emitting plasma, $T \sim 0.2 - 2 \times 10^7$ K (Martin, 1999; Heckman et al., 2000; Veilleux et al., 2005) indicate an outflow velocity of $\sim 1000 - 2000$ km s⁻¹. It was also found that the maximum velocity of the warm gas is larger by a factor of ≈ 1.5 in the presence of an AGN along with star formation (Arribas et al., 2014).

Observations of outflowing warm gas shows a poor $v_{\text{out}}-v_{\text{circ}}$ and $\eta-v_{\text{out}}$ correlation (see Figure 2a and 6b in Heckman et al. (2015) and imply that the wind driving mechanism is not a simple momentum-driven or energy driven. Hybrid models that include both these mechanisms have also been used in many models (Davé et al., 2013; Ford et al., 2013). However, according to Heckman et al. (2015), these assumptions seem to be consistent only in case of a strong outflow and ceases to be valid where the outflow is weak (see Figure 1.10). A strong outflow is defined when the momentum injection rate (\dot{p}_{\star}) by SNe activity is $\gtrsim 10$ times the critical momentum injection rate (\dot{p}_{crit}) that is required to overcome the gravity of that galaxy. Figure 1.10 also shows non-intuitive relations between the mass loading factor and the galaxy properties in general than

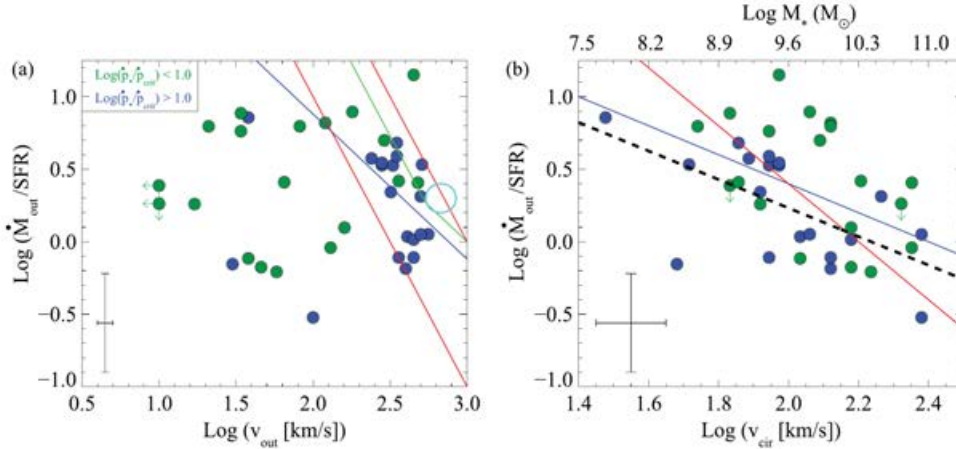


Figure 1.10: Observed correlation of the MLF and the galaxy properties. *Left panel:* The blue and green points represent strong and weak outflowing systems, respectively (see Sec. 1.4.2.2 for definitions). The blue line shows a typical momentum-driven wind with $\epsilon_m = 1$ and the red lines show energy driven wind for $\epsilon_e = 0.1$ (lower) and 1 (upper). The green line shows a typical hybrid model and the red circle represents models assuming $\eta \approx 2$ and a constant velocity. *Right panel:* Scaling for a momentum-driven and energy-driven wind has been shown by the blue and red lines, respectively. Dashed line represents the best fit for the blue data points and show a good agreement with the momentum driven wind. Weak outflows show better agreement with the energy-driven assumption. Image credit- Heckman et al. (2015).

have been assumed in the cosmological simulations.

1.5 Outflow in our Galaxy: the Fermi Bubbles

Several observations in radio, infra-red, X-rays and gamma-rays have revealed excess emission and structures that indicate the presence of a galactic outflow from the centre of our Galaxy. Below, I present a brief review of such observations.

1.5.1 HI shells

The idea that our Galaxy may have a nuclear activity came from the HI observation of two ~ 3 kpc long arms on the plane of the galaxy that are expanding at a velocity of $\sim 135 \text{ km s}^{-1}$ (van Woerden et al., 1957). Subsequent observations confirmed the presence of the shells and estimated the mass contained in these shells to be $\sim 10^7 M_{\odot}$, thereby, indicating the requirement of a powerful activity that can move the heavy shells (Rougeer & Oort, 1960; Cohen & Davies, 1976; Oort, 1977). Several other HI features were also detected outside the Galactic plane. The outward velocity of these features suggest that they could have been ejected from the nucleus in the last ~ 10 Myr time-scale (van der Kruit, 1970). Expanding ($\sim 150 \text{ km s}^{-1}$) dense molecular ring was also detected at ~ 190 pc away from the Galactic centre, marked by the location of the *Sgr A** (Oort, 1977). More recent observation by Lockman & McClure-Griffiths (2016) also found a ~ 2 kpc hole in the HI distribution around the Galactic centre

indicating a major nuclear wind event.

1.5.2 Galactic centre lobe (GCL)

Not only 21 cm HI emission, but continuum radio emission at the Galactic centre was also detected. Using 5 and 10 GHz radio map, [Sofue & Handa \(1984\)](#) found $\approx 1^\circ$ (≈ 150 pc, assuming the Solar radius = 8.5 kpc) Ω -like structure, called the Galactic centre lobe (GCL), towards the Galactic centre but lying on the northern side of the Galactic plane. The explosion energy was estimated to be $\sim 10^{54}$ erg (assuming a similar velocity compared to the high velocity CO gas) which is much larger than the energy ejected by a single SN and indicates multiple SNe activity at the centre ([Sofue & Handa, 1984](#)). Mid-Infrared ($8.3\mu\text{m}$) observations by [Bland-Hawthorn & Cohen \(2003\)](#) revealed the presence of a limb brightened bipolar structure extending till ~ 170 pc on either side of the Galactic plane. This structure is surprisingly coincident with the 3 cm radio image of the GCL. They further speculated that this structure could be associated with a larger structure ($\approx 50^\circ$) called the North Polar Spur and that this would mean a nuclear wind that started 10-15 Myr ago. The coincidence of H α filaments with the GCL also suggested a similar conclusion ([Law, 2010](#)).

1.5.3 Microwave Haze

A much bigger structure, extending till Galactic latitude $|b| \leq 30^\circ$ (≤ 4 kpc) on the both sides of the Galactic plane, was discovered in ~ 10 GHz microwave emission after subtracting foreground models of the radio and HI emission ([Finkbeiner, 2004](#)). Excess emission has also been detected by the *Planck* satellite in recent years by the [Planck Collaboration et al. \(2013\)](#) who also found that the emission is strong for $|b| \leq 30^\circ$, but becomes faint slowly with distance from the Galactic plane and finally disappears at a longitude of $\sim 50^\circ$. It was realised that the spectrum of the haze can be explained if one assumes synchrotron scattering of the high energy ($\sim 1 - 10$ GeV) cosmic ray (CR) electrons in a magnetic field of $5 - 10 \mu\text{G}$. The observed spectrum, $I_\nu \propto \nu^{0.5-0.6}$ ([Dobler & Finkbeiner, 2008](#); [Planck Collaboration et al., 2013](#)), in such a case would mean a pre-scattering CR electron spectral index of $\approx 1.8 - 2.4$ ([Su et al., 2010](#)). More constrained values for the spectral index ($\sim 2.1 - 2.2$) and the magnetic field ($\sim 8 \mu\text{G}$) were obtained by the [Planck Collaboration et al. \(2013\)](#) and [Ackermann et al. \(2014\)](#).

1.5.4 North Polar Spur (NPS)

The North Polar Spur (NPS) is the second biggest structure in the sky that extends from Galactic longitude $l \approx 25^\circ$ to -30° and Galactic latitude $b \sim 10^\circ-70^\circ$ in the form of an arc with average thickness of $\sim 15^\circ$. This is bound by another structure called the Loop-I feature that extends $\sim 10^\circ$ further outside the NPS in almost all directions. These features were first detected by [Piddington & Trent \(1956\)](#) using radio observations at 600 MHz. Later radio observations at other frequencies (≤ 1.4 GHz) also confirmed the presence of the structures ([Hanburry Brown et al., 1960](#); [Berkhuijsen et al., 1971](#); [Haslam et al., 1974](#); [Sofue & Reich, 1979](#)).

Observations at much higher energy bands also revealed the presence of the NPS. For example, [Snowden et al. \(1997\)](#) and [Sofue \(2000\)](#) found the signature of the NPS in X-

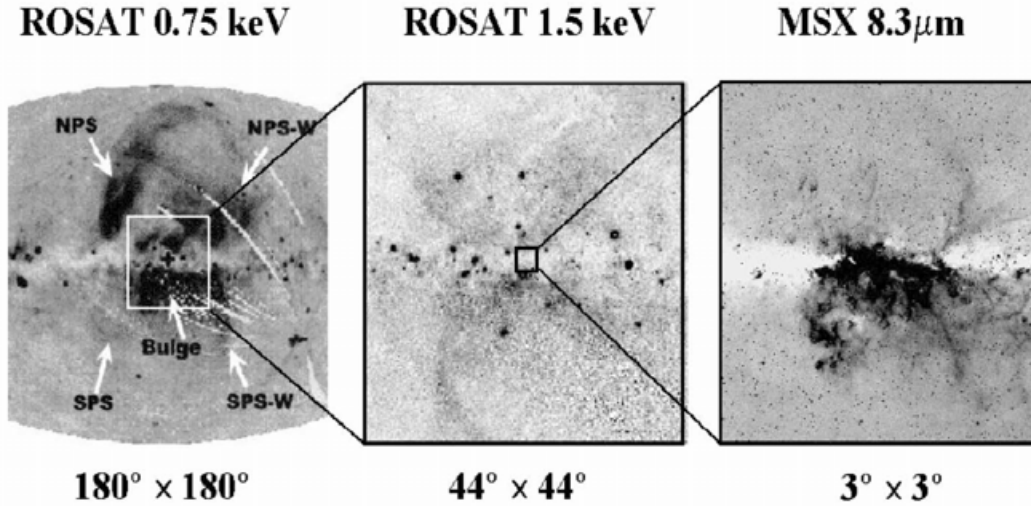


Figure 1.11: Multi-wavelength observation towards the Galactic (GC) centre showing the evidence of an outflow. The GC is situated at the centre of all the maps and is assumed to be at the location of the Sgr A^* . *Left panel:* 0.75keV ROSAT all sky X-ray map showing the NPS and its faint counterpart, south polar spur (SPS) in the southern hemisphere. *Middle panel:* A zoomed in 1.5keV ROSAT map showing the presence of a limb-brightened bipolar structure centres at the GC. *Right panel:* Infrared image taken by Midcourse Space Experiment (MSX) showing dust emission from filamentary structures coming out from the GC. Figure credit- [Bland-Hawthorn & Cohen \(2003\)](#)

ray maps from ROSAT all sky survey. The existence of a much fainter southern counterpart of the NPS was also seen in the X-ray map by [Sofue \(2000\)](#). Clear signature of the NPS was also seen at \sim GeV energy scale by [Ackermann et al. \(2014\)](#). Interestingly, they also find two large arms at $l \sim 30^\circ$ and 330° extending in the southern hemisphere and originating at the same locations as the NPS. This indicates that the NPS may be a dumbbell like structure centred around the Galactic centre (GC) that originated from a nuclear wind ([Sofue, 2000](#)).

1.5.4.1 Proposed origin

Despite several strong claims by [Sofue \(1977, 1984, 1994, 2000, 2003\)](#); [Sofue et al. \(2016\)](#); [Bland-Hawthorn & Cohen \(2003\)](#) and others that the NPS is a result of the nuclear wind, the origin of the NPS still remains debated even after half a century of its first discovery. The main reason is that the NPS is not very apparent in the southern hemisphere. This has attracted alternative explanations for the origin of the NPS. Another fact that apparently goes against the ‘Galactic centre origin’ of the NPS is the superposition of a nearby (~ 200 pc) OB association, Scorpio-Centaurus. It was claimed that NPS may be the outer shell of a supernova remnant of a runaway star ξ -Ophiucus that was initially a member of the OB association, or produced by collective stellar wind and consecutive SNe events from that association ([Berkhuijsen et al., 1971](#); [Egger & Aschenbach, 1995](#)). The size of the NPS to cover the observed area on the sky in such a case would be only ~ 200 pc.

There are, however, growing evidences from recent observations that NPS is indeed

a ‘Galactic centre origin’ phenomena. Observations by [Kataoka et al. \(2013\)](#) and [Lallement et al. \(2016\)](#) using *XMM-Newton* revealed that the X-ray spectrum of the NPS is highly absorbed by neutral hydrogen with required column density $N_{\text{H}} \gtrsim 10^{21} \text{ cm}^{-2}$. Such a high column density is not achievable if NPS was only ~ 200 pc away. In particular, when a low density ($\sim 5 \times 10^{-3} m_{\text{p}} \text{ cm}^{-3}$) and high temperature (10^6 K) local bubble (LB) occupies most of the volume within ~ 200 pc around the Sun ([Egger & Aschenbach, 1995](#)). A high column density could still be achievable if most of the gas is compressed in a $15 - 60$ pc region between the local bubble and the NPS ([Willingale et al., 2003](#)). But such a high density wall has not been reported yet. Another factor that goes against the NPS being a ‘local’ phenomena is the metallicity. Careful fitting of the X-ray spectrum from the NPS shows that the metallicity is $\approx 0.3 - 0.7 Z_{\odot}$ which is almost half of the the values observed in the ISM around the Solar system ([Maciel & Costa, 2010](#)). This value is rather very close to the metallicity (~ 0.5 ; [Miller & Bregman 2015](#)) estimated for the hot CGM of the Milky Way. The NPS metallicity is also in line with the Galactic halo stars ([Gu et al., 2016](#)). This means that the NPS is more likely to be a structure in the CGM than in the ISM. By re-analysing the *Suzaku* and *XMM-Newton* spectrum towards the NPS [Gu et al. \(2016\)](#) also found that the O VIII Ly- β to Ly- α and other Lyman series lines are well explained if one assumes absorption from a $0.17 - 0.20$ keV ionised medium, a value very similar to the Galactic CGM ([Henley & Shelton, 2010](#); [Miller & Bregman, 2013, 2015](#)). The required ionised column density is $5 \times 10^{19} \text{ cm}^{-2}$ which is much more than the contribution from the local bubble ($\sim 5 \times 10^{-3} \times 200 \text{ cm}^{-3} \text{ pc} = 3 \times 10^{18} \text{ cm}^{-2}$). Such a high column density of ionised gas is, however, easily achievable in the Galactic CGM over a path length of ~ 10 kpc (assuming a CGM density of $\sim 10^{-3} m_{\text{p}} \text{ cm}^{-3}$). Given that the Solar distance is ≈ 8.5 kpc from the GC, the ‘Galactic centre origin’ of the NPS seems to be very likely ([Gu et al., 2016](#)). Another striking coincidence is that the inner edge of the NPS in the northern hemisphere traces the outer edge of the Fermi Bubbles (as will be discussed shortly) which is believed to have originated from a Galactic centre event ([Su et al., 2010](#)). All these facts suggests that the NPS is far more likely to have originated from a Galactic centre activity than a nearby event. Therefore, throughout the thesis, we will assume that the NPS is of ‘Galactic centre origin’.

1.5.4.2 Physical parameters

The density, temperature and metallicity of the NPS has been estimated to be $\sim 2 \times 10^{-3} m_{\text{p}} \text{ cm}^{-3}$, $\approx 0.25 - 0.35$ keV and $\sim 0.3 - 0.7 Z_{\odot}$, respectively ([Egger & Aschenbach, 1995](#); [Kataoka et al., 2013](#); [Gu et al., 2016](#)). [Kataoka et al. \(2013\)](#) also found that the emission measure of the X-ray emitting gas near the NPS decreases by $\approx 50\%$ while entering the FBs from outside. The temperature of the NPS and the fact that it is in the CGM suggests a shock of Mach number ≈ 1.5 through the CGM implying a shock velocity of $\sim 300 \text{ km s}^{-1}$. Given that the NPS is extended till $\sim 70^\circ$ at Galactic latitude $b = 0$, the size of the shock can be as large as ~ 10 kpc. This means an age of ~ 30 Myr for the NPS. There is, however, another model which claims a higher Mach number (~ 2.3), and therefore, a much lower age of the NPS (~ 5 Myr; [Miller & Bregman 2016](#)). We will put these models to test in a later chapter.

1.5.5 Energetics at the Galactic centre

Not only the kinematics and other structures, but multi wavelength observations towards the Galactic centre also reveal excess emission in different wavebands that indicate both ongoing star formation and accretion activity at the Galactic centre black hole.

1.5.5.1 Star formation

Several infrared observations indicate an ongoing star formation within central few 100 pc. [Yusef-Zadeh et al. \(2009\)](#) estimated the SFR to be $\sim 0.14 M_{\odot} \text{ yr}^{-1}$ within $400 \times 50 \text{ pc}^2$ region around the GC by counting the number and masses of the young stellar objects (YSO) within the molecular clouds from their compact infrared emission. Later estimates by [Immer et al. \(2012\)](#); [Koepferl et al. \(2015\)](#) suggest SFR $\approx 0.06 - 0.08 M_{\odot} \text{ yr}^{-1}$ after considering probable contamination from older stars and proper radiative transfer in the molecular cloud. Similarly, free-free emission from ionised region around massive stars has also been used to infer their numbers and masses, and consequently the SFR. Using this idea [Murray & Rahman \(2010\)](#) estimated the SFR to be $\approx 0.06 M_{\odot} \text{ yr}^{-1}$ within $300 \times 150 \text{ pc}^2$ around the GC. Total infrared luminosity ($1 - 1000 \mu\text{m}$) has also been used to estimate the SFR from Kennicutt's law ([Kennicutt, Jr., 1998](#)). This suggests SFR $\approx 0.1 M_{\odot} \text{ yr}^{-1}$ within the same region around GC ([Crocker & Aharonian, 2011](#); [Barnes et al., 2017](#)).

1.5.5.2 Black hole accretion rate

Although the Eddington accretion rate for the Galactic centre black hole (GCBH), $M_{\text{BH}} \approx 4.2 \times 10^6 M_{\odot}$ ([Genzel et al., 2010](#)), is $\sim 0.1 M_{\odot} \text{ yr}^{-1}$, the current accretion rate appears to be much lower than the Eddington limit. The detection of linear polarisation of the synchrotron emission at frequencies $\gtrsim 150 \text{ GHz}$ indicates that the current accretion rate for the GCBH is $\sim 10^{-9} - 10^{-8} M_{\odot} \text{ yr}^{-1}$ ([Agol, 2000](#); [Quataert & Gruzinov, 2000](#)). A higher accretion rate would naturally mean a higher gas density and higher magnetic field density in the accreted gas and thus more Faraday depolarisation of the actual signal, leading to un-polarised synchrotron emission. A conservative upper limit ($\lesssim 10^{-7} M_{\odot} \text{ yr}^{-1}$) was inferred from the variability of the position angle and the polarisation fraction by [Marrone et al. \(2006\)](#). All these values correspond to a mechanical luminosity output from the GCBH to be $\sim 5 \times 10^{36-38} \text{ erg s}^{-1}$.

Observations of X-ray reflection nebula near Sgr B2 and Sgr C, however, indicate that the past X-ray luminosity of Sgr A* was $\approx 3 \times 10^{39} \text{ erg s}^{-1}$ ([Murakami et al., 2000](#)). This means that the past accretion rate into the GCBH was almost 10^{3-4} higher than the current rate ([Totani, 2006](#)) (following a radiative inefficient flow model of [Yuan et al. \(2004\)](#)). According to [Totani \(2006\)](#), the GCBH continued to accrete at a higher rate for last $\sim 10 \text{ Myr}$ before the accretion rate dropped to the current value $\sim 300 \text{ yr}$ ago. The elevated accretion rate, therefore, indicates an increased mechanical luminosity output from the GCBH, i.e. $5 \times 10^{39-41} \text{ erg s}^{-1}$. Observations of two stellar disc (mass $\sim 10^4 M_{\odot}$) within 0.5 pc of the GCBH suggests that these stars were formed during an accretion event $\approx 6 \pm 2 \text{ Myr}$ before ([Paumard et al., 2006](#)). Simulations, mimicking such a situation at the GCBH showed that while forming the stars in the accretion disc, 10-30% of the disc could have been accreted onto the GCBH. This would mean

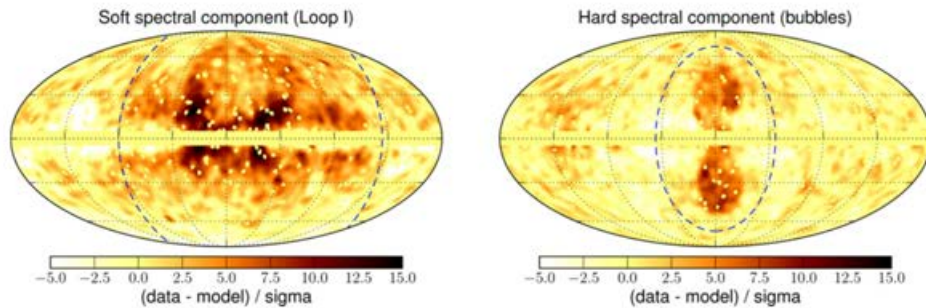


Figure 1.12: Integrated (0.7 – 10 GeV) residual map of the sky after subtracting foreground model for the soft component (left panel) and the hard component (right panel) from data having a standard deviation of σ . The left panel shows the dominance of the Loop-I over the Fermi Bubbles in soft γ -ray (≤ 2 GeV) emission, whereas, the Fermi Bubble dominates in the hard γ -ray sky. The left panel also shows two extra arms in the southern sky indicating a possibility of the counterpart of Loop-I. The dashed lines encloses a typical part of the sky where the Loop I or the FBs are dominated. Note that the position of the γ -ray emission in Loop-I also traces the excess X-ray emission from the Loop-I and NPS. Image Credit - [Ackermann et al. \(2014\)](#)

an accretion rate of $\sim 10^{-4}$ - $10^{-3} M_{\odot} \text{ yr}^{-1}$ corresponding to a maximum luminosity of $\sim 10^{43} \text{ erg s}^{-1}$ over a viscous time-scale 10 Myr ([Bonnell & Rice, 2008](#)).

Interestingly, observation of diffuse X-ray within central 20 pc of the Galaxy shows the presence of a hot ($\sim 10^8$ K) plasma in 2 – 8 keV band ([Muno et al., 2004](#)). Such a plasma would escape the Galaxy and therefore requires its energy to be replenished. The required SNe heating is $\sim 10^{40} \text{ erg s}^{-1}$, corresponding to SFR $\sim 0.1 M_{\odot} \text{ yr}^{-1}$ which is higher than the observed rate only within central 20 pc. One possible explanation is that it was heated by the past activity of the GCBH. But any deviation from collisional ionisation equilibrium, that could be caused if it was heated by the GCBH, is not found in the spectrum of this emission ([Muno et al., 2004](#)). At this point, the origin of such emission is still unknown.

1.5.6 Fermi Bubbles (FBs)

The discovery of two giant gamma-ray bubbles by on-board *Fermi*-Large Area Telescope (*Fermi*-LAT) towards the Galactic centre gave a boost to the study of the Galactic wind ([Su et al., 2010](#)). Although, it uses simple model templates for the foreground, the existence of the bubbles have also been confirmed using much more complex foreground models or algorithm ([Ackermann et al., 2014](#); [Selig et al., 2015](#)) and even in a simple gradient map ([Keshet & Gurwich, 2017](#)). Since, a major part of the thesis involves modelling these bubbles, let us briefly review the observations and attempts made so far to explain them.

1.5.6.1 Morphology and Spectra

The FBs are extended till $|l| \approx 20^{\circ}$ and $|b| \approx 50^{\circ}$ (~ 8 kpc) almost symmetrically about the Galactic plane and the edge of these bubbles are sharp ($\sim 0.5^{\circ} \sim 100$ pc). A much

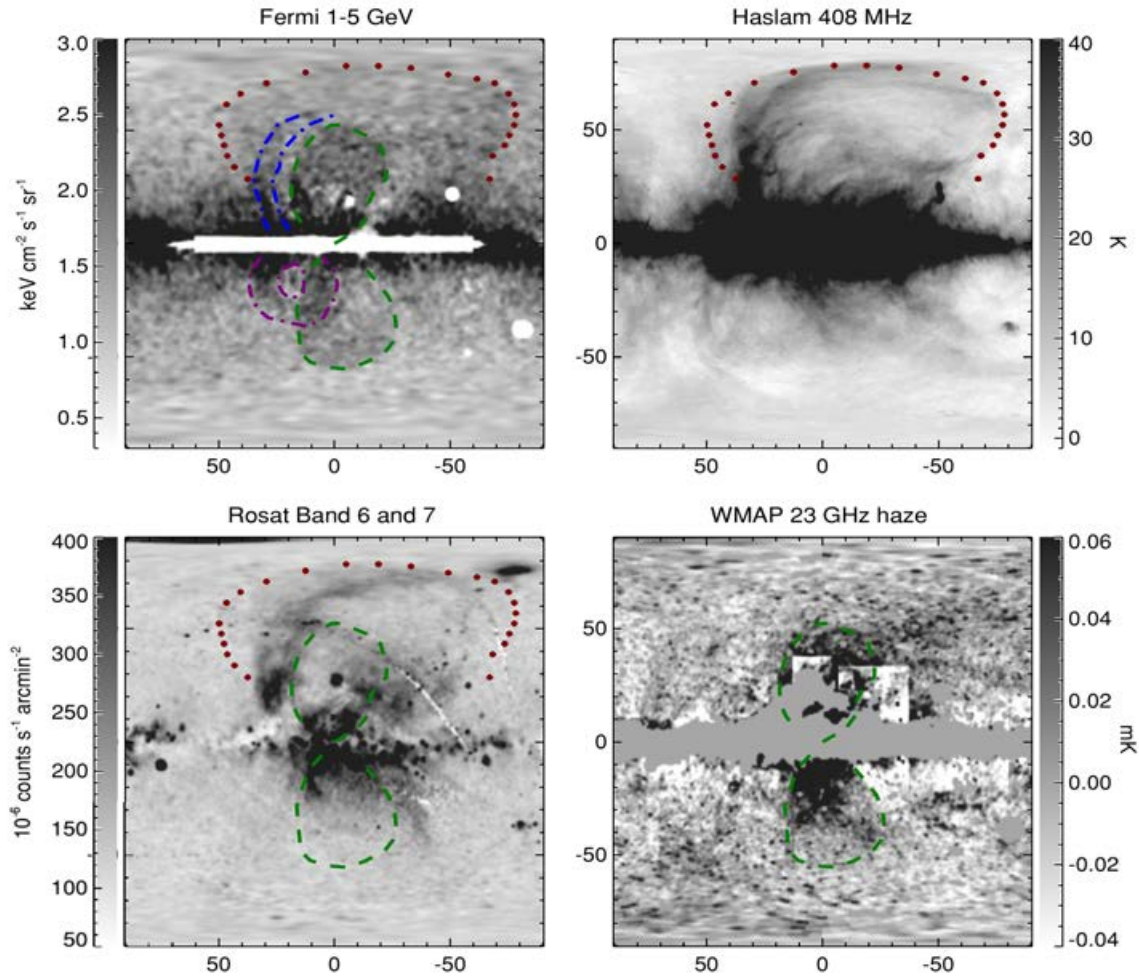


Figure 1.13: Multi-wavelength view of the sky towards the GC. *Top left*: *Fermi* 1 – 5 GeV surface brightness map showing the presence of Fermi Bubbles (region within green line), excess emission within Loop-I (red), Northern arcs (blue) and a donut shaped emission in the southern hemisphere. *Top-right*: radio emission at 408 MHz that follows the Loop-I. The gray-scale represents the brightness temperature. *Bottom-left*: ROSAT 0.7 – 1.7 keV X-ray map. The correspondence with Fermi Bubbles (green line) and Loop-I (red dotted line) has been over-plotted for convenience. *Bottom-right*: microwave haze at 23 GHz. The gray-scale represents brightness temperature in excess to the CMB. The γ -ray and microwave emission has been obtained after subtracting possible contamination from foregrounds. The X and Y axes represent the Galactic longitude and latitude (in degrees), respectively. Image credit- [Su et al. \(2010\)](#)

bigger structure extending till $b \sim 80^\circ$ is also observed in 1 – 5 GeV map of the northern sky and is thought to be associated with the NPS and the Loop-I. The indication of such a loop in the southern sky can be seen in more recent observations by [Ackermann et al. \(2014\)](#) (see figure 1.12).

The presence of the FBs also at higher energies (5 – 50 GeV) indicated that the spectrum is hard compared to the Loop-I feature or the gamma-ray emission from the Galactic disc. Detailed observations in 0.5 – 500 GeV showed that the spectrum of the Loop-I feature is $dN_\gamma(E)/dE_\gamma \propto E_\gamma^{-2.4}$, very close the spectrum arising from the inverse Compton (IC) scattering in the disc but the surface brightness falls off further away from the disc. Fermi Bubbles, however, have a distinct spectral shape of $dN_\gamma(E)/dE_\gamma \propto E_\gamma^{-2}$ which is harder than all the diffuse components in the Galaxy. The spectral index and the surface brightness of the bubbles remain almost constant throughout its entire area. If this emission comes from IC scattering of the ISRF with electrons, then the required spectral index for the electrons is $dN_e(E)/dE_e \propto E_e^{-2} - E_e^{-2.5}$, obtained at $b = 30^\circ$ or $z = 5$ kpc ([Su et al., 2010](#); [Ackermann et al., 2014](#)). Note that this is the same spectral index that could also explain the microwave haze (Sec 1.5.3) and implies that the γ -rays are produced by the the same population of the electrons. The required spectral index of the electrons is, however, uncertain if the distance variation of the ISRF from the stellar disc is taken into account as it would fail to maintain a constant surface brightness. The uniform surface brightness and constant spectral index, therefore, probably indicate IC scattering from an uniform source of photon, like the CMB. We will investigate this option in a later chapter.

1.5.6.2 Kinematics

Observations of UV absorption lines through FBs probe the kinematics of warm gas inside FBs. Observations by [Fox et al. \(2015\)](#) and [Bordoloi et al. \(2017\)](#) find UV absorption lines that are blue-shifted by a velocity of ~ -200 km s $^{-1}$. According to these authors, simple model of the warm gas outflow from the GC within a certain opening angle suggests that the gas might be moving at a velocity of ~ 1000 km s $^{-1}$ therefore implying an age of ~ 10 Myr for the bubbles. As we will see in a later chapter that the actual gas kinematics inside and around the FBs can be, however, quite complex and may not be captured by this simple outflowing model.

Another way to understand the strength of driving source is to probe the expansion velocity of the FBs or the shock created by the FBs. From the O VIII to O VII line ratios towards the FBs, [Miller & Bregman \(2016\)](#) concluded that the shock temperature is 5×10^6 K which can be only generated by a fast shock (~ 500 km s $^{-1}$) indicating the age of FBs to be few Myr. The estimation of the shock temperature, however, may suffer from possible contamination by the Galactic CGM as we will discuss later.

1.5.6.3 Models so far

Since the discovery of the FBs, there have been a lot of attempts to understand the origin of these bubbles. There are mainly two aspects that physicists are struggling to understand.

First, **the driving mechanism**. It is understood from the deficit of X-rays within FBs (see Fig 1.13) that they are filled up with low density gas compared to the sur-

roundings. Therefore, the only way to inflate these bubbles into the Galactic CGM is to supply energy to maintain a higher pressure compared to the CGM. Given that the bubbles are symmetric around the Galactic plane and pointing towards the Galactic centre suggests that the energy supply is coming from the Galactic centre either by SNe explosion or by GCBH accretion activity.

Most of the FB models so far focussed on the GCBH activity as the possible source of mechanical energy to drive FBs assuming that the GCBH was actively accreting in the past. However, because of the poor observational constraints on the past accretion rate, the assumed mechanical output varies from 2×10^{41} to 10^{43} erg s⁻¹. For example, Zubovas et al. (2011) and Zubovas & Nayakshin (2012) argue for a spherical quasar outflow from the GCBH that was active only for ~ 1 Myr during an accretion event ≈ 6 Myr before producing a mechanical energy of $\sim 10^{43}$ erg s⁻¹. They also show that this spherical outflow can be collimated by the central molecular zone (CMZ) which is a $\sim 250 \times 50$ pc² disc like structure at the GC. Similar arguments about the energetics were also given by Guo & Mathews (2011); Guo et al. (2012); Yang et al. (2012) by assuming that the FBs are powered by a jet event instead of a spherical quasar outflow. A much lower value for the mechanical luminosity for the spherical outflow was assumed by Mou et al. (2014, 2015) who found that the FBs can be explained by $\sim 2 \times 10^{41}$ erg s⁻¹ outflow persistent over a time-scale of ≈ 10 Myr.

Models considering a star formation driven wind to explain FBs have been very limited. Crocker & Aharonian (2011); Crocker (2012); Crocker et al. (2015) argue that FBs are steady state plasma structures that originated from star formation driven wind requiring SFR $\sim 0.1 M_{\odot}$ yr⁻¹ that is persistent over a time-scale of few 100 Myr to few Gyr. While the required SFR is close to observations at the GC, the age of the bubble seems to be rather long. Moreover, given that there will be no shock produced by such a steady structure and therefore, no rise in the CGM temperature outside the FBs, which is not consistent with the X-ray observations (Kataoka et al., 2013; Miller & Bregman, 2016). Lacki (2014) argue that the FBs represent the reverse shock generated by a star formation driven wind. However, in such a case, a highly limb brightened bubbles would be seen instead of the observed constant surface brightness.

Second, **the origin of the γ -rays**. Gamma-rays can be generated either by hadronic collisions where proton-proton collision gives rise to γ -rays via neutral pion decay, or leptonic model where IC scattering of lower energy photons such as the ISRF and CMB with high energy CR electrons gives rise to the γ -rays. A crucial problem with the hadronic model is that the gas density within FBs seems to be much lower compared to the CGM (since the X-ray emission is less), therefore, hadronic emission is expected to be sub-dominant within the bubbles. It is however unclear if high CR proton density can make up for the emission. Crocker & Aharonian (2011); Crocker (2012); Crocker et al. (2015) have argued that the γ -rays can come from the interaction between cosmic ray protons and ions injected from a star formation driven wind. In a recent paper, Mou et al. (2014) suggested that the hadronic interaction can happen at the contact discontinuity which would give rise to limb brightened γ -ray shell. They argue that this limb brightened shell is consistent with recent observation by Ackermann et al. (2014). However, the limb brightening does not seem to be very apparent in the data.

There are problems with the leptonic models as well. As mentioned earlier in section 1.5.6.1 that the IC scattering (ICS) of low energy photons to the observed γ -ray spec-

trum would require an electron population with spectral index of 2.0-2.5. This spectral index of electrons is consistent with SN shock acceleration (Biermann et al., 2010) which means that they can be easily shock accelerated. However, transporting such high energy electrons at ~ 10 kpc from the disc without changing its spectral shape is very hard as the IC cooling time becomes shorter than the advection time. Given typical energies of CMB ($\sim 2 \times 10^{-4}$ eV) and ISRF (\sim eV), the required energy of the electrons to boost the photons to ~ 10 GeV γ -rays are ~ 3 TeV (Lorentz factor, $\Gamma_e \sim 10^7$) and ~ 50 GeV (Lorentz factor, $\Gamma_e \sim 10^5$), respectively. The Synchrotron cooling time (time to loose half of its initial energy) of relativistic electrons is $t_{\text{cool}} \approx 8 \times 10^8 / (\Gamma_e B^2)$ sec, where, B is the magnetic field intensity. Assuming that $B = 5 \mu\text{G}$ inside the bubbles, the cooling time-scale for the electrons that are scattering ISRF is ~ 10 Myr. Therefore, if the age of the Fermi Bubbles is ~ 10 Myr, then it should show marginal cooling effect on the spectrum. There are, however, other issues with the ICS of ISRF. The required electron energy (~ 50 GeV) is very close to the observed γ -ray energies, means that the scattering cross section decreases from the classical Thompson's value ($\sigma_T = 6.65 \times 10^{-25}$ cm²) and, therefore, requires very large number of ISRF photons to produce the observed intensity of the γ -rays. Besides, the intensity of the ISRF falls off away from the disc, therefore, a constant surface brightness of the bubbles would mean higher spectral index of ISRF photons away from the disc, which is not feasible.

For the IC scattering of CMB photons, the cooling time for high energy CR electrons in the same magnetic field is ~ 1 Myr. This means that they have to be either transported very fast ($\sim 10^4$ km s⁻¹) from the centre where they are generated at the SNe shocks or has to be generated *in-situ* just below the edge of FBs. While transporting CR electrons at such high energies seems to be difficult, *in-situ* acceleration is much easily achievable. Mertsch & Sarkar (2011) argue that the CR electrons could be accelerated at the plasma turbulence inside the bubbles whereas Lacki (2014) considers that Fermi Bubbles are the location of the reverse shock and particles can be accelerated there.

1.6 Motivations for this thesis

In the previous sections we have encountered many interesting aspects of galactic outflows in the context of galaxy formation and evolution. The goal for this thesis is to understand how outflows work in a typical spiral galaxy and how can we better understand the observational facts of outflows based on simple models. There are several observations and related questions that drive the motivation for the studies included in this thesis.

- *Effect of circumgalactic medium on outflows:*

Supernovae driven outflows in the interstellar medium have been studied in great detail in the literature (Weaver et al., 1977; Mckee & Ostriker, 1977). Their evolution as a freely expanding medium has also been studied in case of dwarf galaxies, like the M82 (Chevalier & Clegg, 1985). Studies incorporating the presence of a hot circumgalactic medium in massive galaxies as has been recently detected in X-rays (Bogdán et al., 2013; Miller & Bregman, 2013), however, have not been done in the full context of a galaxy. This motivates us to study the structure,

dynamics and observability of the galactic outflows in the presence of such CGM around Milky-Way type massive galaxies. While observations mostly produce information regarding only a single phase, either hot or cold and not the full picture, we were motivated to understand the full picture of such multiphase outflows in CGM and the relation between different phases.

- *Origin of the high velocity clouds:* Observations often detect the presence of clouds that are moving at high velocities ($\sim 300 \text{ km s}^{-1}$) several kpc away from the disc (Heckman et al., 1990; Shopbell & Bland-Hawthorn, 1998) in star forming galaxies. The origin of these high velocity cold/warm (10^4 K) gas are still in doubt. They could be entrained by the high velocity wind from the disc or could form *in-situ*, or both. Simple estimates show that the clouds are supposed to be shredded away due to Kelvin-Helmholtz instability between high velocity wind and sluggish cold gas (Thompson et al., 2016). Recent observations show that the cold/warm gas is also present even at $\sim 100 \text{ kpc}$ distance around massive galaxies (Tumlinson et al., 2011; Werk et al., 2014). A detailed understanding of the formation and dynamics of such cold gas is therefore required.
- *Origin of X-ray in galaxies:* Observations of star forming galaxies show that the soft ($\leq 2.0 \text{ KeV}$) X-ray luminosity (L_X) is proportional to the SFR (Mineo et al., 2012a). A simple SNe driven wind model of Chevalier & Clegg (1985), however, suggests $L_X \propto \text{SFR}^2$. More recent observations by Wang et al. (2016) shows an even flatter L_X -SFR relation. These puzzling facts of X-ray emission from galaxies motivated us to study the X-ray properties of a galactic outflow.
- *Origin of the Fermi Bubbles:* As described in section 1.5.6, the origin of the mysterious Fermi Bubbles is still far from being understood and there is no accepted model of either dynamical or spectral origin. Most of the models have focussed on a GCBH accretion scenario to explain FBs. Star formation driven wind scenario has not been studied in detail. Moreover, most of the models focus on either the shape or the γ -ray spectra or cosmic-ray diffusion in the bubbles. A multi-wavelength approach to unify all these features in the sky has only been attempted by Crocker et al. (2015). Their simple analytical model, however, suffers from several shortcomings that can seriously affect the understanding of the bubbles. A much realistic approach to the problem in the actual Milky-Way like environment is required to understand the FBs.

One way to estimate the energetics of the Fermi Bubbles is to probe the shock strength. Analysis of *XMM-Newton* and *Suzaku* spectra by Kataoka et al. (2013) indicated that the shock is a weak one (Mach ~ 1.5) corresponding to a shock velocity of $\sim 300 \text{ km s}^{-1}$. However, using more recent observation of oxygen lines, Miller & Bregman (2015) suggested a stronger shock (Mach ~ 2.3) corresponding to a shock velocity of $\sim 500 \text{ km s}^{-1}$. The apparent mismatch in the results motivated us to examine the details and re-interpret the X-ray data in order to understand the true nature of the shock.

1.7 Tools

The issues we have discussed here involve motion of different phases of gas in a galaxy and interaction between them. The temperature of the gas that is under consideration varies from 10^4 K to 10^8 K, where the gas is in a plasma state with no net charge. It can be shown that for such plasma the *fluid approximation* holds (the mean free path of the gas particles \ll typical length scale of interest) in the context of galactic winds and circumgalactic medium (see Table 1 of [Sharma, 2013](#)). We will further assume that the gas is non-relativistic or even if it is mildly relativistic (in case of AGN winds), the evolution of the wind can be modelled as a non-relativistic one. As we will see later that the free wind region, where the AGN wind is relativistic, is very small compared to the scales of interest. Another assumption that will be made throughout the thesis is that the gas does not contain magnetic fields. While, neglecting magnetic fields may not be always realistic, it greatly simplifies the problem and makes it easier to understand. However, we plan to include the magnetic fields in future studies.

Viscosity is another factor that could be important in galactic wind calculations. For a fully ionised, non-magnetised, thermal plasma, the dynamical viscosity is given as ([Guo et al., 2012](#))

$$\mu = 6 \times 10^3 \left(\frac{\log \Lambda}{37} \right)^{-1} \left(\frac{T}{10^8} \right)^{5/2} \text{ g cm}^{-1}\text{s}^{-1}, \quad (1.25)$$

where, $\log \Lambda \approx 37$ is the Coulomb logarithm term and T is the temperature in K. It is clear that for temperatures $\lesssim 10^7$ K, dynamical viscosity is $\lesssim 1$. A better evaluation of the situation is the Reynold's number that quantifies ratio of inertial force acting on two fluids and the viscous drag force between the fluids. The Reynolds number is written as

$$\mathcal{R} = \frac{\rho v L}{\mu}, \quad (1.26)$$

where, ρ , v and L are typical density, relative velocity and layer thickness between two fluids. For typical numbers in the CGM and outflow, $\rho \sim 10^{-3} m_p \text{ cm}^{-3}$, $v \sim 300 \text{ km s}^{-1}$ and $L \sim \text{kpc}$, indicate $\mathcal{R} \sim 2500$ which means that CGM can be assumed to be inviscid. Although the temperature of the central part of the wind is $\sim 10^7$ K, the density ($\rho \sim 0.1 m_p \text{ cm}^{-3}$) and flow velocity ($v \sim 1000 \text{ km s}^{-1}$) are large enough to make the fluid inviscid ($\mathcal{R} \sim 2500$) even in this part of the wind. However, for the shocked wind region, where the temperature is $\sim 10^7$ K ($\mu \sim 20$) and density is low ($\rho \sim 10^{-3} m_p \text{ cm}^{-3}$), the Reynolds number is ~ 10 which is marginally above the inviscid limit ($\mathcal{R} \gg 1$). To simplify the situation, we will also assume here that the viscosity does not play any role in the evolution of the wind. The viscosity is expected to deform the shape of the shocked wind and thus may affect the shape of the Fermi Bubbles that we obtain. This is a limitation of our calculations that we plan to improve in future works.

1.7.1 Equations used

Equations describing the motion of a fully ionised, non-magnetised and inviscid plasma in spherical coordinates are written in a conservative form as

$$\begin{aligned}
\frac{\partial \rho}{\partial t} + \vec{\nabla} \cdot (\rho \vec{v}) &= \dot{\rho}_{\text{inj}} \\
\frac{\partial M_r}{\partial t} + \vec{\nabla} \cdot (M_r \vec{v}) &= -\frac{\partial p}{\partial r} - \rho \frac{\partial \Phi}{\partial r} + \rho \frac{v_\theta^2 + v_\phi^2}{r} \\
\frac{\partial M_\theta}{\partial t} + \vec{\nabla} \cdot (M_\theta \vec{v}) &= -\frac{1}{r} \left[\frac{\partial p}{\partial \theta} + \rho \frac{\partial \Phi}{\partial \theta} + \rho v_r v_\theta - \rho v_\phi^2 \cot \theta \right] \\
\frac{\partial M_\phi}{\partial t} + \vec{\nabla}_r \cdot (M_\phi \vec{v}) &= -\frac{1}{r \sin \theta} \left[\frac{\partial p}{\partial \phi} + \rho \frac{\partial \Phi}{\partial \phi} \right] \\
\frac{\partial}{\partial t} (E + \rho \Phi) + \vec{\nabla} \cdot [(E + p + \rho \Phi) \vec{v}] &= \mathcal{H} - \mathcal{L}
\end{aligned} \tag{1.27}$$

Here, ρ is density, $\vec{v} = (v_r, v_\theta, v_\phi)$ is the velocity, $M_i = \rho v_i$ is the momentum in i -th direction, p is the pressure, $E = \frac{1}{2} \rho |\vec{v}|^2 + \frac{p}{\gamma-1}$ is the total energy density, $\gamma = 5/3$ is the adiabatic index for a mono-atomic gas, Φ is the gravitational potential, $\dot{\rho}_{\text{inj}}$ is the rate of density injection from SNe, \mathcal{H} is the SNe heating rate and \mathcal{L} is the radiative cooling term. The divergence terms are given as

$$\begin{aligned}
\vec{\nabla} \cdot \vec{A} &= \frac{1}{r^2} \frac{\partial}{\partial r} (r^2 A_r) + \frac{1}{r \sin \theta} \frac{\partial}{\partial \theta} (\sin \theta A_\theta) + \frac{1}{r \sin \theta} \frac{\partial}{\partial \phi} F_\phi \\
\vec{\nabla}_r \cdot \vec{A} &= \frac{1}{r^3} \frac{\partial}{\partial r} (r^3 A_r) + \frac{1}{r \sin^2 \theta} \frac{\partial}{\partial \theta} (\sin^2 \theta A_\theta) + \frac{1}{r \sin \theta} \frac{\partial}{\partial \phi} F_\phi
\end{aligned} \tag{1.28}$$

Note that, throughout this thesis we will assume the galaxy as a two-dimensional and axisymmetric system but include the evolution of v_ϕ . Such systems are also known as 2.5-dimensional systems. However, note that the evolution of the system along ϕ direction is not considered in such calculation. Therefore, any derivative of ϕ in the above equations will be set to zero.

1.7.2 Code used

To solve the equations considered above, even in very simplified situations, is not simple to do analytically unless extreme assumptions have been made about the geometry and the source terms. Most of the analytical works, therefore, have been performed only in spherical symmetric situations. The main limitation for such analysis is the inability to include variety of hydrodynamical instabilities, such as Kelvin-Helmholtz and Rayleigh-Taylor. Based on the importance of such instabilities, even the qualitative picture may completely change. Numerical approach, on the other hand, has the advantage of including all these effects self consistently and evaluate the situation more realistically. The only disadvantage of the numerical approach is that it can take up to several millions of cpu hours to solve a particular problem, of course with far more realistic solution than a simplified analytical calculation. Therefore, it becomes difficult to experiment using different values in the parameter space. However, with increasing computational power and powerful new algorithms this issue is becoming less and less important.

We use `PLUTO-4.0` numerical code (Mignone et al., 2007) to solve the fluid equations given in 1.27. `PLUTO` solves the conservative variables like, density (ρ), momentum (\vec{M}) and energy density (E) using finite volume method and uses finite difference method to include the effect of pressure (p), gravitational(Φ) field and other source terms. The code, however, uses primitive variables like velocity (\vec{v}) and pressure (p) for assigning input and producing output. The conservative variables are solved using Godunov’s scheme where a variety of Riemann solvers can be used to calculate the flux at the cell boundaries. Radiative cooling is solved by sub-cycling a full hydrodynamical time step.

1.8 Structure of the thesis

This thesis is structured as follows.

In **Chapter 2**, we study the effect of the circumgalactic medium on SNe driven outflows. We set up gaseous distribution of an axisymmetric Milky-Way type galaxy including the effect of gravity from dark matter and stellar disc. The set up includes a cold (10^4 K) disc gas component and a hot (3×10^6 K) CGM component. SNe energy and mass are injected within a spherical region of radius 60 pc at the centre of the galaxy. We study the evolution and dynamics of the outflowing gas in such a scenario with varying star formation rate. We also study the origin of multiphase gas and produce different quantitative measures from observational perspectives. The mass loading factor and velocity of the outflowing gas close to the galaxy and at the virial radius in case of single or multiple star-bursts have been quantified.

In **Chapter 3**, We study the origin of diffuse X-ray emission from the interaction of SNe driven outflows and the CGM. We compare the X-ray emission from the central region of the galactic wind and the CGM. We asses the possible enhancement of the mass loading factor in increasing the X-ray emission from central region. We also verify our analytical estimations of the X-ray luminosity by performing numerical simulations. We apply our understanding of the X-ray emission from galactic wind and CGM to understand recent X-ray observations from star forming galaxies, specifically, the L_X -SFR relation.

In **chapter 4**, we turn our attention to our Galaxy where two giant gamma-ray bubbles, called the Fermi Bubbles, have been detected. We simulate a SNe driven wind in a set-up that closely matches the Galactic environment. By using morphological and X-ray information, we constrain the age of the bubbles and required star formation rate at the centre of our Galaxy. Since our simulations do not include any cosmic ray of magnetic field, we assume these energy densities are proportional to the total energy content at any point in the simulation. We then compare the synchrotron emission calculated from our simulation with the observed microwave haze to constrain the magnetic field inside the bubbles. We find that the leptonic (IC of CMB by CR electrons) gamma-ray emission produced in our simulations is very close to the observations. We also report close similarity of the simulated cloud kinematics to the observed UV absorption lines through the Fermi Bubbles.

In **Chapter 5**, we re-interpret the observed O VIII and O VII X-ray lines to asses the shock strength outside the Fermi Bubbles. We generate synthetic line ratios of O VIII and O VII from our simulations and compare them with the observed values. We also consider situations where the electrons and protons are not in equilibrium and

estimate the observable electron temperature that will contribute to the observed line ratios. We find that the energetics of the Fermi Bubbles is consistent with our previous estimate. We also rule out much higher energetic phenomena as a possible origin of the Fermi Bubbles.

We summarise our findings in **chapter 6** and indicate future directions. Supplement materials used in the thesis have been provided in the appendix.

Chapter 2

Effect of circumgalactic medium on outflows and generation of high velocity cold gas

Based on:

“Long way to go: how outflows from large galaxies propagate through the hot halo gas” by Sarkar K. C., Nath B. B., Sharma P., Shchekinov Y., 2015, *MNRAS*, 448, 328 ([Sarkar et al., 2015a](#))

Galaxies do not evolve as closed systems, and the amount and nature of infall and outflow regulate the crucial aspects of galactic evolution. The movement of gas in and out of a galaxy plays a crucial role in dictating the star formation history of the galaxy, which in turn determines other aspects of its evolution. The infall and outflow of gas also shape the so-called galaxy eco-system, in the immediate vicinity of the galaxy. Not only the evolution of the galaxy itself, but galactic outflows also have cosmological importance because they enrich the intergalactic medium (IGM) with metals. The infall of the IGM gas into a galaxy depends, among other things, on the cooling efficiency of this gas, which in turn depends on the efficiency of outflows in depositing mass and metals into the IGM. Parameters that are most important in regulating the star formations rate in a galaxy are the mass outflow rate compared to the star formation rate, and the velocity of the outflow. We investigate outflow properties for Milky Way type galaxies by varying the star formation rate. We particularly pay attention to the effects of extended hot halo gas surrounding such massive galaxies.

Main results

- We find that the total mass loss at inner radii scales roughly linearly with total mass of stars formed, and that the mass loading factor ($\eta =$ ratio of mass outflow to the star formation) at the virial radius can be several times its value at inner radii because of the swept up hot halo gas.
- The temperature distribution of the outflowing material in the inner region (~ 10 kpc) is bimodal in nature, peaking at 10^5 K and 3×10^6 K, responsible for optical and X-ray emission, respectively. The contribution of cold/warm gas with temperature $\leq 10^{5.5}$ K to the outflow rate within 10 kpc is ≈ 0.3 – 0.5 .
- The warm mass loading factor, η_{3e5} ($T \leq 3 \times 10^5$ K) is related to the mass loading factor at the virial radius (η_v) as $\eta_v \approx 25 \eta_{3e5} (\text{SFR}/\text{M}_{\odot}\text{yr}^{-1})^{-0.15}$ for a baryon fraction of 0.1 and a starburst period of 50 Myr.
- The outflow speed at the virial radius is close to the sound speed in the hot halo, $\lesssim 200$ km s $^{-1}$. We also identify two ‘sequences’ of outflowing cold gas at small scales: a fast (≈ 500 km s $^{-1}$) sequence, driven by the unshocked free-wind; and a slow sequence ($\approx \pm 100$ km s $^{-1}$) at the conical interface of the superwind and the hot halo.

2.1 Introduction

The mass loss rate in outflows has been estimated in various ways in the literature. In the standard scenario, outflows are believed to be excited mostly through the effect of multiple supernovae (SNe) arising from vigorous star formation in a galaxy. Recently other possible mechanisms, such as radiation pressure on dust grains embedded in the outflowing gas, and cosmic rays have also been invoked in launching these outflows. In the SNe driven scenario, [Larson \(1974\)](#) estimated the total mass lost by equating the total thermal energy deposited in the interstellar medium (ISM) by multiple SNe, to the escape energy of the outflowing gas in a galaxy (which depends on the total mass, baryonic mass and the size of the galaxy). Equivalently, the mass lost equals the total thermal energy of the ISM divided by the square of the wind speed, which is likely of order the sound speed of the hot gas. This led to an estimate that a galaxy of mass (all baryonic) $\sim 5 \times 10^9 M_\odot$ would lose half of its mass in an outflow, and larger galaxies would lose relatively less mass. This idea led [Dekel & Silk \(1986\)](#) to consider the effect of such winds in the evolution of dwarf galaxies, and they found that outflows from halos with virial speed less than $\sim 100 \text{ km s}^{-1}$ have sufficient energy to eject most of the halo gas. This result suggested a dividing line between bright and diffuse dwarf galaxies (see also [Babul & Rees \(1992\)](#)). If the outflow speed is comparable to the escape speed (which scales with the disk rotation speed, v_c), then it also means that the ratio of mass loss rate to SFR, $\eta (\equiv \dot{M}/\text{SFR}) \propto v_c^{-2}$, for energy driven outflows. Such estimates of mass (and metals) lost were used in the early, semi-analytical calculations for the enrichment of the IGM ([Tegmark et al., 1993](#); [Nath & Trentham, 1997](#); [Ferrara et al., 2000](#)). If other mechanisms such as radiation pressure should dominate, then it has been shown that the outflow would be momentum driven instead of being driven by energy, and that $\eta \propto v_c^{-1}$ ([Murray et al., 2005](#)).

However, as observations of typical multiphase outflows (such as in M82) suggest, the estimate of mass lost is likely to be more complicated than as outlined above. The outflowing material consists of gas at different temperatures (ranging from the X-ray emitting hot gas to a cold phase containing molecular gas), and the speed throughout the outflow is hardly uniform. The multiphase temperature/density structure and dynamics is further complicated by the non-spherical morphology of the outflow, which is moulded into a biconical shape by the interaction with the stratified disk material of the star forming galaxy.

The multidimensional and multiphase nature of galactic outflows calls for a more detailed numerical modelling, especially because only certain phases at smaller scales are accessible to observations. For the IGM, however, the scales close to the virial radius are the most important. Therefore, it is essential to understand the relation between outflows at various scales via controlled numerical simulations.

Numerical simulations have helped one to overcome the limitations of 1-D semi-analytical calculations. [Mac low & Ferrara \(1999\)](#) simulated SNe driven superbubbles of various mechanical luminosities in disks embedded in dark matter halos, and determined their efficiency in driving outflows from low-mass galaxies. The central source of energy (and mass) injection had a constant luminosity maintained for 50 million years. They found the range of luminosities (related to the star formation rate) that can drive out gas, completely or partially, from galaxies of different masses. They found that only a small fraction of the total gas mass was expelled, except in the smallest galaxy

considered (with $10^6 M_\odot$ gas). However, because of the absence of the hot halo gas in their simulations, the results cannot be directly applied to higher mass galaxies ($M \gtrsim 10^{12} M_\odot$). The hot gas density in the halo is expected to be non-negligible, $n \sim 10^{-4} \text{ cm}^{-3}$ (e.g., see [Sharma et al. 2012](#)), for a Milky-Way mass galaxy, and therefore the halo gas must be included in order to study outflows at scales > 10 kpc.

We find that the properties of supernovae driven outflows in a circumgalactic medium (CGM) is less explored compared to the studies where such CGMs are neglected. In this chapter we investigate outflow properties varying the star formation rate over a wide range, keeping the ISM and halo properties fixed to the Milky Way values. Our study is similar in spirit to that of [Mac low & Ferrara \(1999\)](#), but we include the effect of hot halo gas in constraining the outflowing gas. We have also investigated the relation between outflows in the cold phase and the total outflow rate at smaller scales and at the virial radius. Moreover, we investigate the detailed kinematics of the cold/warm gas and relate it with observations and point towards the origin of such cold gas.

The chapter is organised as follows. In §2, we discuss the mass model of the simulated galaxy, setting an equilibrium initial condition and selection of the injection parameters. In §3, we describe the PLUTO simulation code and various settings that we use. In §4, we present the results of our runs, in §5, we discuss some of the implications of our work and finally in §6 we summarise our key findings.

2.2 Mass model of the Galaxy

2.2.1 Gravitational potentials

To model the density distribution of the gas, we consider two gravitational potentials. For the disk, we use the Miyamoto & Nagai potential ([Miyamoto & Nagai, 1975](#)) (in cylindrical coordinates (R, z)),

$$\Phi_{\text{disk}}(R, z) = -\frac{GM_{\text{disk}}}{\sqrt{R^2 + (a + \sqrt{z^2 + b^2})^2}}, \quad (a, b \geq 0) \quad (2.1)$$

where a and b represent the scale length and the scale height of the disk (mass M_{disk}) respectively. For the dark matter, we use a modified form of the NFW dark matter (DM), which unlike the original NFW profile ([Navarro et al., 1997](#)), has a core with a finite dark matter density at the centre. The potential is given as

$$\Phi_{\text{DM}} = -\left(\frac{GM_{\text{vir}}}{f(c)r_s}\right) \frac{\log(1 + \sqrt{R^2 + z^2 + d^2}/r_s)}{\sqrt{R^2 + z^2 + d^2}/r_s} \quad (d \geq 0), \quad (2.2)$$

where $f(c) = \log(1+c) - c/(1+c)$ with $c = r_{\text{vir}}/r_s$, the concentration parameter and d is the core radius of the DM distribution (see appendix [A.2](#) for the DM density profile). M_{vir} , r_{vir} and r_s are the total mass of the galaxy (including DM), the virial radius and scale radius respectively. A full list of parameters for the model galaxy is given in the Table [2.1](#).

parameters	values
$M_{\text{vir}}(M_{\odot})$	10^{12}
$M_{\text{disk}}(M_{\odot})$	5×10^{10}
$T_{\text{vir}} \text{ K}$	3×10^6
$r_{\text{vir}} \text{ (kpc)}$	258
c	12
$r_s \text{ (kpc)}$	21.5
$a \text{ (kpc)}$	4.0
$b \text{ (kpc)}$	0.4
$d \text{ (kpc)}$	6.0
$c_{s,\sigma} \text{ (km s}^{-1}\text{)}$	20.8
$Z_{\text{disk}} (Z_{\odot})$	1.0
$Z_{\text{halo}} (Z_{\odot})$	0.1
$\rho_c(0, 0) \text{ (m}_p\text{cm}^{-3}\text{)}$	3.0
$H_R \text{ (kpc)}$	~ 2.2
$H_z \text{ (kpc)}$	$\simeq 0.2$
$M_{\text{WIM}}(M_{\odot})$	7×10^8
$\rho_{\text{hot}}(0, 0) \text{ (m}_p\text{cm}^{-3}\text{)}$	1.1×10^{-3}

Table 2.1: Parameters used in our simulations.

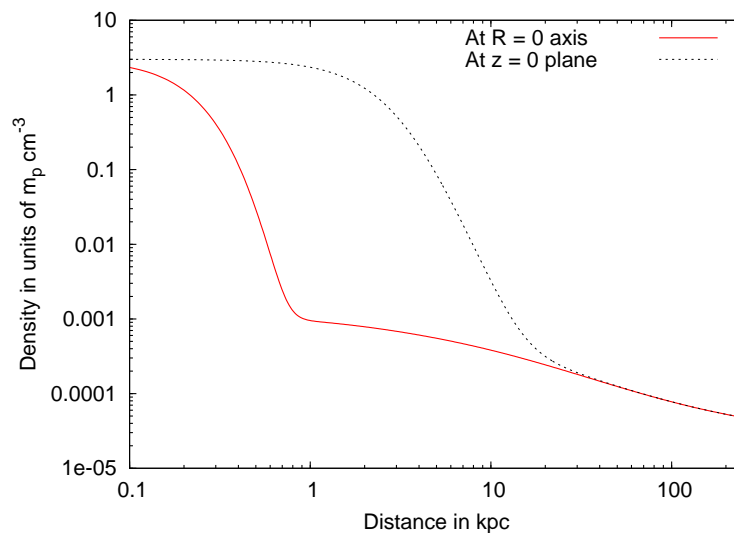


Figure 2.1: Gas density profiles for the model galaxy along R and z . It shows that the disk component dominates at smaller R and z , and at larger distances, the halo component dominates.

2.2.2 Setting the initial density distribution

In our model, we consider two components of the interstellar medium (ISM): warm ionised medium (WIM), and a hot ionised medium (HIM). Since the WIM ($T \sim 10^4\text{K}$, hereafter we call it the disk gas) is a part of the disk gas which is rotating along with the stars, we consider the effect of rotation on the density distribution of the WIM. The HIM, however, according to the galaxy formation theory, traces out the potential of the dark matter with no net rotation and has a temperature close to the virial temperature of the halo ($T_{\text{halo}} \sim 3 \times 10^6\text{K}$ for MW type galaxy). This prescription is similar to the set-up of [Suchkov et al. \(1994\)](#).

To construct the initial density distribution for the combined gas, we consider the Euler's equation in steady state

$$-\frac{\nabla p}{\rho} - \nabla(\Phi_{\text{DM}} + \Phi_{\text{disk}}) + \frac{v_{\phi,g}^2}{R} \hat{R} = 0, \quad (2.3)$$

for each of the components. Here, p is pressure, ρ is density and $v_{\phi,g}$ is the gas rotation velocity. Since for the gas in the disk, the gravitational force is balanced by rotation and gas pressure together, the rotation speed is less than the particle rotation velocity, $v_{\phi,G} = \sqrt{R \left[\frac{\partial \Phi}{\partial R} \right]_{z=0}}$, which is solely determined by gravity. For simplicity, we take the rotation velocity of the gas as a fraction ($f = \text{constant}$, chosen to be 0.95) of $v_{\phi,G}$ at that point: $v_{\phi,g} = f v_{\phi,G}$. Therefore, the density distribution for the warm disk gas can be written as,

$$\rho_d(R, z) = \rho_c(0, 0) \exp\left(-\frac{1}{c_{\text{sc}}^2} [\Phi(R, z) - \Phi(0, 0) - f^2(\Phi(R, 0) - \Phi(0, 0))]\right), \quad (2.4)$$

and for the hot halo gas,

$$\rho_h(R, z) = \rho_h(0, 0) \exp\left(-\frac{1}{c_{\text{sh}}^2} [\Phi(R, z) - \Phi(0, 0)]\right), \quad (2.5)$$

where, $\rho_c(0, 0)$ and $\rho_h(0, 0)$ are the warm and hot central densities and c_{sc} and c_{sh} are the isothermal sound speeds of the warm disk and hot halo, respectively (more details on the set-up are given in appendix A.3). In Figure 2.1 we show the steady state gas density distribution along the minor axis (red solid line) and the major axis (black dotted line). This figure shows that each profile consists of two features, one high density structure at lower radii representing the disk material, and another, low density and comparatively flatter distribution at larger radii representing the halo gas.

In disk galaxies, along with the thermal pressure, there is pressure due to turbulence, magnetic fields and cosmic rays, which arises because of the continuous stirring of gas by supernovae. Therefore, the dynamics of the disk is determined by both thermal and non-thermal pressures, for which the effective sound speed can be written as

$$c_{s,\text{eff}}^2 = c_{s,T}^2 + c_{s,\sigma}^2, \quad (2.6)$$

where, $c_{s,T}$ is the isothermal sound speed corresponding to a temperature T and $c_{s,\sigma}$ is the effective sound speed due to non-thermal components. We include these effects by assuming a disk temperature of $4 \times 10^4\text{K}$, with an effective sound speed $c_{s,\text{eff}} = 24\text{ km s}^{-1}$ (larger than $c_{s,T}$, the sound speed of WIM at 10^4K).

For the disk, we set the central density to be 3.0 particles per cm^3 . The hot halo is however less constrained by observations. In order to fix the central density of the hot halo, we normalise the halo mass distribution to give a total halo gas mass $M_{h,\text{gas}} = 0.11M_{\text{vir}}$ and ratio of the stellar disk mass to the virial mass M_{vir} is 0.05, as in the scenario of [Mo et al. \(1998\)](#). Thus, the halo has a global baryon fraction of 0.16, consistent with the cosmic value of $f_b = \Omega_b/\Omega_m$. Some of the recent observations have revealed that the baryon fraction can be ~ 0.1 for massive spirals ([Bogdán et al., 2013](#)), and in our MW, this fraction can be ~ 0.16 for a gas with polytropic index $\gamma = 5/3$ in hydrostatic equilibrium ([Fang et al., 2013](#); [Gatto et al., 2013](#)). Though here we assume $f_b = 0.16$, we have also checked the effect of f_b on the mass loading factor at virial radius (see §2.4.3).

The total density is the sum of the densities of the hot halo and warm disk components, $\rho = \rho_d + \rho_h$. Since the halo gas does not rotate, the effective rotation speed $v_{\phi,\text{net}}$ for the combined gas is given as

$$\rho v_{\phi,\text{net}}^2 = \rho_d v_{\phi,g}^2, \quad \Rightarrow \quad v_{\phi,\text{net}} = f \sqrt{\frac{\rho_d}{\rho} R \left[\frac{\partial \Phi}{\partial R} \right]_{z=0}}. \quad (2.7)$$

We have found that the above prescription for the initial set up is remarkably stable over a time scale of 1 Gyr. In reality (in 3D), the interaction between the non-rotating halo gas and the rotating disk gas could generate instabilities. We can estimate the time scale for Kelvin-Helmholtz instability at the interface of the rotating disk and the non-rotating halo. The dominant wavelength of perturbation is ~ 10 kpc, the corresponding relative velocity $\sim 100 \text{ km s}^{-1}$, and the ratio of densities of two gases is ~ 100 (for gases with temperature 10^4 and 10^6 K and in pressure equilibrium). The time scale for the growth of perturbations is therefore ~ 1 Gyr. We have also checked with a 3D simulation run that this steady state holds up to ~ 1 Gyr. Therefore the set up described above is adequate for our simulations.

2.3 Simulation set-up

In this section we describe various simulations that we carry out and the numerical set-up. We have carried out two kinds of simulations to study galactic outflows: small-scale, short-duration (50 Myr) simulations going out to 30 kpc to focus on the inner regions where most observational constraints come from; and large-scale, longer-duration (1 Gyr) simulations going out to 250 kpc to study cosmological impact of galactic outflows. In cases where we focus on observations of multiphase outflows we use the high-resolution small-scale runs (c.f. Figs. 2.2, 2.3, 2.10, 2.14, 2.15, & 2.16). The large-scale runs are used to infer outflow properties at the halo scale (c.f. Figs. 2.4, 2.5, 2.6, 2.12, & 2.13).

We have studied mechanical luminosities ranging from $10^{40.3}$ to $10^{43} \text{ erg s}^{-1}$ keeping the model parameters fixed. We have chosen a fiducial run corresponding to a mechanical luminosity injection of $\mathcal{L} = 10^{42} \text{ erg s}^{-1}$ or $\text{SFR} = 14.3 M_{\odot} \text{ yr}^{-1}$ (see §2.3.1), lying in the intermediate regime of luminosities that we have explored. A full list of runs is given in Table 2.2.

2.3.1 Injection parameters

In this chapter we only focus on supernovae (SNe) driven outflows. Since a single supernova, or even a large number of SNe, is not energetic enough to launch an outflow on larger scales unless they are coherent in space and time (Nath & Shchekinov, 2013; Vasiliev et al., 2015), we consider the effect of multiple SNe from a large OB association in the central region of the galaxy. We consider a constant energy input of mechanical luminosity \mathcal{L} from the SNe confined in a spherical region of radius r_{inj} at the centre of the galaxy. We deposit thermal energy to the gas within r_{inj} . Sharma et al. (2014b) have shown that for such an implementation to work, the injection radius (r_{inj}) should be such that the energy deposition time is shorter than the cooling time, and we have adjusted our r_{inj} ($= 60$ pc) according to this constraint. We also assume that each SN releases an energy of 10^{51} ergs, and for a Salpeter mass function, on average, $\dot{M}_{\text{inj}} = 0.1 \times \text{SFR}$ of mass is injected into the interstellar medium (ISM). Therefore, the relation between the mechanical luminosity and SFR can be written as

$$\mathcal{L} = 10^{51} \times \epsilon \times f_{\text{SN}} \times \text{SFR} \text{ erg s}^{-1}, \quad (2.8)$$

where, f_{SN} is the number of supernovae explosions per unit mass of stars formed, and ϵ is the efficiency of heating the gas. We assume $\epsilon = 0.3$, consistent with observations (Strickland & Heckman, 2007) and theoretical estimates from numerical simulations (Vasiliev et al., 2015). For Salpeter IMF, $f_{\text{SN}} = 7.4 \times 10^{-3} / M_{\odot}$ for lower and upper limits of stars at 0.1 and 100 M_{\odot} . This gives,

$$\mathcal{L} = 7 \times 10^{40} \text{ erg s}^{-1} \frac{\text{SFR}}{(1 M_{\odot} \text{ yr}^{-1})}. \quad (2.9)$$

This in turn gives the relation between luminosity (\mathcal{L}) and the rate of mass injection as

$$\dot{M}_{\text{inj}} = 0.014 \times \frac{\mathcal{L}}{10^{40} \text{ erg s}^{-1}} M_{\odot} \text{ yr}^{-1}. \quad (2.10)$$

The duration of mass and energy injection is assumed to be 50 Myr, the typical lifetime of an OB association. The effect of different star burst duration is also discussed in §2.4.2.

2.3.2 The code settings

We use the publicly available hydrodynamic code PLUTO (Mignone et al., 2007) for our simulations. We run our simulations in 2D (r, θ) spherical coordinates, assuming axisymmetry ($\partial/\partial\phi = 0$). However, we do allow for a non-zero azimuthal velocity v_{ϕ} . To solve the hydrodynamic equations (Euler equations with numerical dissipation and with mass and energy source terms which drive the outflows), we use piecewise parabolic reconstruction of the primitive variables. We use the advection upstream splitting method (AUSM+; Liou 1996) as the Riemann solver and a third-order Runge-Kutta scheme (RK3) to advance the solution in time.

- *Grid* : Since we inject the SNe energy and mass in a small region of space ($= 60$ pc) at the centre of the galaxy and try to observe the effects near the virial radius

Name	r_{\max} (kpc)	\mathcal{L} (erg s ⁻¹)	t_{inj} (Myr)	cooling
L1	250	10 ^{40.3}	50	on
L2	250	10 ⁴¹	50	on
L3*	250	10 ⁴²	50	on
L4	250	10 ⁴³	50	on
L5	350	10 ^{41.3}	RSB	on
L6	250	10 ^{41.7}	50	on
L7	250	10 ^{42.3}	50	on
L8	250	10 ^{42.6}	50	on
L9	250	10 ⁴²	25	on
L10	250	10 ⁴²	100	on
L11	250	10 ⁴²	200	on
L12	250	10 ⁴²	25	off
L13	250	10 ⁴²	50	off
L14	250	10 ⁴²	100	off
L15	250	10 ⁴²	200	off
S1	30	10 ^{40.3}	50	on
S2	30	10 ⁴¹	50	on
S3*	30	10 ⁴²	50	on
S4	30	10 ⁴³	50	on

Table 2.2: List of runs: The L-series and S-series represents the large-scale and small-scale simulations respectively. The corresponding box size is given in 2nd column, where r_{\max} gives the maximum extent of grid in radial direction. The 3rd and 4th column provides the mechanical luminosity and the injection time of the runs, while the 5th column gives the information about cooling. For L5, RSB means Repeated Star Bursts. The fiducial runs are denoted by an “*”. Other than these runs, we have also run some simulations with variable baryon fraction (f_b).

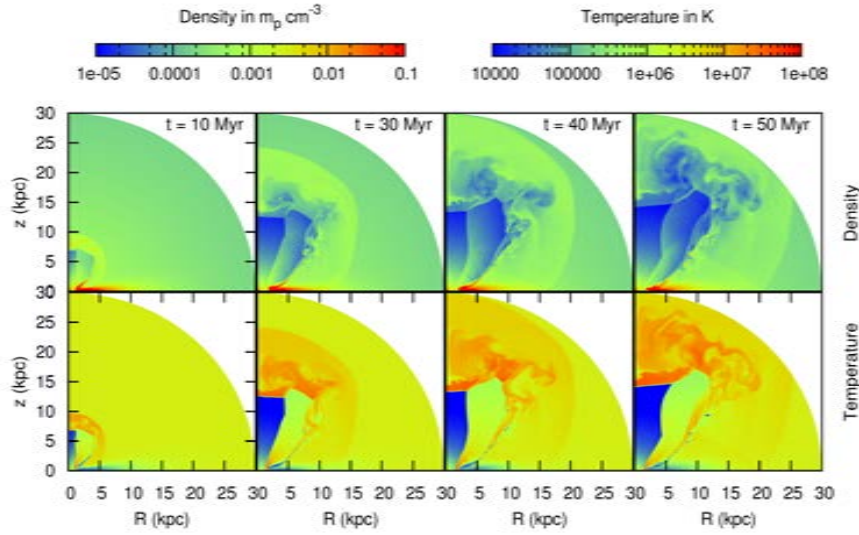


Figure 2.2: Snapshots of density (top panel) and temperature (bottom panel) at 10, 30, 40 and 50 Myr for $\mathcal{L} = 10^{42} \text{ erg s}^{-1}$ for a box size of $r_{\text{max}} = 30 \text{ kpc}$. Notice that the cold, multiphase gas, which is mainly due to the uplifted disc gas, is confined to the outer wall of the outflow.

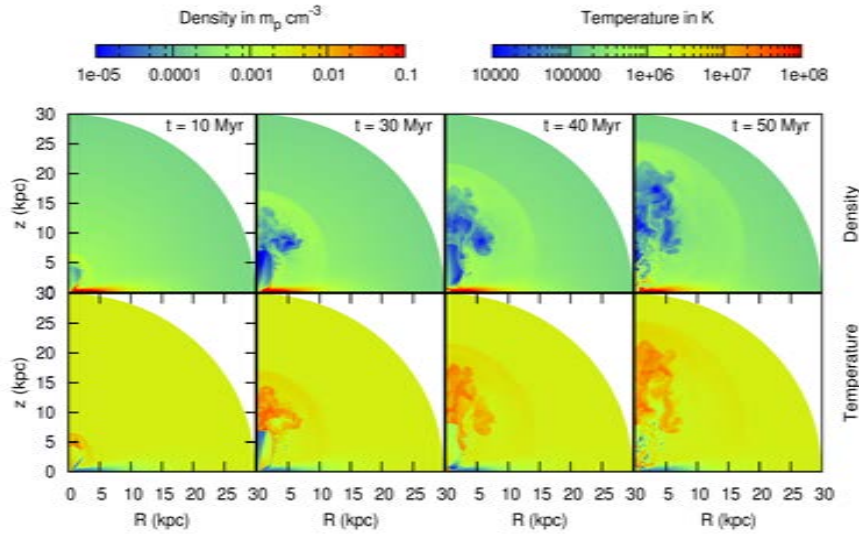


Figure 2.3: Snapshots of density (top panel) and temperature (bottom panel) at 10, 30, 40 and 50 Myr for $\mathcal{L} = 10^{41} \text{ erg s}^{-1}$ for a box size of $r_{\text{max}} = 30 \text{ kpc}$. The evolution is different from Figure 2.2 in that, in addition to the cold gas at the outer wall, there is volume-filling cold disk gas at 50 Myr dredged up by the ram pressure of the outflow. It will be shown later in §2.4.4 that the cold gas at the outer wall is slower compared to the volume-filling cold gas.

(~ 250 kpc), we use a logarithmic grid in the radial (r) direction. It starts from 20pc and goes till 250 kpc for the large scale simulations and till 30 kpc for the small-scale simulations. A uniform grid is used in the θ direction going from $\theta = 0$ to $\pi/2$.¹ For the results mentioned in this chapter, we use 512 grid points along both r and θ directions. We have also carried out resolution studies with double and half this resolution in each direction.

- *Boundary conditions* : The inner and outer radial boundary values for mass and energy densities are set to their equilibrium values at $t = 0$ (as discussed in §2.2.2). The velocities are copied in the radial ghost zones from the nearest active zones. The θ boundary conditions are set as reflective.
- *Metallicity*: Since the mixing of metals at kpc range in ISM densities and temperatures is dominated by the dynamical evolution of the gas rather than diffusion, we track the metallicity by treating it as a passive scalar which follows the simple advection equation. We set the disk metallicity to be equal to the solar metallicity (Z_{\odot}) and the halo metallicity to be $0.1 Z_{\odot}$.
- *Cooling* : PLUTO can include optically thin losses in a fractional step formalism¹. It has several different cooling modules, among which, we use the tabulated cooling method which solves the internal energy equation from a given $T - \Lambda(T)$ table. We include the metallicity effect in the cooling rate by using linear interpolation of the cooling curves corresponding to $Z = Z_{\odot}$ and $Z = 0.1 Z_{\odot}$ (Sutherland & Dopita, 1993), to all other metallicities from Z_{\odot} to $0.1 Z_{\odot}$.

In our calculation, we express the temperature as $T = p/\rho$, which includes the dynamical pressure in addition to the thermal pressure, and therefore the effective temperature of the gas in the disk becomes large enough to induce strong cooling, unlike in the WIM at 10^4 K. To stop this cooling, we constrain the cooling function of the disk material (but not the injected material) to be zero within a box of size $R \times z = 15 \times 2$ kpc², This can be thought of as a crude model of continuous SNe/stellar heating or turbulent support of gas in the disk, which prevents disk cooling.

- *Units* : To avoid the calculation of very small ($\sim 10^{-24}$) or very large ($\sim 10^{33}$) numbers, PLUTO works with non-dimensional, arbitrary units. The basic units used in our simulations are length (L_0) = 1 kpc, velocity (v_0) = 100 km s⁻¹ and density (ρ_0) = 1.67×10^{-23} gm cm⁻³ = $10 m_p$ cm⁻³. All other units are derived from these basic units as time (t_0) = $L_0/v_0 = 9.8$ Myr and pressure (p_0) = $\rho_0 v_0^2 = 1.67 \times 10^{-9}$ dyne cm⁻². Therefore, the rate of energy and mass injection to the spherical starburst region (using Eq. 2.9 and 2.10) can be written in terms

¹More can be found in the user's guide of PLUTO - <http://plutocode.ph.unito.it/Documentation.html>

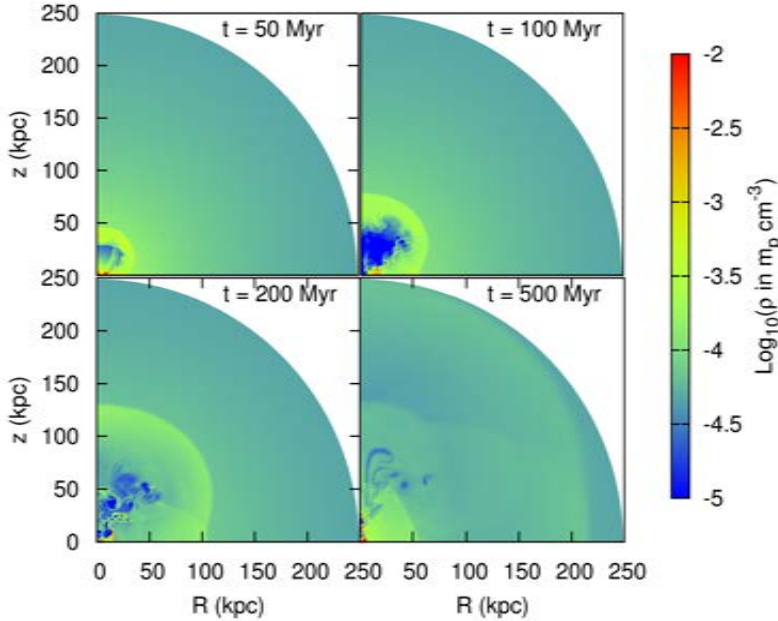


Figure 2.4: Density distribution at 50, 100, 200 and 500 Myr for $\mathcal{L} = 10^{43} \text{ erg s}^{-1}$ for a box size of $r_{\text{max}} = 250 \text{ kpc}$. Note that these plots are on a scale ~ 10 times larger than the ones in Figures 2.2 & 2.3.

of pressure and density as

$$\begin{aligned} \dot{p} &= \frac{2}{3} \frac{\mathcal{L}}{(4\pi/3) r_{\text{inj}}^3} \\ &= 9.7 \times \left(\frac{\mathcal{L}}{10^{40} \text{ erg s}^{-1}} \right) \left(\frac{100 \text{ pc}}{r_{\text{inj}}} \right)^3 p_0/t_0 \end{aligned} \quad (2.11)$$

$$\begin{aligned} \dot{\rho} &= \frac{\dot{M}_{\text{inj}}}{(4\pi/3) r_{\text{inj}}^3} \\ &= 0.118 \times \left(\frac{\mathcal{L}}{10^{40} \text{ erg s}^{-1}} \right) \left(\frac{100 \text{ pc}}{r_{\text{inj}}} \right) \rho_0/t_0 \end{aligned} \quad (2.12)$$

where, p_0 , ρ_0 and t_0 are the code units of pressure, density and time respectively.

2.4 Results

In this section we present our simulation results on the effect of outflows with different mechanical luminosities. Figure 2.2 shows the evolution of density and temperature for the zoomed-in (box size of $30 \times 30 \text{ kpc}^2$) fiducial run ($\mathcal{L} = 10^{42} \text{ erg s}^{-1}$). It shows the standard stellar wind structure, with a free wind (Chevalier & Clegg 1985) in the inner region characterised by dilute gas with high velocity, surrounded by the shocked wind and the shocked ISM. After breaking out from the disk, the free wind forms a conical

shape, because of the interaction with the halo gas. The shocked wind and the shocked ISM form a multiphase structure. Because of radiative cooling, parts of this interaction zone with high density gas breaks into smaller clumps and forms clouds which are then carried away by the outflow or they fall back towards the galactic center due to gravity.

Similar wind structure is found in general for all mechanical luminosities. However, for low luminosity cases, because of the relatively low pressure in the central region, the disk material can press inwards after a certain time. Figure 2.3 shows one such example for $\mathcal{L} = 10^{41} \text{ erg s}^{-1}$ where, at 40 Myr, the advancement of the disk material almost completely covers the injection region (at a scale of $\sim 1 \text{ kpc}$). The increase in pressure, because of the continuing injection of energy and mass, thereafter blows away the disk material and forms a filamentary multiphase outflow. We discuss the characteristics of these clouds and filaments later in §2.4.4. The interference of the disk material into the base of free wind can also add ripples to the conical shape of the free wind as witnessed in Figure 2.2.

After injection is switched off ($t > 50 \text{ Myr}$), the free wind disappears and the inner region develops a complex density and velocity structure, which then gradually falls back towards the galactic center as shown in Figure 2.4. The forward shock, however, keeps propagating through the halo medium, finally becoming an acoustic disturbance of the medium for lower luminosities ($L \lesssim 10^{42} \text{ erg s}^{-1}$). The material that falls back to the center with non-zero velocity, collides with other gas clumps and generates secondary shocks which then push the infalling material away (lower panel of Fig. 2.4). After few such bouncing back and forth, the gas finally settles down at the center to form a disk-like structure (right-bottom panel of Fig. 2.4). In this whole process of infall and outflow, some dilute ($\rho \sim 10^{-5} \text{ m}_p \text{ cm}^{-3}$) and hot ($T \sim 10^7 \text{ K}$) gas is left behind in the halo in the form of eddies. This gas neither takes part in outflow nor contributes to infall, rather becomes a part of the circumgalactic medium via dynamical mixing.

Quantitatively, the parameters of interest are, 1) the mass loading factor, which tells us the amount of mass that goes out of the virial radius, 2) the temperature distribution of the outflowing material, which holds the information regarding the various phases of the gas, and which determines the observability of these phases. 3) the velocity structure, which gives an overview of the motions of different gas phases and the coupling between them. We will discuss these properties, below, one by one.

2.4.1 Mass loading factor

The mass outflow rate across a spherical shell of radius r can be written as

$$\dot{M}_{\text{out}}(r, t) = 4\pi r^2 \int_0^{\pi/2} (\rho v_r) \sin \theta d\theta, \quad (2.13)$$

where θ is the zenith angle. Note that the velocity v_r in the integrand has both positive and negative values, so that, after integrating, it gives the net mass outflow rate. This outflow rate is finally integrated over time to obtain the total amount of outflowing mass (M_{out}) at each radius for different luminosities.

This mass outflow can be compared with the total mass of new stars formed (M_*^+), and one defines a mass loading factor as

$$\eta(r, T) = \frac{M_{\text{out}}}{M_*^+} = \frac{1}{M_*^+} \int_0^T \dot{M}_{\text{out}}(r, t) dt. \quad (2.14)$$

The choice of the integration time, T , depends upon the spatial scale of interest and is discussed later in this section.

Figure 2.5 shows the evolution of the mass outflow rate \dot{M}_{out} in units of starburst SFR at two different radii, $r = 16, 160$ kpc (shown with red (thick) and blue (thin) lines), as a function of time (in Myr) for three different injection luminosities, $10^{41,42,43}$ erg s $^{-1}$ (shown with dot-dashed, double dotted and solid lines, respectively). Consider the blue and red dot-dashed lines, denoting the evolution of \dot{M}_{out} for $L = 10^{41}$ erg s $^{-1}$ with time. We find that a shell of shocked ISM and shocked wind travels outward, reaching ~ 160 kpc (blue) in ~ 600 Myr. The negative values of \dot{M}_{out} corresponds to infall, which at the very outer radii arises due to acoustic oscillations of the halo gas, but at inner radii corresponds to the infall of gas due to various instabilities. The interaction region between the halo and the wind suffers from thermal and Kelvin-Helmholtz instabilities, as well as the Rayleigh-Taylor instability when there is acceleration (Fraternali & Binney, 2006; Sharma et al., 2014a). These instabilities are the key mechanisms behind the formation of clouds, some of which are the part of a galactic fountain.

The time integrated outflowing mass presents a less chaotic behaviour. In Figure 2.6 we show the time integrated values of the mass loading factor η (eqn 2.14) for our fiducial run ($\mathcal{L} = 10^{42}$ erg s $^{-1}$), integrated over different periods for each distance (shown in different colours/styles). The figure shows the gradual outward progression of the outflowing material in the halo. E.g., the shell reaches a distance of ~ 50 kpc in 100 Myr, and finally reaches the virial radius at a time scale of ~ 800 Myr. The figure also shows that the mass loading factor in the inner region can have small values when integrated over a long time scale, because of the infall of material in absence of injection. Therefore the behaviour of η at the inner region can be better understood if it is integrated over an appropriate, and short time scale (~ 100 Myr). On the contrary, for the mass loading factor near the virial radius, it is reasonable to average it over a long (\sim Gyr) time scale. The mass outflow at smaller scale is commonly compared with the current (ongoing) star formation process. However, since the effect of central starburst reaches the virial radius only after sufficient time has elapsed (the travel time, \sim Gyr), the mass outflow at large radii cannot be connected to the present day star formation. Instead, it should be compared with the past SF which caused it (i.e. the injection epoch). We define the outer mass loading factor (to be precise, the mass loading factor at virial radius) as $\eta_v = \eta(r_{\text{vir}}, t_v)$, where the integration time t_v is the roughly the time taken by outflow to reach 200–230 kpc. Depending on the luminosity, t_v varies from 750 Myr to 900 Myr. In order to evaluate the inner mass loading factor we take integration time $t_v = 100$ Myr. Since the shell of outflowing material reaches a distance 20–50 kpc in 100 Myr, we denote the inner mass loading factor as η_{20} . The outflow is mainly contributed by a shell of mass moving out through the medium (Figure 2.6). Therefore, we take the peak value of the shell as the mass loading factor at that epoch.

The dependence of these two values of η (i.e. η_{20} and η_v) on \mathcal{L} is shown in the left panel of Figure 2.7, where the red open squares show the values of η_{20} , appropriate for the inner region, and the blue filled squares show η_v , the values at the virial radius. The curves show that in the inner regions, the mass loading factor decreases with \mathcal{L} , ranging between ~ 0.3 –1, with an approximate power-law scaling $\eta \propto \mathcal{L}^{-0.25}$. The values at the outer radii also scale with \mathcal{L} with a similar power-law index, and ranges between $\eta \sim 1.0$ –5.0. The negative slope of η can be understood with very simple arguments.

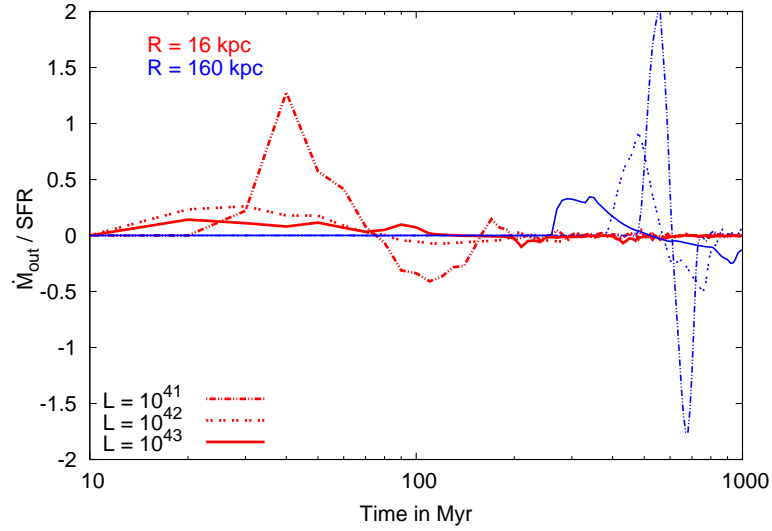


Figure 2.5: The evolution of the mass outflow rate in the units of starburst SFR at two different radii, 16 kpc (red, thicker lines) and 160 kpc (blue, thinner lines) as a function of time (in Myr) for different luminosities (shown in different line styles: 10^{41} erg s $^{-1}$ (dot-dashed), 10^{42} erg s $^{-1}$ (double dotted) and 10^{43} erg s $^{-1}$ (solid)). The results are for a simulation box size of $r_{\max} = 250$ kpc.

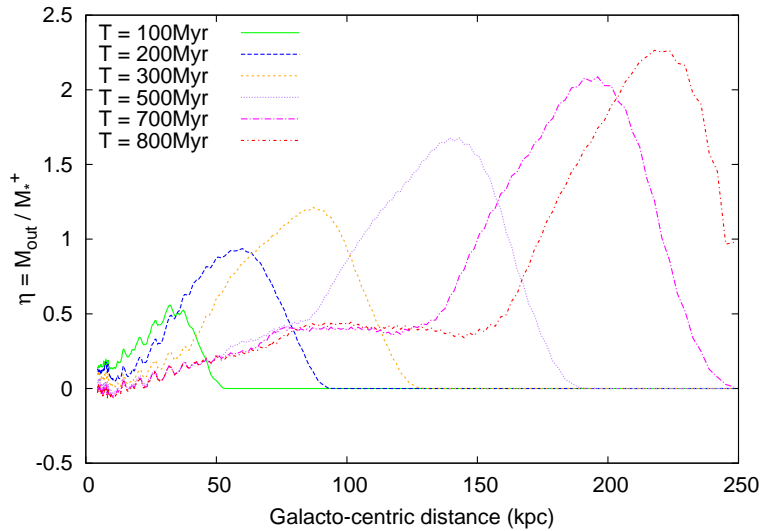


Figure 2.6: Mass loading factor (η) as a function of the galacto-centric radius, for $\mathcal{L} = 10^{42}$ erg s $^{-1}$. The values of η shown in different colours/styles correspond to different periods of integration time, from 100 Myr to 800 Myr.

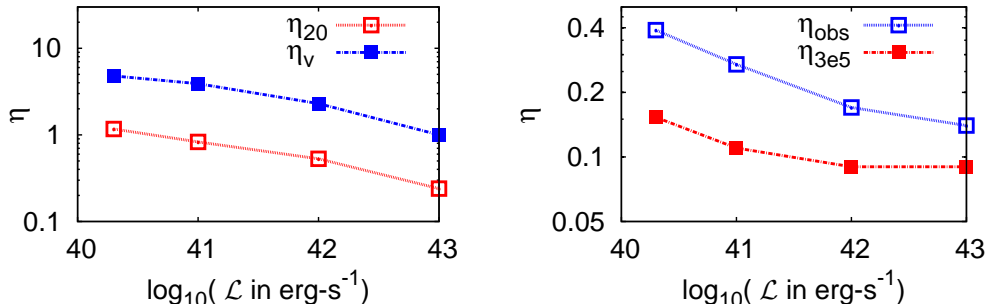


Figure 2.7: Left panel: The mass loading factor (η) at smaller radii (red open squares) and at virial radius (blue filled points) based on large-scale runs. Right panel: Observational mass loading factor (Eq. 2.18) based on small-scale runs. The blue open squares show the total η_{obs} and red filled squares show the warm mass loading factor.

Consider a blast wave with energy E propagating in an uniform density medium. The shock radius and velocity can be given as $r_{os} \sim E^{1/5}$ and $v_{os} \sim E^{1/5}$ at any particular time. Therefore the mass outflow rate inside the shell can be written as $\dot{M}_{\text{out}} \sim r^2 v$ which in turn gives $\dot{M}_{\text{out}}/E \sim E^{-2/5}$, which is equivalent to the mass loading factor we have defined here. Hence, the negative dependence of η on \mathcal{L} appears naturally. Physically, explosions with smaller \mathcal{L} produce an outflow that is strongly coupled to the halo gas, because (a) of low speed and (b) small conical angle in which the outflow is confined. Strong explosions, on the other hand, tend to propagate through the halo gas quickly, sweeping it with high speed, instead of much coupling.

We have checked that in the absence of the hot halo gas, the mass-loading factor η approaches 0.1 in the whole range of \mathcal{L} considered here. It is connected with the fact that the typical mechanical luminosities in active central starbursts are always much higher than the critical luminosity necessary to break through the galactic ISM disk : $\mathcal{L}_{\text{cr}} \sim 10^{38} \text{ erg s}^{-1}$ for the ISM parameters used above (Nath & Shchekinov, 2013). Once the wind breaks out of the disk, there is no halo resistance to stop it. Therefore, the total outflowing mass is equal to the injected mass, and the mass loading factor becomes equal to the injection value (η_{inj}), 0.1 (see Fig. 2.11).

2.4.2 Effect of multiple bursts and injection time

So far we have considered the effect of a single starburst (injecting from $t = 0$ to 50 Myr). The real situation may, however, differ in particular cases as there may be multiple bursts at the centre, or the injection time period may differ. We consider two extreme cases. First, in which the active star formation periods are well separated in time from each other, i.e. they are almost independent event. In the second case, the star bursts are so close in time that they can be considered as a continuous event. We use our fiducial run to compare with the other variants (with different \mathcal{L} and t_{inj}).

The first case is implemented by putting starbursts of $\mathcal{L} = 10^{41.3} \text{ erg s}^{-1}$ with $t_{\text{inj}} = 50 \text{ Myr}$ at large time separation. We put five such starbursts at the centre separated by 200 Myr in time so that the total injected energy becomes equal to the fiducial value ($\mathcal{L} = 10^{42} \text{ erg s}^{-1}$). We have calculated the average mass outflow rate as,

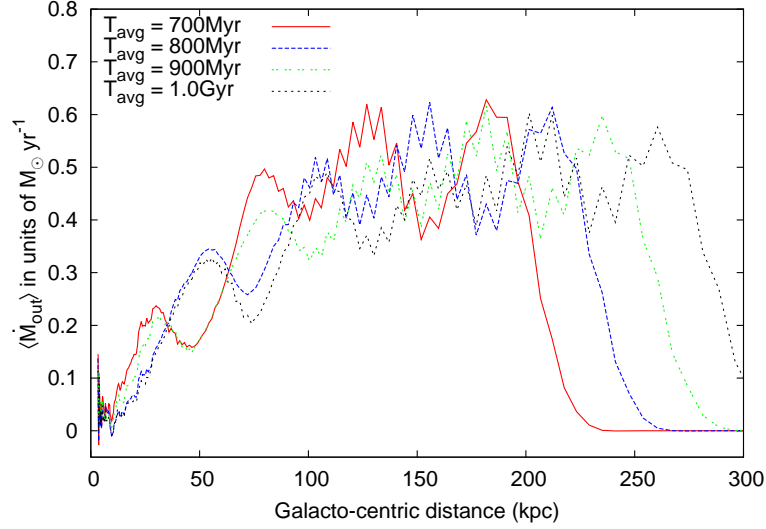


Figure 2.8: Effect of multiple bursts, each of $\mathcal{L} = 10^{41.3} \text{ erg s}^{-1}$ and $t_{\text{inj}} = 50 \text{ Myr}$, on the time averaged mass outflow rate, $\langle \dot{M}_{\text{out}} \rangle$, at each radius. The individual peaks corresponding to the individual starburst events show almost similar behaviour. The box size in this case is $r_{\text{max}} = 350 \text{ kpc}$.

$\langle \dot{M}_{\text{out}}(r) \rangle = \frac{1}{T_{\text{avg}}} \int_0^{T_{\text{avg}}} \dot{M}_{\text{out}} dt$, where T_{avg} is varied between 700 Myr and 1 Gyr. This choice of T_{avg} is motivated by the fact that the shell corresponding to the first burst takes roughly a Gyr to reach the virial radius, and subsequent shell lags behind it by roughly 200 Myr. The result of such bursts is shown in Fig. 2.8. The figure clearly shows that the individual outflowing shells corresponding to the independent starbursts move through the halo medium almost uninterrupted by the previous bursts and create the same effect as it would have done for a single burst of $\mathcal{L} = 10^{41.3} \text{ erg s}^{-1}$. Hence, multiple starbursts separated by a long time interval can be treated in the same way as we treat an individual burst.

In order to understand the effect of t_{inj} on η_v , we use $\mathcal{L} = 10^{42} \text{ erg s}^{-1}$ with different injection times (t_{inj}) of 25, 100, and 200 Myr. The increment in the injected energy due to the increased t_{inj} gives rise to lower mass loading factor compared to the constant t_{inj} cases. The values of η_v for these cases depend on the total energy as $\eta_v \propto \mathcal{E}^{-0.5}$ (see Fig. 2.9), where $\mathcal{E} = \mathcal{L} \times t_{\text{inj}}$. Figure 2.9 shows that η_v decreases when the injection time lasts for more than $\sim 50 \text{ Myr}$ compared to runs which have same energy but where the injection lasts only for 50 Myr.

A comparison with the adiabatic counterparts of these runs (shown by the green triangles in Fig. 2.9) shows that this decrease in the mass loading factor can be attributed to the radiative cooling of the free wind which lasts long enough ($> 50 \text{ Myr}$) to radiate away a significant fraction of the total energy. The inset of Fig. 2.9 shows the temperature profiles of a $(10^{42}, 200 \text{ Myr})$ run at $t = 150 \text{ Myr}$. This plot shows the decrease of temperature (or the internal energy) due to radiative losses in the free wind. Thus it is evident that if the free wind phase lasts for a long time (due to prolonged injection time), then it radiates away a good fraction of the energy.

The above results allow us to write the variation of η_{20} and η_v as a function of the total energy or total mass of stars formed within the injection time (obtained from the

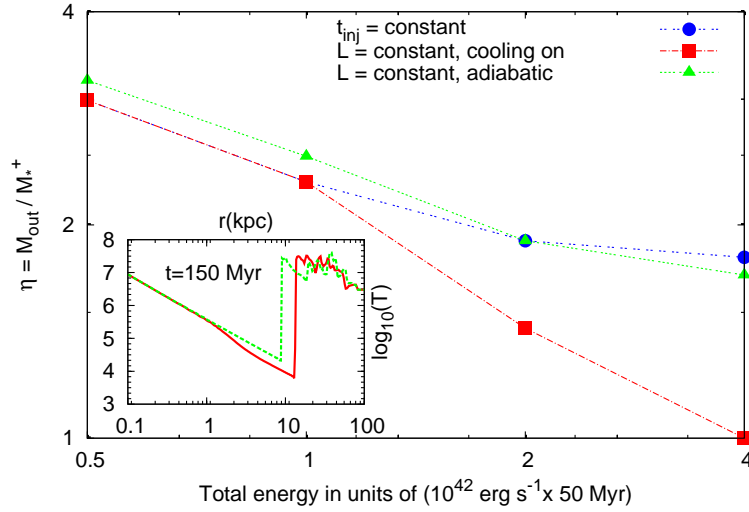


Figure 2.9: The effect of increasing energy on the mass loading factor η_v is shown by increasing the injection time and injection mechanical luminosity. The blue dots show the results when the injection time is constant ($t_{\text{inj}} = 50 \text{ Myr}$) and luminosity is varied. The red squares show the result when the mechanical luminosity constant ($\mathcal{L} = 10^{42} \text{ erg s}^{-1}$) but energy is increased by increasing the injection time. The green triangles show the run for variable t_{inj} , but, with cooling switched off. The inset shows the temperature profiles at $t = 150 \text{ Myr}$ for $t_{\text{inj}} = 200 \text{ Myr}$ run. The red (solid) line corresponds to the case where radiative cooling is switched on, and the green (dotted) line represents the case where radiative cooling is absent.

fits of Fig. 2.7) as

$$\eta_{20} \approx 0.4 \times \left(\frac{\mathcal{E}}{\mathcal{E}_F} \right)^{-0.25} = 0.4 \times \left(\frac{M_*^+}{M_*^F} \right)^{-0.25}, \quad (2.15)$$

and

$$\eta_v \approx 2.5 \times \left(\frac{\mathcal{E}}{\mathcal{E}_F} \right)^{-0.25} = 2.5 \times \left(\frac{M_*^+}{M_*^F} \right)^{-0.25}. \quad (2.16)$$

where, $\mathcal{E}_F = 10^{42} \text{ erg s}^{-1} \times 50 \text{ Myr}$ is the energy for the fiducial run and $M_*^F (= 14.0 M_\odot \text{ yr}^{-1} \times 50 \text{ Myr})$ is the corresponding mass of new stars formed. However, for long $t_{\text{inj}} (\gtrsim 50 \text{ Myr})$ in case of $\mathcal{L} > 10^{42} \text{ erg s}^{-1}$, the cooling affects the dynamics and the mass loading factor can be written as

$$\eta_v \approx 2.5 \times \left(\frac{\mathcal{E}}{\mathcal{E}_F} \right)^{-0.5} = 2.5 \times \left(\frac{M_*^+}{M_*^F} \right)^{-0.5}. \quad (2.17)$$

2.4.3 Comparison with observed mass loading factor

We compare the values of η obtained from our simulations with those estimated from observations, where only partial information about the velocity and density structure is available. The mass loading factor in observations is defined as $\eta = \frac{M \times v_r}{r \times \text{SFR}}$, where, M is the total mass of outflowing gas (observed as molecular or ionised gas), r is the typical scale of the outflowing region and v_r is an estimate of the outflowing gas velocity (Arribas et al., 2014; Bolatto et al., 2013) or the sound speed (Strickland & Heckman, 2007). In order to compare with the observed values of mass loading factor, we define η_{obs} , the mass loading factor within a outflowing region of radius r_d at any time t as

$$\eta_{\text{obs}}(r_d, t) = \frac{M v_r}{\text{SFR } r_d} = \frac{1}{\text{SFR}} \frac{2\pi}{r_d} \int_0^{r_d} r^2 dr \int_0^\pi (\rho v_r) \sin \theta d\theta, \quad (2.18)$$

where, r_d is taken to be 10 kpc, the radius within which most of the observations are limited. It is to be noted that the velocity inside the integral is the actual velocity of any individual fluid packet rather than some characteristic speed of the whole fluid as usually considered by the observations. Since, during a starburst the mass outflow rate is not constant because of the halo-wind interactions and formation of clouds and eddies, to get a reliable value, and to connect with the current SFR, we average it over the injection period (50 Myr). The values of time averaged η_{obs} is shown in the right panel of Figure 2.7 by the blue open squares. These values show the same behaviour as seen previously in η_{20} only with a shallower dependence on \mathcal{L} ($\eta_{\text{obs}} \propto \mathcal{L}^{-0.15}$).

However, the estimation of the mass loading factor from observations is either for the cold molecular gas (Bolatto et al., 2013) or the ionised (Arribas et al., 2014) or the hot gas (Strickland & Heckman, 2007), and not for all the phases taken together. Therefore, to determine the mass loading factors for different phases and find the correlation between them, it is important to study the temperature distribution of η_{obs} . Figure 2.10 shows that the outflowing mass is divided mainly into two temperature domains, one at $\sim 10^5 \text{ K}$, and, another at $\sim 5 \times 10^6 \text{ K}$. The 10^5 K gas comes from the evaporation of the disk gas and adiabatically expanded wind material, and, the hot gas ($T \sim 5 \times 10^6 \text{ K}$) comes from the shocked ISM and wind material. We also notice a small peak near

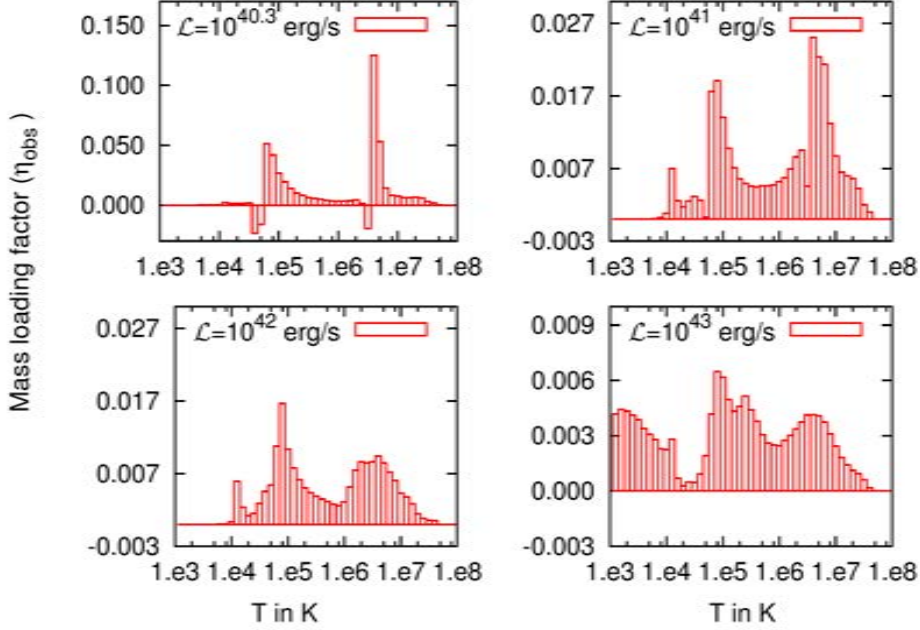


Figure 2.10: Temperature distribution of the outflowing gas for different luminosities at a galacto-centric radius 10 kpc, averaged over 50 Myr.

$T = 10^4$ K, which arises because of the clouds formed from the interaction between wind and halo material and from the condensation of the evaporated disk material. The extended outflowing gas at $T < 10^4$ K in case of $\mathcal{L} = 10^{43}$ erg s $^{-1}$ arises due to the adiabatic cooling of the free wind (see right-bottom plot of Figure 2.10).

The temperature plots imply that observations aimed to detect either the cold or ionised or hot gas are likely to miss a significant fraction of the outflowing material even at small radii. Therefore, to determine the contribution of the warm gas which is the commonly used observational tracer of outflow, we define a new mass loading factor η_{3e5} which counts only $T < 3 \times 10^5$ K gas. This is represented by red filled squares in the right panel of Figure 2.7, which also shows that η_{3e5} is less than the total mass loading factor η_{obs} by a factor of 2–3. Moreover, the mass loading factor is almost equal to the injection value, 0.1 (see §2.3.1), which is of a similar magnitude as estimated by Arribas et al. (2014) in case of MW type galaxies (dynamical mass $\sim 10^{11} M_{\odot}$).

To understand the relations between different mass loading factors we have fitted them with simple power-law relations:

$$\eta_{\text{obs}} \simeq 0.4 \times \mathcal{L}_{40}^{-0.15} \simeq 0.3 \times \left(\frac{\text{SFR}}{M_{\odot} \text{ yr}^{-1}} \right)^{-0.15}, \quad (2.19)$$

$$\eta_{3e5} \simeq 0.15 \times \mathcal{L}_{40}^{-0.1} \simeq 0.12 \times \left(\frac{\text{SFR}}{M_{\odot} \text{ yr}^{-1}} \right)^{-0.1}. \quad (2.20)$$

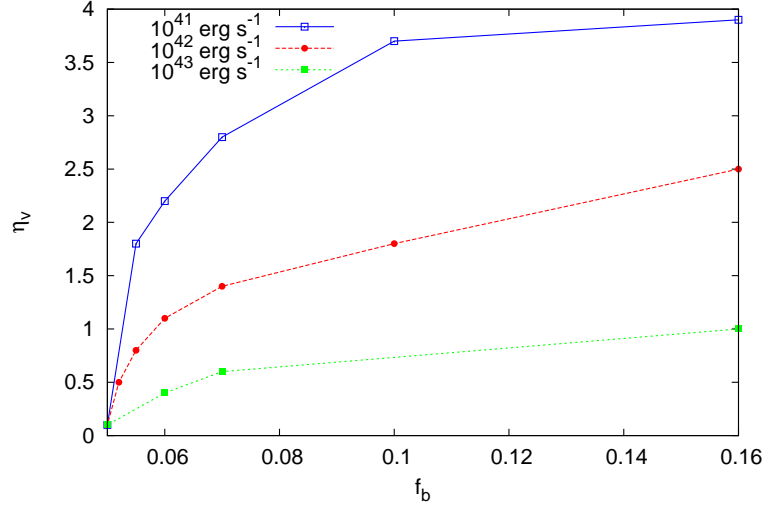


Figure 2.11: Variation of outer mass loading factor (η_v) with baryon fraction of the galaxy in the case of different luminosities of $\mathcal{L} = 10^{41,42,43} \text{ erg s}^{-1}$ (or runs L1, L2 and L3 in Table 2.2).

Comparing these equations with Eq. 2.16 and using Eq. 2.9, we can write

$$\begin{aligned} \eta_v &\approx 5 \times \left(\frac{\text{SFR}}{\text{M}_{\odot}\text{yr}^{-1}} \right)^{-0.25} \times \left(\frac{t_{\text{inj}}}{50\text{Myr}} \right)^{-0.25} \\ &\approx 40 \times \left(\frac{\text{SFR}}{\text{M}_{\odot}\text{yr}^{-1}} \right)^{-0.15} \times \left(\frac{t_{\text{inj}}}{50\text{Myr}} \right)^{-0.25} \times \eta_{3e5}. \end{aligned} \quad (2.21)$$

This gives a relation between the warm mass loading factor, η_{3e5} (relevant for observations), and the outer mass loading factor (η_v) (relevant for cosmological scales) for a given starburst period and SFR. Eq. 2.21 shows that the mass loading factor at the virial radius is larger by a factor ~ 40 than the mass loading factor that is observable near the central region. This relation is almost independent of SFR but depends upon the starburst activity time.

The ratio η_v/η_{3e5} also depends on the baryon fraction of the galaxy, in particular, the fraction of the total mass that is in the form of halo gas. Since the main contribution to the outflowing mass at the outer radii comes from the swept up halo material, the outer mass loading factor strongly depends on the mass budget of the background halo gas. Figure 2.11 shows the variation of η_v as a function of the baryon fraction (f_b). The figure shows that, for $f_b \gtrsim 0.1$ i.e. when more than half of the baryon is in the hot halo phase, η_v varies weakly with f_b . However, for $f_b \lesssim 0.1$, mass loading factor decreases steeply and finally for $f_b = 0.05$ (the stellar mass fraction), it becomes equal to the injection value, 0.1. Therefore, η_v/η_{3e5} can vary between ~ 1 –40 depending on the baryon fraction.

In this work, we have only varied the mechanical luminosity and injection time; the other parameters like total galactic mass have been kept fixed. The observational scaling of $\eta(\text{SFR})$, on the other hand, may be contaminated by these additional variables. Indeed, a larger mechanical luminosity suggests, in general, a higher star formation rate, which in turn may indicate a larger galactic mass, and a more massive and extended

hot halo.

We have also carried out simulations at various resolutions, and we find excellent convergence for the various mass loading factors (η_{20} & η_v) in case of the large-scale runs. The small-scale runs, which study the multiphase gas, are somewhat resolution-dependent as they do not resolve the transition regions between the cold and hot phases in the absence of thermal conduction (see [Koyama & Inutsuka, 2004](#)). However, the relation between the mass loading factors in Eq. 2.21 holds within a factor of two for all resolutions.

2.4.4 Velocity structure

Figure 2.12 shows the velocity profiles at three different epochs (50, 200, 500 Myr) along the vertical direction ($R = 0$) for the fiducial run ($\mathcal{L} = 10^{42}$ erg s $^{-1}$). The red solid curve for the profile at 50 Myr (when the injection is still on) shows the structure of a standard luminosity-driven wind, with an inner region of free wind travelling at high speed, which is surrounded by the shocked wind, and then by the shocked ISM, which drives an outer shock through the ambient medium. After this period (50 Myr), when the injection stops, the interaction zone produces clumps which sometimes fall back and create regions with negative velocity. However, the outer shock continues to propagate through the ambient gas and reaches a distance of 200 kpc in 500 Myr in this case. The speed of the hot gas in the interior region depends crucially on the assumption of the mass loading factor at injection, and in the case of $\dot{M} = 0.1$ SFR, it reaches 1600 km s $^{-1}$. This is consistent with the analytical velocity of luminosity driven winds ($\sqrt{2\mathcal{L}/\dot{M}}$; e.g., [Sharma & Nath 2013](#), [Chevalier & Clegg 1985](#)). We also note that, although the initial speed of the outflowing gas is ~ 1000 km s $^{-1}$ or above, it is not sustained for long and at later times when injection is turned off, the velocity becomes so small that it can be considered as a sound wave moving through the hot medium. This can be seen in Figure 2.13 which plots the Mach number of the gas as a function of distance at 500 Myr for different luminosities. The Mach number of the outflowing gas at large distances decreases to $\lesssim 1$, for the mechanical luminosities considered here. Therefore the outflows eject the gas out of the virial radius with speeds comparable to the sound speed of the halo gas. This has important implications for the enrichment models of the IGM. Next, we focus on the wind structure at observable scales (~ 10 kpc) based on our small-scale/short-duration simulations.

While ploughing through the ISM, the wind fluid entrains the warm disk gas with it. For low luminosities ($\lesssim 10^{41}$ erg s $^{-1}$) this entrained gas mixes with the wind and forms filaments and cloud-like structures embedded within the 10 kpc free wind. For higher SFR, the disk gas is mainly located near the contact discontinuity of wind cone. While being carried away by the high velocity wind, a fraction of the cold clumps gets evaporated and the rest propagates outwards due to the ram pressure of the free wind. Therefore, the dynamics of the clouds and filaments is momentum conserving, for which the velocity increases with the distance ([Murray et al., 2005](#)). As the density of the hot gas decreases with distance, the ram pressure decreases, leading to an asymptotic speed of the clouds. However, this result pertains to a steady state situation, which is not the case here. The result obtained here is suitable for comparing the cloud kinematics at a particular time as obtained in observations.

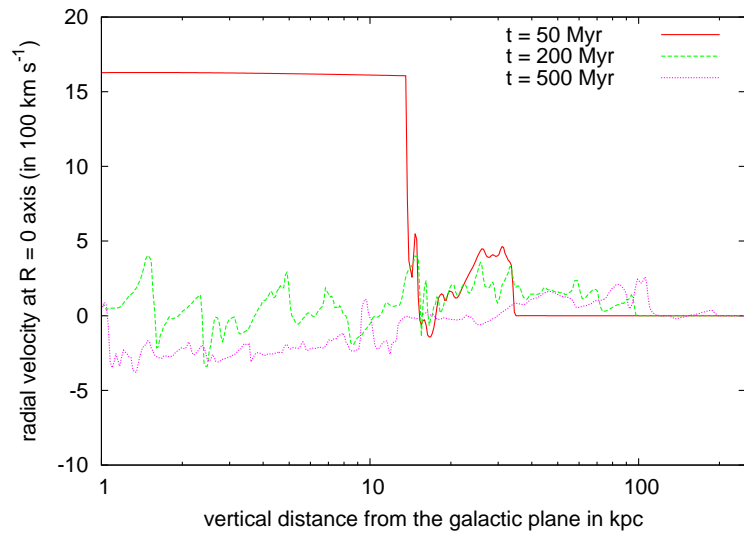


Figure 2.12: Velocity profiles along $R = 0$ axis at 50, 200, 500 Myr for the case of $\mathcal{L} = 10^{42} \text{ erg s}^{-1}$.

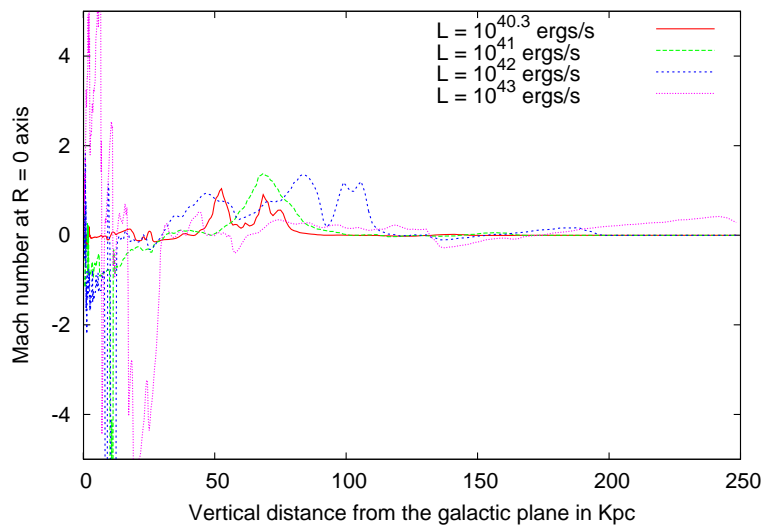


Figure 2.13: The Mach number profiles along the $R = 0$ axis at 500 Myr for different luminosities.

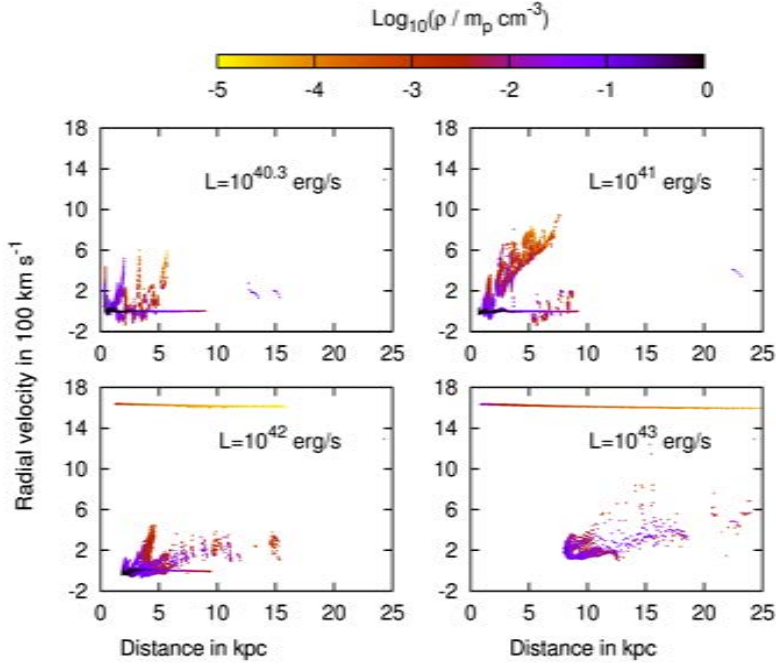


Figure 2.14: Scatter plot of the velocity of the warm gas ($T < 3 \times 10^5$ K) and radial distance at 50 Myr. Top panel is for $\mathcal{L} = 10^{40.3}$, 10^{41} erg s⁻¹ and bottom panel is for $\mathcal{L} = 10^{42}$ and 10^{43} erg s⁻¹ respectively.

Figure 2.14 shows the position and velocity of warm/cold gas ($T < 3 \times 10^5$ K) for four different luminosities at 50 Myr. The figure shows that the velocity of the cold and warm gas ranges from ~ -150 km s⁻¹ to ~ 800 km s⁻¹. The points with constant velocity at $\simeq 1600$ km s⁻¹ represent the adiabatically cooled free wind in case of $\mathcal{L} = 10^{42}$ and 10^{43} erg s⁻¹, while the points with nearly zero velocity represent the stationary disk gas.

For $\mathcal{L} = 10^{41,42}$ erg s⁻¹, we also notice two sequences of velocity points, one which is a dominant sequence (referred to as the main sequence here), which extends from zero velocity to a velocity of ~ 800 km s⁻¹, and, a secondary sequence which is almost parallel to the main sequence but extends from -150 km s⁻¹ to $+200$ km s⁻¹. Both sequences are almost linearly dependent on the radius. This can be understood as the effect of ram pressure of the outgoing free/shocked wind, as mentioned previously. The radial dependence of the velocity of the warm gas in our simulation can be compared with the results obtained by [Shopbell & Bland-Hawthorn \(1998\)](#) in case of H α filaments in M82, who also observed a roughly linear relation between velocity and height above the disk (their Figure 10).

The origin of these two sequences are quite similar. The main sequence is entrained by the high velocity free wind, thereby giving it a relatively higher velocity. On the other hand, the secondary sequence arises because of the entrainment of the clouds by the lower velocity shocked wind. As shown in the evolution of wind for $\mathcal{L} = 10^{41}$ erg s⁻¹ in Figure 2.3, the main sequence corresponds to the clouds formed after the disk material advances inwards and is blown away into a filamentary structure (see snapshots at 40 and 50 Myr in Figure 2.3). The second sequence of clouds corresponds

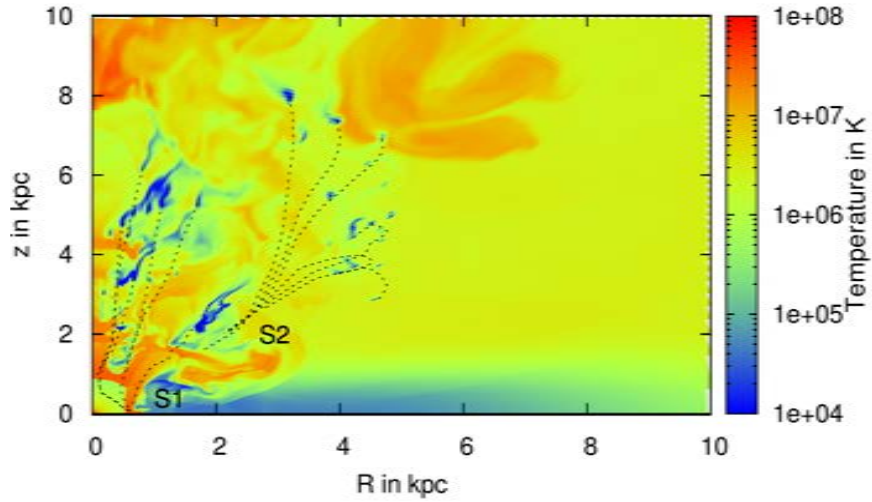


Figure 2.15: Temperature map for $\mathcal{L} = 10^{41} \text{ erg s}^{-1}$ at 50 Myr for, on which we superpose the tracks for cold clouds. The main sequence (S1) clouds (entrained by high velocity free wind) are tracked back for 17 Myr, and the secondary sequence (S2) clouds (entrained by the low velocity shocked wind) are tracked back for 40 Myr.

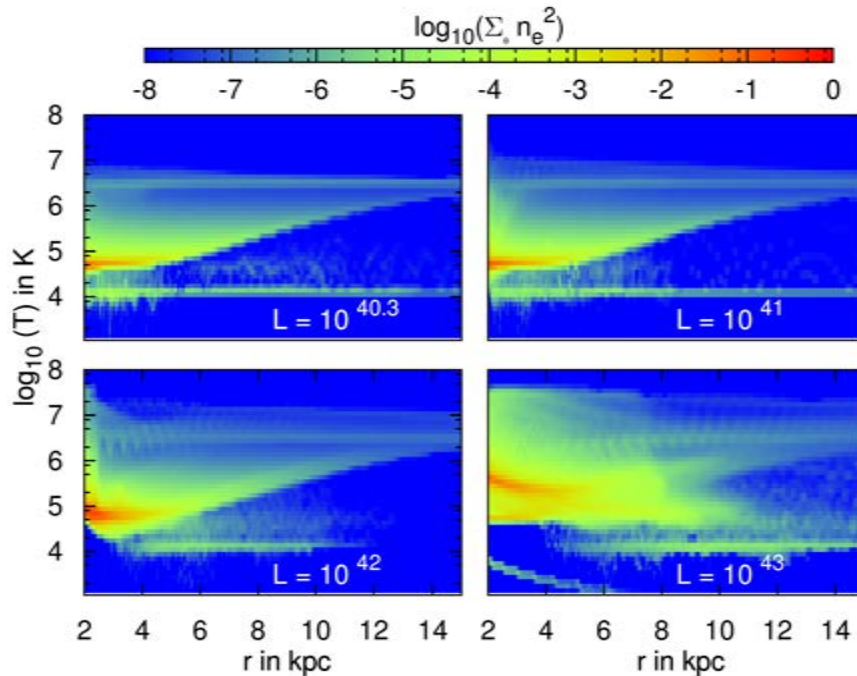


Figure 2.16: Scatter plot of temperature and radial distance of gas particles, colour coded by the time average of density squared (averaged over 50 Myr), shown for four different mechanical luminosities.

to the ones formed in the interaction zone between the hot halo gas and shocked ISM due to various instabilities like thermal, Rayleigh-Taylor instabilities. (see Fig. 2.2).

Figure 2.14 also shows the cloud gas density in colours. The clouds at large distances are in general more tenuous than those at inner region, which can be understood from adiabatic expansion of clouds moving in an ambient medium (free wind) whose pressure decreases with distance.

The extension of the secondary sequence from $\sim -150 \text{ km s}^{-1}$ to $+200 \text{ km s}^{-1}$ means that few clouds are also falling back to the centre. The fraction of mass that falls back to the center, however, is small to trigger any noticeable star formation, as will be discussed in the next section. Figure 2.15 shows the time tracks of these two sequences of clouds seen at 50 Myr for $\mathcal{L} = 10^{41} \text{ erg s}^{-1}$. The main sequence (labelled S1) are tracked back for 17 Myr, and represents relatively younger disk material, whereas the secondary sequence clouds (S2) are tracked for 40 Myr, which are basically older population clouds. These two families of tracks clearly shows the source of the clouds and supports our previous discussion about their origin in the free and shocked wind. Other than these two sequences, we also notice some island points (in Figure 2.14) at a galacto-centric radius of $\sim 15\text{--}25 \text{ kpc}$ having velocity close to $\sim 400 \text{ km s}^{-1}$, which may represent rare high velocity-high latitude clouds as observed by Sembach et al. (2003).

Figure 2.16 shows the temperature and position of gas parcels, colour coded by the time average of the square of particle density (averaged over 50 Myr), for four different mechanical luminosities. Only the parcels of gas within 15 kpc are represented here. The two horizontal streaks at $10^{6.5} \text{ K}$ and 10^4 K corresponds to the hot halo and warm clouds, respectively, whereas the rising envelope of increasing temperature with radial distance corresponds to the mixture of the disk and halo gas in the plane of the disk. The $1/r^2$ fall of temperature in case of $\mathcal{L} = 10^{43} \text{ erg s}^{-1}$ is easily understood as the adiabatically expanding gas. The regions marked in red and orange (back and deep gray in gray-scale) correspond to gas with high emissivity, and therefore are important from the consideration of observability. The figure suggests that for very low luminosity outflows, most of the emission would arise from gas at $\sim 10^5 \text{ K}$ gas within $\sim 5 \text{ kpc}$. X-ray emitting gas becomes important for $\mathcal{L} \geq 10^{42} \text{ erg s}^{-1}$, corresponding to SFR of $\sim 10 M_{\odot} \text{ yr}^{-1}$. These results are consistent with observations of X-rays from outflows (Strickland & Heckman, 2007), including the X-ray emission from the outflow in Milky Way (Snowden et al., 1995; Breitschwerdt & Schmutzler, 1994).

2.4.5 Mass inventory

In addition to the mass loading factor, the velocity and the temperature distribution, we have also estimated the total outflowing mass. This is an important parameter in the context of the evolution of the galactic disk and halo, as well as the enrichment of the IGM. The total mass injected into the halo is assumed to be proportional to the SFR or \mathcal{L} (Eq. 2.10), and it is a small fraction of the gas mass in the halo, even for the largest SFR considered here. However, the total mass of the outflowing gas ranges between 0.2–10% of the total gas content ($10^{11} M_{\odot}$), increasing roughly linearly with SFR, between 1.5–150 $M_{\odot} \text{ yr}^{-1}$. Therefore outflows corresponding to large SFR can change the halo gas density by $\leq 10\%$. We have also found that the average disk mass does not change appreciably by either ejection or fall back of gas ($\leq 1\%$ for the most vigorous outflows) and in all cases, the change in the disk mass is much smaller than the

injected mass. Previous works have discussed the role of the halo gas in massive galaxies either suppressing or triggering star formation in the disk by absorbing the outflowing gas or pushing it back on to the disk, respectively. The massive halo is expected to play an important role in quenching star formation in massive galaxies by cutting off the supply of fresh cooling gas. The halo also suppresses appreciable fall back of outflowing gas and quenches star formation, although the detailed mechanism of such quenching remains uncertain (Gabor & Davé, 2015; Oppenheimer et al., 2010). The above mass estimation implies that the injected material mostly gets deposited in the halo. Hence these outflows do not trigger further star formation by recycling mass to the disk (e.g., as in a galactic fountain). In other words, outflows in the presence of an extended hot halo gas can quench star formation in the galaxy.

2.5 Discussion

We discuss a few implications of our results presented in the preceding sections.

2.5.1 Definition of mass loading factor

We have defined the mass loading factor here as the ratio between the total outflowing mass and the total mass of stars formed. This is in contrast with the usual definition, as the ratio between the mass outflow rate to the *current* SFR. Our definition is motivated by the fact that by the time the outflowing mass reaches the outer halo, its dependence on the *current* SFR loses its significance, since the duration of the SFR (t_{inj}) is usually much smaller than ~ 1 Gyr, the time taken by the outflow to reach the virial radius. However, these two definitions are related to each other, and here we briefly discuss their inter-relation.

These two definitions coincide if in the case of (a) outflows at small length scales and (b) when the starburst activity last for a long time. In the first case, the observed *current* SFR is related to the cause of the outflow. In the case, if the starburst activity lasts long time ($\gtrsim 300$ Myr) or there are repeated bursts at the centre, the outflow properties (viz. velocity, metallicity etc) at ~ 100 – 200 kpc also can be connected to the ongoing star formation process, as observed by Tumlinson et al. (2011). Suppose one had defined the outer mass loading factor as the ratio between averaged mass outflow rate and the SFR as

$$\langle \eta_v \rangle = \frac{\langle \dot{M}_{\text{out}} \rangle}{\text{SFR}} = \frac{1}{\text{SFR} \times t} \int_0^t \dot{M}_{\text{out}}(r_v, t') dt', \quad (2.22)$$

where, t is the averaging time, which can be taken roughly equal to the time taken by the shell to reach that particular radius. This definition of $\langle \eta_v \rangle$ can be connected to our earlier definition in Eq. 2.14 as

$$\eta_v = \frac{M_{\text{out}}}{M_*^+} = \frac{\langle \dot{M}_{\text{out}} \rangle}{\text{SFR}} \times \frac{t}{t_{\text{inj}}} = \langle \eta_v \rangle \times \frac{t}{t_{\text{inj}}}. \quad (2.23)$$

Note that, this relation holds only when $t > t_{\text{inj}}$. For $t < t_{\text{inj}}$, the total mass of new stars formed is $M_*^+ = \text{SFR} \times t$, therefore, $\eta_v = \langle \eta_v \rangle$. The ratio t/t_{inj} can be estimated from

our simulations as follows. The shell arrival time in our simulation can be written as $r_{sh} \approx 1.3 \text{ kpc } \mathcal{L}_{42}^{1/5} t_{\text{Myr}}^{3/4}$ which in turn gives $t/t_{\text{inj}} \approx 17 r_{200\text{kpc}}^{4/3} \mathcal{L}_{42}^{-4/15} t_{\text{inj},50\text{Myr}}^{-1}$. Therefore, Eq. 2.23 gives us

$$\eta_v \approx 17 \langle \eta_v \rangle r_{200\text{kpc}}^{4/3} \mathcal{L}_{42}^{-4/15} t_{\text{inj},50\text{Myr}}^{-1}. \quad (2.24)$$

From this equation we can clearly see that when the star formation lasts long i.e $t \approx t_{\text{inj}}$, $\eta_v \approx \langle \eta_v \rangle$. In other words, the two definitions (one w.r.t. the average outflow rate, and another, presented here, w.r.t. the total outflowing mass) are equivalent in the case of long duration starbursts.

2.5.2 Dust in clouds

Clouds formed in the galactic outflows are not only important for containing ions that make them observable, but they can also contain dust particles. Our result shows that roughly half the outflowing mass (inside 10 kpc) resides in gas of temperature $\sim 10^6$ K and the other half in warm clouds of temperature $\sim 10^5$ K, has important implications for the types of dust particles that are likely to be embedded in outflows. The thermal sputtering rate of dust grains at 10^5 K is small, and the time scale required to destroy even the smallest dust grains ($\sim 0.003 \mu\text{m}$) in warm clouds is ~ 15 Gyr considering a density of $\sim 10^{-3} \text{ m}_p \text{ cm}^{-3}$ in these clouds, as inferred from the density distributions in Figures 2.2 and 2.3. These clouds can therefore preserve even the smallest grains, as long as the clouds can survive. The hotter regions in which half the mass of the outflowing gas resides, has a larger sputtering rate. At $\sim 10^6$ K, the smallest grains that can survive after 50 Myr is roughly $0.003 \mu\text{m}$ for graphites and $0.03 \mu\text{m}$ for silicates. These clouds therefore contain ‘grey’ dust. In other words, half the dust mass carried by outflows are likely to be rendered ‘grey’ during the transport from the disk to the outer halo.

2.5.3 Absorption study of clouds

Our Galaxy has a SFR of $\approx 3 \text{ M}_\odot \text{ yr}^{-1}$, which corresponds to a mechanical luminosity of $\sim 10^{41.3} \text{ erg s}^{-1}$. Therefore the results of simulations with $\mathcal{L} = 10^{41} \text{ erg s}^{-1}$ are appropriate for comparison with our Galaxy. The numerous clouds that are formed during different stages would correspond to clouds observed in various wavelengths in the halo of Milky Way. Cold clouds with $T \leq 10^4$ K would correspond to HI clouds or MgII absorption clouds. The cold clouds seen in the temperature distributions in Figure 2.15 portray a visual impression of a likely scenario of clouds responsible for MgII absorption, although we emphasise that we do not aim to reproduce the Milky Way observations in our work. Shooting lines of sight from the centre in the range of $\theta = 0-70^\circ$ (avoiding lines of sight within 20° of the disk), we estimate a covering fraction of $\sim 60\%$ for MgII clouds. This is consistent with the estimate of Lehner et al. (2012) for fraction of high velocity clouds with MgII, although the correspondence should be interpreted with caution.

2.5.4 Redshift dependence

The specific star formation rate (sSFR, defined as the SFR per unit stellar mass) of Milky Way type galaxies increases at high redshift. Weinmann et al. (2012) found the

sSFR of galaxies with stellar mass $\sim 10^{10} M_{\odot}$ to increase by a factor of ~ 20 at $z \sim 2$. The corresponding star formation time scale ($1/\text{sSFR}$) decreases from the current value of ~ 10 Gyr to ~ 0.5 Gyr. Therefore, the appropriate mechanical luminosity for counterparts of Milky Way at high redshift would be $\mathcal{L} \sim 10^{42.6} \text{ erg s}^{-1}$. As Fig. 2.7 shows, for mechanical luminosities of this order, the mass loading factor at the virial radius is close to unity.

2.5.5 IGM enrichment

The result that outflows leave the virial radius with a speed comparable to the sound speed of the halo gas may affect the enrichment history of the IGM. The sound speed of the halo gas at virial temperature is roughly half the escape speed at the virial radius, over a large range of masses and redshift. It is generally believed that the speed of the outflows is much larger than the escape speed. If the outflow speed is decreased as found here, then the radius of influence of the outflows in the IGM will be smaller than previously thought. However, we should note that this result holds only for large galaxies with hot halo gas, whereas most of the contribution to the enrichment of the IGM comes from low mass galaxies (e.g., Nath & Trentham 1997; Madau et al. 2001; Ferrara & Tolstoy 2000; Oppenheimer & Davé 2006), which may not harbour a hot gas in the halo.

2.6 Summary

In this chapter, we have presented an extensive numerical study of SN driven galactic outflows for a MW type galaxy. Our modelled galaxy contains a gaseous disk of $T = 10^4$ K, and an extended hot ($T = 3 \times 10^6$ K) halo gas around it. The SN feedback was implemented in the form of mechanical energy within a compact region (< 60 pc) at the center of the galaxy. We have studied the effect of such energy inputs in small scales (~ 30 kpc) and in large scales (~ 200 kpc). The small scale studies reveal the presence of multiphase structure of the outflowing material and a temperature dependent outflow rate and thus help us to connect the mass loading factor at virial radius to the observable mass loading factor.

We summarise our work as follows.

(i) *Mass loading factor*: The presence of hot halo gas in galaxies increases the mass loading factor compared to the no-halo case. In the inner region (within ~ 10 kpc), the mass loading factor can increase up to a factor of ≈ 5 compared to η_{inj} when the mass fraction of the hot halo gas is ~ 0.1 . In comparison, the mass loading factor near the virial radius (η_v), can increase up to 10–40 when compared with η_{inj} . For low value of baryon fraction (f_b), the mass loading factor can be as low as 0.1 (i.e. equal to the η_{inj}). The effect of the halo gas in determining outflow rate is more pronounced in case of low star formation rates compared to the higher ones.

Though we have mainly considered a single starburst of duration 50 Myr, we have also shown that multiple bursts at the center that are well separated in time, have similar effects on gas at large radii. A comparative study with different star formation periods suggests that η_v depends only on the total mass of new stars formed. However, for higher mechanical luminosity ($\mathcal{L} \gtrsim 10^{42} \text{ erg s}^{-1}$) cases, a star formation period

longer than ~ 50 Myr leads to significant radiative cooling and η_v in this case also depend on the injection time scale.

We also found that the hot halo gas helps to quench star formation in the disk by inhibiting any appreciable recycling of mass into the disk.

(ii) *Temperature distribution and observability*: The temperature distribution of the outflowing gas is approximately bimodal, peaking at 10^5 and $10^{6.5}$ K. This bimodality implies that half of the outflowing gas is in form of warm clouds/gas and other half is in the form of hot X-ray emitting gas. This result allows us to connect the mass outflow rate for cold/warm gas to the outflow rate at the virial radius. We find that for a SFR of $1 M_\odot \text{ yr}^{-1}$, the total (all of it in the hot phase) mass loading factor at the virial radius is roughly 25 times the mass loading factor for cold/warm gas near the center for a baryon fraction of 0.1 and injection time ~ 50 Myr.

(iii) *Velocity*: The velocity of the free wind is found to be close to $\sim 1600 \text{ km s}^{-1}$ when the energy injection is still active. Velocity of the outflow decreases once the injection is switched off and for SFR $\lesssim 10 M_\odot \text{ yr}^{-1}$ after ~ 400 Myr, it becomes comparable to the sound speed of the medium. Therefore, the velocity with which the outflow exits the galaxy is close to the sound speed of the hot medium ($c_s \sim 200 \text{ km s}^{-1}$) and the density of the outflow is also close to the halo medium ($\sim 10^{-4} m_p \text{ cm}^{-3}$). We also notice that, even for a SFR $\sim 150 M_\odot \text{ yr}^{-1}$, the whole galaxy is not ‘blown away’. Due to the presence of the hot halo, a strong starburst acts like only a perturbation at the center, after which, the galaxy relaxes and forms a disk-like structure again.

(iv) *Cloud velocity*: The velocity of the warm clouds in our small-scale simulations found to form two sequences in position-velocity diagram. One, extends almost linearly from 0 to $\sim 800 \text{ km s}^{-1}$, another, extends from ~ -200 to $\sim +200 \text{ km s}^{-1}$. These two sequences are signature of entrainment of warm clouds by the high velocity free wind and the low velocity shocked wind respectively.

To conclude, our work focuses on the relation between the mass loading factor at various radii and connects them to the SFR without coupling it to the total mass or gas surface density of the galactic disk. Therefore, relations obtained in this chapter can be used to extrapolate the observed outflow rate near the center to the outflow rate at the virial radius, for Milky Way type galaxies. A more general study of the dependence of mass loading factor on the galactic mass will be addressed in a future study.

Chapter 3

Origin of diffuse X-ray emission in star-forming galaxies

Based on:

“Diffuse X-ray emission from star forming galaxies” by Kartick C Sarkar, Biman B Nath, Prateek Sharma and Yuri Shchekinov, 2016, The Astrophysical Journal Letters, 818, 24 (Sarkar et al., 2016)

*In previous chapter we have seen that a significant fraction ($\sim 0.3 - 0.5$) of the outflowing mass is in hot ($\gtrsim 10^6 K$) phase. One way to characterise this hot phase is to probe the diffuse X-ray emission from the galaxies subtracting out the stellar and compact binary contributions. However, inverting back the X-ray emission to characterise the properties of outflow requires knowledge of the origin of such X-rays. In this chapter, we perform analytical and hydrodynamical calculations to understand the origin of the X-ray and their corresponding contributions. We finally, apply our results to understand recently observed X-ray data.*¹

Main results

- We find that the mass loading factor of the outflows, a crucial parameter for determining the X-ray luminosity, is constrained by the availability of gas in the central star forming region, and a competition between cooling and expansion.
- We show that the allowed range of the mass loading factor can explain the observed scaling of L_X with star formation rate (SFR) as $L_X \propto \text{SFR}^2$ for $\text{SFR} \gtrsim 1 M_\odot \text{ yr}^{-1}$, and a flatter relation at low SFRs.
- We show that the emission from the hot circumgalactic medium (CGM) in the halo of massive galaxies can explain the large scatter in the $L_X - \text{SFR}$ relation for low SFRs ($\lesssim \text{few } M_\odot \text{ yr}^{-1}$). Our results suggest that galaxies with small SFRs and large diffuse X-ray luminosities are excellent candidates for detection of the elusive CGM.

¹In this chapter, we use β for denoting the mass loading factor.

3.1 Introduction

In the case of stellar feedback processes producing a gaseous outflow, the hot gas can form in (i) the central region where star formation occurs, (ii) the free wind, (iii) the interaction zone between the wind and halo gas surrounding the galaxy, and (iv) the interaction region of wind and dense clouds (Suchkov et al., 1994, 1996; Strickland & Stevens, 2000; Cooper et al., 2008, 2009; Thompson et al., 2016). In addition, there is a non-negligible contribution from the hot halo gas surrounding the galaxies. For well-resolved galaxies, this basic scenario can be used to investigate the kinematic properties of the wind. For example, using X-ray observations, Strickland & Heckman (2007) found that the velocity of the outflow in the central region (~ 100 pc) of M82 can be as large as $\sim 10^3$ km s $^{-1}$ and the mass outflow rate in the hot phase can be $\sim 1/3$ of the SFR in that galaxy.

However, some aspects of the diffuse X-ray emission remain puzzling. Using 2D axisymmetric simulations for a galaxy with SFR ~ 1 M $_{\odot}$ yr $^{-1}$, Suchkov et al. (1994) found that the shocked halo emission dominates over the emission from the central part. In contrast, using a full 3D simulation of M82 (SFR ~ 10 M $_{\odot}$ yr $^{-1}$) Cooper et al. (2008) showed that most of the emission comes from the central region and free wind rather than halo. Cooper et al. (2008, 2009) also noticed that a part of the emission comes from the interaction of clouds and the high velocity wind. However, a quantitative description of this emission is unavailable.

Another problem involves the scaling relation between the diffuse X-ray luminosity (not associated with point sources directly or indirectly) and the SFR. A thermally driven wind model (Chevalier & Clegg, 1985, hereafter, CC85)² suggests that the hot gas density at the central region of galactic wind is \propto SFR, and therefore, the X-ray luminosity \propto SFR². The temperature of the gas related to the wind or shocked halo is $\lesssim 2 \times 10^7$ K which emits mostly in the soft band (0.5-2.0 keV). A recent observational study of diffuse X-ray emission, however, suggests that the soft X-ray luminosity, L_X , \propto SFR (Mineo et al., 2012a, hereafter, M12), though other scalings cannot be ruled out. Zhang et al. 2014 and Bustard et al. 2016 attempted to reconcile the observations with the expected scaling by adjusting parameters such as the mass loading factor (MLF; mass outflow rate/SFR = β) and the thermalisation efficiency (α). They suggested an inverse dependence of β on SFR in order to explain the observed L_X –SFR relation. However, the physical origin for such an inverse relation remains unexplained.

Yet another problem is that galaxies with low SFR (\leq few M $_{\odot}$ yr $^{-1}$) show a flatter L_X –SFR relation with large scatter in the diffuse X-ray luminosity (Wang et al., 2016, hereafter, W16), implying that other factors beyond stellar feedback contribute significantly to X-ray emission.

In this Chapter, we constrain the mass loading factor based on the amount of interstellar medium (ISM) mass available and by the requirement that the cooling time be longer than the outflow expansion time. Using this, we show that at large SFRs the X-ray luminosity (L_X) indeed scales as SFR², but at smaller SFRs the X-ray emission from the circumgalactic medium (CGM; which is insensitive to SFR) starts to dominate.

²Note that, the CC85 model with a smooth thermalised wind is only applicable for SFRs larger than a critical value (≈ 0.1 M $_{\odot}$ yr $^{-1}$) (Sharma et al., 2014b). Therefore, CC85 is a good approximation in the range of SFRs of our interest.

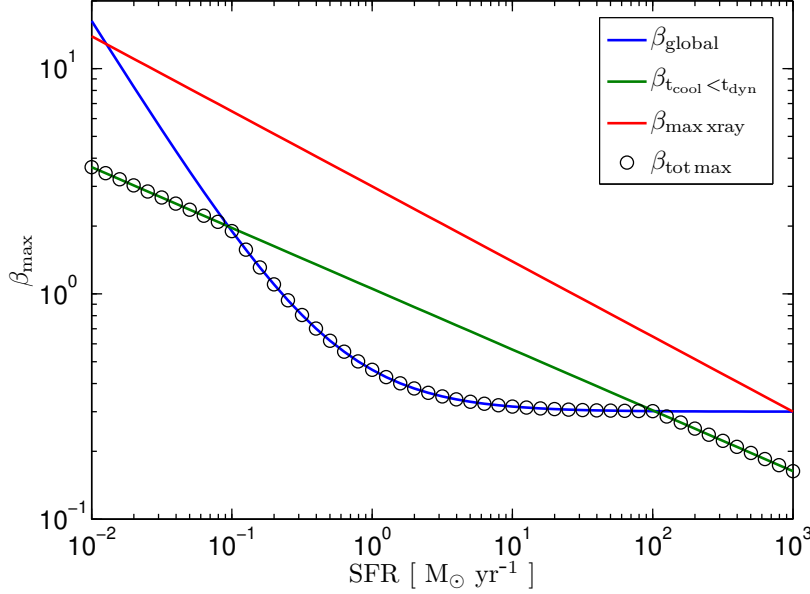


Figure 3.1: Threshold values of MLF (β) as a function of SFR from various considerations: the availability of gas mass (blue); cooling time (green); and X-ray luminosity (0.5 – 2.0 keV) in the central region (red). The maximum allowed β is shown by circles. Parameters used here are $R = 200$ pc, $n_{\text{ism}} = 10 \text{ cm}^{-3}$, $\Delta t = 30$ Myr, $\alpha = 0.3$ and metallicity = Z_{\odot} .

This behaviour can lead to the observed $L_X \propto \text{SFR}$ or even flatter relation if one fits a single power law to observations.

3.2 Mass loading of outflows

Consider galaxies with outflows driven by thermal feedback from star formation, which we model as a thermal wind within a central region of size R (following CC85). The energy and mass injection in the central zone is parametrised by \dot{M} and \dot{E} , which are respectively the mass deposition rate and the energy deposition rate, and are given by $\dot{M} = \beta \text{SFR}$ and $\dot{E} = 5 \times 10^{15} \alpha \text{SFR}$ (assuming a Kroupa/Chabrier mass function, and an efficiency $\alpha \approx 0.3$ for energy deposition; here \dot{E} , \dot{M} and SFR are in CGS units).

The X-ray luminosity of a galactic wind sensitively depends on the MLF β (Zhang et al. 2014), which is governed by following considerations: (a) Stellar evolution models suggest that stellar winds and supernova ejecta (without entrainment from the surrounding ISM) contribute to $\beta_0 \approx 0.3$ (Leitherer et al., 1999), (b) the outflowing gas entrains mass from the surrounding ISM. However, the entrained mass (due to conduction and KH instabilities) cannot be larger than the total ISM mass $M_g (= 4\pi\mu m_p n_{\text{ism}} R^3/3)$ available within the central starburst region of radius R . Therefore, an upper limit of MLF is given by

$$\beta_{\text{global}} = \beta_0 + \frac{M_g/\Delta t}{\text{SFR}} = 0.3 + 0.06 \times \frac{n_{\text{ism}} R_{100\text{pc}}^3}{\text{SFR}_{M_{\odot} \text{ yr}^{-1}} \Delta t_{\text{Myr}}}, \quad (3.1)$$

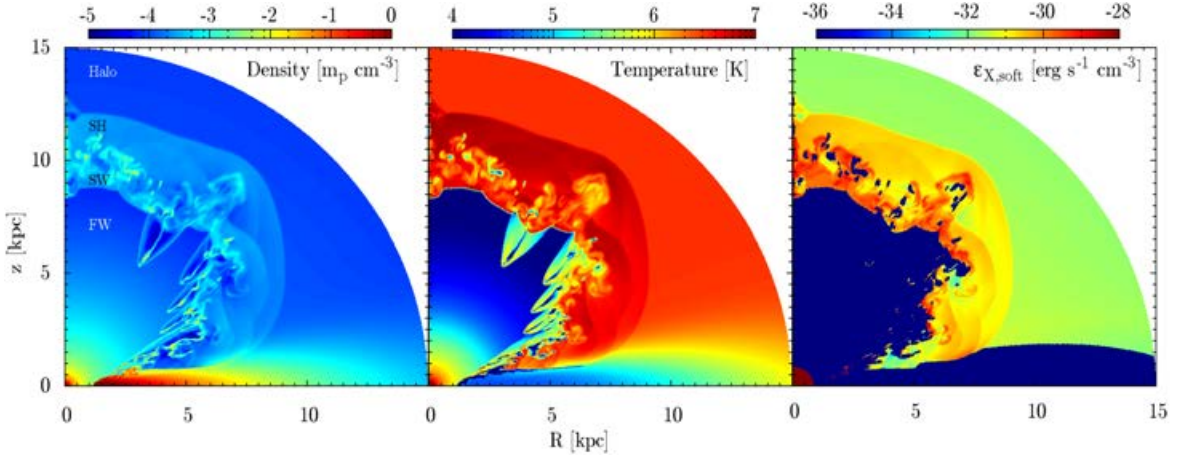


Figure 3.2: Snapshots of density (left panel), temperature (middle panel) and soft X-ray (0.5-2.0 keV) emissivity (right panel) contours at $t = 20$ Myr for $\text{SFR} = 5 M_{\odot} \text{ yr}^{-1}$ and central halo density $\rho_{h0} = 3 \times 10^{-4} m_p \text{ cm}^{-3}$ with total grid points = 512². The labels in the left panel are as follows: FW- Free Wind, SW- Shocked Wind and SH- Shocked Halo. Note that we have used colourbar between 10^{-36} and $10^{-28} \text{ erg s}^{-1} \text{ cm}^{-3}$ (right panel) but the core emissivity is $\sim 10^{-21} \text{ erg s}^{-1} \text{ cm}^{-3}$.

where, n_{ism} is the ambient ISM number density, Δt is the age of the starburst. (c) A further constraint arises from the cooling time of this central gas to be longer than the expansion time, otherwise most mass will condense radiatively and drop out of the outflow (see equation 10 of [Thompson & Krumholz 2016](#); for the curve shown in figure 3.1, we use a wind opening angle of 60°). (d) A related constraint is that for the total X-ray luminosity of the central region ($\approx 4\pi n_c^2 \Lambda(T_c) R^3 / 3$; where, $n_c = 0.3 \dot{M}^{3/2} \dot{E}^{-1/2} R^{-2} / \mu m_p$ is the central ISM number density; $\mu = 0.6$, is the mean molecular weight; Λ is the X-ray emission function ($\text{erg s}^{-1} \text{ cm}^3$); $T_c = 1.4 \times 10^7 \alpha / \beta$, is the central temperature (see CC85)) should be smaller than the energy deposition rate (\dot{E}), This gives an upper limit on MLF, namely,

$$\beta_{\text{max xray}} = \left(\frac{13.5 \alpha_{0.3}^2 R_{100pc}}{\text{SFR}_{M_{\odot} \text{ yr}^{-1}} \Lambda_{-23}(T, Z)} \right)^{1/3}, \quad (3.2)$$

where, $\Lambda_{-23}(T, Z)$ is the emission function at a particular X-ray energy band (in units of $10^{-23} \text{ erg s}^{-1} \text{ cm}^3$), temperature (T) and metallicity (Z). For the calculation of $\beta_{\text{max xray}}$ in figure 3.1, we fix $\Lambda_{-23}(T_c, Z_{\odot}) = 1$. Note that argument (d) is not completely independent of argument (c).

In the case of high β , the outflowing gas has a large ram pressure ($\propto \dot{M}^{1/2} \dot{E}^{1/2} \propto \beta^{1/2}$) on the surrounding gas, and is likely to entrain more gas. It is therefore reasonable to assume that β is likely to attain the maximum allowed value under the above considerations (b,c,d in previous paragraph). Figure 3.1 shows various threshold values of β as a function of SFR. Open circles show the maximum values of β allowed by these considerations.

3.3 Simulation details

We perform 2-D axisymmetric hydrodynamic simulations using [PLUTO-v4.0](#) (Mignone et al., 2007). We simulate only one quadrant of a MW type galaxy (total mass $M_{\text{vir}} = 10^{12} M_{\odot}$). The initial condition for the galaxy is in dynamical equilibrium with a warm, rotating disc ($T \sim 4 \times 10^4$ K; with Solar metallicity) and a hot gaseous halo ($T = 3 \times 10^6$ K; with 0.1 Solar metallicity) surrounding the galaxy. We vary SFR for the same disc/halo properties. The disc gas is not allowed to cool if it is not shocked/perturbed; i.e., unless $\sqrt{v_r^2 + v_{\theta}^2} \geq 20 \text{ km s}^{-1}$. Other details of the model can be found in S15.

The SNe energy is deposited continuously in form of thermal energy in a spherical region of radius R at the centre of the galaxy. In reality, most of the SNe occurs in a low density medium created by the previous SNe explosions and stellar winds. To mimic this, we create an artificially low density medium ($10^{-2} m_p \text{ cm}^{-3}$) at $t = 0$ for $r \leq R$ (in local pressure equilibrium with the region outside) and then deposit the SNe energy and mass (with Z_{\odot}) inside it. This also prevents artificial cooling losses due to lack of sufficient numerical resolution. For estimating the X-ray emission function ($\Lambda_X(T, Z)$), we use Mekal model at 0.2 and 1.0 Z_{\odot} and linearly interpolate for all other metallicities (from 0.1 to 1.0 Z_{\odot}).

3.4 Results

Figure 3.2 shows snapshots of density, temperature and soft X-ray emissivity for SFR = $5 M_{\odot} \text{ yr}^{-1}$ and background halo density $\rho_{\text{h0}} = 3 \times 10^{-4} m_p \text{ cm}^{-3}$ at $t = 20 \text{ Myr}$. It shows a typical structure containing free wind, termination shock, shocked wind, shocked halo and un-shocked halo as labelled in the left panel (Weaver et al., 1977). The soft X-ray (0.5-2.0 keV) emissivity (rightmost panel) shows the origin of X-ray emission in a typical galactic wind. It shows that the soft X-ray emissivity of the central region is very high and is followed by shocked wind, shocked halo and halo region.

We find that the luminosity of the central region becomes constant after $t \gtrsim 1 \text{ Myr}$ (which is essentially the time to set up a steady wind at the centre for a constant mass and energy injection rate, and is given by the sound crossing time ($\propto R/\sqrt{\dot{E}/\dot{M}}$) for the hot wind). Though the contribution of the outer parts (consisting of the shocked wind, shocked halo and the CGM) increases with time because of the increased volume of the shocked halo gas and continuous energy pumping from the wind, the X-ray luminosity from the central injection region and the CGM dominates. Here we present analytic scalings of these components.

Following CC85, the central luminosity (for $r \leq R$) can be estimated in the case of a uniform density ($\rho_c = \mu m_p n_c$) central region (of volume $4\pi R^3/3$) as $L_{X,C} = 1.3 \times 10^{40} \alpha^{-1} \beta^3 \text{SFR}^2 R_{100\text{pc}}^{-1} \Lambda_{-23}(T, Z) \text{ erg s}^{-1}$. However this is an overestimate since the density in the central region is not quite uniform. Results from our simulations are well fit by,

$$\frac{L_{X,C}}{\text{erg s}^{-1}} \approx 3 \times 10^{39} \alpha^{-1} \beta^3 \text{SFR}^2 R_{100\text{pc}}^{-1} \Lambda_{-23}(T, Z). \quad (3.3)$$

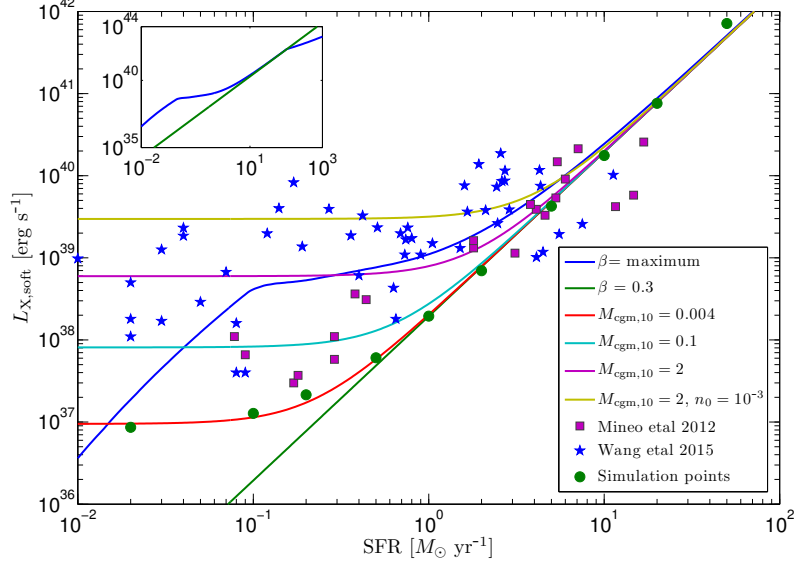


Figure 3.3: Comparison of the soft X-ray luminosities and observed data (magenta squares for M12 and blue asterisk for W16) for various models. The green and blue lines show $L_{X,C}$ for $\beta = 0.3$ and β_{\max} for $R = 200$ pc. The inset shows that $L_X \propto \text{SFR}$ at larger SFRs ($\gtrsim 100 M_{\odot} \text{ yr}^{-1}$) where cooling threshold becomes more important than mass loading (see Fig. 1). The red, cyan and magenta lines show $L_X (= L_{X,C}(\beta = 0.3) + L_{X,CGM})$ for $n_{0,-3} = 0.3$, whereas, the golden line shows L_X for $n_{0,-3} = 1$. Notice that, high values of $L_X (\sim 10^{40} \text{ erg s}^{-1})$ for low SFR galaxies can be obtained for moderate values of M_{CGM} but using a higher value of $n_{0,-3}$ (also see eq. 3.4).

The next important contribution towards X-ray emission comes from the CGM which contains a significant fraction of the missing baryonic mass, as seen in X-ray (Anderson & Bregman, 2011; Bogdán et al., 2013; Dai et al., 2012) and absorption studies (Bordoloi et al., 2014; Borthakur et al., 2015).

The CGM density profile can be approximated as $n_0 (1 + r/r_c)^{-3/4}$, with a core radius r_c (≈ 3 kpc) and central density n_0 (see Figure 1 of S15). While this is clearly an approximation, the density values are not that different from estimates in the literature (e.g., Sharma et al. 2012; Fang et al. 2013; Gatto et al. 2013). If the CGM gas is spread over a length scale $r/r_c = x \gg 1$, then the X-ray luminosity can be expressed in terms of $M_{CGM} (= 10^{10} M_{CGM,10} M_{\odot})$, the total CGM gas mass (we express the dependence of $L_{X,CGM}$ on the extent of the CGM in terms of M_{CGM}), as $L_{X,CGM} \approx 5.4 \times 10^{40} n_{0,-3}^{4/3} r_{c,3} \Lambda_{-23} M_{CGM,10}^{2/3} \text{ erg s}^{-1}$, where $n_0 = 10^{-3} n_{0,-3} \text{ cm}^{-3}$ and $r_c = 3 r_{c,3}$ kpc. However, our simulation results show that the actual luminosity from CGM is somewhat less than this, because of the approximation ($x \gg 1$) used in arriving at it, and is better represented by,

$$\frac{L_{X,CGM}}{\text{erg s}^{-1}} \approx 8.6 \times 10^{39} n_{0,-3}^{4/3} r_{c,3} \Lambda_{-23}(T, Z) M_{CGM,10}^{2/3}. \quad (3.4)$$

Next we compare the X-ray luminosity from our simulations (scaled according to Eqs 3.3 and 3.4 for different star formation and CGM properties) with the observed data. Figure 3.3 shows the L_X -SFR relation from our models. The green and blue

lines show $L_{X,C}$ for the cases of $\beta = 0.3$ and the maximum β (circles in Figure 3.1), respectively. We find that the data from M12, shown in red squares, are explained by $L_{X,C}$ for the range of $0.3 \leq \beta \leq \beta_{max}$, where β_{max} is determined by the available ISM mass and the radiative cooling time, as discussed in section 3.2, whereas, a higher β for smaller SFRs due to the ISM mass loading makes the relation shallower at smaller SFRs. The data, which have hitherto been fit with a linear scaling between L_X and SFR, actually belong to two different regimes: a quadratic scaling at large SFRs and a flattening at smaller SFRs. In fact, the constraint of MLF from available ISM mass predicts $\beta \propto \text{SFR}^{-2/3}$ from 0.1 to a few $M_\odot \text{ yr}^{-1}$ (Figure 3.1), which when put in eqn 3.3 makes L_X independent of SFR. Note that the ISM mass availability constraint, which we highlight for the first time, is the most stringent for SFRs of interest.

The different lines that flatten towards the lowest SFRs in Figure 3.3 show the total luminosity (for $\beta = 0.3$) after adding the contribution from CGM with different masses and densities for $T = 3 \times 10^6 \text{ K}$ and $Z = 0.1 Z_\odot$. We find that these curves can reasonably explain the data from W16 (shown with the blue stars in Figure 3.3). The X-ray luminosity in data flattens out at low SFRs because of the contribution from the CGM. W16 also find a dependence of L_X on stellar mass; namely, $L_X/L_K \propto (\text{SFR}/M_\star)^{0.3}$ (which is equivalent to $L_X/\text{SFR} \propto [M_\star/\text{SFR}]^{0.7}$ assuming $L_K \propto M_\star$), where L_K and M_\star are K-band luminosity and stellar mass of the galaxies, respectively. The stellar/halo mass dependence can naturally come from the CGM, which is more massive for larger galaxies (see Eq. 3.4). In fact, the relations above indicate a ‘fundamental plane’ in L_X , M_\star and SFR space, i.e. $L_X \propto M_\star^{0.7} \text{SFR}^{0.3}$ (for $\text{SFR} \lesssim \text{few } M_\odot \text{ yr}^{-1}$), the existence of which can be tested with future observations.

Since the CGM mass is not yet reliably measured from observations, we can study the relation of L_X with the expected scaling of CGM mass with stellar/halo mass. Recent observations suggest that about half of the missing baryons is in the form of cold clumps, and the rest could be warm-hot CGM gas (Werk et al., 2014). Since stellar mass comprises about a third, the mass of the warm-hot component of CGM gas can be comparable to M_\star .

Assuming that the CGM gas mass is equal to the total stellar mass, in Figure 3.4 we show the relation between L_X/SFR and M_\star/SFR , where M_\star is the total stellar mass. The data from W16 are shown along with the curves for different values of $M_{CGM}(= M_\star)$. The highest SFR systems lie to left in this plot. The lines with different stellar/CGM masses look reasonably consistent with the data. The observed scaling of $L_X/\text{SFR} \propto (M_\star/\text{SFR})^{0.6}$ can be easily explained by the scaling of $L_{X,CGM} \propto M_{CGM}^{2/3}$ (eqn 3.4), for the CGM X-ray emission, which dominates in the low SFR (right portion of Figure 3.4). We also notice that the curves in Fig 3.4 show a negative slope for high SFR galaxies (on the left), which is consistent with the observed trend for high SFR galaxies in W16.

3.5 Discussion

Our key result is that the diffuse X-ray emission from star-forming galaxies can be understood in terms of contributions from the central thermalised wind (extending over $\sim 100 \text{ pc}$) and the extended CGM. For higher SFRs $L_X \propto \text{SFR}^2$, whereas, the CGM contribution dominates for $\text{SFR} \lesssim 1 M_\odot \text{ yr}^{-1}$ and accounts for the flattening of

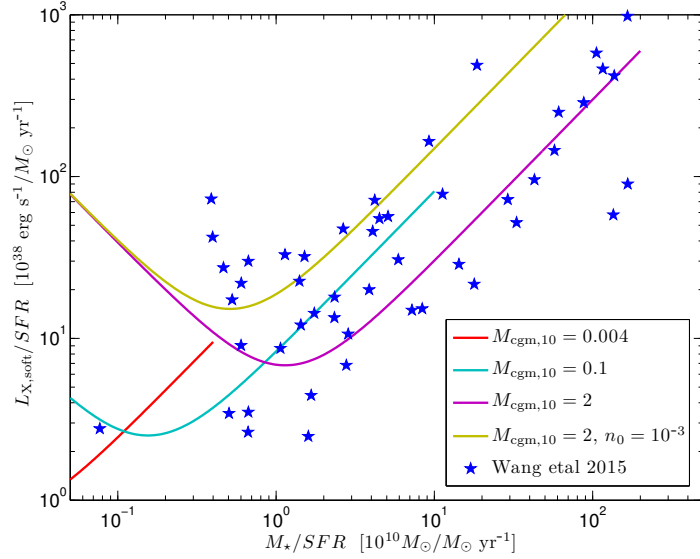


Figure 3.4: Data from W16 along with curves for total diffuse X-ray luminosities for different values of M_{CGM} . These correspond to the same models as in Figure 3.3 but normalised to $M_{CGM} = M_*$.

the L_X –SFR relation at low SFRs. Our model also predicts that the relation can be even flatter with a large scatter, depending on the halo properties. Since the CGM mass is expected to increase with the stellar/halo mass, at smaller SFRs a higher L_X can result from the CGM contribution. In fact, the galaxies with low SFRs but high L_X are likely to contain a large amount of CGM gas at temperatures of a few million degrees K, and are good candidates for spiral galaxies with a detectable X-ray emitting CGM (few such systems are reported by [Anderson & Bregman 2011](#); [Bogdán et al. 2013](#)).

The X-ray luminosity from the CGM (eqn 3.4) depends on the CGM gas mass, density and temperature. We find that for the typical range in temperature (as found in, say, W16) of $2\text{--}8 \times 10^6$ K, the $L_{X,CGM}$ varies between $3 \times 10^{38}\text{--}2.4 \times 10^{40}$ erg s $^{-1}$, for $M_{CGM} = 10^{10} M_\odot$. This spread arises from (a) the difference in emissivity with temperature and (b) the density profile of CGM gas at different temperatures. Figure 3.3 shows that this spread in X-ray luminosity from the CGM gas can explain the data. We should however keep in mind that the spread in the data (Figure 3.4) can partly arise from the spread in the relation between SFR and galaxy dynamical mass, which is likely related to M_* ([Karachentsev & Kaisina, 2013](#)). We also note that the central SFR used in our models is an underestimation of a disc-wide SFR. This can also be responsible for the spread in the observed data.

It is generally believed that the CGM around low mass galaxies ($M_* \lesssim \text{few} \times 10^9 M_\odot$) would have a low virial temperature (few $\times 10^5$ K), which would make the CGM vulnerable to radiative cooling as the cooling time would become less than the dynamical time of the galaxy ([Singh et al., 2015](#)). However, hot CGM around low mass galaxies can be formed from the hot and low density material ejected from disc supernovae which does not have sufficient energy to escape the galactic potential but have a long cooling time. This rejuvenated halo around low mass galaxies may give rise to the X-rays seen in low

mass galaxies (which are also low SFR galaxies, in the presented data). The spread in L_X –SFR relation at the low SFR end can be partly due to the ill-understood, complex thermodynamic state of such low speed outflows.

Though observations of the *total* X-ray emission (0.5-8.0 keV) (Mineo et al., 2014) show a linear relation, it is, however, supposed to be contaminated by high mass X-ray binaries (HMXB) (Grimm et al., 2003) and should best be considered as an indicator to the SFR (since, number of HMXBs \propto SFR) rather than diffuse X-ray related to the galactic wind.

We also note that the linear relation of X-ray luminosity from the shocked wind and halo as observed in highly inclined galaxies by Strickland et al. (2004b); Tullmann et al. (2006); Li & Wang (2013) have to be studied separately as the soft X-ray emission from the central part of these galaxies is heavily absorbed by the galactic disc and does not represent the total emission. We will address these issues in detail in a future work.

Chapter 4

Multi-wavelength features of Fermi Bubbles as signatures of a supernovae-driven Galactic wind

Based on:

“Multi-wavelength features of Fermi Bubbles as signatures of a Galactic wind” by Kartick C Sarkar, Biman B Nath and Prateek Sharma, 2015, Mon. Not. R. Astron. Soc., 453, 3827 ([Sarkar et al., 2015b](#))

Interaction of galactic wind with the circumgalactic medium not only produces multiphase medium and emits X-rays, but also harbours many more complex physics and emission mechanisms. Recent discovery of two giant gamma-ray bubbles towards the centre of our Galaxy are examples of such complex physics inside the outflows. While the origin of the gamma-ray emission in these bubbles is being investigated intensively, little attention has been put in order to understand the multi-wavelength features related to them. In a first, we try to understand the observations of gamma-ray, X-ray, radio emission and UV absorption lines by performing hydrodynamical simulations of supernovae driven wind in a realistic environment that is close to Milky-Way conditions.

Main Results

- We show that an episode of star formation in the centre of the Milky Way, with a star-formation-rate (SFR) $\sim 0.5 M_{\odot} \text{ yr}^{-1}$ for ~ 30 Myr, can produce bubbles that resemble the Fermi Bubbles (FBs), when viewed from the solar position. The morphology, extent and multi-wavelength observations of FBs, especially X-rays, constrain various physical parameters such as SFR, age, and the circumgalactic medium (CGM) density.
- We show that the interaction of the CGM with the Galactic wind driven by star formation in the central region can explain the observed surface brightness and morphological features of X-rays associated with the Fermi Bubbles.
- Furthermore, assuming that cosmic ray electrons are accelerated *in situ* by shocks and/or turbulence, the brightness and morphology of gamma-ray emission and the microwave haze can be explained.
- The kinematics of the cold and warm clumps in our model also matches with recent observations of absorption lines through the bubbles.

4.1 Introduction

Several observations point toward the existence of a gaseous outflow from the centre of Milky Way. An enhancement in the diffuse soft X-ray emission in the longitude range $-20^\circ \leq l \leq 35^\circ$ with an emission scale height (in the southern hemisphere) of $b \sim -17^\circ$ suggests a large-scale flow of gas out of the disc (Snowden et al., 1995; Everett et al., 2008). This emission was modelled by Snowden et al. (1995) with a mid plane gas density $n_e \sim 3.5 \times 10^{-3} \text{ cm}^{-3}$ and temperature $T \sim 4 \times 10^6 \text{ K}$. Observations by Almy et al. (2000) proved that at least half of the central emission comes from more than 2 kpc from the Sun, and most likely lies near the Galactic centre (see also, Park et al. (1997); Yao & Wang (2007)). Almy et al. (2000) took into account other components (stellar, extragalactic), and improved the model density and temperature to $n_e \sim 10^{-2} \text{ cm}^{-3}$ and $T \sim 8.2 \times 10^6 \text{ K}$. Interestingly, this emission was predicted from a model of cosmic ray driven Galactic outflow by Breitschwerdt & Schmutzler (1994). In fact, using mid-infrared ($8.3\mu\text{m}$) and ROSAT (1.5keV) observations, Bland-Hawthorn & Cohen (2003) first showed the existence of a bi-conical Galactic outflow. They also speculated about the existence of projected x-ray bubbles on the both sides of the galactic plane extending up to $\sim 80^\circ$ in latitude.

The discovery of γ -ray bubbles in the similar part of the sky, known as the Fermi Bubble, has given spurt to exploring the high energetic implications of a Galactic outflow. These twin bubbles, extending up to $\sim 50^\circ$ ($\sim 8 \text{ kpc}$ in height) above and below the Galactic centre, are marked by γ -ray emission with a remarkably uniform surface brightness and a ($dN/dE \sim E^{-2}$) spectrum that is harder than the emission from the disc (Su et al., 2010).

The X-ray and γ -ray features also coincide with emission features in other wavelengths, such as the microwave haze found by WMAP and *Planck* (Finkbeiner, 2004; Planck Collaboration et al., 2013) and the polarized radio lobes seen at 2.3 GHz (Carretti et al., 2013). Incidentally, Lockman (1984) had noted a HI hole in the inner Galaxy. These morphological similarities, to the extent of the edges of the features in different wavelength almost coinciding with each other, suggest a common physical origin.

Several models have been proposed to explain the FBs. As far as γ -ray emission mechanism is concerned, there remains an uncertainty whether the inverse Compton scattering of cosmic microwave background photons by relativistic electrons is the source (Su et al., 2010) or the interactions of high energy protons with protons in the medium (Crocker & Aharonian, 2011). The high energy electrons or protons can either be accelerated *in situ* by internal shocks and turbulence (Mertsch & Sarkar, 2011), or advected from the disc. Outflows triggered by star formation in the Galactic centre (GC) region (Crocker 2012; Lacki 2014) and by the black hole at the GC (Guo & Mathews, 2012; Yang et al., 2012; Mou et al., 2014) have been proposed for the dynamical origin of the FBs.

The AGN-based models (both jet and wind driven) generally consider a shorter age (\lesssim few Myr) for the FBs because the inverse-Compton cooling time (due to up-scattering of starlight) for $\sim 100 \text{ GeV}$ electrons responsible for gamma ray emission is a few Myr (Guo & Mathews 2012; Yang et al. 2012). The speed required to reach $\sim 10 \text{ kpc}$ in 1 Myr is $\sim 10^4 \text{ km s}^{-1}$, achievable by relativistic jets slowed down by the hot circumgalactic medium (CGM). The power required for inflating young FBs is much higher and the outer shock is much stronger (Guo & Mathews 2012; Zubovas

& Nayakshin 2012), and X-ray emissivity and temperature much higher than what is observed (Kataoka et al. 2013). The SNe-driven models of FBs consider them to be long lived ($\gtrsim 10$ Myr), and thus the injected power is smaller. In fact, Crocker et al. (2014) suggest a hadronic origin for gamma ray emission and consider the FBs to be steady features older than few 100 Myr. The outer shock is weaker in the SNe-driven models and the temperature and emissivity jumps are modest, consistent with X-ray observations.

While the AGN jet and wind models have been explored numerically, simulations of a SNe driven model for FBs have not yet been carried out. The dynamical modelling is limited to simple arguments invoking a steady wind, termination shock, thermal instabilities, etc. (Crocker et al. 2015; Lacki 2014). A realistic SNe-driven wind is expected to be affected by disc stratification and the presence of a CGM. Moreover, thermal and Rayleigh-Taylor instabilities are expected to mix the hot bubble gas with the halo gas. We capture these complex, time-dependent, multidimensional effects in the hydrodynamic numerical simulations presented in this chapter.

In our model, the FB is a time dependent phenomenon and is currently expanding. Our goal is to study the time dependent signatures of a star formation triggered Galactic wind, and to identify various features observed in different wavebands (γ -rays, X-rays, microwave and radio) with various structural features of a Galactic wind. In doing so, we pay particular attention to projection effects from the vantage point of the solar system in the Galactic disc.

This chapter is organised as follows. In section 4.2, we discuss the initial set up, the simulation settings and the parameters. The morphology and the importance of projection effects in the observations of the FBs are described in section 4.3. In section 4.4, we describe the X-ray, microwave and γ -ray emission from the FB. Section 4.5 points out some kinematics aspects of the cold/warm clumps. We discuss the implications and improvements of our work in section 4.6. Finally, in section 4.7, we summarise the main conclusions of this chapter.

4.2 Simulation

4.2.1 Initial set up

The details of the initial set up for milky way (MW) type galaxies are given in a previous paper Sarkar et al. (2015a). However, for the sake of completeness, we briefly discuss the set up below.

In our set up, we consider two gas components, a warm component ($T = 4 \times 10^4$ K, including the contribution from non-thermal pressure) representing the disc gas, and a hot component ($T = 2.5 \times 10^6$ K) representing the extended circum-galactic medium (CGM). Since the warm gas represents the disc, we also consider azimuthal rotation for this component. The hot CGM, however, is considered to be non-rotating.

These two gas components are considered to be in steady state equilibrium with background gravitational potential of the stellar disc and dark matter (DM). For the

disc, we use the Miyamoto & Nagai potential (Miyamoto & Nagai, 1975)

$$\Phi_{\text{disc}}(R, z) = -\frac{GM_{\text{disc}}}{\sqrt{R^2 + (a + \sqrt{z^2 + b^2})^2}}, \quad (a, b \geq 0) \quad (4.1)$$

where a and b are the model parameters representing the scale length and the scale height of a disc of mass M_{disc} respectively, and, R and z are the cylindrical coordinates. For the dark matter, we use a modified form of NFW profile (Navarro et al., 1996) introducing a core at the center. The modified form of the potential is given as

$$\Phi_{\text{DM}}(R, z) = -\left(\frac{GM_{\text{vir}}}{f(c)r_s}\right) \frac{\log(1 + \sqrt{R^2 + z^2 + d^2}/r_s)}{\sqrt{R^2 + z^2 + d^2}/r_s} \quad (d \geq 0), \quad (4.2)$$

where $f(c) = \log(1 + c) - c/(1 + c)$ with $c = r_{\text{vir}}/r_s$ as the concentration parameter and d is the radius of the core which gives a finite DM density at the centre. r_{vir} and r_s are, respectively, the virial radius and scale radius for a DM halo of mass M_{vir} .

The steady state density distribution in a combined potential $\Phi(R, z) = \Phi_{\text{disc}}(R, z) + \Phi_{\text{DM}}(R, z)$ for the warm gas can be written as

$$\rho_d(R, z) = \rho_d(0, 0) \exp\left(-\frac{1}{c_{\text{sd}}^2} [\Phi(R, z) - \Phi(0, 0) - f^2(\Phi(R, 0) - \Phi(0, 0))]\right), \quad (4.3)$$

and for the hot CGM,

$$\rho_h(R, z) = \rho_h(0, 0) \exp\left(-\frac{1}{c_{\text{sh}}^2} [\Phi(R, z) - \Phi(0, 0)]\right), \quad (4.4)$$

where, $\rho_d(0, 0)$ and $\rho_h(0, 0)$ are the warm and hot gas central densities and c_{sd} and c_{sh} are the isothermal sound speeds of the warm disc and the hot CGM, respectively. Here, f is the ratio of the disc gas rotation velocity and the stellar rotation velocity at any R and taken to be a constant ($= 0.95$). The density of a given location is, therefore, $\rho_d + \rho_h$. A full list of model parameters is given in Table 4.1.

4.2.2 Code settings

We use the publicly available code `PLUTO-v4.0` (Mignone et al., 2007) for our hydrodynamic simulations. We perform the simulations in 2D spherical coordinates assuming axi-symmetry around $\theta = 0$. The simulation box extends from $r_{\text{min}} = 20$ pc to $r_{\text{max}} = 15$ kpc in radial direction using logarithmic grids and from $\theta = 0$ to $\theta = \pi/2$ in theta direction using uniform grids. This implies that the disc lies on the $\theta = \pi/2$ plane and our simulation box includes the first quadrant of the 2D slice taken along the θ plane of our Galaxy.

In our simulation, we express the temperature as $T \sim p/\rho$ which includes the hot gas pressure in addition to the 4×10^4 K gas pressure inside the disc. The effective temperature of the disc is large enough to induce strong cooling unlike the warm gas at $T = 10^4$ K gas. In reality the disc gas is always being heated by the supernovae and other processes. Since we are interested in the Galactic wind and not the disc ISM, we constrain the cooling of the disc material (but not the injected material) to be zero for a height less than 1.2 kpc above the disc plane. A more detailed description about the code implementation can be found in Sarkar et al. (2015a).

parameters	values
$M_{\text{vir}}(M_{\odot})$	10^{12}
$M_{\text{disc}}(M_{\odot})$	5×10^{10}
$T_{\text{halo}}(\text{K})$	2.5×10^6
$r_{\text{vir}}(\text{kpc})$	258
c	12
$a(\text{kpc})$	4.0
$b(\text{kpc})$	0.4
$d(\text{kpc})$	6.0
$Z_{\text{disc}}(Z_{\odot})$	1.0
$Z_{\text{halo}}(Z_{\odot})$	0.1
$\rho_d(0,0)(\text{m}_p\text{cm}^{-3})$	3.0
$\rho_h(0,0)(\text{m}_p\text{cm}^{-3})$	2.2×10^{-3}

Table 4.1: Parameters used in our simulations. Hot gas central density $\rho_h(0,0)$ is obtained after normalising the total baryonic content (stellar plus gaseous) to 0.16 of M_{vir} , consistent with the cosmic baryonic fraction. While exploring the parameter space, we make this assumption flexible.

4.2.3 Injection parameters

The mechanical luminosity of a starburst activity can be written as

$$\mathcal{L} \approx 10^{40} \text{ erg s}^{-1} \epsilon_{0.3} \left(\frac{\text{SFR}}{0.1 M_{\odot} \text{ yr}^{-1}} \right), \quad (4.5)$$

where, $\epsilon_{0.3}$ is the thermalisation efficiency in units of 0.3 and SFR is the star formation rate. Here we have considered Kroupa/Chabrier mass function, for which there is ~ 1 SN for every $100 M_{\odot}$ of stars formed.

As we show later, the morphology and X-ray emission properties of FBs depend mostly on the combination of \mathcal{L} and the CGM gas density. After scanning through various combinations of these two parameters, we show later (in §4.1, Figure 4) that a fiducial combination of $\mathcal{L} = 5 \times 10^{40} \text{ erg s}^{-1}$ and $\rho_{h0} = 2.2 \times 10^{-3} \text{ cm}^{-3}$ best matches the observations. The implied star formation rate, according to eqn 4.5, is $\sim 0.5 M_{\odot} \text{ yr}^{-1}$ (considering $\epsilon_{0.3} = 1$). The current rate of star formation in the central molecular zone of Milky Way is of order $0.1 M_{\odot} \text{ yr}^{-1}$. Mid-infrared observations by Yusef-Zadeh et al. (2009) have led to an estimate of SFR ranging between $0.007\text{--}0.14 M_{\odot} \text{ yr}^{-1}$, over the last 10 Gyr. Observations of young stellar objects in the central molecular zone (CMZ) in the $5\text{--}38 \mu\text{m}$ band with *Spitzer* allowed Immer et al. (2011) to estimate a SFR of $\sim 0.08 M_{\odot} \text{ yr}^{-1}$. The diffuse hard X-ray emission in the Galactic centre region was used by Munro et al. (2004) to estimate an energy input of $\sim 10^{40} \text{ erg s}^{-1}$. However, the star formation activity in the central region of the Galaxy is likely to be episodic. Our fiducial SFR, averaged over the last several tens of Myr, is therefore not unreasonable although it is a few times larger than the current SFR.

The mass injection rate has been taken as (Leitherer et al., 1999)

$$\dot{M}_{\text{inj}} = 0.3 \text{ SFR}. \quad (4.6)$$

In our fiducial simulation, the considered mechanical luminosity, $\mathcal{L} = 5 \times 10^{40} \text{ erg s}^{-1}$, corresponds to $\text{SFR} = 0.5 M_{\odot} \text{ yr}^{-1}$ and therefore $\dot{M}_{\text{inj}} = 0.15 M_{\odot} \text{ yr}^{-1}$.

Name	\mathcal{L} (erg s ⁻¹)	ρ_{h0} (m _p cm ⁻³)
S1	1.0×10^{40}	0.5×10^{-3}
S2	1.0×10^{40}	1.0×10^{-3}
S3	1.0×10^{40}	3.0×10^{-3}
S4	2.0×10^{40}	0.5×10^{-3}
S5	2.0×10^{40}	1.0×10^{-3}
S6	2.0×10^{40}	2.0×10^{-3}
S7	2.0×10^{40}	3.0×10^{-3}
S8	4.0×10^{40}	0.7×10^{-3}
S9	5.0×10^{40}	1.1×10^{-3}
S10*	5.0×10^{40}	2.2×10^{-3}
S11	6.0×10^{40}	3.0×10^{-3}
S12	1.0×10^{41}	1.1×10^{-3}
S13	1.0×10^{41}	2.2×10^{-3}

Table 4.2: The list of runs showing the injected mechanical luminosity and the central density in column 2 and 3, respectively. The fiducial run (S10) has been pointed out by an asterisk in the list.

We inject this mass and energy in density and energy equations inside a region of $r \leq r_{\text{inj}}$ (60 pc). The injection rates can then be written as

$$\dot{p} = \frac{2}{3} \frac{\mathcal{L}}{(4\pi/3) r_{\text{inj}}^3} \quad (4.7)$$

and

$$\dot{\rho} = \frac{\dot{M}_{\text{inj}}}{(4\pi/3) r_{\text{inj}}^3}, \quad (4.8)$$

where, p is the pressure. A full list of all the runs is given in Table 4.2.

4.3 Results: wind & bubble morphology

The result of an episodic explosive event at the centre of Milky Way would depend mainly on the rate of energy and mass input (and therefore on the SFR), the distribution of density through which the bubble ploughs its way (the disc and CGM gas density profile) and the epoch under consideration. We fix these parameters based on the morphology of the resulting bubble, in light of the observed morphology of the FBs, and the emission properties. Therefore, we first discuss the morphology.

Figure 4.1 shows the colour-coded contours of density and temperature for our fiducial run, $\mathcal{L} = 5 \times 10^{40}$ erg s⁻¹ at $t = 27$ Myr (corresponding to $\approx 10^5$ supernovae over this time). The snapshot clearly shows the structure of a standard stellar wind scenario (Weaver et al., 1977). There is an outer shock (at a vertical distance of ≈ 10 kpc), an enhancement of density in the shocked CGM/ISM and shocked wind region, near the contact discontinuity (at a vertical distance of 6–8 kpc), as well as the inner free wind region (below a vertical distance of ~ 6 kpc). The figure also shows a second reverse shock at height of ~ 2 kpc which arises because of the presence of two component density structure related to the CGM and the disc.

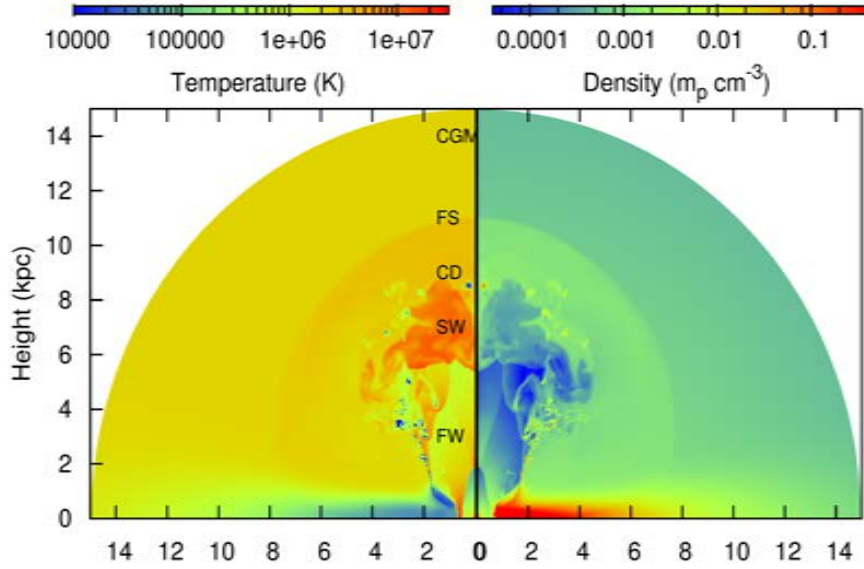


Figure 4.1: Snapshot of density (right panel) and temperature (left panel) contours at 27 Myr for our fiducial run (S10). The wind structure has been pointed out by different labels, from outside to inside as, CGM: circumgalactic medium, FS: forward shock, CD: contact discontinuity, SW: shocked wind and FW: free wind.

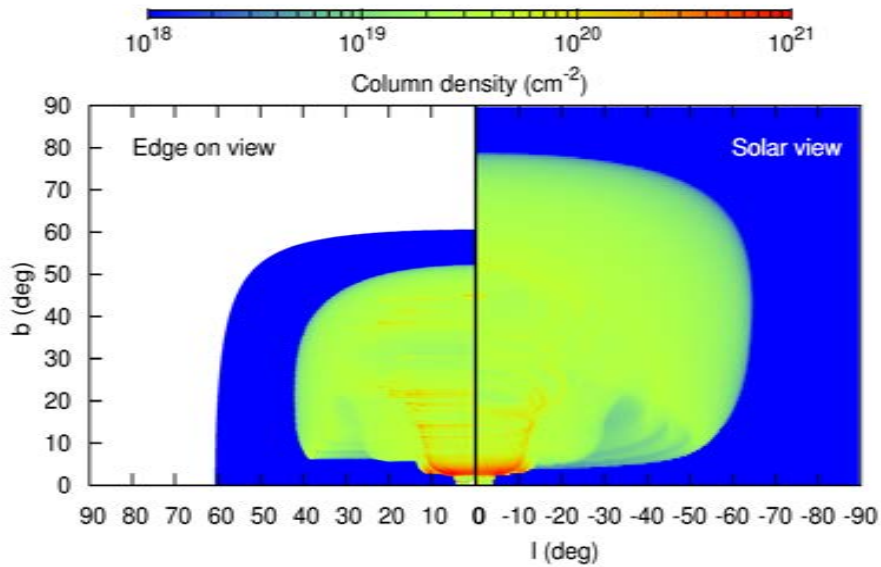


Figure 4.2: Snapshots of column density from edge-on position but without projection effects (left panel) and Solar vantage point with projection effects (right panel), for the same physical parameters as in Figure 4.1. The boundary of our simulation box (15 kpc) corresponds to an angle $\sim 60^\circ$ from a distance of 8.5 kpc, and shows up in the left panel.

Since we are at a distance of 8.5 kpc from the centre of the Galaxy, and the wind-cone extends ~ 4 kpc at a height of 5 – 6 kpc, much of the observed structure is influenced by geometrical projection effects. Figure 4.2 illustrates the idea by showing the map of column density as viewed from an edge-on vantage point from infinity, as well as its appearance from the point of view of the solar system. In order for the column density not to be dominated by the disc material, we have considered only the gas for which the total non-azimuthal speed ($\sqrt{v^2 - v_\phi^2}$) is larger than 20 km s^{-1} . From the edge-on position, the Galactic coordinates are computed as $l = \tan^{-1}(R/8.5 \text{ kpc})$, $b = \tan^{-1}(z/8.5 \text{ kpc})$,¹ whereas, from Solar view point (right panel), we have considered the projection effects accurately (see Appendix B.1 for details). In projection from the Solar system position, the bubble appears bigger in angular size. Note that we have used the axisymmetry property of our 2D simulations to get the projected maps presented in this chapter.

The difference between the left and right panels of Figure 4.2 highlights the importance of taking projection effects into account when comparing the morphology of the simulated bubble with the observed FBs. With the projected column density map at hand, we can discuss the logic behind fixing the epoch of the phenomenon at 27 Myr.

As explained below, the X-ray emission expected from the outer shock (shocked circumgalactic medium, CGM) is likely associated with the observed Loop-I feature in X-rays. This feature is also observed in soft γ -rays. The location of the outer shock depends strongly on the time elapsed, and helps us to fix the time at 27 Myr. The radius of the outer shock in a constant luminosity-driven wind, according to Weaver et al. (1977), is given by $\mathcal{R} \approx (\mathcal{L}t^3/\rho)^{1/5}$

$$\approx 10 \text{ kpc} \left(\frac{\mathcal{L}}{5 \times 10^{40} \text{ erg s}^{-1}} \frac{0.001 m_p}{\rho} \left[\frac{t}{27 \text{ Myr}} \right]^3 \right)^{1/5}, \quad (4.9)$$

matching the outer shock location in Figure 4.1. Moreover, with this choice, we find that the location of the contact discontinuity matches the edge of the FBs. This indicates that the emission in different bands coming from the FBs is created within the the contact discontinuity. In addition, as shown below, the morphology of emission in different wavebands remarkably matches the predictions based on this choice of time elapsed (namely, 27 Myr) and therefore, in turn, supports the idea that some part of the Loop-I feature is likely associated with the FBs. A point to note in Eq. 4.9 is that the outer shock radius depends more sensitively on time rather than SFR or the CGM density.

While Eq. 4.9 is strictly valid only for an homogeneous and isotropic medium, and with isotropic energy injection, we expect it to be roughly valid, even with anisotropic AGN jets. Most AGN-based models consider a shorter age (~ 1 Myr), which comes at the expense of a much larger mechanical power (up to $10^{44} \text{ erg s}^{-1}$, Guo & Mathews 2012; Yang et al. 2012). The velocity of the outer shock is given as $\mathcal{V} \approx 3\mathcal{R}/5t$

$$\approx 200 \text{ km s}^{-1} \left(\frac{\mathcal{L}}{5 \times 10^{40} \text{ erg s}^{-1}} \frac{0.001 m_p}{\rho} \left[\frac{10 \text{ kpc}}{\mathcal{R}} \right]^2 \right)^{1/3}, \quad (4.10)$$

¹These formulae are valid only for $R, z \ll 8.5 \text{ kpc}$, or equivalently $l, b \ll 45^\circ$.

comparable to the sound speed in the hot CGM ($\sim 180 \text{ km s}^{-1}$), implying a weak shock in case of $\mathcal{L} = 5 \times 10^{40} \text{ erg s}^{-1}$ as seen in Figure 4.1. A more powerful AGN jet acting for 1 Myr with $\mathcal{L} \sim 10^{44} \text{ erg s}^{-1}$ will result in a very strong shock, ruled out by X-ray observations that show only a slight enhancement of temperature and density across the FB edge as observed by Kataoka et al. (2013).

Though we assume that the injection region is spherical symmetric, a departure from this assumption does not change the qualitative/quantitative picture much. The effect of different injection geometries has been discussed in section 4.6.4.

4.4 Results: emission in different wavebands

We discuss the results of our calculation for the emission in different bands in this section, and compare with the observed features. Various emission mechanisms have been discussed in the literature for different bands – gamma-rays, X-rays, microwave and radio, and most of the debate so far has centred around the γ -ray radiation mechanism (hadronic or leptonic), whether or not particles are being advected from the disc or accelerated *in situ*. However, among the emission in different bands, the X-ray emission from thermal gas suffers the least from any assumptions regarding accelerated particles and magnetic fields. We, therefore, discuss the X-ray emission first.

Since we have estimated the age of the Fermi bubbles to be 27 Myr (as discussed in the previous section), we perform detailed analysis for the fiducial run (S10; see Table 4.2), at $t = 27 \text{ Myr}$ in this as well as in all the following sections.

4.4.1 X-ray

Observationally, two limb-brightened X-ray arcs, called ‘northern arcs’, are seen in the north-east quadrant adjacent to the FB. In the southern hemisphere, a ‘donut’ feature is observed. Then there is the Loop-I feature extending up to $b \sim 80^\circ$ and from 50° to -70° in longitude. The diffuse X-ray emission also shows a dip in intensity in the FB region (Su et al., 2010). Recently Kataoka et al. (2013) have scanned the FB edge to look for differences in the X-ray brightness. They found that the temperature does not vary across the edge but there is a 50% decrease of the emission measure (EM) when moving from outside to inside of the bubble.

We show the surface brightness of X-ray emission from the simulated bubble in Figure 4.3, in the 0.7–2.0 keV band (ROSAT R6R7 band) considering the Mekal plasma model (from XPEC) for emission. While calculating the X-ray surface brightness, we also consider the contribution from an extended CGM where the hydrostatic state has been extrapolated to 100 kpc.²

From Fig 4.3, we find that (1) the diffuse emission has a dip at FB and extends to the Loop-I feature in the form of a parachute (this fixes the age of FBs in our model, as mentioned earlier), and roughly delineates the feature leaving aside the slight asymmetry. (2) The location of the two arcs roughly matches the enhanced brightness

² For our isothermal CGM the density profile is centrally peaked so that surface brightness (SB) is dominated by the inner CGM, but halo gas extended out to 100 kpc makes a non-negligible contribution (50%) compared to when it is confined to the 15 kpc box. The contribution of extended halo depends somewhat on the CGM density profile at large radii which is observationally unconstrained.

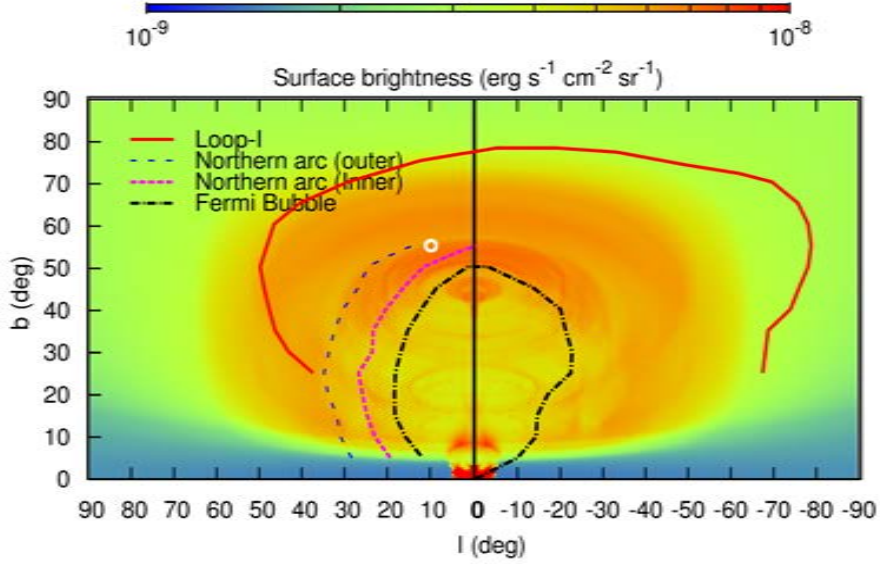


Figure 4.3: Simulated X-ray emission map in 0.7–2.0 keV band for the fiducial run (S10), over plotted with the observed edges of the Loop-I, northern arcs and the northern FB. The white circle represents the region where we have compared the estimated emission measure with the observations mentioned in the text .

(between $60^\circ < b < 50^\circ$, at $l \sim 0$). (3) The surface brightness is $\approx 6 \times 10^{-9} \text{ erg s}^{-1} \text{ cm}^{-2} \text{ sr}^{-1}$, also consistent with observations [Su et al. \(2010\)](#) who found $\sim 2 \times 10^{-8} \text{ erg s}^{-1} \text{ cm}^{-2} \text{ sr}^{-1}$. Although the contrast of the X-ray dip in the figure shown here is a bit less than observed, we note that the final observed counts through an instrument will depend on the details of spectral modelling. It is clear from figure 4.1 that the gas inside the bubble has a temperature ($\sim 2 \times 10^6 \text{ K}$), lower than the shell temperature ($\sim 3.5 \times 10^6$). Therefore, the intensity when folded through an instrument to estimate counts will show a higher contrast. These simulated features reasonably match the observed structure in X-ray images. Since the intensity of the ‘X-ray parachute’ mainly depends on the background CGM density, we use the emission measure (EM) of the parachute at $(l, b) \approx (10, 55)^\circ$ to match the EM of N1 point as observed by [Kataoka et al. \(2013\)](#) (shown by the white circle in Figure 4.3). Figure 4.4 shows the estimated values of the emission measure ($\text{EM} \equiv \int n^2 dl$) for 0.24–0.38 keV gas compared to the observed value of $0.05 \text{ cm}^{-6} \text{ pc}$ for different runs (see Table 4.2). The figure shows that only for the central densities of $2\text{--}3.5 \times 10^{-3} \text{ m}_p \text{ cm}^{-3}$, the estimated EM is close to the observed value. This, along with the surface brightness of the ‘X-ray parachute’ sets a constrain on the allowed background density of the CGM.

The different straight lines in figure 4.4 represent different values of \mathcal{L}/ρ_{h0} (this ratio determines the radius of the outer shock for a given time; see Eq. 4.9). These lines of constant \mathcal{L}/ρ_{h0} are also found to be crucial in determining the shape of the wind, and hence the projected shape within the contact discontinuity. For lower values of \mathcal{L}/ρ_{h0} , the opening angle of the wind is much smaller than observed in FB (we assume that the gamma-rays of FBs come from the free and the shocked wind, as we discuss later). For larger values of \mathcal{L}/ρ_{h0} , though the opening angle matches with the base of the FB, the extent of the wind (in l) at high latitudes exceed the observed width of the bubble. However, the shapes arising from the runs lying on $\mathcal{L}/\rho_{h0} = 2 \times 10^3 \times 10^{40} \text{ erg s}^{-1} \text{ m}_p^{-1}$

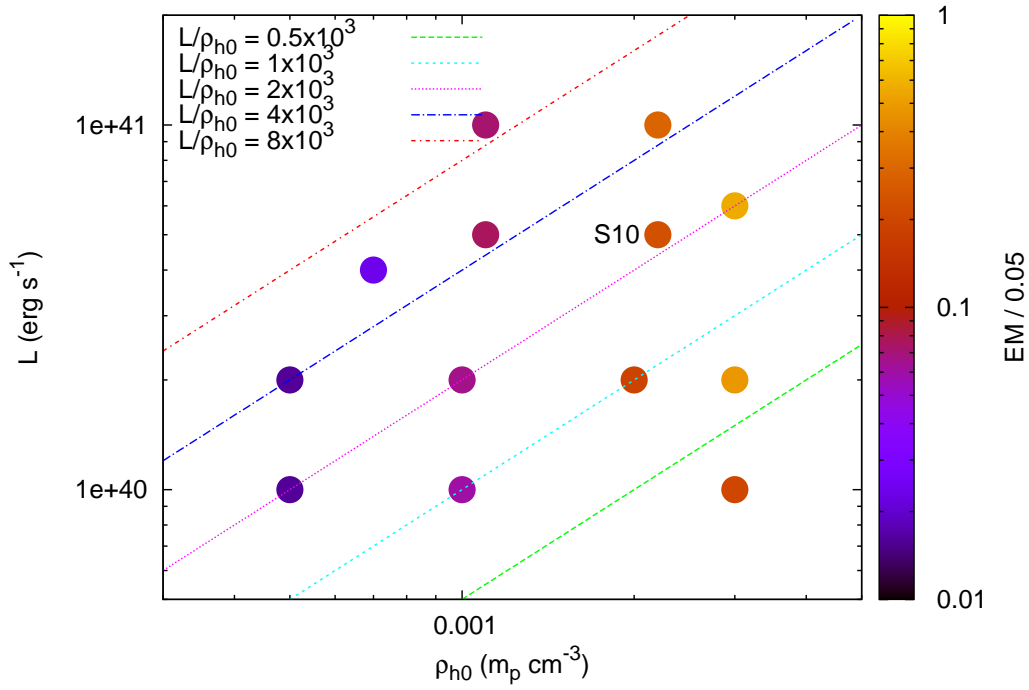


Figure 4.4: Comparison of the estimated emission measure (EM) of the 'X-ray parachute' with the observed value $0.05 \text{ cm}^{-6} \text{ pc}$. The filled circles represent the position of individual runs in parameter space (as mentioned in Table 4.2) and the colour of each point represents the value of $EM/0.05$. Different values of \mathcal{L}/ρ_{h0} in $10^{40} \text{ erg s}^{-1} m_p^{-1} \text{ cm}^3$ have been shown by different straight lines. The fiducial run has been shown by 'S10' in this Figure.

cm³ line have maximum similarity with the observed FB shape.

Therefore, the constraint on ρ_{h0} ($\approx 2 - 3.5 \times 10^{-3}$) from X-rays and the requirement for the FB shape leave us with a small parameter space in figure 4.4 which implies $\mathcal{L} \approx 5-7 \times 10^{40}$ erg s⁻¹. Since modelling of thermal X-rays is least uncertain as compared to the non-thermal radio and gamma-ray emission, we consider $\mathcal{L} = 5 \times 10^{40}$ erg s⁻¹ and $\rho_{h0} = 2.2 \times 10^{-3}$ m_p cm⁻³ for our Galactic wind model parameters to calculate microwave and γ -ray emission.

4.4.2 Microwave Haze

Microwave observations (23 GHz, with *WMAP and Planck*; Dobler & Finkbeiner 2008; Planck Collaboration et al. 2013) show emission from $|b| \lesssim 35^\circ$ region on either side of the plane, termed the ‘microwave haze’. Diffuse radio emission is also seen in the 408 MHz map (Haslam, C. G. T.; Salter, C. J.; Stoffel, H.; Wilson, 1982) where the emission traces the Loop-I feature. The 23-70 GHz emission spectrum shows a spectral index $\beta = 2.56$ (brightness temperature $T_b \propto \nu^{-\beta}$) which indicates the presence of an electron spectrum of spectral index $x = 2.2$ (Planck Collaboration et al., 2013). The 2.3 GHz observation also reveals polarised lobes and ridges in both hemispheres. The polarisation level in the ridges is 25–31%. The ridges in the north-east quadrant coincides with the FB edge and the x-ray shells, and it is found that the magnetic field is aligned with the ridges (Carretti et al., 2013). The low-frequency emission extends westward beyond the FBs in both hemispheres and the spectrum 2.3-23 GHz spectrum becomes softer as we go away from the Galactic center.

In order to estimate the emission from relativistic particles, we assume that the particle (either hadrons or leptons) energy density is a fraction of the *total* energy density of the gas (internal or thermal energy as well as the energy density due to fluid motion). This is expected in the case of internal shocks and turbulence in the gas, and due to *in situ* acceleration of particles from these shocks. As Figure 4.1 shows, the strong shocks that are likely to accelerate particles are traced by the shocked wind material which is the region inside the contact discontinuity (CD). Therefore, in order to trace the *freshly produced* accelerated particles, we use a tracer in the simulation that tracks the injected wind material from where most of the microwave/gamma-rays are emitted. Also, in order to avoid the disc material along the line of sight, we discard from our analysis the gas with a non-azimuthal velocity less than 20 km s⁻¹.

We can estimate the microwave emission in our model assuming synchrotron emission and that the cosmic ray (CR) energy density is given by $u_{\text{cr}} = \epsilon_{\text{cr}} u_{\text{gas}}$, where $u_{\text{gas}} = u_{\text{th}} + u_{\text{kin}}$ is the total energy density of the gas as discussed above. The CR electron energy density is assumed to be $u_{\text{cr,e}} = 0.05 u_{\text{cr}}$ as expected from the ratio $(m_e/m_p)^{(3-x)/2}$ for $x = 2.2$ (see, e.g., Persic & Rephaeli (2015)). This fixes the electron spectrum, $n(E)dE = \kappa E^{-x}dE$, where the normalisation constant κ is given by $\kappa = u_{\text{cr,e}}(x-2)/(m_e c^2)^{2-x}$ (assuming a lower cut-off of Lorentz factor ~ 1). The synchrotron emissivity, in the presence of a magnetic field B in the optically-thin limit, is

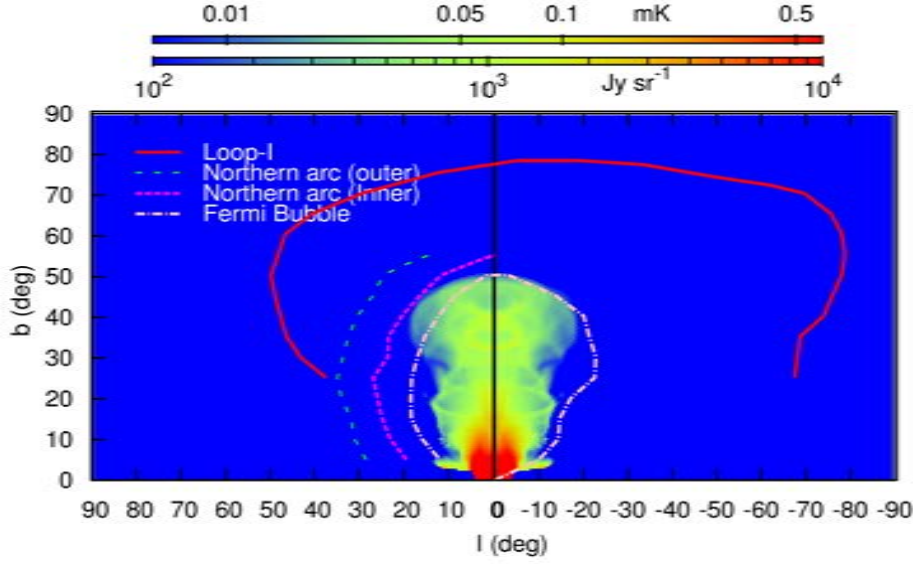


Figure 4.5: 23 GHz synchrotron emission (surface brightness) map for $\mathcal{L} = 5 \times 10^{40}$ erg s^{-1} and $\rho_{h0} = 2.2 \times 10^{-3}$ $\text{m}_p \text{ cm}^{-3}$ with $\epsilon_{\text{cr}} = 0.15$ and $\epsilon_B = 0.4$. The upper colourbar shows the brightness temperature in mK and the lower colourbar shows the brightness in units of Jy sr^{-1} .

(Eq. 18.18 in Longair (1981)).

$$\begin{aligned} \frac{\epsilon_{\nu}^{\text{syn}}}{\text{erg s}^{-1} \text{cm}^{-3} \text{Hz}^{-1}} &= 1.7 \times 10^{-21} a(x) \kappa B^{\frac{x+1}{2}} \\ &\times \left(\frac{6.26 \times 10^{18} \text{ Hz}}{\nu} \right)^{\frac{x-1}{2}}, \end{aligned} \quad (4.11)$$

where, $a(2.2) \approx 0.1$. For the magnetic field, we assume that the magnetic energy is also a fraction of the thermal energy and is given as $u_B = \epsilon_B u_{\text{gas}}$.

We therefore have the volume emissivity per unit solid angle as

$$\begin{aligned} \frac{J_{\nu}^{\text{syn}}}{\text{erg s}^{-1} \text{cm}^{-3} \text{Hz}^{-1} \text{sr}^{-1}} &= 2.6 \times 10^{-20} \epsilon_{\text{cr}} \epsilon_B^{0.8} p^{1.8} \\ &\times \left(\frac{23 \text{ GHz}}{\nu} \right)^{0.6}. \end{aligned} \quad (4.12)$$

where, we have taken $u_{\text{gas}} = (3/2) p$, and $p = p_{\text{th}} + 1/3 \rho v^2$ is the total pressure (thermal plus kinetic).

After calculating the surface brightness at 23 GHz from the FBs with $\epsilon_{\text{cr}} = \epsilon_B = 1.0$, we found it to be approximately 15 times larger than the observed value of 800 Jy sr^{-1} . This implies that

$$\epsilon_{\text{cr}} \epsilon_B^{0.8} \approx 1/15. \quad (4.13)$$

Note that we have an independent constrain on ϵ_{cr} because these same particles will also emit γ -rays. Assuming $\epsilon_{\text{cr}} = 0.15$, we get a constrain on the magnetic energy density that $\epsilon_B = 0.4$. This gives a magnetic field of strength $B = 3\text{--}5 \mu\text{G}$ considering $u_{\text{gas}} \approx 0.7\text{--}3.0 \times 10^{-12}$ erg cm^{-3} inside the bubble; thus, 23 GHz emission comes from

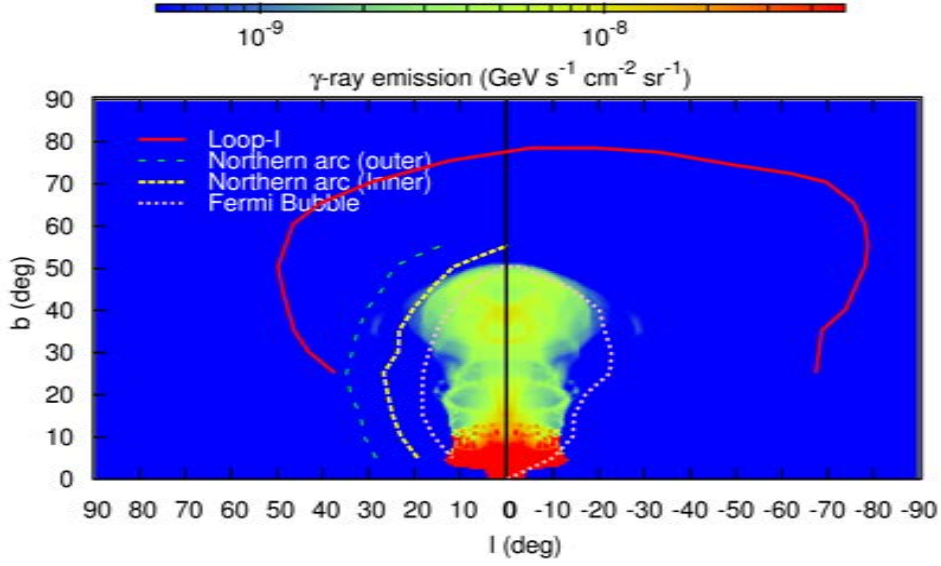


Figure 4.6: Hadronic γ -ray emission map (surface brightness) as seen from the solar system location. Over plotted are the edges of the observed emission maps.

electrons with $\gamma \approx 2 \times 10^4$. Notice that our estimate of magnetic field is somewhat lower than but consistent with other estimates (Su et al., 2010; Carretti et al., 2013; Crocker et al., 2015).

The surface brightness of the 23 GHz emission is shown in Figure 4.5 and is consistent with observations. We also notice that the emission fills up the whole bubble volume which is consistent with recent observation. *Planck* has detected microwave emission from the whole FB region, although the intensity is rather small above $\sim b \geq 40^\circ$ (see fig 9 of Planck Collaboration et al. (2013)), consistent with our results, given the uncertainties.

4.4.3 γ -ray

Observations show two γ -ray bubbles (1.0–50.0 GeV) on either side of the Galactic plane, being roughly symmetric about the plane. The northern bubble extends up to $b < 50^\circ$ and $|l| \lesssim 25^\circ$, which is almost same for the southern bubble. Another limb-brightened γ -ray feature extends up to 80° in b and $\pm 70^\circ$ in l in northern hemisphere and is known as Loop-I feature. The FB surface brightness is fairly uniform over the bubble and shows no limb brightening. The γ -ray spectrum of the FB is also flat ($dN/dE \sim E^{-2}$) and shows almost no softening with increasing height. The Loop-I feature, however, has a softer spectrum, $dN/dE \sim E^{-2.4}$, and this has led Su et al. (2010) to conclude that Loop-I is a part of the disc and has no connection with the bubble.

In order to estimate the γ -ray emission from the simulated bubble, we consider two possible emission mechanisms, hadronic and leptonic. Below we discuss them in detail.

4.4.3.1 Hadronic emission

In the hadronic model, cosmic ray (CR) protons undergo hadronic collisions with thermal gas protons and produce γ -ray via pion decay. The volume emissivity for this

emission in the Fermi-LAT band (1GeV-100GeV) can be written as

$$L^{pp} \simeq \frac{3}{2} \times \frac{1}{3} \times f_{\text{bol}} u_{\text{cr,p}} n_p \sigma_{pp} \kappa_{pp} C, \quad (4.14)$$

where, n_p is the gas proton number density, $u_{\text{cr,p}} \approx u_{\text{cr}}$, is the CR proton energy density, $f_{\text{bol}} \simeq 0.4$ is the fraction of the total luminosity that is emitted in the Fermi-LAT band. The factor $3/2$ corrects for the presence of heavy ions among the beam and target nuclei, $\sigma_{pp} = 4 \times 10^{-26} \text{ cm}^2$ is the corresponding interaction cross-section and $\kappa_{pp} = 0.5$ is the hadronic in-elasticity (Crocker et al., 2014).

Figure 4.6 shows the emission map in 1-100 GeV from hadronic collisions assuming $\epsilon_{\text{cr}} = 0.15$ as discussed in the previous section. The surface brightness is fairly uniform and fills the observed region of FB. However, the average intensity is only $\lesssim 1\%$ of the observed value of $1.4 \times 10^{-6} \text{ GeV s}^{-1} \text{ cm}^{-2} \text{ sr}^{-1}$ (Su et al., 2010) in this band.

4.4.3.2 Leptonic

In the leptonic model, CMB photons are inverse Compton scattered by relativistic electrons and produce γ rays.³ The required CR electron energy is 1–100 TeV to produce γ rays of 1-100 GeV. Therefore, the corresponding Lorentz factors of the electrons range from $\gamma = 2 \times 10^6$ to 2×10^7 . However, at such high γ values the electron spectrum would likely suffer a cooling break because of synchrotron and IC losses. Assuming a typical age of the electrons to be $t_{\text{age}} = 1.5 \text{ Myr}$, and considering the magnetic field to be $B = 4 \mu\text{G}$, as obtained in section 4.4.2, we get the Lorentz factor at the break to be $\gamma_b = 10^6$. Typically in a simple steady-state model for the evolution of the relativistic electron distribution function, the cooling break occurs at a γ for which the cooling time equals the age. However, here we are considering time-dependent particle acceleration in turbulence and internal/termination shocks, and the effective age of electrons can be much shorter than the FB age.

Since $\gamma = 10^6$ is close to the Lorentz factors needed for the leptonic emission to be in 1-100 GeV band, we consider a broken power law electron spectrum which has a spectral index $x_1 = 2.2$ (same as considered in synchrotron emission) below the break and the index drops by $\Delta x = 1$ after the break. The electron spectrum can be written as

$$n(\gamma) = \begin{cases} C \gamma^{-x_1} & \text{for } \gamma_l < \gamma \leq \gamma_b \\ C \gamma_b^{x_2-x_1} \gamma^{-x_2}, & \text{for } \gamma_b < \gamma \leq \gamma_h \end{cases} \quad (4.15)$$

where, $x_2 = x_1 + 1$ is the spectral index after the break, γ_l and γ_h are the lower and higher cut-off of the spectrum. The normalisation factor C can be written as

$$\begin{aligned} C &= \frac{u_{\text{cr,e}}}{m_e c^2} \left[\frac{\gamma_l^{2-x_1}}{x_1 - 2} + \frac{\gamma_b^{2-x_2}}{x_2 - 2} \right]^{-1} \\ &\approx \frac{u_{\text{cr,e}}}{m_e c^2} \frac{x_1 - 2}{\gamma_l^{2-x_1}}. \end{aligned} \quad (4.16)$$

³We do not consider up-scattering of UV and IR photons because CMB dominates far away from the galactic disc. A proper modelling of the γ -ray emission due to interstellar radiation field (ISRF) is beyond the scope of this chapter.

The output power per unit volume at an energy ϵ_1 can be calculated as (Eq. 7.28a in Rybicki & Lightman (1979))

$$\begin{aligned} \epsilon_1 \frac{dE}{dV dt d\epsilon_1} &= \frac{3}{4} c \sigma_T C \epsilon_1 \int d\epsilon \left(\frac{\epsilon_1}{\epsilon} \right) v(\epsilon) \\ &\times \left[\int_{\gamma_l}^{\gamma_b} \gamma^{-x_1-2} f \left(\frac{\epsilon_1}{4\gamma^2\epsilon} \right) d\gamma + \gamma_b \int_{\gamma_b}^{\gamma_h} \gamma^{-x_2-2} f \left(\frac{\epsilon_1}{4\gamma^2\epsilon} \right) d\gamma \right], \end{aligned} \quad (4.17)$$

where,

$$f(x) = 2x \log(x) + x + 1 - 2x^2, \quad \text{for } 0 < x < 1 \quad (4.18)$$

and for seed photons with a blackbody spectrum at temperature T_{cmb} ,

$$v(\epsilon) = \frac{8\pi}{h^3 c^3} \frac{\epsilon^2}{\exp(\epsilon/k_B T_{\text{cmb}}) - 1}. \quad (4.19)$$

Here we use $u_{\text{cr,e}} = 0.05 \times u_{\text{cr}} = 0.05 \epsilon_{\text{cr}} u_{\text{gas}}$ with $\epsilon_{\text{cr}} = 0.15$ (same as considered previously for synchrotron emission). The lower and the higher cut-off Lorentz factors are taken to be $\gamma_l = 1$ and $\gamma_h = \infty$. Eqn. 4.17 can be numerically integrated to give the resulting spectrum, which is shown in Figure 4.7. The spectrum shows a reasonable match with the spectra as observed by Su et al. (2010) and Ackermann et al. (2014). The figure also shows that the spectrum is consistent with the observations for γ_b ranging from 5×10^5 to 2×10^6 and therefore it is robust under small uncertainties in the magnetic field or age of the electrons. While the flux in 1-100 GeV decreases for a smaller γ_b , it can be boosted by the additional IC up-scattering of the ambient starlight.

We also show the leptonic emission map at 10 GeV in Figure 4.8. It shows a good match with the observed morphology of FBs. The surface brightness is also reasonably uniform over the region. Though the edge of the simulated bubble is not as smooth as observed, an introduction of magnetic field in the simulation can potentially make the bubble edge smoother.

4.5 Results: kinematics

It is important to study the kinematics of FBs in order to infer their origin, as it can give us crucial information about the speed of gas inside and around the bubbles. Recently, Fox et al. (2015) have detected ultraviolet absorption features in cold ($\sim 5 \times 10^4$ K) and warm gas ($\sim 10^5$ K) phases at line of sight velocities of -200 , $+130$ and $+250$ km s^{-1} towards quasar PDS 456 ($10.4^\circ, 11.2^\circ$). Using a simple model of biconical nuclear outflow, to obtain a line-of-sight velocity of ~ -200 km s^{-1} , they needed a cold/warm radial Galacto-centric outflow with velocity (v_{gsr}) $\gtrsim 900$ km s^{-1} . This is essentially because of the radial outflow assumption and the low inclination of the quasar sightline.

The velocity structure in our simulated FBs has a more complicated structure than the simple models studied by Fox et al. (2015). In our simulation, the cold/warm clouds are formed by thermal and Rayleigh-Taylor instabilities at the interface of the injected gas with the CGM (the contact discontinuity). The clouds formed at the conical surface of the contact discontinuity sometimes fall back due to the gravity (essentially a fountain

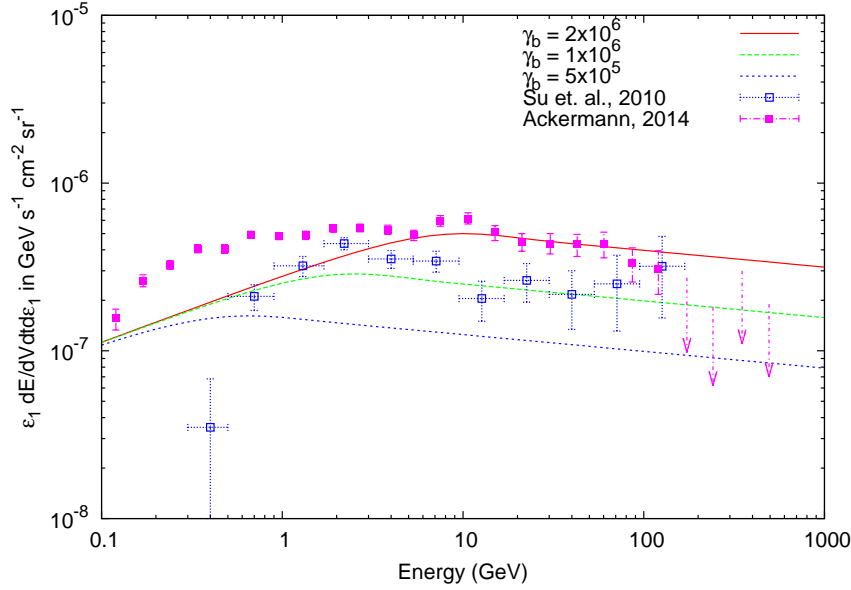


Figure 4.7: Output spectra for leptonic γ -ray emission (green dashed line). The blue empty squares and the magenta filled squares show the observed data points (Su et al., 2010; Ackermann et al., 2014), and the green (dashed) line shows the spectra calculated by us for $\gamma_b = 10^6$. The plot also shows the spectrum for $\gamma_b = 5 \times 10^5$ (blue dotted line) and $\gamma_b = 2 \times 10^6$ (red solid line) for comparison. Notice that we do not consider a high energy cutoff for the electron distribution, which can account for the lack of gamma ray emission beyond few 100 GeV.

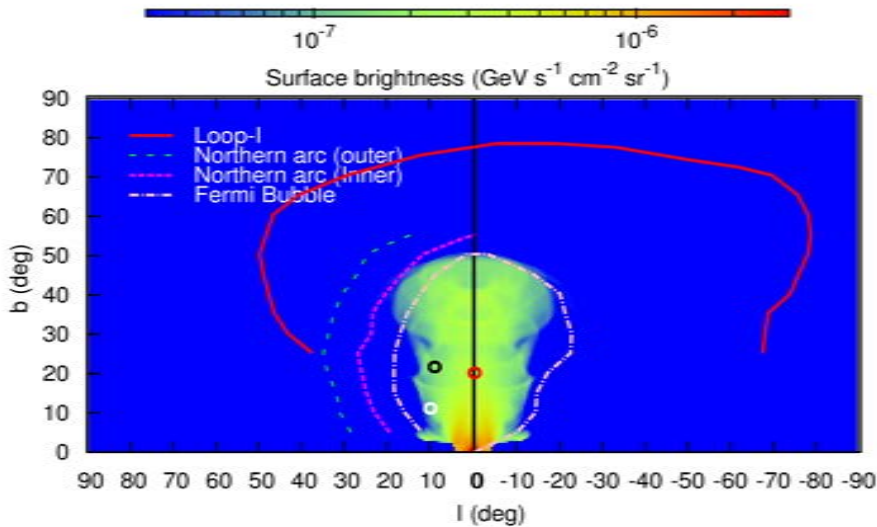


Figure 4.8: Leptonic γ -ray emission map at 10 GeV as seen from the solar system location. The red and black circles represent the regions for which the velocity histograms have been shown in Figure 4.10. The white circle is the one where Fox et al. (2015) have UV absorption data.

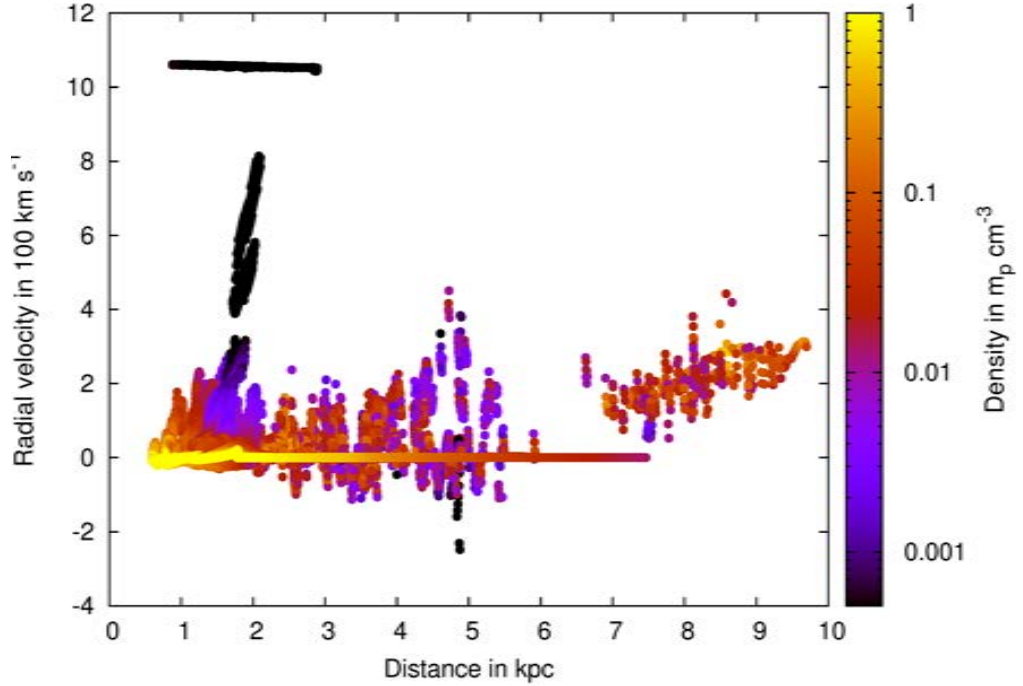


Figure 4.9: Position-Velocity diagram of the gas parcels with $T < 2 \times 10^5$ K. The colourbar represents the density of the gas parcels.

flow; Shapiro & Field 1976). However, the clouds at the top of the cone keep moving away from the centre because of the wind ram pressure. The low latitude cold/warm gas can have a wide angle and a large ($\sim 100 \text{ km s}^{-1}$) line-of-sight velocity because the clouds are following non-radial trajectories (e.g., see the S2 sequence of clouds in Fig. 12 of Sarkar et al. 2015a).

Figure 4.9 shows the position-velocity diagram as seen from the Galactic centre. It shows that along with the positive velocity components of the warm gas, there are gas parcels which have negative velocities extending up to -100 km s^{-1} . This infalling gas can contribute to the negative velocities as observed by Fox et al. (2015).

In figure 4.10, we show the line-of-sight velocity (v_{los}) histograms of the cold, warm and hot gas along two different lines-of-sights (shown by the black and red circles in Figure 4.8) that pass through the FB. We take into account the solar rotation velocity of $v_{\phi, \odot} = 220 \text{ km s}^{-1}$ for this calculation (see Appendix B.1 for more details). The central peak in all the histograms represent the stationary disc and halo gas. The upper panels clearly show that the v_{los} for the cold and warm gas can reach up to -150 km s^{-1} and $+200 \text{ km s}^{-1}$. We also show the velocity-histograms of the hot ($T > 10^6$ K) gas in the lower panel of Figure 4.10. Though the hot gas velocities extend all the way from -200 to $+600 \text{ km s}^{-1}$ for these two line of sights (LOS), the other LOSs show hot gas velocities extending from -500 to 700 km s^{-1} . Notice that though the hot gas in our simulation has high velocity ($\sim 1000 \text{ km s}^{-1}$) within the free wind region, the shape of the histograms differ from that of the high velocity gas considered by Fox et al. (2015). This is essentially because of the non-radial flow of hot gas induced by Kelvin-Helmholtz instability.

The above-mentioned results show that the kinematic signatures of our model are

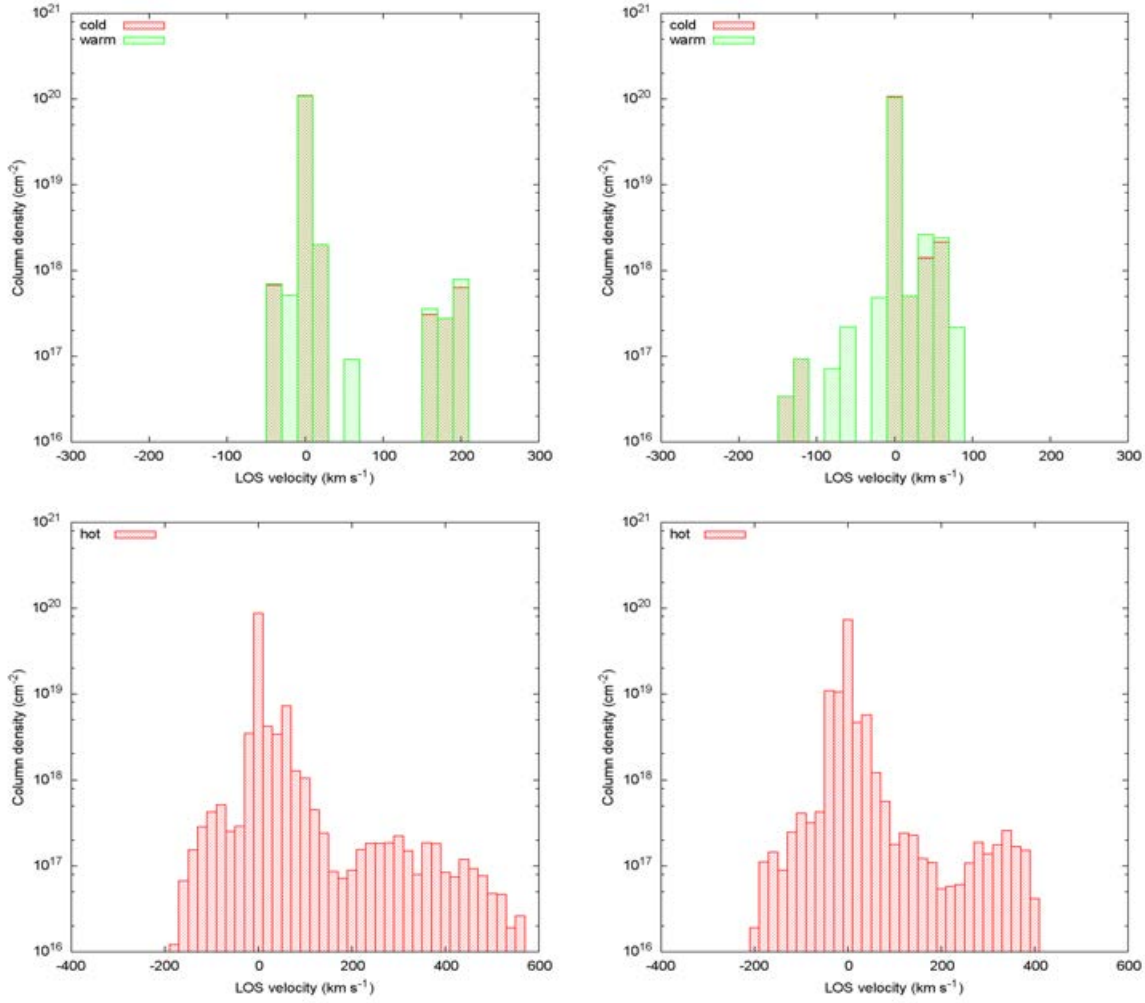


Figure 4.10: Velocity histograms of the gas along $(0^\circ, 20^\circ)$ in left panel and along $(9^\circ, 21.5^\circ)$ in right panel. X-axis represents the line of sight velocity and the y axis represents the $N(\text{HII})$ corresponding to that velocity. The upper panel shows the velocity histogram for cold ($T < 4 \times 10^4$ K) and for warm ($4 \times 10^4 < T < 2 \times 10^5$ K), whereas the lower panel shows for the hot gas ($T > 10^6$ K). The LOSs have been pointed out in Figure 4.8.

consistent with observations and one does not necessarily need cold/warm gas with velocities $\gtrsim 900 \text{ km s}^{-1}$.

4.6 Discussion

4.6.1 Diffusion of CRs

In this chapter, we have so far tracked CRs by using a tracer which confine them within the contact discontinuity (CD). In reality, CRs diffuse beyond the CD and produce extended γ -ray and synchrotron emissions. Since turbulence is not expected to be significant outside the CD, the *in-situ* acceleration of CRs becomes ineffective and the emission contains a signature of ageing in its spectrum. We can estimate this length scale over which the relativistic electrons diffuse before they lose their energy, by considering the diffusion coefficient to be (Gabici et al., 2007)

$$D(E, B) = 10^{28} \left(\frac{E}{10 \text{ GeV}} \right)^{1/2} \left(\frac{B}{3 \mu\text{G}} \right)^{-1/2}. \quad (4.20)$$

For electrons of energy $E \sim 1 \text{ TeV}$ moving in a magnetic field of $B \sim 10 \mu\text{G}$ (estimated from fluid compression at the forward shock), the length-scale of diffusion in $t_{\text{age}} = 1.5 \text{ Myr}$ (see §4.3.2) is $\sigma = \sqrt{6Dt_{\text{age}}} \approx 1.3 \text{ kpc}$. This implies that CR would diffuse up to $\sim 10^\circ$ beyond the CD at a height of 8 kpc. This extended emission can appear as 2.3 GHz radio lobe as observed by Carretti et al. (2013).

4.6.2 Note on Loop-I

The accelerated relativistic particles from the outer shock may also produce gamma-ray emission at the shock position. However, because of the absence of further acceleration mechanisms (*viz.* turbulence) behind the shock, the particles will lose their energy and may have a spectrum that is different from that of FB. In case of leptonic emission at the outer shock, the electrons lose their energy after $t_{\text{age}} = 1.5 \text{ Myr}$ giving rise to a faint gamma ray shell which can appear as a diffuse emission when viewed from the Solar vantage point. This may partially explain the observed emission from Loop-I feature.

Incidentally, we note that recent observations by Ackermann et al. (2014) (Fig. 13) have revealed a Southern counterpart of the Loop-I feature. This lends an additional support for the connection between the Loop-I and the FBs.

4.6.3 Kinematics of the cold/warm gas

The speed of the cold/warm gas is complex in nature as shown in Figure 4.9, ranging from -150 to $+1000 \text{ km s}^{-1}$. The density of the clouds, however, decreases with increasing velocity making them hard to detect. Moreover, very high velocity clouds may appear to be moving with low LOS velocity because of our vantage point. Therefore, even if star formation at the Galactic centre produces very high velocity clouds (VHVC), several factors can make them undetectable as VHVCs from the Solar vantage point. The $+1000 \text{ km s}^{-1}$ streak in the figure represents adiabatically expanding

free wind. Because of its cone-like geometry, the velocity dispersion along a line-of-sight can become large enough for a given column density that any absorption feature corresponding to the free wind may not be visible.

4.6.4 Effects of the injection geometry and CGM rotation

Although we have considered the injection region to be spherically symmetric with radius $r_{\text{inj}} = 60$ pc, star formation can occur in a region of complicated geometry as observed by [Molinari et al. \(2011\)](#). To understand the effect of different injection geometries, we have carried out the following set of runs for our fiducial value:

- spherically symmetric, with $r_{\text{inj}} = 40$ pc.
- spherically symmetric, with $r_{\text{inj}} = 100$ pc.
- axisymmetric (about $R = 0$ axis) disc-like injection region, with a radius $R = 110$ pc and midplane to edge height $h = 42$ pc ([Lacki, 2014](#)).
- axisymmetric ring-like injection region, with inner radius $R_{\text{in}} = 70$ pc, outer radius $R_{\text{out}} = 100$ pc and midplane to edge height $h = 50$ pc.
- spherically symmetric, with $r_{\text{inj}} = 60$ pc, same as the fiducial run but this time we have considered that the halo gas is also rotating with a speed equal to 10% of the stellar rotation speed at $z = 0$ at that R .

The other parameters, namely $\epsilon_{\text{cr}}, \epsilon_B, \gamma_b (= 10^6)$, have been kept fixed to those values mentioned in the text for the fiducial run. The projected leptonic γ -ray emission maps at 10 GeV for all the cases (at $t = 27$ Myr) have been shown in figure [B.2](#). The figures show that apart from a slight corrugation of the FB edge, the morphologies and intensities match quite well with each other. Therefore, the conclusions in this chapter are not affected significantly by our assumptions regarding the geometry of the star formation region and halo rotation.

4.6.5 Effects of CR and magnetic pressure

In our model, the magnetic and the CR energy densities are, respectively, 0.4 and 0.15 times the gas energy density. The addition of these forms of energy would surely increase the total energy content and hence the pressure inside the bubble. More so, because CRs and magnetic fields do not suffer significant radiation losses. Therefore, for the same bubble energetics the required SNe energy injection, and consequently, the SFR will decrease approx. by a factor of 1.5 if we consider a strong coupling of these nonthermal pressures with the gas. This can bring down the required SFR to $0.3 - 0.4 M_{\odot} \text{ yr}^{-1}$.

4.7 Summary

In this chapter, we have presented the results of numerical simulations of SNe driven outflows in our Galaxy, taking into account a gaseous disc ($T \simeq 10^4$ K) and halo gas

($T = 2.5 \times 10^6$ K), in order to explain the origin of the Fermi Bubbles and multi-wavelength features related to it. We injected continuous SNe energy at the Galactic centre for 50 Myr. We assumed *in situ* acceleration of relativistic particles inside the contact discontinuity. Our model can explain the gamma-ray emission and microwave haze as coming from the interior of the contact discontinuity via leptonic and synchrotron emission respectively. In addition, X-ray is emitted mostly by the shocked CGM. Given our vantage point at the Solar position, we considered the projection effects properly to calculate the morphology of the bubble. In order to understand the dynamics of the bubble, we have also studied the cold, warm and hot gas kinematics.

In our analysis, we have used the observed surface brightness in different bands in order to constrain the background CGM density, the star formation rate at the Galactic centre and the magnetic field inside the bubble, self consistently. We summarise the main results of this chapter below.

- The X-ray emission appears to have a parachute-like structure with a dip in intensity within the boundaries of the Fermi Bubbles. The surface brightness of the parachute is comparable to the observed value only if the central CGM gas density is taken to be $2\text{--}3.5 \times 10^{-3} \text{ m}_p \text{ cm}^{-3}$ and an extended CGM up to 100 kpc. Considering the morphological aspects of the Fermi Bubbles along with the CGM, the injected mechanical luminosity is found to be $5\text{--}7 \times 10^{40} \text{ erg s}^{-1}$ which corresponds a SFR $\approx 0.5\text{--}0.7 \text{ M}_\odot \text{ yr}^{-1}$.
- Assuming that a relativistic electron population of spectral index $x = 2.2$ gives rise to the microwave haze via synchrotron emission, we estimated the magnetic field inside the bubble to be $3\text{--}5 \mu\text{G}$ which is little lower but consistent with other estimations. This electron population diffuses out from the contact discontinuity and produces polarised radio emission as observed.
- Considering the above constrained CGM, SFR and the magnetic field, the γ -ray emission from the region inside contact discontinuity appears to have the shape and brightness comparable to observations.
- The speed of the cold ($T < 4 \times 10^4$ K) and warm ($4 \times 10^4 < T < 2 \times 10^5$ K) clumps can vary from -150 km s^{-1} to $+200 \text{ km s}^{-1}$ (warm), whereas, the hot ($T > 10^6$ K) gas have a higher dispersion in their velocities which range from ~ -500 to $+700 \text{ km s}^{-1}$. The kinematics of the cold/warm clumps appear to have the characteristics that are similar to recent observations. While [Fox et al. \(2015\)](#) argue for a large radial velocity outflow (e.g., associated with AGN-driven outflows) because of a small angle between the radial direction and the line of sights through low latitudes, [Figure 4.10](#) shows that we can obtain line-of-sight velocities consistent with observations because of non-radial trajectories and the negative radial velocities of entrained cold clumps without requiring large radial velocity of cold/warm gas.

To conclude, our work shows that star formation at the Galactic centre can give rise to the observed Fermi Bubbles and the multi-band structures related to it. Furthermore, modelling these structures can yield the basic Galactic parameters such as the hot CGM density and magnetic field and opens up a new window to study high energy interactions in the Milky Way.

Chapter 5

Origin of Fermi Bubbles: Clues from O VIII/O VII line ratio

Based on:

“Clues to the origin of Fermi Bubbles from O VIII/O VII line ratio” by Kartick C. Sarkar, Biman B. Nath and Prateek Sharma, 2017, *Mon. Not. R. Astron. Soc.*, 467, 3544 ([Sarkar et al., 2017](#))

We have seen in the previous chapter that it is possible for a supernovae-driven wind to produce the multi-wavelength features of the Fermi Bubbles. However, it is not clear whether these bubbles could also be produced by an activity at the Galactic centre black hole. The biggest uncertainty in modelling a black hole driven wind is the mechanical luminosity output and the duration over which the black hole was active. One way to estimate the mechanical luminosity and its duration is to probe the shock temperature from the bubbles using O VIII/O VII line ratio. We simulate both the supernovae-driven and black hole driven wind and compare their synthetic O VIII/O VII line ratios from our simulations to the observed ones. This helps us to constrain the age of the Fermi Bubbles and the mechanical luminosity required to produce these bubbles.

Main Results

- Our results suggest that independent of the driving mechanisms, a low luminosity ($\mathcal{L} \sim 0.7 - 1 \times 10^{41} \text{ erg s}^{-1}$) energy injection best reproduces the observed line ratio for which the shock temperature is $\approx 3 \times 10^6 \text{ K}$.
- We estimate the shock velocity to be $\sim 300 \text{ km s}^{-1}$ for a weak shock. The corresponding estimated age of the Fermi bubbles is $\sim 15 - 25 \text{ Myr}$. Such an event can be produced either by a star formation rate of $\sim 0.5 \text{ M}_{\odot} \text{ yr}^{-1}$ at the Galactic centre or a very low luminosity jet/accretion wind arising from the central black hole.
- Our analysis rules out any activity that generates an average mechanical luminosity $\gtrsim 10^{41} \text{ erg s}^{-1}$ as a possible origin of the Fermi Bubbles.

5.1 Introduction

The discovery of Fermi Bubbles (FBs) (Su et al., 2010; Ackermann et al., 2014) has given a boost for studying the interaction of Galactic wind and the circum-galactic medium (CGM) of the Milky Way (MW). They are also excellent laboratories to study high energy astrophysics phenomena in such systems as they produce radiation ranging from radio to gamma-rays. However, the dynamical and spectral origin of these bubbles still remain debatable even after ~ 6 years of their discovery.

The dynamical models of the FBs can be divided mainly into two categories. First, AGN driven models in which the bubbles originate from a past accretion activity of the MW central black hole over a time scale of 3–12 Myr, with a luminosity of $\sim 2 \times 10^{41} - 10^{43} \text{ erg s}^{-1}$, either via an accretion wind (AGNW) (Zubovas et al., 2011; Zubovas & Nayakshin, 2012; Mou et al., 2014, 2015) or via a jet (Guo & Mathews, 2012; Yang et al., 2012) from the Galactic centre black hole. Second, a star formation (SF) driven wind model (SFW) in which the bubbles originate from supernovae activity due to star formation at the centre of our Galaxy (Lacki, 2014; Crocker et al., 2015; Sarkar et al., 2015b). Based on the star formation rate (SFR) at the centre, the age of the bubbles has been estimated to range from ~ 25 Myr (Sarkar et al., 2015b, hereafter, S15) to ~ 200 Myr (Crocker et al., 2015).

Although the observations suggest that the current accretion rate of the Galactic centre black hole (GCBH) is $\sim 10^{-9} - 10^{-7} M_{\odot} \text{ yr}^{-1}$ (Quataert & Gruzinov, 2000; Agol, 2000; Yuan et al., 2003; Marrone et al., 2006) corresponding to a mechanical luminosity of $\sim 5 \times 10^{36-38} \text{ erg s}^{-1}$, it has been suggested that it could have been several orders of magnitude higher in the past (Totani, 2006). On the other hand, infra-red observations suggest that the current SFR is $\approx 0.1 M_{\odot} \text{ yr}^{-1}$ (Yusef-Zadeh et al., 2009), compared to the rate of $\approx 0.3 M_{\odot} \text{ yr}^{-1}$ required to produce the bubbles (Sarkar et al., 2015b).

The spectral models of the FBs can also be divided into mainly two types. First, the hadronic models, in which the gamma-rays are emitted via interactions between cosmic ray (CR) protons and gas phase protons (Crocker & Aharonian, 2011; Crocker, 2012; Mou et al., 2014; Crocker et al., 2015; Mou et al., 2015). Second, the leptonic models, in which low energy photons (either cosmic microwave background or interstellar radiation field) are energised *in situ* by high energy cosmic ray electrons to produce gamma rays (Su et al., 2010; Mertsch & Sarkar, 2011; Sarkar et al., 2015b).

While modelling the gamma rays requires knowledge of the local cosmic ray (CR) energy density, magnetic field and gas density, and involves some assumptions about the acceleration processes and diffusion of the CRs, the modelling of the bubbles is much simpler in X-rays as it involves only the local gas density and its temperature. From the lack of X-ray emission inside the bubbles it has been suggested that these bubbles are under-dense compared to the surroundings. However, measuring the density inside and outside the bubbles requires a careful fitting of the emission or absorption spectra.

An ideal place to measure the spectra would be the northern polar spur (NPS) where the shell is X-ray bright. However, there have been debates over the actual distance of the NPS. Early observations suggested that the NPS can be a nearby low density bubble created by the stellar wind from the Scorpio-Centaurus OB association or could be a supernova remnant situated at a distance of a few hundred pc (Berkhuijsen et al., 1971). Using X-ray observations Sofue (1994); Snowden et al. (1995); Lallement et al.

(2016), however, found that the NPS feature is heavily absorbed towards the Galactic plane requiring a hydrogen column density of $\sim \text{few} \times 10^{21} \text{ cm}^{-2}$ which makes it unlikely to be a nearby feature. Recent observations using *Suzaku* and *XMM-Newton* also found that the spectra can be better explained if the NPS feature is of the ‘Galactic centre origin’ (see section 4.3 of Kataoka et al. (2013) for a detailed discussion). Another recent observation of OVIII Ly- α to Ly- β ratio by Gu et al. (2016) also supported the ‘Galactic centre origin’ of the NPS (Sofue, 1977, 2000; Bland-Hawthorn & Cohen, 2003; Sarkar et al., 2015b; Sofue et al., 2016). Also it would be a *dramatic coincidence* that the inner edge of the NPS traces the outer edge of the FBs even at high latitudes if the NPS is not related to the FBs.

Individual pointings towards NPS, therefore, have been used several times to estimate the post shock temperature of the FBs. Observations by Snowden et al. (1995); Kataoka et al. (2013); Gu et al. (2016) suggested that the temperature of the NPS is $\sim 0.25 - 0.3 \text{ keV}$ corresponding to a Mach number (\mathcal{M}) of ~ 1.5 , considering the halo temperature $\approx 2 \times 10^6 \text{ K}$ (estimated from the OVIII to OVII line ratio (Miller & Bregman, 2015)). Not only at the NPS, absorption study of OVII lines towards 3C 273, $\approx (-60^\circ, +60^\circ)$, also suggests a shock velocity of $\approx 200\text{--}300 \text{ km s}^{-1}$ (Fang & Jiang, 2014). These suggest a star formation driven or a low luminosity AGNW driven origin for the FBs (since the stronger AGNW would produce a stronger shock with $\mathcal{M} \gg 1$). However, in a recent observation of the OVIII to OVII line intensity ratio Miller & Bregman 2016, (hereafter, MB16) found that the sight-lines passing through FBs and the surroundings (except the NPS) have a temperature $\approx 5 \times 10^6 \text{ K}$. This led them to conclude that the shock is because of an AGN activity at the Galactic centre and the age of the FBs is $\sim 4 \text{ Myr}$ (see also Nicastro et al. (2016)). This differs from other estimates of a lower temperature and a weaker shock, and therefore a longer age of the FBs.

In this paper, we perform 2D hydrodynamical simulations of both star formation driven and accretion wind driven bubbles in a realistic MW gravity and a self consistent halo gas which is also close to the observed density distribution. We generate projected OVIII to OVII line intensity maps and ratio towards the FBs for a range of injected luminosities and compare them with the observations of MB16. Based on our simulated intensity maps, we constrain the age of the FBs and the strength of the star formation or the accretion wind/ jet activity at the Galactic centre. We also discuss the effects of conduction and the electron-proton equilibration time-scale on our results.

The paper is organised as follows. Section 5.2 discusses the choice of dark matter and disc potential, and the hydrostatic hot halo gas. The simulation details and other code parameters are explained in section 5.3. In section 5.4 we discuss the tools for projecting our 2D simulation results into a surface brightness map of OVIII to OVII line ratio at the Solar location. We present our results in section 5.5 and finally discuss the implications of the results in section 5.6.

5.2 Galactic halo distribution

One issue while modelling the FBs is the density and temperature distribution of the Galactic halo gas which carries crucial information about the soft X-ray background and also determines the shape and speed of any shock travelling through it. Because

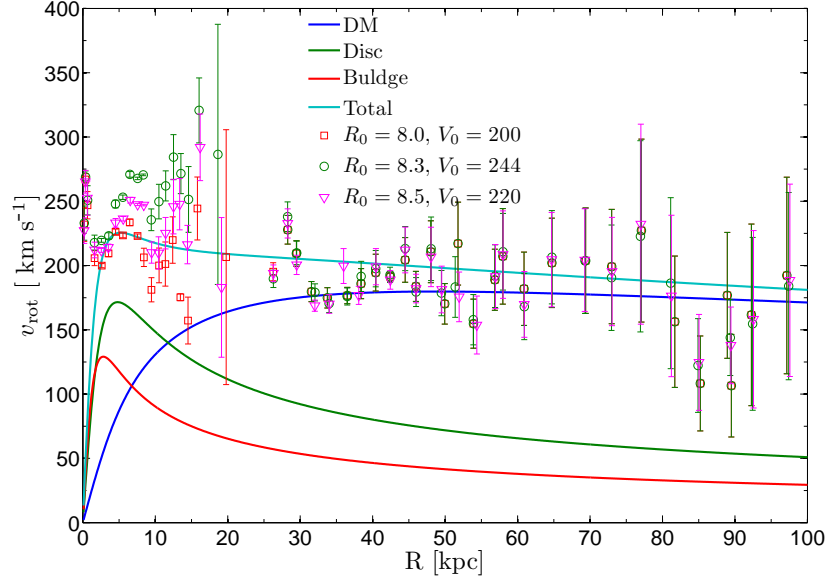


Figure 5.1: Rotation curve for the assumed gravitational fields for the parameters given in table 5.1. Data points from [Bhattacharjee et al. \(2014\)](#) have been shown with the errorbars. Different color of the data points represent assumed Solar distance from the Galactic centre (R_0 in kpc) and Solar rotation velocity (V_0 in km s^{-1}).

of our off-centred location, which is ~ 8.5 kpc away from the Galactic centre, it is in principle possible to determine the density distribution of the halo. However, there is a split in the opinion as to the correct density distribution. Based on ram pressure stripping of the dwarf satellites, the density has been estimated to be $\sim 1.3\text{--}3.8 \times 10^{-4} m_p \text{ cm}^{-3}$ within 50–90 kpc ([Gatto et al., 2013](#)), whereas, based on the distribution of the OVII and OVIII lines, [Miller & Bregman \(2015\)](#) find

$$n(r) = n_0 \left(1 + (r/r_c)^2\right)^{-3\beta/2} \quad (5.1)$$

with $\beta = 0.5$, $n_0 r_c^{3\beta} = 1.35 \times 10^{-2} \text{ cm}^{-3} \text{ kpc}^{3\beta}$ and $r_c < 5$ kpc, which predicts a higher density at the same distance range. A probable solution is that the metallicity of the halo is gradually decreasing with radius. Therefore, a higher density is not apparent in OVII or OVIII line emission ([Troitsky, 2017](#)). However, there is much to be worked out before making any firm conclusion.

In this paper we assume that the hot halo gas (isothermal at temperature, $T_{\text{halo}} = 2 \times 10^6$ K) is in hydrostatic equilibrium with the gravity of the dark matter, the disc stars and the bulge. For the dark matter, we use NFW gravity ([Navarro et al., 1996](#)), with an added core to ensure finite dark matter density at $r = 0$,

$$\Phi_{\text{DM}} = -\frac{GM_{\text{vir}}}{f(c)} \frac{\log\left(1 + \sqrt{r^2 + d^2}/r_s\right)}{\sqrt{r^2 + d^2}}. \quad (5.2)$$

Here, M_{vir} is the dark matter mass, $f(c) = \log(1 + c) - c/(1 + c)$ with c as the concentration parameter of the dark matter distribution, r_s is the scale radius, d is the core radius. For the disc gravity, we use the Miyamoto & Nagai potential ([Miyamoto](#)

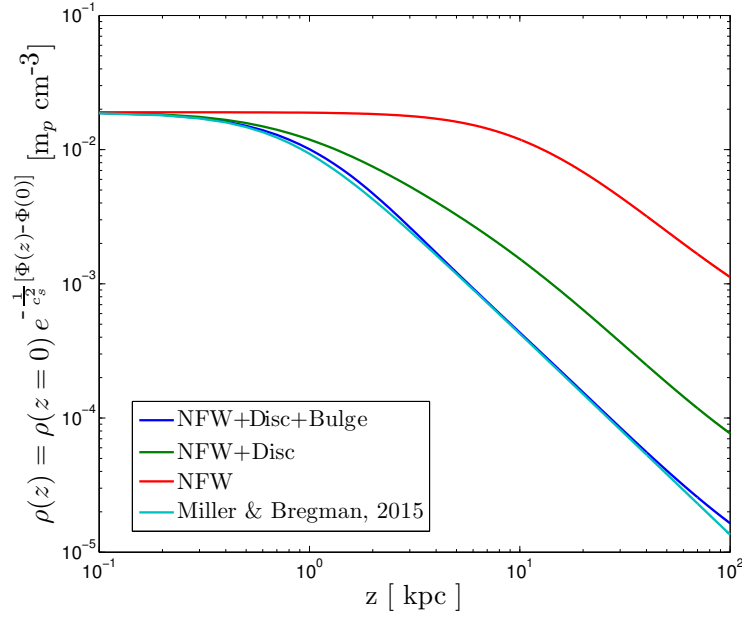


Figure 5.2: Equilibrium density distribution of the halo gas (Eq. 5.5) for the parameters given in table 5.1. The red curve shows the distribution in case of only NFW potential, green curve shows the distribution if the stellar disc is added, blue curve shows the distribution once all the components have been added together. The cyan curve shows the best fitting halo distribution from Miller & Bregman (2015).

& Nagai, 1975)

$$\Phi_{\text{disc}} = -\frac{GM_{\text{disc}}}{\sqrt{R^2 + (a + \sqrt{z^2 + b^2})^2}}, \quad (5.3)$$

where, M_{disc} is the disc mass, R and z are, respectively, the cylindrical radius and height, a and b represent the scale radius and scale height for the disc gravity. To make the gravity realistic near the Galactic centre, we also add a bulge potential of the form

$$\Phi_{\text{bulge}} = -\frac{GM_{\text{bulge}}}{\sqrt{r^2 + a_b^2}}, \quad (5.4)$$

where, a_b is the scale radius for the bulge.

The hydrostatic density distribution for the combined gravity, $\Phi = \Phi_{\text{DM}} + \Phi_{\text{disc}} + \Phi_{\text{bulge}}$ can, therefore, be written as

$$\rho(R, z) = \rho(0, 0) \exp\left(-\frac{1}{c_s^2} (\Phi(R, z) - \Phi(0, 0))\right), \quad (5.5)$$

where, $\rho(0, 0)$ is the density at $r = 0$ and $c_s = \sqrt{k_B T / \mu m_p}$ is the isothermal sound speed at temperature T (for a detailed discussion, see Sarkar et al. (2015a)). However, note that unlike S15, we do not use a rotating cold disc component as our focus is to study the interaction of the wind and the halo gas, in particular the outer shock properties. The interaction of the wind with the disc gas affects the formation of cold

parameters	values
$M_{\text{vir}}(M_{\odot})$	1.2×10^{12}
$M_{\text{disc}}(M_{\odot})$	6×10^{10}
$M_{\text{bulge}}(M_{\odot})$	2×10^{10}
$T_{\text{halo}} \text{ (K)}$	2×10^6
c	12
$r_s \text{ (kpc)}$	21.5
$a \text{ (kpc)}$	3.0
$b \text{ (kpc)}$	0.4
$d \text{ (kpc)}$	6.0
$\rho_c(0,0) \text{ (m}_p\text{cm}^{-3}\text{)}$	1.9×10^{-2}

Table 5.1: Parameters used for the mass model of our Galaxy. The assumed mass for different components are roughly consistent with the measurements by [McMillan \(2011, 2017\)](#).

clumps. These cold clumps, however, will not affect the observed OVII and OVIII properties.

Figure 5.1 shows the rotation velocity on $z = 0$ plane for the parameters given in table 5.1. For comparison with the observations, data from [Bhattacharjee et al. \(2014\)](#) are shown in the same figure. It shows an excellent consistency with the observed rotation curve of the Galaxy.

The gas density distribution that is in hydrostatic equilibrium with the given gravity (Eq. 5.5) is shown in figure 5.2. The figure also shows the effects of adding all the gravity components together. In fact, for the given parameters, the equilibrium density distribution shows an excellent match with the standard β -model obtained by [Miller & Bregman \(2015\)](#) (equation 5.1 and shown by the cyan line in figure 5.2) with $\beta = 0.5$ and $r_c = 0.8$ kpc. Therefore, the hydrostatic equilibrium of MW halo gas distribution can be naturally explained by the total gravitational fields of the MW.

5.3 Simulation details

The simulations have been performed in 2-dimensional spherical coordinates using Eulerian grid code PLUTO-v4.0 ([Mignone et al., 2007](#)). The computation box extends till 15 kpc in the radial direction and from 0 to $\pi/2$ in the θ -direction. The box has been divided into 256×256 grid cells with uniform grid spacing in both the directions. The inner boundary of the radial direction has been set initially to the static distribution and the outer boundary condition is set to outflow. Both the θ -boundaries have been set to reflective type.

While the injection of AGN and stellar mechanical energy into the ISM differ in detail, we use simplified models for them, roughly valid at the scales of the CGM. While stellar feedback has a lower velocity and is injected at a larger scale (~ 100 pc), AGN wind velocity is much faster and the injection radius is smaller (~ 10 pc). The essential difference between the two is that the latter have a smaller mass loading and higher velocity. The two broad classes of the models discussed here can therefore be termed as SF/low-velocity wind model and AGN/high-velocity wind model.

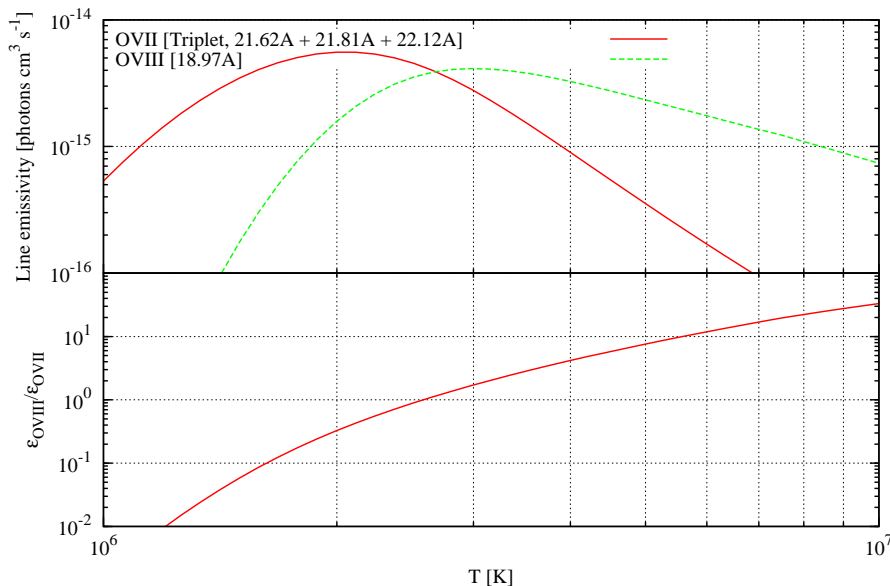


Figure 5.3: Top panel: Temperature dependence of emissivities of OVII and OVIII lines in units of photons $\text{s}^{-1} \text{cm}^3$ from CLOUDY-C13.04. Bottom panel: Temperature variation of the OVIII to OVII line ratio. The emissivities obtained here are for per unit hydrogen density.

5.3.1 Star formation driven wind (SFW)

In case of the star formation driven winds, the energy at the base of the wind is mostly thermal and gets deposited into ~ 100 pc region. However, in the presence of the interstellar medium (ISM) disc, the outgoing wind gets collimated and forms a biconical shape. The amount of collimation depends on the rate at which the energy is being injected from the SNe and the density and pressure structure of the ISM. Understanding the detailed structure of this component in the central region, as it was at the time of launching the winds, is difficult to do. Since our aim is to study the outer shock strength for a range of mechanical luminosities, we avoid these issues and consider that the wind has been somehow collimated by the ISM. Therefore, we inject SNe energy at the inner boundary within some opening angle. We also tune the opening angle of the energy and mass injection for each case to roughly match the shape of the contact discontinuity with the FBs. The opening angles for individual runs and other information is provided in table 5.2.

The inner boundary in this case is chosen to be at $r_{\text{ej}} = 100$ pc, which is also the point where we inject the SNe ejected mass and energy. This radius is assumed to be the transonic point of the wind¹. Therefore, the velocity at the base (v_{ej}) is kept half of the free wind velocity ($\approx 1000\sqrt{\alpha/\eta}$ km s^{-1}) (Chevalier & Clegg, 1985). Here,

¹The choice of this radius is not crucial for the results presented here. However, for the sake of completeness, we compare our results for different injection radii, i.e. different transonic radii in appendix C.1

$\alpha = 0.3$ is the assumed heating efficiency of the supernovae (SNe) and $\eta = 0.3$ is the mass loading factor from stellar feedback (Leitherer et al., 1999). The pressure is set to be $p = \rho_{\text{ej}} v_{\text{ej}}^2 / \gamma$, where $\gamma = 5/3$ is the adiabatic index and ρ_{ej} is the density at the base. The mechanical luminosity and the mass injection rate in this case can be written in terms of α and η as

$$\mathcal{L} \approx 3 \times 10^{41} \alpha \text{ SFR}_{\text{M}_{\odot} \text{ yr}^{-1}} \text{ erg s}^{-1} \quad (5.6)$$

and

$$\dot{M}_{\text{inj}} = \eta \text{ SFR}, \quad (5.7)$$

respectively. Therefore, density at the base can be written as

$$\rho_{\text{ej}} = \frac{\mathcal{L}}{2\Omega r_{\text{ej}}^2 v_{\text{ej}}^3}, \quad (5.8)$$

where, Ω is the solid angle within which the mass and energy are injected.

5.3.2 Accretion wind (AGNW)

For AGN feedback, the spherical accretion wind is likely to be collimated by the presence of the central molecular zone (CMZ) which is extended till ~ 250 pc in radial direction and ~ 50 pc in vertical direction. Following Zubovas et al. (2011); Mou et al. (2014), we model the CMZ to be a disc-like structure on the $z = 0$ plane having inner radius of 80 pc and outer radius of 240 pc. The height to radius ratio (H/R) for the CMZ is set to be H/R = 0.25. We have also checked for H/R = 0.15, but the results are not affected by this change. The CMZ is in local pressure balance with the hot halo and is rotationally supported by its azimuthal velocity $v_{\phi} = \sqrt{R \frac{d}{dR} \Phi(R, 0)}$. The density of the CMZ has been kept constant at $50 m_{\text{p}} \text{ cm}^{-3}$ which means that the total CMZ mass considered is $\sim 10^8 M_{\odot}$, close to the observed value. The CMZ in our set up admittedly is not in exact equilibrium with the surroundings because of unbalanced forces in z-direction. The current set up, however, is able to hold up the CMZ in its original position for more than 40 Myr.

The wind for this case has been launched spherically at $r_{\text{ej}} = 20$ pc with a velocity $v_{\text{ej}} = 0.05c$, where c is the speed of light in vacuum. The wind is considered to be dominated by kinetic energy and therefore, the density at the base is set to be $\rho_{\text{ej}} = 2\mathcal{L}/\Omega r_{\text{ej}}^2 v_{\text{ej}}^3$ for a mechanical luminosity of \mathcal{L} .

5.4 Analysis Tools

5.4.1 Projection tool

Since we are at the Solar position, ≈ 8.5 kpc away from the Galactic centre, which is roughly comparable to the height (~ 10 kpc) and width (~ 4 kpc) of FBs, the projection effects are important. A special purpose code, called Projection Analysis Software for Simulations (PASS)², has been written to project the 2D simulation data to a viewer

²PASS is made public and is available for download at http://www.rri.res.in/~kcsarkar/pages/about_me/codes.html

Table 5.2: List of runs and the parameters used in these runs.

Name	Type	Luminosity (erg s ⁻¹)	Half opening angle
S5e40	SFW	5×10^{40}	45°
S7e40	SFW	7×10^{40}	45°
S1e41	SFW	10^{41}	45°
A5e40	AGNW	5×10^{40}	180°
A1e41	AGNW	10^{41}	180°
A1e42	AGNW	10^{42}	180°

from the Solar location (assuming axisymmetry). It can also project an 1D profile into a 2D sky map, assuming spherical symmetry of the profile. The surface brightness along any line of sight (l, b) is calculated as

$$I(l, b) = \frac{1}{4\pi} \int_{\text{los}} n^2 \varepsilon(T) dx \quad \text{erg s}^{-1} \text{ cm}^{-2} \text{ Sr}^{-1}, \quad (5.9)$$

where, n is the particle density and $\varepsilon(T)$ is the emissivity (erg s⁻¹ cm³) at any local point along the line of sight (LOS). It can also produce mock X-ray spectra along different LOSs assuming plasma emission code MEKAL (Mewe-Kaastra-Liedahl). Since our simulation box only extends till 15 kpc, to produce realistic emission maps, we consider the density distribution extending till 250 kpc, and include a local bubble centred at Sun with a radius of 200 pc, density of $4 \times 10^{-3} m_p \text{ cm}^{-3}$ and a temperature of $= 1.2 \times 10^6$ K following MB16.

5.4.2 Oxygen emission lines

We assume that the plasma is in collisional ionisation equilibrium at all temperatures $\gtrsim 10^4$ K. We can therefore obtain the density of different ionisation levels given the metallicity and temperature. The line intensity for any species X can be obtained by assuming the total gaseous number density n and emissivity $\varepsilon(X, T)$. In the present case we will consider only two of the ionisation levels of oxygen, *viz.* OVII and OVIII among many other ionisation species present in the medium at that temperature. Therefore, the emissivities considered here will be $\varepsilon_{\text{OVII}}$ and $\varepsilon_{\text{OVIII}}$. These emissivities have been obtained from CLOUDY-C13.04 (Ferland et al., 2013) and are described in figure 5.3. It is clear from the figure that the OVIII to OVII line ratio is sensitive to the temperature, making it a very useful for temperature diagnostics in the range of 10^6 – 10^7 K.

5.5 Results

Figure 5.4 shows the evolution of density and temperature for the AGNW and SFW models. Within the opening angle, they show a typical structure of the wind blown bubble containing free wind, shocked wind and shocked halo gas (Weaver et al., 1977). Note that, the free wind region in case of AGNW is very small and not visible in the density plot because of the colour bar. In a typical wind scenario, the reverse

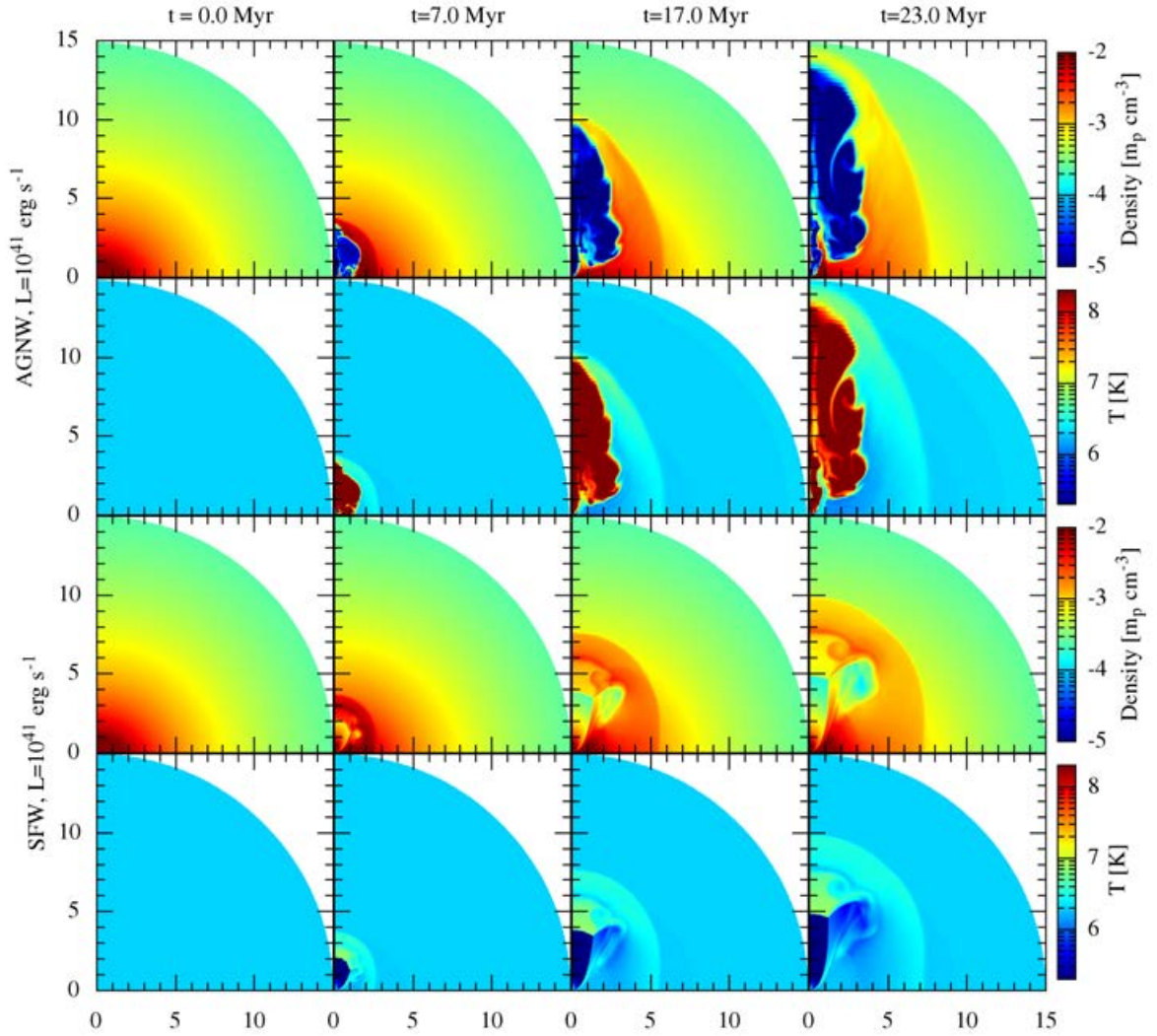


Figure 5.4: Evolution of density and temperature contours for AGNW and SFW cases. Top two panels represent evolution of an accretion driven wind corresponding to luminosity $\mathcal{L} = 10^{41} \text{ erg s}^{-1}$, whereas, bottom two panels represent the evolution of a SF driven wind of luminosity $\mathcal{L} = 10^{41} \text{ erg s}^{-1}$ ($\text{SFR} = 1 M_{\odot} \text{ yr}^{-1}$). The X-axis represents the on-plane distance R [kpc], and the Y-axis represents the vertical distance, z [kpc], from the Galactic disc.

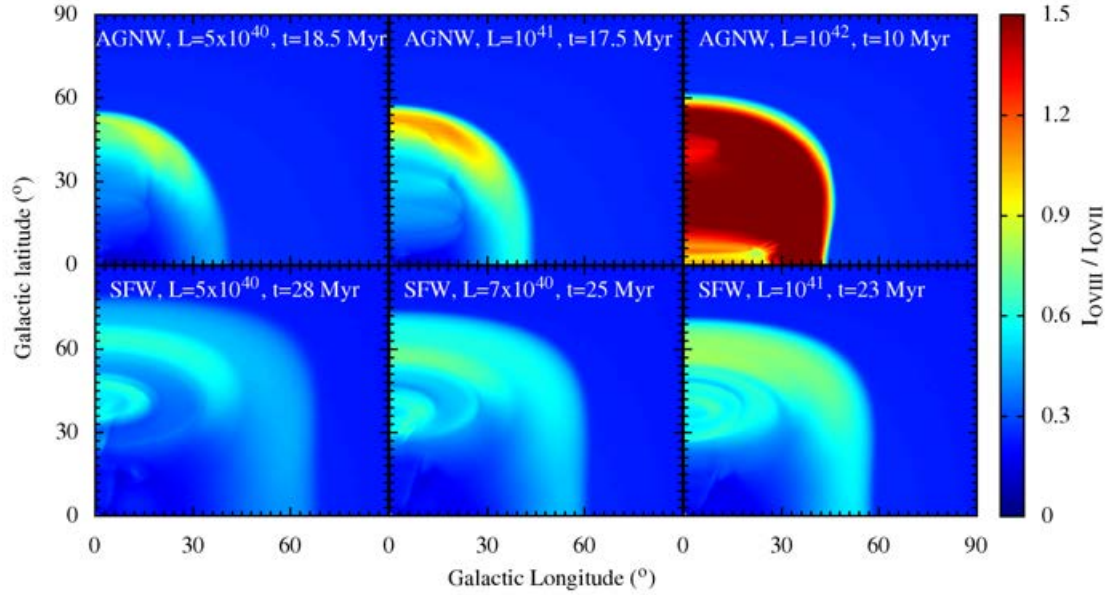


Figure 5.5: Simulated OVIII to OVII line ratio map for all the runs mentioned in table 5.2. The upper panel shows the ratio for AGNW cases and the lower panel shows for SFW cases. The maps are obtained at $t = t_{\text{fb}}$, when the contact discontinuity reaches $b \approx 50^\circ$ for each case.

shock appears when the wind ram pressure balances the shocked halo pressure. In a spherically symmetric case, the reverse shock position can be written as (see equation 12 of Weaver et al. (1977))

$$r_{\text{rs}} \propto \mathcal{L}^{3/10} \rho_0^{-3/10} v_w^{-1/2} t^{2/5}, \quad (5.10)$$

where \mathcal{L} is the mechanical luminosity and v_w is the free wind velocity, ρ_0 is the constant background density and t is the time. Here, we have assumed the mass injection rate, $\dot{M} = 2\mathcal{L}/v_w^2$. It is, therefore, clear that the reverse shock in AGNW ($v_w = 0.05c$) will be much closer to the centre compared to the SFW for the same luminosity.

One important difference between the AGNW and SFW scenarios is the temperature of the shocked wind. For AGNW, it is much higher ($T_{\text{sw}} \gtrsim 10^8\text{K}$) compared to the SFW ($T_{\text{sw}} \sim 10^7\text{K}$), and the density in AGNW case is much lower ($\rho_{\text{sw}} \sim 10^{-5} m_{\text{p}} \text{cm}^{-3}$) compared to the SFW case ($\rho_{\text{sw}} \sim 10^{-3} m_{\text{p}} \text{cm}^{-3}$). This is because of the following reasons. Assuming that the total energy is released in the form of kinetic energy, the density of the free wind at any radius, r , can be given as

$$\rho_w = 2\mathcal{L}/(\Omega r^2 v_w^3), \quad (5.11)$$

where, Ω is the wind opening solid angle. The pressure and temperature of the reverse shocked gas are, therefore, given as $P_{\text{sw}} \propto \rho_w v_w^2 = 2\mathcal{L}/(\Omega r^2 v_w)$ and $T_{\text{sw}} \propto v_w^2$, respectively. This means that a high velocity wind will always create a higher temperature and low density shocked wind.

It is clear from the above arguments that knowledge of the density structure inside the FBs will help to distinguish between the AGNW and SFW cases. In fact, the best fit model of MB16 (their figure 10a) prefers a high density ($\sim 10^{-3} m_{\text{p}} \text{cm}^{-3}$) interior

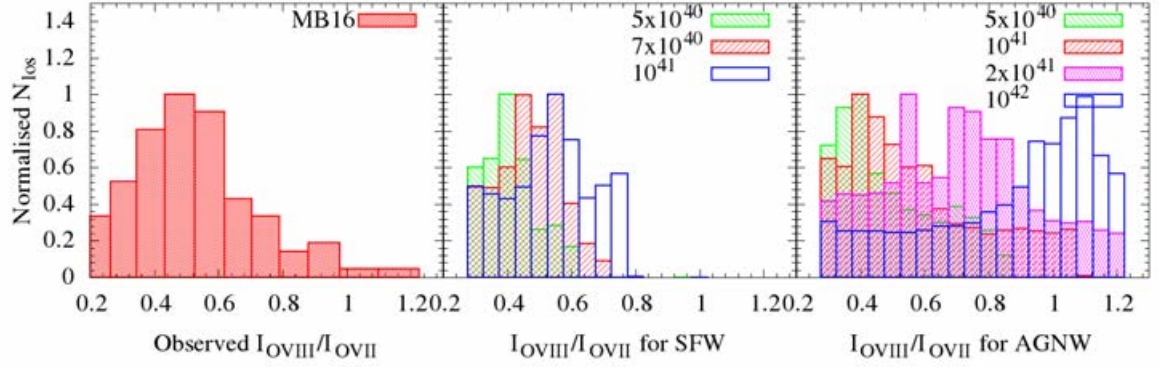


Figure 5.6: Normalised histograms of the OVIII to OVII line ratio obtained at $t = t_{\text{fb}}$ as mentioned in Figure 5.5. The histogram for $\mathcal{L} = 2 \times 10^{41} \text{ erg s}^{-1}$ in AGNW case was obtained at $t = 15 \text{ Myrs}$. The observed values of MB16 are shown in the left panel. The middle and the right panels show the obtained line ratio histograms for the SFW and AGNW cases, respectively. Different mechanical luminosities (given in erg s^{-1}) are represented by different box styles. All the N_{los} values are normalised with respect to the maximum number of LOSs obtained in corresponding mechanical luminosities. Note that the histograms of intensity ratios are similar for a similar mechanical luminosity, irrespective of whether energy is put via stellar or AGN feedback

of the FBs, which is possible if either SF luminosity is $\sim 10^{41} \text{ erg s}^{-1}$ ($\text{SFR} \sim 1 M_{\odot} \text{ yr}^{-1}$) or AGNW luminosity is $\sim 5 \times 10^{44} \text{ erg s}^{-1}$ ($\approx 0.8 \mathcal{L}_{\text{edd}}$, for a black hole mass of $4 \times 10^6 M_{\odot}$), assuming $r_{\text{rs}} \sim 2 \text{ kpc}$ and $\Omega = 2\pi$ in equation 5.11. *This is a consequence of the fact that the AGNWs are much less mass loaded compared to the SFWs.*

In AGNW case, it is hard to produce the fitted OVIII volume emissivity (shown in figure 10d of MB16) inside the bubble since the emissivity of OVIII lines at $\gtrsim 3 \times 10^8 \text{ K}$ is $n^2 \varepsilon(T) \sim 10^{-28} \text{ photons s}^{-1} \text{ cm}^{-3}$, assuming $n \sim 10^{-5} \text{ cm}^{-3}$ and $\varepsilon(3 \times 10^8 \text{ K}) \sim 2 \times 10^{-18} \text{ photons s}^{-1} \text{ cm}^3$ (see figure 5.3). This value is clearly ~ 7 orders of magnitude lower than the fitted one. Conduction can, in principle, increase the density inside the bubble and reduce the temperature. Tests with 1D simulations including conduction (see section 5.6.3) show that the temperature of the bubble (i.e. inside the contact discontinuity, which in this case is at $\approx 5 \text{ kpc}$) is $\gtrsim 10^7 \text{ K}$ and the density is $\lesssim 5 \times 10^{-4} m_{\text{p}} \text{ cm}^{-3}$. Therefore, the volume emissivity can increase to $2 \times 10^{-24} \text{ photons s}^{-1} \text{ cm}^{-3}$, which is still ~ 3 orders of magnitude lower than the fitted value $\sim 10^{-21} \text{ photons s}^{-1} \text{ cm}^{-3}$. However, we should keep in mind that estimating the emissivity inside the low density bubble is a complex process as it may be contaminated by the shell emission and may not be distinguishable by a simple fitting of a bubble and a shell.

On the other hand, for SFW, the bubbles density $n \sim 10^{-3} \text{ cm}^{-3}$ and the bubble temperature is $\sim 10^6 - 10^7 \text{ K}$, for which the OVIII volume emissivity is $\sim 4 \times 10^{-22} \text{ photons s}^{-1} \text{ cm}^{-3}$ (assuming $\varepsilon = 10^{-15} \text{ photons s}^{-1} \text{ cm}^3$) which is much closer to the fitted value.

In case of the intensity ratio between OVIII and OVII lines, the comparison becomes non-trivial as the LOS may consist of gas at different temperatures and therefore can have different line ratios compared to a single temperature medium. For direct comparison with the observations, it is necessary to consider the effects of any intervening

or background medium. We, therefore, use our projection software PASS to produce the line intensity maps including the effects of the local bubble and the halo medium extending till ~ 250 kpc as explained in section 5.4.1.

While producing line emission maps, it is necessary to know the age of the FBs because the forward shock velocity and hence the shocked halo temperature depends on time as

$$v_{\text{fs}} \sim \left(\frac{\mathcal{L}}{\rho_0} \right)^{1/5} t^{-2/5}, \quad (5.12)$$

where, the symbols have same meanings as in equation 5.10. Therefore, it is necessary to know the region where the gamma-rays are produced. It could either be the forward shock or the reverse shock (Lacki, 2014) or the contact discontinuity (Mou et al., 2015; Crocker et al., 2015) or the region within the contact discontinuity (Mertsch & Sarkar, 2011; Sarkar et al., 2015b). Here, we follow Sarkar et al. (2015b) and assume that the gamma-rays originate from the region within the contact discontinuity. Therefore, we, set the age of FBs when the contact discontinuity reaches latitude $b \approx 50^\circ$ (height of the FBs). Since the forward shock radius $r_{\text{fs}} \sim (\mathcal{L}t^3/\rho_0)^{1/5}$, this age of the FBs is different for different luminosities and is shown in the corresponding panels in figure 5.5.

Figure 5.5 shows the OVIII to OVII line ratio maps for AGNW (top panel) and SFW (bottom panel) models obtained at the age of the FBs (as explained above) for different luminosities. It shows that the line ratio is highest on the top of the bubble where the shock is the strongest and becomes lower on the either sides where the shock is weaker, a typical behaviour for a bow shock. Notice that in some cases the emission forms a shell-like feature, this is because the low density interior does not contribute much to the line ratio and most of the emission comes from the shell-like shocked halo gas.

For a better comparison with the observed data, in Figure 5.6, we also plot histograms of the OVIII to OVII line ratios for different mechanical luminosities and injection scenarios. In this figure we intentionally excluded all the LOSs that have line ratio less than 0.3 to avoid contamination from the halo gas.

It is clear from the above figures that only $\mathcal{L} \approx 7 \times 10^{40}$ erg s $^{-1}$ in case of SFW and $\mathcal{L} \approx 10^{41}$ erg s $^{-1}$ in case of AGNW match the observed line ratio. A higher (lower) luminosity in either case produces a line ratio that is more (less) than the observed ones. We, therefore, can constrain the mechanical luminosity of the source of the FBs to be $\mathcal{L} \approx 7 \times 10^{40}$ erg s $^{-1}$ for the star formation scenario and $\mathcal{L} \approx 10^{41}$ erg s $^{-1}$ for the Accretion wind scenario. Note that both the peak and the cut-off of the histograms are characteristic of the injected luminosity rather than just the peak.

The post shock temperature for the SF case corresponds to $\sim 3 \times 10^6$ K, whereas, for the AGNW case, the temperature is $\sim 5 \times 10^6$ K at $\theta = 7^\circ$ and falling rapidly to $\sim 3 \times 10^6$ K at an angle of 45° from the rotation axis. This estimate of temperature is consistent with the measurements by Kataoka et al. (2013); Gu et al. (2016) at the NPS. The similarity of the NPS temperature to the other parts of the FBs is another *dramatic coincidence* that has to be explained if the NPS is not related to the FBs.

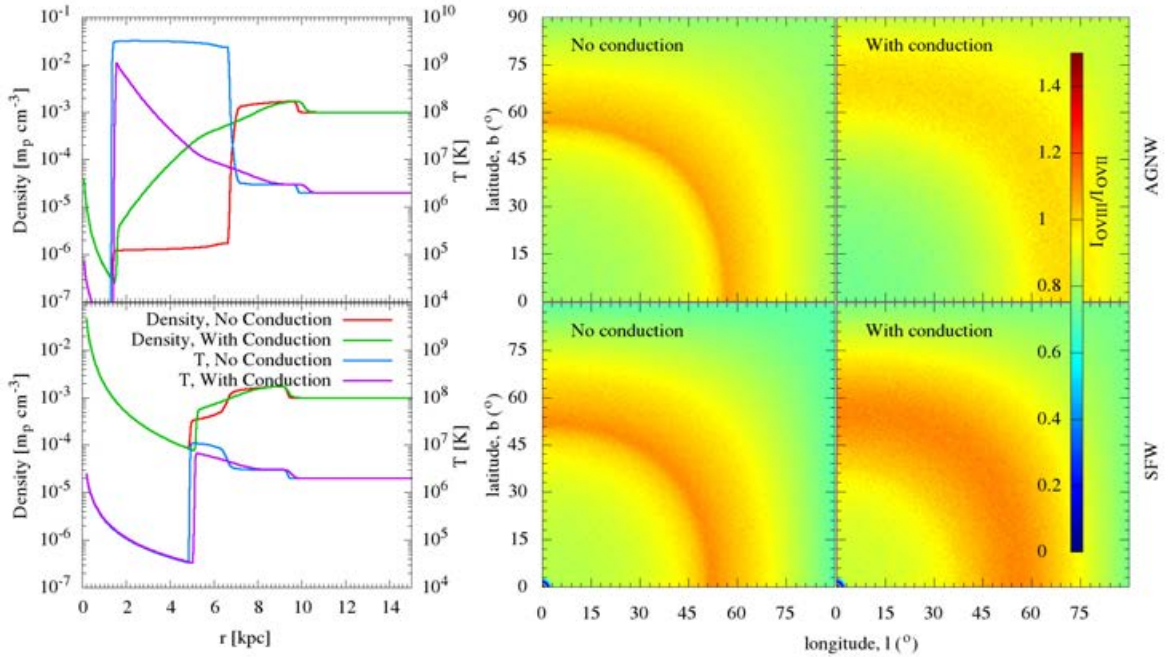


Figure 5.7: Effects of conduction for one dimensional test runs of AGNW (top panel) and SFW (bottom panel) having mechanical luminosity of $\mathcal{L} = 2 \times 10^{41} \text{ erg s}^{-1}$ at 20 Myr. This time-scale has been chosen such that the contact discontinuity reaches longitude $\approx 50^\circ$ when projected. The one dimensional density (left axis) and temperature (right axis) profiles for runs with/without conduction have been shown in the left panel of the figure. The corresponding effects on the O VIII to O VII line ratios have been shown in the middle and right panels. The colour represents the O VIII to O VII line intensity ratio. While calculating the line intensity ratio, we kept the box only till 15 kpc to avoid contribution from the background halo gas.

5.6 Discussion

5.6.1 Effects of cosmic ray and magnetic pressure

So far in our simulations we have not considered cosmic ray or magnetic pressure on the dynamics of the gas. However, it has been shown that the cosmic ray pressure and the magnetic pressure can contribute approximately half of the thermal energy of the Galactic wind (Sarkar et al., 2015b). Therefore, the required energy solely from star formation process to drive the FBs is $\sim 5 \times 10^{40} \text{ erg s}^{-1}$, which corresponds to $\sim 0.5 M_{\odot} \text{ yr}^{-1}$ consistent with the estimates by Sarkar et al. (2015b). The estimated mechanical luminosity required only from a SFW wind is, however, dependent on the fraction of the thermal energy in CRs and in the magnetic field.

5.6.2 Enhanced emission beyond FBs

One point to notice in Figure 5.5 is that the line ratio is enhanced beyond the edge of the FBs (extended till 50° in latitude and $\sim 20^{\circ}$ in longitude). Interestingly, such an extended emission (till $\sim 60^{\circ} - 70^{\circ}$ in both longitude and latitude) in OVIII intensity and the OVIII to OVII line ratio is also noticed in the observations (see figure 4 and 6 of MB16). We speculate that this extended emission can be an indication of the forward shock travelling through the circumgalactic medium.

5.6.3 Effects of conduction

Conduction also can affect the dynamics and the density and temperature profiles of the bubble. We, therefore, use isotropic conduction module given in PLUTO. The heat flux is calculated as

$$F = \frac{F_{\text{sat}}}{F_{\text{sat}} + F_{\text{class}}} F_{\text{class}}, \quad (5.13)$$

where, $F_{\text{class}} = 5.6 \times 10^{-7} T^{5/2} \nabla T$ is the classical thermal conduction flux. In cases where the temperature gradient is very large, the above equation also takes care of the saturation effects by including $F_{\text{sat}} = 5\phi\rho c_{\text{iso}}^3$, where, $\phi = 0.3$ and c_{iso} is the isothermal sound speed. The effects of conduction are, therefore, more in the case of AGNW because of the high temperature compared to the SFW case. However, incorporation of the thermal conduction in AGNW runs makes the structure of the outer shock highly elongated along the $\theta = 0$ axis and forms a very thin jet like feature. In reality, conduction can get suppressed due to the presence of magnetic field. A proper treatment will require incorporation of anisotropic conduction which is beyond the scope of this work. Instead, we present one-dimensional test runs with/without conduction to understand the effects of conduction. However, we alert the reader that these runs should be taken only as indicative of the actual situation. Moreover, electrons and protons may not have the same temperature behind the shock, as the Coulomb interaction time-scale between these two species can be long, as discussed in section 5.6.4. This may also suppress the thermal conduction.

Figure 5.7 shows the 1D runs with/without conduction. The upper panel shows the runs for AGNW and the lower panel shows the runs for SFW for a mechanical luminosity $= 2 \times 10^{41} \text{ erg s}^{-1}$ at 20 Myr. The density and temperature profiles for the

SFW case show little variation if conduction is present. The effects are large in case of AGNW because of the large temperature inside the bubble. Although the outer shock structure remains almost same, the structure of the density and temperature inside the contact discontinuity (≈ 5 kpc) changes by almost two orders of magnitude. To compare the integrated line intensity ratio, we put these 1D bubbles at the Galactic centre and produce the line intensity maps as shown by the colour contours in middle (without conduction) and right panel (with conduction) of Figure 5.7. The contours show little variation in the line intensity ratio even if conduction is included. This is because the contribution to the line intensity mainly comes from the outer shock which remains almost unaffected by the conduction. Therefore, the line intensity maps presented in Figure 5.5 are likely to be unaffected by conduction.

One aspect, however, immediately improves in case of AGNW is the OVIII emissivity inside the contact discontinuity. As mentioned earlier, conduction can increase the OVIII emissivity in this case to $\sim 2 \times 10^{-24}$ photons $\text{s}^{-1} \text{cm}^{-3}$. The exact value however depends on the definition of the bubble i.e. the region where the gamma-ray emission is generated. This will involve careful modelling of the diffusion of CR particles in this scenario.

Also, notice that the effects of conduction have been overestimated in these simulations. Presence of the magnetic field will decrease the effects of conduction. However, a simple estimate of the average OVIII emissivity in the region within the outer shock shows that the average emissivity is $\sim 4 \times 10^{-21}$ photons $\text{s}^{-1} \text{cm}^{-3}$ in all the cases i.e with/without conduction in AGNW/SFW cases. Since we are looking at projected emission, even the bubble region emits significantly in OVIII because of the outer shock along the sightline. Therefore, it is difficult to distinguish between AGNW and SFW using the OVIII emissivity fitted by MB16.

5.6.4 Electron-proton energy equilibration

Eq. 5.13 assumes that electrons and protons have the same temperature. This assumption is valid only when the electron-proton energy exchange time due to Coulomb collisions is short enough compared to the dynamical time. This time-scale is (using Eq. 5-31 in Spitzer 1956),

$$t_{eq} \sim 0.25 \text{ Myr } T_6^{3/2} / n_{-3} , \quad (5.14)$$

where, T_6 is the electron temperature in the units of 10^6 K and n_{-3} is the proton/electron number density in units of 10^{-3} cm^{-3} . The corresponding length scale required to attain equilibrium is $l_{eq} = vt_{eq} \sim 75 T_6^{3/2} / n_{-3}$ pc for $v = 300 \text{ km s}^{-1}$ (v is the flow velocity). Thus, for the outer shock density and temperature (for both SFW and AGNW scenarios considered here) t_{eq} is shorter than the age of FBs, and therefore the electron and proton temperature behind the outer shock can be treated as equal.

For the much stronger reverse shock in the AGNW scenario (top-left panel of Fig. 5.7), the post-shock temperature is $\sim 10^9$ K and density is $\sim 10^{-6} \text{ cm}^{-3}$. The electron-proton energy exchange time for these parameters is $\sim 10^7$ Myr ! For the SFW scenario (top-left panel of Fig. 5.7) t_{eq} is ~ 15 Myr, and even here the assumption of equal electron and proton temperature is only marginally valid. Thus the strong reverse shock is in the collisionless regime, and the electron temperature is expected to be

much smaller than the proton temperature (e.g., see Fig. 2 in Ghavamian et al. 2007). Therefore, the effects of thermal conduction are exaggerated in the top panels of Figure 5.7, and in reality the density in the bubble (particularly for the AGNW scenario) may be closer to the case without conduction.

For a strong outer shock ($M \sim 10$, representative of a high luminosity wind) the forward shock temperature can become $T \sim 10^8$ K for which $t_{\text{eq}} \sim 100$ Myr (Eq. 5.14). In such a case, the electrons are expected to be much cooler than the protons and, therefore, the outer shock strength may be underestimated by the OVIII/OVII ratio. We can estimate the maximum luminosity for which our analysis, which hinges on equal electron and proton temperature, of the outer shock strength is valid. The outer shock temperature for a mechanical luminosity \mathcal{L} can be approximated in a spherically symmetric and constant background density case as

$$T_{\text{shock}} \approx 2.5 \times 10^7 \mathcal{L}_{42}^{2/5} n_{-3}^{-2/5} t_{\text{dyn,Myr}}^{-4/5} \text{ K}, \quad (5.15)$$

where, $\mathcal{L} = 10^{42} \mathcal{L}_{42} \text{ erg s}^{-1}$ and $t_{\text{dyn,Myr}}$ is the time in units of Myr which is given by

$$t_{\text{dyn,Myr}} = 11 R_{10\text{kpc}}^{5/3} n_{-3}^{1/3} \mathcal{L}_{42}^{-1/3}. \quad (5.16)$$

Here, $R = 10R_{10\text{kpc}}$ kpc is the outer shock radius. Therefore, we can write Eq. 5.14 as

$$t_{\text{eq,Myr}} \sim 1.74 \mathcal{L}_{42} n_{-3}^{-2} R_{10\text{kpc}}^{-2}. \quad (5.17)$$

Now, for the electron and proton temperature to be equal, $t_{\text{eq}} \lesssim t_{\text{dyn}}$, which means

$$\mathcal{L} \lesssim 4 \times 10^{42} n_{-3}^{7/4} R_{10\text{kpc}}^{11/4} \text{ erg s}^{-1}. \quad (5.18)$$

Therefore, our analysis of the outer shock strength is valid for $\mathcal{L} \lesssim 4 \times 10^{42} \text{ erg s}^{-1}$. Note that the above calculation assumes that the shock is expanding in a constant density medium. In reality, the shock expands in a stratified CGM for which an analytical solution in general is difficult to obtain. We can obtain an upper limit on \mathcal{L} by plugging in the lowest plausible value for n ($\sim 5 \times 10^{-4} \text{ cm}^{-3}$; the minimum CGM density within 10 kpc; see Fig. 5.2) in Eq. 5.18. This assures that the assumption of electron-proton equilibrium at the outer shock is definitely valid for $\mathcal{L} \lesssim 10^{42} \text{ erg s}^{-1}$.

For higher mechanical luminosities, the electron temperature (T_e) can be lower than the equilibrium shock temperature (T_{shock}) obtained from shock jump conditions. However, T_e at $t = t_{\text{dyn}}$ (time at which the outer shock reaches the observed size of the X-ray shell) is still higher than the electron temperatures corresponding to low luminosity cases (see appendix C.2 for details). Therefore, any luminosity more than $10^{42} \text{ erg s}^{-1}$ would yield electron temperature higher than the electron temperature of $\mathcal{L} = 10^{42} \text{ erg s}^{-1}$ case and would be observable in the OVIII/OVII ratio map. Therefore, a weak outer shock strength is the only possible solution for explaining the observed OVIII to OVII line ratio.

5.6.5 AGNW vs. SFW

In case of a SFW, the obtained mechanical luminosity ($5 \times 10^{40} \text{ erg s}^{-1}$) corresponds to a SFR $\sim 0.5 M_{\odot} \text{ yr}^{-1}$ (see equation 5.6 and section 5.6.1). Notice that this value is

slightly larger compared to the observations by [Yusef-Zadeh et al. \(2009\)](#), who found $\text{SFR} \sim 0.1 M_{\odot} \text{ yr}^{-1}$. However, recent discovery of a ~ 100 pc molecular ring can, in principle, host a higher SFR. Also, note that the required rate of SFR depends on the exact amount of CR and magnetic energy density inside the bubbles.

On the other hand, linear polarisation of $\gtrsim 150$ GHz emission, and IR and X-ray variability of the Sgr A* suggests that the current accretion rate of the GCBH is $\sim 10^{-9} - 10^{-7} M_{\odot} \text{ yr}^{-1}$ ([Quataert & Gruzinov, 2000](#); [Agol, 2000](#); [Yuan et al., 2003](#); [Marrone et al., 2006](#)), which corresponds to a mechanical luminosity of $\sim 5 \times 10^{36-38} \text{ erg s}^{-1}$, assuming an efficiency factor of 0.1 (see section 5.1). However, in order to explain the X-ray luminosity around the Sgr A*, it has been suggested that the past accretion rate of the GCBH could have been 10^{3-4} higher than the present day accretion rate ([Totani, 2006](#)). This means that the GCBH mechanical luminosity was $\lesssim 5 \times 10^{39-41} \text{ erg s}^{-1}$. Although there is a large uncertainty in the past mechanical luminosity, it is surprisingly close the required rate of $10^{41} \text{ erg s}^{-1}$. Also, we must note that the black hole activity is highly variable in time and it is the average mechanical luminosity that should be considered.

In this paper, though we constrain the mechanical luminosity for the source driving the FBs, the degeneracy between the SFW and the AGNW models still remains. One way to distinguish between these two models is probably the kinematics of the hot gas inside the bubbles (i.e. inside the contact discontinuity). As noted by [Sarkar et al. \(2015b\)](#), the velocity range of the hot wind for SFW can be $\sim \pm 600 \text{ km s}^{-1}$. However, in case of AGNW, This velocity range will be much higher. Another way is to measure the temperature along the outer edge of the FBs. In AGNW case, the outer shock is relatively more anisotropic than the SFW case. This is because the AGNW is completely kinetic energy driven and has a large velocity anisotropy perpendicular to the disc thus producing a strong bow shock and, therefore, producing a somewhat anisotropic shock temperature. The SFW, on the other hand, has a large fraction of energy in the form of internal energy and hence the outer shock structure is more isotropic (see Figure 5.4). However, one must note that measuring the temperature along the edge of the FBs using the OVIII to OVII line ratio is likely to be contaminated by the detailed structure of the MW halo gas as the contribution from the background halo gas is non-negligible.

5.7 Summary

We have explored different driving mechanisms to inflate the FBs: one, a central black hole driven wind (AGNW), and second, a star formation driven wind (SFW). The winds have been launched at the Galactic centre and have been allowed to propagate through a realistic distribution of the MW halo gas. We compare our numerical simulations of SNe and AGN wind models with the best fit model of [Miller & Bregman \(2016\)](#). We find that irrespective of the driving mechanism - AGNW or SFW, the total luminosity required to produce the observed OVIII to OVII line ratio is $\approx 0.7 - 1 \times 10^{41} \text{ erg s}^{-1}$. The given luminosity also constrains the age of the FBs to be ~ 20 Myr.

The shocked halo temperature is estimated to be $\approx 3 \times 10^6 \text{ K}$ in most of the forward shock. For a weak shock travelling through a $2 \times 10^6 \text{ K}$ halo gas, this temperature would correspond to a shock velocity of $\sim 300 \text{ km s}^{-1}$. The corresponding temperature is

highly anisotropic in case of a AGNW for which the temperature ranges from 5×10^6 K to 3×10^6 K. These values are slightly lower compared to the estimates by [Miller & Bregman \(2016\)](#) who found the temperature to be $\approx 5 \times 10^6$ K based on the same data. Our temperature estimate is, however, consistent with the temperature measurements by [Kataoka et al. \(2013\)](#) and [Gu et al. \(2016\)](#) at the NPS, which indicates that the NPS has likely originated from the same activity that gave rise to the FBs.

Summary and Conclusion

In this thesis, we have studied the properties of supernovae-driven outflows in a circumgalactic medium (CGM) environment that is common for massive galaxies. We used numerical ([PLUTO-v4.0](#), developed by [Mignone et al. 2007](#)) as well as analytical tools to characterise the outflows. Our initial gas distribution contains a warm (10^4 K) and dense ($\sim 1 m_p \text{ cm}^{-3}$) disc component which is supported against the gravitational potentials by its turbulence and its rotation around the galactic centre. The distribution also contains a hot ($\sim \text{few} \times 10^6$ K) and low density ($\sim 10^{-3} m_p \text{ cm}^{-3}$) but non-rotating circumgalactic medium. Both these components are in steady state hydrostatic equilibrium with the combined gravity of the stellar disc, dark matter and bulge in some cases. Such an initial condition allowed us to explore the outflow properties in a realistic galaxy environment. We assumed that the supernovae (SNe) energy is completely thermalised initially. The thermalisation process can occur when a large number of SNe occurs within a small enough volume to suppress the radiative cooling of individual SN remnants ([Larson, 1974](#); [Nath & Shchekinov, 2013](#); [Roy et al., 2013](#)). For a constant star formation rate (SFR), we assumed that the mechanical luminosity from the stellar winds and SNe is constant after few Myr ([Leitherer et al., 1999](#)). We, therefore, continuously injected this energy at the centre of the galaxy during the considered period of star formation. We varied the star formation rate and the CGM density to study different properties of the outflows such as (i) the mass loading factor and velocity of different phases of the outflowing gas, (ii) the generation of warm clouds from the interaction of the outflow and the CGM and (iii) the X-ray emission from galactic outflows and the CGM. We also applied our understanding of the outflows to explain the gamma-ray, X-ray and radio features of the Fermi Bubbles that are observed towards the centre of our Galaxy. We now summarise the works presented in this thesis below and discuss future directions.

Outflow in a circumgalactic medium

In chapter 2, we performed 2-dimensional axisymmetric hydrodynamic simulations of SNe-driven outflow in a CGM that is suitable for milky Way-type galaxies. We injected

SNe ejected mechanical luminosity within 60 pc region at the centre of the galaxy to overcome artificial cooling at the gaseous disc (Sharma et al., 2014b). We found a bipolar wind structure perpendicular to the gaseous disc and has a qualitatively similar structure as a stellar wind in the interstellar medium (Weaver et al., 1977) as expected. The outer shock in this case is, however, non-radiative as it runs through the hot and low density CGM. Due to the presence of a realistic disc-CGM gas distribution in our set-up, we noticed that the interstellar medium (ISM), that is carried away by the wind to the CGM, cools radiatively and fragments into clouds. Some of these clouds fall back because of the gravity, while some of them travel away from the disc. The disc material is also entrained by the high velocity free wind from the base of the wind. We assumed a typical star formation duration of 50 Myr after which we stopped injecting the mechanical energy. After the energy injection is stopped, the warm clouds fall back to the stellar disc but the low density, hot bubble produced by the shocked wind rises through the CGM due to the buoyancy and finally becomes a part of the CGM.

The mass loading factor (MLF), defined by the ratio of mass outflow rate to the star formation rate during an active star formation period, is 0.2 – 0.4 if estimated within ≤ 10 kpc of the centre. This MLF is almost equally divided into two main phases, one peaking at $\sim 10^5$ K, and another peaking at 3×10^6 K. The first component comes from the mixing of entrained ISM with the wind material whereas, the second component comes mainly from the shocked CGM. The warmer ($\leq 3 \times 10^5$ K) component is more likely to be probed by UV/optical absorption/emission studies that are used to estimate the mass loading from star forming galaxies. We define this mass loading factor as η_{3e5} . This phase, however, does not become a part of the outflow at large scales (~ 200 kpc) where the outflow is dominated by the shocked CGM material. Detection of such low density outflowing CGM material is not trivial in observations because of the low emissivity of the material. Even if detected, this outflow will not be causally connected to the current episode of the star formation period due to the shock travel time (\sim few 100 Myr). We, however, found that the mass loading factor at such large distances from the central galaxies (η_v) is almost a magnitude higher than η_{3e5} , for a baryonic fraction of 0.1. The situation remains same for multiple such starbursts that are well separated in time ($\Delta t \sim 200$ Myr). The change in CGM mass, even for a $100 M_\odot \text{ yr}^{-1}$ star formation rate, is negligible ($\lesssim 10\%$). We also notice that for high star formation rate ($\gtrsim 10 M_\odot \text{ yr}^{-1}$) that is going for more than ~ 50 Myr, the free wind suffers significant amount of radiative cooling to suppress the mass loading factor at the virial radius by a factor of 2.

The Mach number of the outflowing material at large radii ($\gtrsim 100$ kpc) is marginally above 1. Therefore, the outflow velocities at those radii is almost same as the sound speed of the CGM ($\sim 200 \text{ km s}^{-1}$) and roughly corresponding to the virial temperature of the dark matter halo. However, we found that the velocity of the warm clumps ($\lesssim 3 \times 10^5$ K) near the centre ($\lesssim 10$ kpc) are divided into ‘two sequences’. The ‘main sequence’ extends from ~ 0 to $\sim 800 \text{ km s}^{-1}$ and originates due to the entrainment of the disc gas by the high velocity wind material. The ‘second sequence’ extends from $\sim -150 \text{ km s}^{-1}$ to $\sim +200 \text{ km s}^{-1}$ that hosts clouds that are generated by radiative cooling and thereby fragmentation of the disc gas at the contact discontinuity.

In future works, we plan to relax some of the assumptions made in this chapter such as the constant and centralised energy injection. We plan to improve our simulation by considering all the 3-dimensions with increasing resolution. We also, plan to understand

the mixing of metals in the CGM in the context of SNe ejected outflows and formation of the observed warm clouds far away from the galaxies as observed by [Tumlinson et al. \(2011\)](#); [Werk et al. \(2014\)](#).

Diffuse X-rays from galaxies

In chapter 3, we investigated the origin of the soft X-ray (0.5 – 2.0 keV) emission from a SNe driven outflow within a CGM. We realised that one important source of such X-ray is the central region of a SNe-driven outflow where the density ($\gtrsim 0.1 m_p \text{ cm}^{-3}$) and temperature ($\sim 10^7 \text{ K}$) can be high enough to produce noticeable X-ray emission. This emission, however, depends crucially on the SFR and the MLF (η). For a constant MLF, the central density is $\propto \text{SFR}$ and, therefore, the central soft X-ray luminosity ($L_{X,c}$) is $\propto \text{SFR}^2$. The dependence of $L_{X,c}$ on η is, on the other hand, slightly complicated as it increases the central density but also reduces the temperature of the central wind. We can, however, put an upper limit on the MLF from various considerations. It has been shown previously that the maximum value of the MLF in an outflow is constrained by heavy cooling of the wind at the central region ([Thompson et al., 2016](#)). We argued that, this value can be further constrained by a factor of few based on the availability of entrainable gas in the central region of the wind. This constrain is particularly important for SFRs ranging from 0.1 to 100 $M_\odot \text{ yr}^{-1}$.

CGM in a massive galaxy is another source of soft X-rays as the temperature of the CGM is $\sim \text{few} \times 10^6 \text{ K}$. We found that the for low mass ($M_\star \lesssim 10^{10} M_\odot$) and high SFR ($\gtrsim 1 M_\odot \text{ yr}^{-1}$) galaxies, the X-rays from the centre of the wind dominates, whereas, for higher mass and lower SFR galaxies, it is the CGM that dominates the soft X-ray emission. We found that the sub-linear relation between the L_X and the SFR in the observed data ([Mineo et al., 2012b](#); [Wang et al., 2016](#)) can be well understood by a combined contribution from the central region where $L_X \propto \text{SFR}^2$ and the CGM where $L_X = \text{constant}$.

One aspect that we have not considered in our analysis is the absorption of soft X-rays in the ISM of the host galaxy that is expected to suppress the contribution for central region of the winds. We plan to include this effect in our future works and produce more realistic results that can be compared with the data.

Fermi Bubbles and their multi-wavelength features as signatures of SNe-driven Galactic wind

In chapter 4, we have performed 2-dimensional axisymmetric hydrodynamical simulations of SNe-driven outflows to investigate the origin of two giant ($\approx 50^\circ$) gamma-ray bubbles ([Su et al., 2010](#)), called the Fermi Bubbles (FBs), observed in our Galaxy. The initial set up of the simulation box is similar to as described in section 6 but adapted to match the Milky-Way parameters. We varied the star formation rate at the Galactic centre and the CGM density to match the observed X-ray surface brightness ([Kataoka et al., 2013](#)) and the morphology of the Fermi Bubbles as would be seen from the vantage point of the Sun.

We found that the X-ray emission of the outflow is dominated by the emission from shocked CGM, consistent with the previous chapter. The X-ray emission from the CGM takes shape of a ‘parachute’ as observed in ROSAT maps. We found that a star formation rate of $0.5\text{-}0.7 M_{\odot} \text{ yr}^{-1}$ and a central CGM density of $2\text{-}3 \times 10^{-3} m_{\text{p}} \text{ cm}^{-3}$ matches well with the X-ray and the morphology constrains. We also noticed that the outer edge of the shock can extend till a longitude of $\sim 80^{\circ}$ and may explain the Loop-I feature. To compare the synchrotron surface brightness with the *Microwave Haze* at 23 GHz, we assume that the cosmic rays are generated and confined within the contact discontinuity, and therefore marks the boundary of the Fermi Bubbles. We further assumed that the magnetic and the cosmic ray energy densities inside the FBs are ϵ_B and ϵ_{cr} times the total energy content of the gas. Considering the spectral index of the cosmic ray electrons to be 2.2 (Ackermann et al., 2014) and $\epsilon_{\text{cr}} = 0.15$, we found that $\epsilon_B \approx 0.4$ which corresponds to a magnetic field of $3\text{-}5 \mu\text{G}$. To describe the gamma-ray emission, we assume that the low energy cosmic microwave background (CMB) photons are being energised to GeV energies via inverse Compton effect by the same population of the electrons that produces the *Microwave Haze*. We recovered the surface brightness and the spectrum of the gamma-ray emission from our analysis without doing further assumptions. We further tested a hadronic model for the gamma-rays but found that the hadronic emission is only $\sim 1\%$ of the total emission. We also compared the kinematics of the warm ($\sim 10^4$ K) clouds with recently observed UV absorption data through the FBs (Fox et al., 2015) and found that the clouds in our simulations also show a similar behaviour to the observed ones. Our results suggest that a SNe-driven wind from the centre of our Galaxy can, in principle, explain the multi-wavelength features of the Fermi Bubbles.

One aspect of our result that limits us from claiming that the Fermi Bubbles are generated by a SNe-driven wind is the required mechanical luminosity at the Galactic centre. The required mechanical luminosity is $\mathcal{L} \approx 5 \times 10^{40} \text{ erg s}^{-1}$ corresponding to a SFR of $\sim 0.5 M_{\odot} \text{ yr}^{-1}$ which is factor of few more than the observed values (Yusef-Zadeh et al., 2009; Barnes et al., 2017). One possible factor that can bring down the required SFR is the inclusion of the magnetic and the cosmic ray pressure along with the SNe ejected mechanical energy. Given that $\epsilon_{\text{cr}} \approx 0.15$ and $\epsilon_B \approx 0.4$, the contribution of the non-thermal energy could, therefore, reduce the required mechanical energy only from SNe to be $\approx 3 \times 10^{40} \text{ erg s}^{-1}$ corresponding to a SFR $\approx 0.3 M_{\odot} \text{ yr}^{-1}$. Although this value is closer to the observed SFR, it is still larger by a factor of few. The exact contribution of the non-thermal components, however, can only be understood once the assumptions regarding the magnetic field and cosmic rays have been relaxed. We plan to include these physics in our future simulations to verify or nullify the SNe-driven wind scenario as the origin of the Fermi Bubbles.

Probing the origin of the Fermi Bubbles via OVIII and OVII lines

In chapter 5, we generated synthetic X-ray lines, such as O VIII and O VII, from our simulations and compared them with the observed data. Our simulation set up, in this case, contains the effect of bulge gravity along with the stellar and the dark matter gravity of the Milky-Way. We, however, did not include any rotating cold disc in

our simulations since our focus is to study the outer shock structure of the FBs. The hydrostatic density distribution of the CGM that has been considered here matches well with recently estimated density profile for the CGM of our Galaxy [Miller & Bregman \(2015\)](#). We simulated both the SNe and central black hole-driven winds from the Galactic centre. We found that the density inside the FBs in case of a AGN-driven wind (AGNW) is much lower compared to the SNe-driven wind (SNW) for the same luminosity. This is mainly because of the fact that the AGNW is very lightly mass loaded compared to a SNW and contains almost all of its energy in the form of kinetic energy of the wind. The high velocity of the AGNW and its directional anisotropy makes the outer shock more elongated towards the pole of the Galaxy producing an anisotropic temperature distribution, whereas, the outer shock in SNW is more spherical and shock temperature is more uniform across different latitudes.

We used [CLOUDY-V13.0 \(Ferland et al., 2013\)](#) to generate synthetic O VIII and O VII emission lines. We included the effect of the local bubble ($T \approx 1.2 \times 10^6$ K, $\rho \approx 4 \times 10^{-3} m_p \text{ cm}^{-3}$) and the CGM extended till 200 kpc to produce realistic line ratios. We compared our results to recently observed data from [Miller & Bregman \(2016\)](#). We found that the O VIII/O VII line ratios can be well explained only if the injecting mechanical luminosity $\mathcal{L} = (0.7-1) \times 10^{41} \text{ erg s}^{-1}$, irrespective of whether the driving source is an AGN or SNe activity. Our analysis suggests that the shock velocity is $\sim 300 \text{ km s}^{-1}$ and the age of the bubbles is $\approx 15-25$ Myr.

It is, principle, possible that the Mach number of the outer shock and, therefore the shock temperature, is so high that the electron-proton equilibrium time is longer than the dynamical time-scale. This would mean that the electrons have lower temperature than the protons. We have also explored this possibility. We found that although the electron temperature lags the proton temperature for luminosities $\gtrsim 10^{42} \text{ erg s}^{-1}$, the electron temperature rises monotonically with the luminosity. Therefore, much stronger shocks can not produce an electron temperature that is similar to $\mathcal{L} \lesssim 10^{42} \text{ erg s}^{-1}$. We, therefore, rule out any driving source with mechanical luminosity $\gtrsim 10^{41} \text{ erg s}^{-1}$ to be a possible origin for the Fermi Bubbles.

Appendix **A**

A.1 Rotation curve and gravitational acceleration

For the mass model of the galaxy, we take $M_{\text{disk}} = 5 \times 10^{10} M_{\odot}$, $a = 4.0$ kpc, $b = 0.4$ kpc (Smith et al., 2007), $c = 12.0$ (Macciò et al., 2007), $d = 6.0$ kpc (the flattening length) and $M_{\text{vir}} = 10^{12} M_{\odot}$, which gives us $r_{\text{vir}} = 258$ kpc and $r_s = 21.5$ kpc. We note that Smith et al. (2007) used a rotation velocity $\simeq 220 \text{ km s}^{-1}$ with $c = 24$, and our assumption of $c = 12$ decreases the rotation velocity by 15%, which we consider to be negligible. The rotation curve can be found from the equation

$$\begin{aligned} \frac{v_T^2}{R} &= \left[\frac{\partial \Phi}{\partial R} \right]_{z=0} \\ &= \left[\frac{\partial}{\partial R} (\Phi_{\text{DM}} + \Phi_{\text{MN}}) \right]_{z=0} \end{aligned} \quad (\text{A.1})$$

which gives (in units of $10^{14} (\text{cm s}^{-1})^2$)

$$\begin{aligned} v_T^2 &= -\frac{12.3 R^2}{(d^2 + R^2) \left(1 + \frac{\sqrt{d^2 + R^2}}{r_s} \right)} + \frac{21.5 R^2}{(R^2 + (a + b)^2)^{3/2}} \\ &\quad + \frac{12.3 R^2 r_s \log \left[1 + \frac{\sqrt{d^2 + R^2}}{r_s} \right]}{(d^2 + r^2)^{3/2}} \end{aligned} \quad (\text{A.2})$$

The rotation curve is shown in Figure A.1.

To visualise the gravitational acceleration (g) in the plane and perpendicular to the plane, we plot different components of g in Figure A.2. These curves show that the acceleration is not constant in the central region of the Galaxy. This happens because when we go up in z -direction, the total gravitating mass, which can influence a test particle, increases with height. However, at a certain height contribution from the stellar disk becomes maximum, and after that distance, the gravitating mass does not increase much and the acceleration decreases purely due to distance effect.

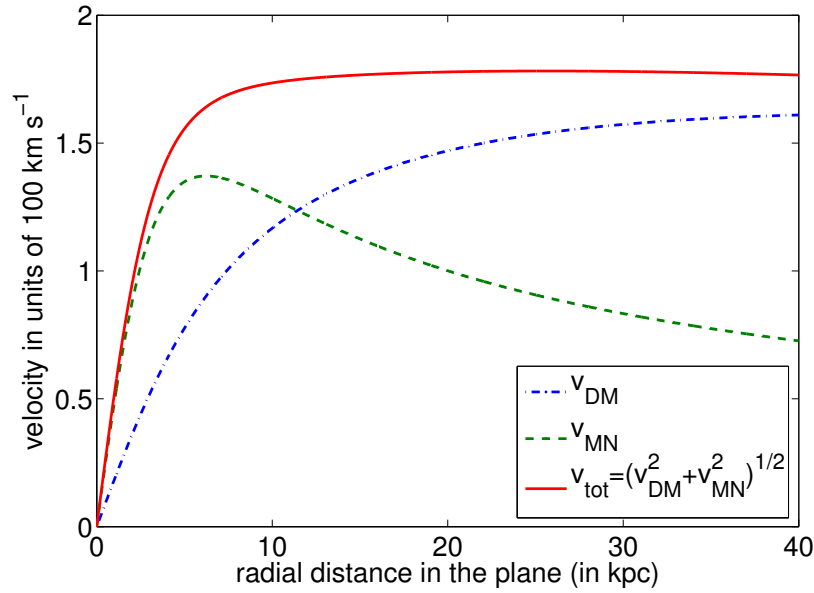


Figure A.1: The rotation curve for the galaxy. The plot also shows the contributions from different potential components.

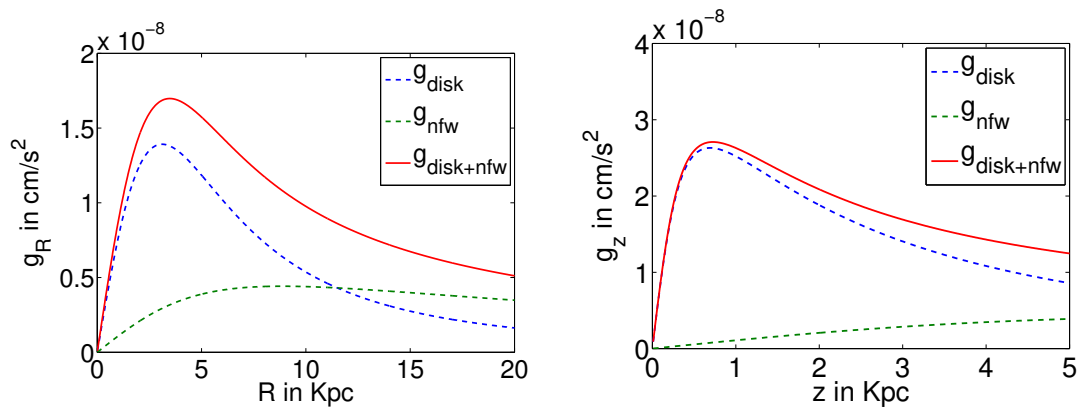


Figure A.2: The gravitational acceleration in the plane (left panel) and perpendicular to the plane (right panel).

A.2 Modified NFW profile

The modified form of NFW profile considered by us is

$$\Phi_{\text{DM}} = - \left(\frac{GM_{\text{vir}}}{f(c)r_s} \right) \frac{\log(1 + \sqrt{R^2 + z^2 + d^2}/r_s)}{\sqrt{R^2 + z^2 + d^2}/r_s}, \quad (\text{A.3})$$

which avoids a singularity at the center. The dark matter density distribution of such a potential can be found using the Poisson's equation,

$$\begin{aligned} \rho_{\text{DM}}(r) &= \frac{1}{4\pi G} \nabla^2 \Phi_{\text{DM}} \\ &= \frac{1}{4\pi G} \frac{1}{r^2} \frac{d}{dr} \left(r^2 \frac{d}{dr} \Phi_{\text{DM}} \right) \end{aligned} \quad (\text{A.4})$$

which gives

$$\begin{aligned} K \rho_{\text{DM}}(r) &= \frac{3r^2}{(d^2 + r^2)^2 \left(1 + \frac{\sqrt{d^2+r^2}}{r_s}\right)} - \frac{3}{(d^2 + r^2) \left(1 + \frac{\sqrt{d^2+r^2}}{r_s}\right)} \\ &+ \frac{r^2}{(d^2 + r^2)^{3/2} \left(1 + \frac{\sqrt{d^2+r^2}}{r_s}\right)^2} - \frac{3r^2 r_s \log \left[1 + \frac{\sqrt{d^2+r^2}}{r_s}\right]}{(d^2 + r^2)^{5/2}} \\ &+ \frac{3r_s \log \left[1 + \frac{\sqrt{d^2+r^2}}{r_s}\right]}{(d^2 + r^2)^{3/2}}. \end{aligned} \quad (\text{A.5})$$

where, $K = \frac{4\pi f(c)r_s}{M_{\text{vir}}}$. This equation reduces to the standard NFW DM density distribution for $d = 0$. The density distribution of the dark matter can be shown in Figure [A.3](#).

A.3 Initial density setup

In steady state, for a rotating fluid, force balance along R and z gives

$$0 = -\frac{\partial \Phi}{\partial R} - \frac{1}{\rho} \frac{\partial p}{\partial R} + \frac{v_{\phi,g}^2}{R} \quad (\text{A.6})$$

$$0 = -\frac{\partial \Phi}{\partial z} - \frac{1}{\rho} \frac{\partial p}{\partial z}. \quad (\text{A.7})$$

Here, we use $v_{\phi,g}(R)$ (gas angular velocity is a function of R only) as the rotational velocity of the gas ($p \neq 0$) compared to $v_{\phi,G} = \sqrt{R \frac{\partial \Phi}{\partial R}}$, which we use for the rotational velocity for a pressure-less test particle at $z = 0$. Eq. [A.7](#) can be solved as

$$\begin{aligned} \frac{kT}{\mu m_p \rho} \frac{\partial \rho}{\partial z} &= -\frac{\partial \Phi}{\partial z} \\ \log \rho &= -\frac{\mu m_p}{kT} \Phi + f_1(R) \\ \rho(R, z) &= \rho_{0R}(R) \exp \left(-\frac{\mu m_p}{kT} \Phi \right), \end{aligned} \quad (\text{A.8})$$

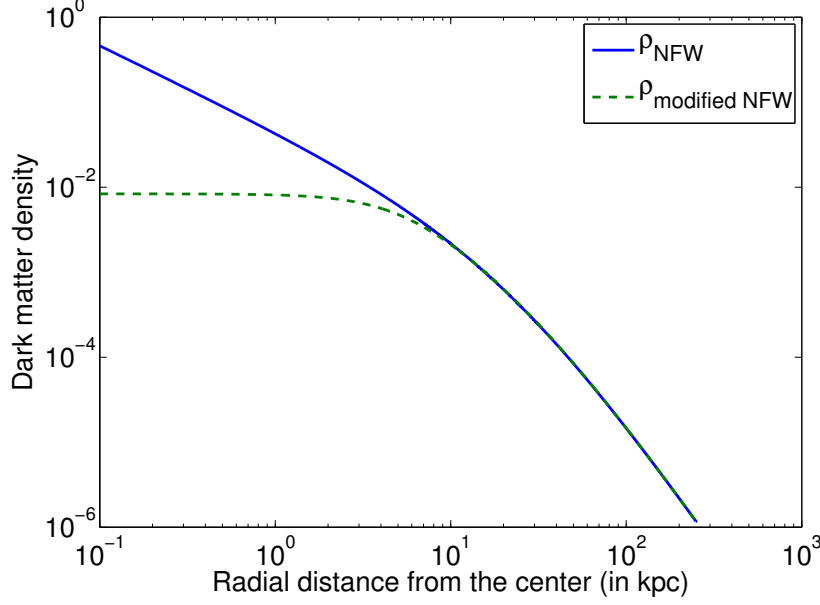


Figure A.3: The dark matter density distribution in the Galaxy in units of $\frac{M_{\text{vir}}}{4\pi f(c) r_s}$. The plot uses the parameters for the MW type galaxy mentioned in Table 2.1.

where, $\rho_{0R}(R) = \exp[f_1(R)]$. From Eq. A.6, we write,

$$\begin{aligned} \frac{kT}{\mu m_p \rho} \frac{\partial \rho}{\partial R} &= -\frac{\partial \Phi}{\partial R} + \frac{v_{\phi,g}^2}{R} \\ \log \rho &= -\frac{\mu m_p}{kT} \left(\Phi - \int \frac{v_{\phi,g}^2}{R} dR \right) + f_2(z) \end{aligned} \quad (\text{A.9})$$

Eq. A.8 then gives

$$\begin{aligned} -\frac{\mu m_p}{kT} \Phi + \log \rho_{0R} &= -\frac{\mu m_p}{kT} \left(\Phi - \int \frac{v_{\phi,g}^2}{R} dR \right) + f_2(z), \\ \rho_{0R}(R) &= \exp \left(\frac{\mu m_p}{kT} \int \frac{v_{\phi,g}^2}{R} dR \right) \times \text{constant}. \end{aligned} \quad (\text{A.10})$$

Since, ρ_{0R} is only a function of R by definition, $f_2(z)$ must be a constant. Combining equations A.8 and A.10, we get,

$$\rho(R, z) = \text{constant} \times \exp \left(-\frac{\mu m_p}{kT} \left[\Phi - \int \frac{v_{\phi,g}^2}{R} dR \right] \right). \quad (\text{A.11})$$

For simplicity, let us assume that the gas rotation velocity is a fraction of the particle rotation on the plane ($z = 0$), i.e. $v_{\phi,g} = f v_{\phi,G}$, where, f is a constant. Then, Eq. A.11 can be written as

$$\rho(R, z) = \text{constant} \times \exp \left(-\frac{1}{c_s^2} [\Phi(R, z) - f^2 \Phi(R, 0)] \right). \quad (\text{A.12})$$

Here, $c_s = \sqrt{\frac{kT}{\mu m_p}}$ is the isothermal sound speed of the gas. For a non-rotating gas, the equation becomes

$$\rho(R, z) = \text{constant} \times \exp\left(-\frac{1}{c_s^2} [\Phi(R, z)]\right). \quad (\text{A.13})$$

The constant can be determined by normalising the density.

Several isothermal components can be combined, as we do for a rotating WIM disc and a non-rotating hot halo.

Appendix *B*

B.1 Projection effects

In our analysis, we consider the Cartesian coordinates whose origin is at the GC and the variables are calculated from the local standard of rest (LSR) and in terms of galactic coordinates (l, b) .

Figure B.1 explains the working geometry. For a given (l, b) , the unit vector along the line of sight can be given as

$$\hat{\mathbf{L}} = -\hat{\mathbf{i}} \cos(b) \cos(l) - \hat{\mathbf{j}} \cos(b) \sin(l) + \hat{\mathbf{k}} \sin(b). \quad (\text{B.1})$$

The unit vectors in spherical coordinates, used in the simulation, can be written in terms of the Cartesian unit vectors as

$$\begin{aligned} \hat{\mathbf{r}} &= \hat{\mathbf{i}} \sin(\theta) \cos(\phi) + \hat{\mathbf{j}} \sin(\theta) \sin(\phi) + \hat{\mathbf{k}} \cos(\theta) \\ \hat{\theta} &= \hat{\mathbf{i}} \cos(\theta) \cos(\phi) + \hat{\mathbf{j}} \cos(\theta) \sin(\phi) - \hat{\mathbf{k}} \sin(\theta) \\ \hat{\phi} &= -\hat{\mathbf{i}} \sin(\phi) + \hat{\mathbf{j}} \cos(\phi). \end{aligned} \quad (\text{B.2})$$

Therefore, the component of the actual velocity, $\vec{v} = \hat{\mathbf{r}}v_r + \hat{\theta}v_\theta + \hat{\phi}v_\phi$, along the LOS is

$$v_{\text{los}} = \vec{v} \cdot \hat{\mathbf{L}}. \quad (\text{B.3})$$

However, because of the solar rotation of $v_{\phi, \odot}$ on the plane, the actual LOS velocity along some (l, b) is

$$\begin{aligned} v_{\text{los}} &= \vec{v} \cdot \hat{\mathbf{L}} - v_{\phi, \odot} \sin(l) \cos(b) \\ &= -\cos(b) \cos(l) \left[v_r \sin(\theta) \cos(\phi) + v_\theta \cos(\theta) \cos(\phi) - v_\phi \sin(\phi) \right] \\ &\quad - \cos(b) \sin(l) \left[v_r \sin(\theta) \sin(\phi) + v_\theta \cos(\theta) \sin(\phi) + v_\phi \cos(\phi) \right] \\ &\quad + \sin(b) \left[v_r \cos(\theta) - v_\theta \sin(\theta) \right] - v_{\phi, \odot} \sin(l) \cos(b). \end{aligned} \quad (\text{B.4})$$

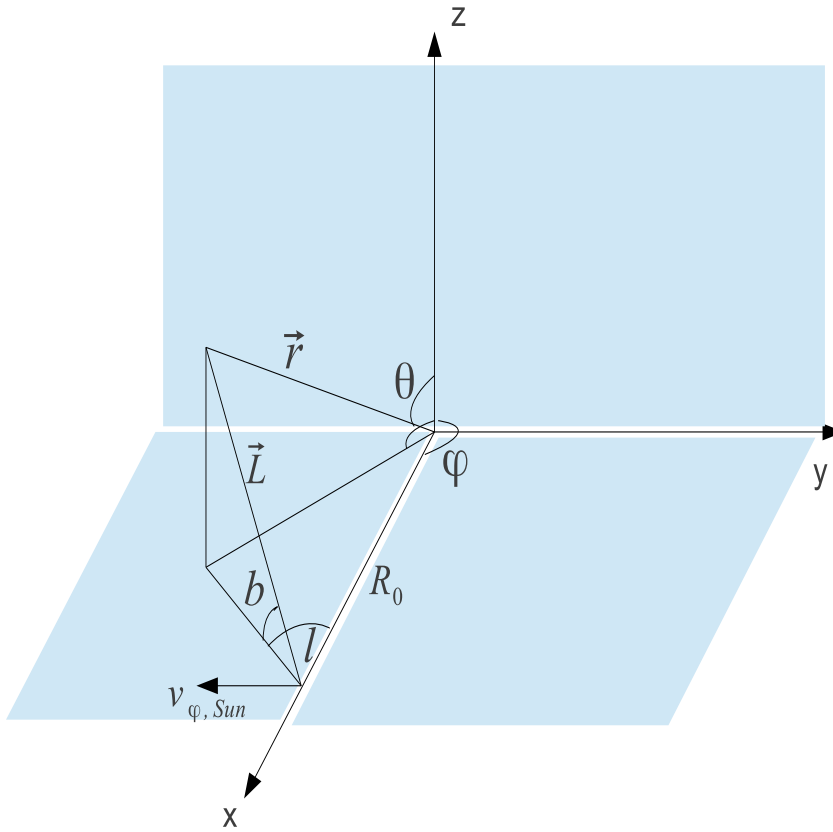


Figure B.1: The geometry for calculating the projected maps and LOS velocity from the Solar vantage point. The coordinate system has its origin at the Galactic center (GC), whereas the Sun is situated at a distance of $R_0 = 8.5$ kpc from the GC along the X-axis. The Y-Z plane represents the plane perpendicular to the Galactic disc. The Galactic coordinates are marked as l and b , the simulation coordinates are shown as r and θ in the diagram and L is the distance of the point under consideration from the Sun.

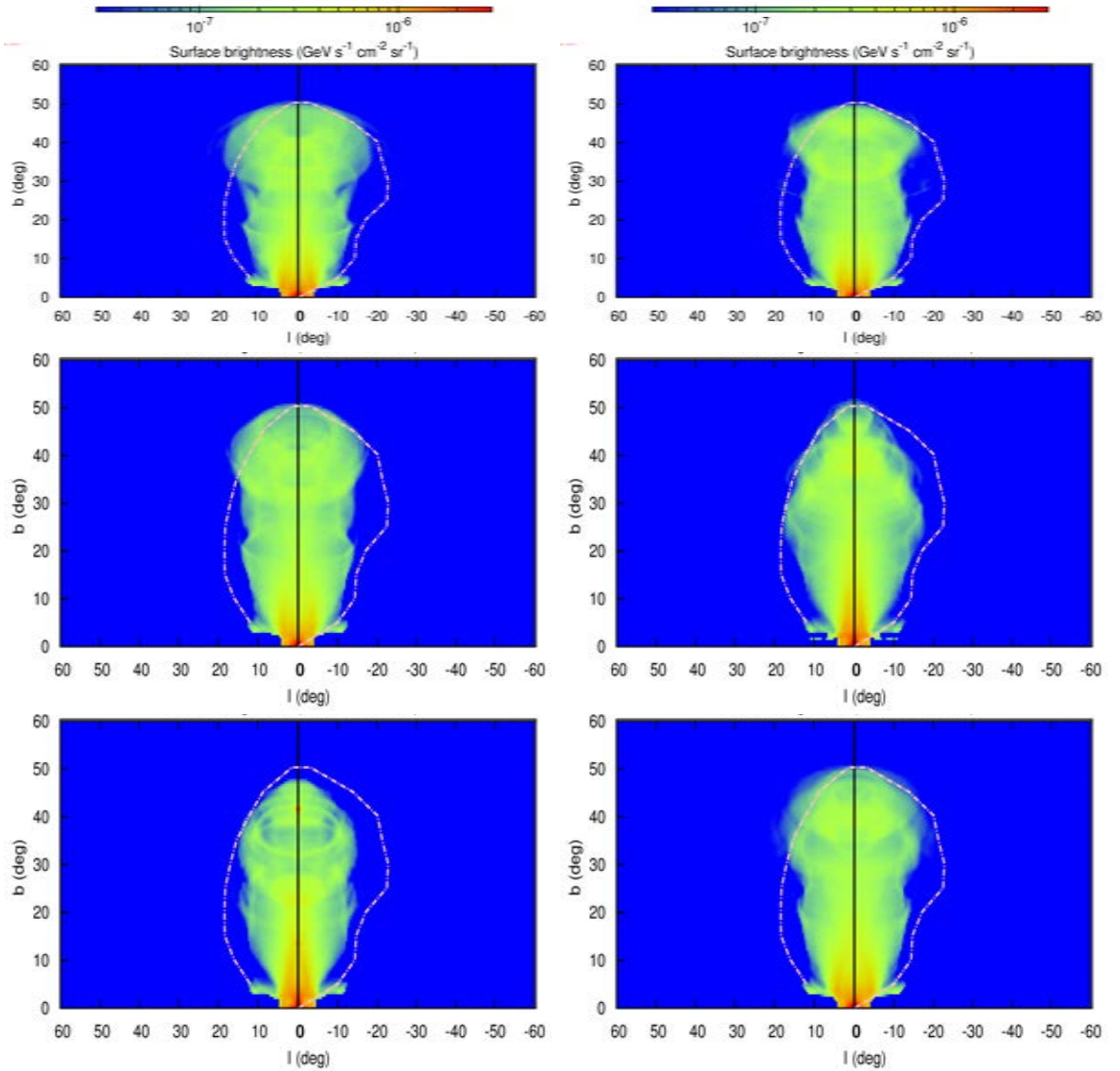


Figure B.2: Effect of different injection geometry and CGM rotation for our fiducial run S10 (see Table 4.2) on the γ -ray emission at 10 GeV. The geometries of the injection regions, from top-left to bottom-right, are i) spherically symmetric, with injection radius $r_{\text{inj}} = 60$ pc (the fiducial value), ii) spherically symmetric, with $r_{\text{inj}} = 40$ pc, iii) spherically symmetric, with $r_{\text{inj}} = 100$ pc, iv) axisymmetric, with disc-like injection zone, v) axisymmetric with a ring-like injection region and vi) spherically symmetric, with $r_{\text{inj}} = 60$ pc and a rotating halo. The dot-dashed line shows the observed edge of the FB.

Appendix C

C.1 Injection radius for SNe driven winds

As mentioned in the main text, we have chosen the injection radius (which is the same as the radius of the inner boundary) for the SFW to be at $r_{\text{inj}} = 100$ pc which is also assumed to be the sonic radius of the wind. Though this particular choice of the radius is somewhat arbitrary, any deviation from it does not affect the results. Figure C.1 shows the density contours and the corresponding histograms of OVIII to OVII line ratios for $\mathcal{L} = 7 \times 10^{40}$ erg s⁻¹ at $t = 25$ Myr but for injection radii of 50, 100 and 200 pc. Other than some tiny details, the results are consistent with each other.

C.2 Electron temperature for high luminosity winds

To study the evolution of electron temperature T_e and ion temperature T_i , we assume the simplest picture that these two species exchange energy only via Coulomb collisions, that there is no relative bulk velocity between them and that the electron and ion number densities are equal, i.e. $n_i \approx n_e \equiv n$. The energy equations for these two species can then be approximated as (Braginskii, 1965)

$$n_e k_B \left(\frac{3}{2} \frac{dT_e}{dt} + T_e \vec{\nabla} \cdot \vec{v} \right) = -3 \frac{m_e}{m_p} \frac{n k_B}{\tau_e} (T_e - T_i), \quad (\text{C.1})$$

$$n_i k_B \left(\frac{3}{2} \frac{dT_i}{dt} + T_i \vec{\nabla} \cdot \vec{v} \right) = 3 \frac{m_e}{m_p} \frac{n k_B}{\tau_e} (T_e - T_i), \quad (\text{C.2})$$

where \mathbf{v} is the bulk velocity, $\tau_e = 3.44 \times 10^5 \frac{(k_B T_e / \text{eV})^{3/2}}{n \lambda}$ sec and $\lambda \approx 15$ is the Coulomb logarithm. Other constants have their usual meanings. Setting the compression term to zero ($\vec{\nabla} \cdot \vec{v} = 0$ in Eqs. C.1 & C.2), we can solve for the electron and ion temperatures of the post-shock gas. We assume that $T_i(t = 0) = T_{i,2}$ and $T_e(t = 0) = T_{e,2}$, the ion and electron post shock temperature respectively. Assuming that both electron and ion bulk kinetic energies are thermalised independently at shocks (observations

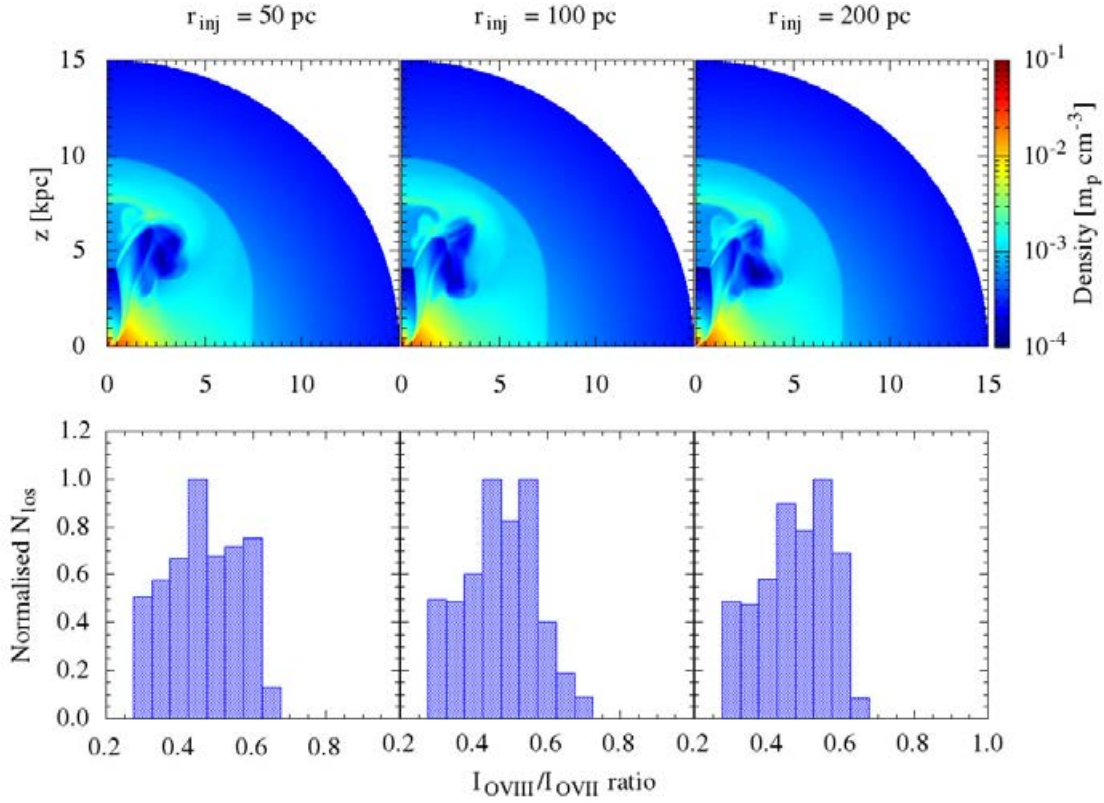


Figure C.1: Effects of different injection radius for SFW cases. The top panel shows the density contours for $\mathcal{L} = 7 \times 10^{40} \text{ erg s}^{-1}$ at $t = 25 \text{ Myr}$ and the bottom panel shows the corresponding histograms of OVIII to OVII line ratios.

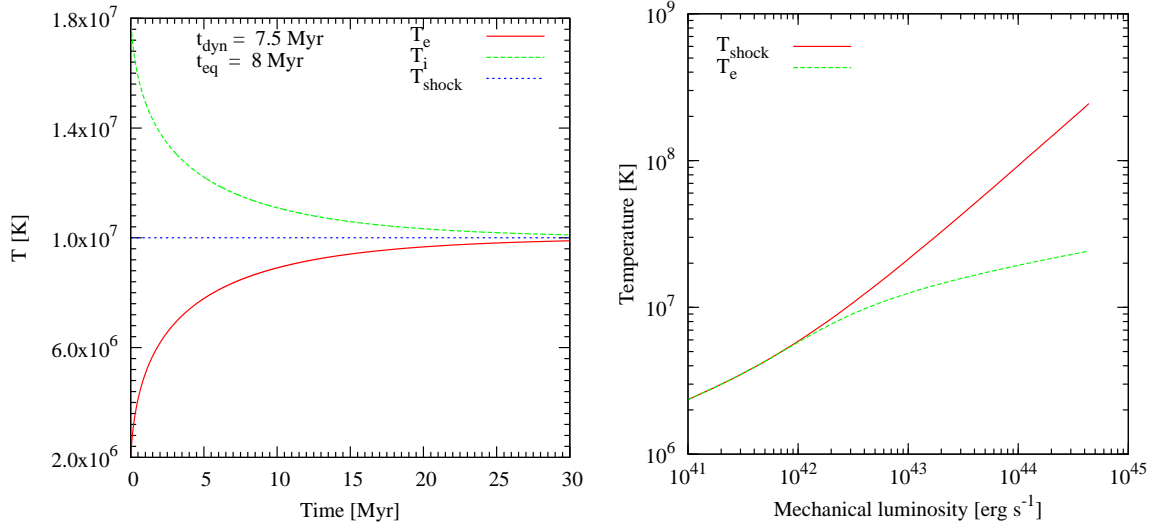


Figure C.2: Left panel: Evolution of the electron and proton temperatures (Eqs. C.1, C.2) towards an equilibrium shock temperature of 10^7 K corresponding to $\mathcal{L} \approx 3 \times 10^{42}$ erg s $^{-1}$. Right panel: Electron temperature at $t = t_{\text{dyn}}$ (time appropriate for FB observations; see Eq. 5.16) compared to the equilibrium shock temperature ($T_{\text{shock}} \equiv [T_e + T_i]/2$) for different luminosities shows a monotonic increase (although slower than T_{shock}) in T_e with an increasing luminosity even in the collisionless regime. Both the figures are obtained for $n = 10^{-3}$ cm $^{-3}$.

suggest that electrons are heated more than this estimate so we can treat our T_e as a conservative lower limit on the electron temperature), the shock energy gets distributed among electrons and protons according to their mass and the Mach number of the shock. Therefore, the post shock electron and ion temperatures can be written, respectively, as (see Eqs. 19, 21 in Vink et al. 2015)

$$T_{e,2} = T_{e,1} \chi^{\gamma-1} + \frac{\mu_e m_p v_s^2}{2k_B} \left(\frac{\gamma-1}{\gamma} \right) \left(1 - \frac{1}{\chi^2} \right), \quad (\text{C.3})$$

$$T_{i,2} = T_{i,1} (2 - \chi^{\gamma-1}) + \frac{\mu_i m_p v_s^2}{2k_B} \left(\frac{\gamma-1}{\gamma} \right) \left(1 - \frac{1}{\chi^2} \right), \quad (\text{C.4})$$

where, $T_{e,1} = T_{i,1} = 2 \times 10^6$ K is the pre-shocked halo temperature,

$$\chi = (\gamma + 1) M^2 / ((\gamma - 1) M^2 + 2)$$

is the density jump behind the shock for a Mach number of M , v_s is the shock velocity, $\mu_e = m_e/m_p$ and $\mu_i = 1.27$ for Solar metallicity.

Figure C.2 shows the evolution of the electron and ion temperatures (Eqs. C.1 & C.2) with $\nabla \cdot \mathbf{v} = 0$ and initial conditions given by Eqs. C.3 & C.4) behind the outer shock. The left panel of the figure shows that although it takes few $\times t_{\text{eq}}$ (Eq. 5.14) to come to equilibrium ($T_e \approx T_i$), initially T_e rises very sharply and attains a value $\approx 90\%$ of $T_{\text{shock}} \equiv (T_e + T_i)/2$ within an equilibrium time t_{eq} . For comparison with FB observations the electron temperature behind the shock should be evaluated at $t = t_{\text{dyn}}$ (see Eq. 5.16). We plot this $T_e(t = t_{\text{dyn}})$ in the right panel of figure C.2. We notice that although current T_e lags the equilibrium shock temperature, it still increases

monotonically with the mechanical luminosity. Therefore, even if $t_{\text{eq}} > t_{\text{dyn}}$ for high luminosity cases (i.e. the shock is collisionless for $\mathcal{L} \gtrsim 10^{42} \text{ erg s}^{-1}$), the electron temperature is still too high to explain the observed O VIII / O VII line ratio.

Bibliography

- Ackermann M., et al., 2014, [The Astrophysical Journal](#), 793, 64
- Agol E., 2000, [The Astrophysical Journal](#), 538, L121
- Almy R. C., McCammon D., Digel S. W., Bronfman L., May J., 2000, [The Astrophysical Journal](#), 545, 290
- Anderson M. E., Bregman J. N., 2010, [The Astrophysical Journal](#), 714, 320
- Anderson M. E., Bregman J. N., 2011, [The Astrophysical Journal](#), 737, 22
- Armillotta L., Werk J. K., Prochaska J. X., Fraternali F., Marinacci F., 2016, preprint, 10, 1 ([arXiv:1608.05416](#))
- Arribas S., Colina L., Bellocchi E., Maiolino R., Villar-Martín M., 2014, [Astronomy & Astrophysics](#), 568, A14
- Asplund M., Grevesse N., Sauval A. J., Scott P., 2009, [Annual Review of Astronomy & Astrophysics](#), 47, 481
- Babul A., Rees M. J., 1992, [Mon. Not. R. Astron. Soc.](#), 255, 346
- Barnes D. J., Kay S. T., Henson M. A., McCarthy I. G., Schaye J., Jenkins A., 2017, [Monthly Notices of the Royal Astronomical Society](#), 465, 213
- Baugh C. M., 2006, [Reports on Progress in Physics](#), 69, 3101
- Behroozi P. S., Conroy C., Wechsler R. H., 2010, [The Astrophysical Journal](#), 717, 379
- Berkhuijsen E. M., Haslam C. G. T., Salter C. J., 1971, [Astronomy & Astrophysics](#), 14, 252
- Bertschinger E., 1985, [The Astrophysical Journal Supplement Series](#), 58, 39
- Bhattacharjee P., Chaudhury S., Kundu S., 2014, [The Astrophysical Journal](#), 785, 63
- Biermann P. L., Becker J. K., Dreyer J., Meli A., Seo E.-S., Stanev T., 2010, [The Astrophysical Journal](#), 725, 184
- Birnboim Y., Dekel A., 2003, [Mon. Not. R. Astron. Soc.](#), 345, 349
- Bland-Hawthorn J., Cohen M., 2003, [The Astrophysical Journal](#), 582, 246

- Blitz L., Robishaw T., 2000, *The Astrophysical Journal*, 541, 675
- Blumenthal G. R., Faber S. M., Primack J. R., Rees M. J., 1984, *Nature*, 311, 517
- Bogdán Á., et al., 2013, *The Astrophysical Journal*, 772, 97
- Bolatto A. D., et al., 2013, *Nature letter*, 499, 450
- Bonnell I., Rice W., 2008, *Science*, 321, 1060
- Bordoloi R., et al., 2014, *The Astrophysical Journal*, 796, 136
- Bordoloi R., Heckman T. M., Norman C. A., 2016, preprint ([arXiv:1605.07187v1](https://arxiv.org/abs/1605.07187v1))
- Bordoloi R., et al., 2017, *The Astrophysical Journal*, 834, 1
- Borthakur S., et al., 2015, *The Astrophysical Journal*, 813, 46
- Braginskii S. I., 1965, *Reviews of Plasma Physics*, 1, 205
- Breitschwerdt D., Schmutzler T., 1994, *Nature*, 371, 774
- Bullock J. S., Kolatt T. S., Sigad Y., Somerville R. S., Kravtsov A. V., Klypin A. A., Primack J. R., Dekel A., 2001, *Monthly Notices of the Royal Astronomical Society*, 321, 559
- Burbidge E. M., Burbidge G. R., Rubin V. C., 1964, *The Astrophysical Journal*, 140, 942
- Bustard C., Zweibel E. G., D’Onghia E., 2016, *The Astrophysical Journal*, 819, 29
- Carretti E., et al., 2013, *Nature*, 493, 66
- Cecil G., Bland-Hawthorn J., Veilleux S., Filippenko a. V., 2001, *The Astrophysical Journal*, 555, 338
- Chattopadhyay I., Sharma M., Nath B. B., Ryu D., 2012, *Monthly Notices of the Royal Astronomical Society*, 423, 2153
- Chevalier R. A., Clegg A. W., 1985, *Nature letter*, 317, 44
- Chisholm J., Tremonti C. A., Leitherer C., Chen Y., 2016, *Monthly Notices of the Royal Astronomical Society*, 463, 541
- Churazov E., Sunyaev R., Forman W., Böhringer H., 2002, *Monthly Notices of the Royal Astronomical Society*, 332, 729
- Churazov E., Sazonov S., Sunyaev R., Forman W., Jones C., 2005, *Monthly Notices of the Royal Astronomical Society*, 363, L91
- Cicone C., et al., 2014, *Astronomy & Astrophysics*, 562, A21
- Cohen R. J., Davies R. D., 1976, *Mon. Not. R. Astron. Soc.*, 175, 1

- Cole S., Aragon-Salamanca A., Frenk C. S., Navarro J. F., Zepf S. E., 1994, *Mon. Not. R. Astron. Soc.*, **271**, 781
- Cooper J., Bicknell G., Sutherland R., Bland-Hawthorn J., 2008, *The Astrophysical Journal*, **674**, 157
- Cooper J. L., Bicknell G. V., Sutherland R. S., Bland-Hawthorn J., 2009, *The Astrophysical Journal*, **703**, 330
- Cowie L. L., Songaila A., Kim T.-S., Hu E. M., 1995, *Astronomical Journal*, **109**, 1522
- Crain R. A., McCarthy I. G., Frenk C. S., Theuns T., Schaye J., 2010, *Mon. Not. R. Astron. Soc.*, **407**, 1403
- Crain R. A., McCarthy I. G., Schaye J., Theuns T., Frenk C. S., 2013, *Monthly Notices of the Royal Astronomical Society*, **432**, 3005
- Crocker R. M., 2012, *Monthly Notices of the Royal Astronomical Society*, **423**, 3512
- Crocker R. M., Aharonian F., 2011, *Physical Review Letters*, **106**, 101102
- Crocker R. M., Bicknell G. V., Carretti E., Hill A. S., Sutherland R. S., 2014, *The Astrophysical Journal Letters*, **791**, L20
- Crocker R. M., Bicknell G. V., Taylor A. M., Carretti E., 2015, *The Astrophysical Journal*, **808**, 107
- Dai X., Anderson M. E., Bregman J. N., Miller J. M., 2012, *The Astrophysical Journal*, **755**, 107
- Davé R., Katz N., Oppenheimer B. D., Kollmeier J. A., Weinberg D. H., 2013, *Mon. Not. R. Astron. Soc.*, **434**, 2645
- Davis M., Peebles P. J. E., 1983, *The Astrophysical Journal*, **267**, 465
- Dekel A., Birnboim Y., 2006, *Mon. Not. R. Astron. Soc.*, **368**, 2
- Dekel A., Silk J., 1986, *The Astrophysical Journal*, **303**, 39
- Dobler G., Finkbeiner D. P., 2008, *The Astrophysical Journal*, **680**, 1222
- Dutton A. A., Conroy C., van den Bosch F. C., Prada F., More S., 2010, *Mon. Not. R. Astron. Soc.*, **407**, 2
- Egger R. J., Aschenbach B., 1995, *Astronomy & Astrophysics*, **294**, 25
- Everett J. E., Zweibel E. G., Benjamin R. A., McCammon D., Rocks L., Gallagher III J. S., 2008, *The Astrophysical Journal*, **674**, 258
- Fang T., Jiang X., 2014, *The Astrophysical Journal Letters*, **785**, L24
- Fang T., Bullock J., Boylan-Kolchin M., 2013, *The Astrophysical Journal*, **762**, 20

- Feldmann R., Hopkins P. F., Quataert E., Faucher-Giguère C.-A., Kereš D., 2016, [Mon. Not. R. Astron. Soc.](#), **458**, L14
- Ferland G. J., et al., 2013, *Revista Mexicana de Astronomia y Astrofisica*, **49**, 137
- Ferrara A., Tolstoy E., 2000, [Mon. Not. R. Astron. Soc.](#), **313**, 291
- Ferrara A., Pettini M., Shchekinov Y., 2000, [Mon. Not. R. Astron. Soc.](#), **319**, 539
- Ferrarese L., Merritt D., 2000, *The Astrophysical Journal*, **539**, L9
- Finkbeiner D. P., 2004, [The Astrophysical Journal](#), **614**, 186
- Ford A. B., Oppenheimer B. D., Dav R., Katz N., Kollmeier J. A., Weinberg D. H., 2013, [Mon. Not. R. Astron. Soc.](#), **432**, 89
- Fox A. J., et al., 2015, [The Astrophysical Journal](#), **799**, L7
- Fraternali F., Binney J. J., 2006, [Mon. Not. R. Astron. Soc.](#), **366**, 449
- Fukumura K., Kazanas D., Shrader C., Behar E., Tombesi F., Contopoulos I., 2017, [Nature Astronomy](#), **1**, 0062
- Gabici S., Aharonian F. A., Blasi P., 2007, [Astrophysics and Space Science](#), **309**, 365
- Gabor J. M., Davé R., 2015, [Mon. Not. R. Astron. Soc.](#), **447**, 374
- Gatto A., Fraternali F., Read J. I., Marinacci F., Lux H., Walch S., 2013, [Monthly Notices of the Royal Astronomical Society](#), **433**, 2749
- Genzel R., Eisenhauer F., Gillessen S., 2010, [Review of modern physics](#), **82**, 3121
- Ghavamian P., Laming J. M., Rakowski C. E., 2007, *The Astrophysical Journal Letters*, **654**, L69
- Girichidis P., et al., 2016, [The Astrophysical Journal Letters](#), **816**, L19
- Grimes J. P., et al., 2007, [The Astrophysical Journal](#), **668**, 891
- Grimm H. J., Gilfanov M., Sunyaev R., 2003, [Mon. Not. R. Astron. Soc.](#), **339**, 793
- Gu L., Mao J., Costantini E., Kaastra J., 2016, [Astronomy & Astrophysics](#), **594**, A78
- Guo F., Mathews W. G., 2011, [The Astrophysical Journal](#), **728**, 121
- Guo F., Mathews W. G., 2012, [The Astrophysical Journal](#), **756**, 181
- Guo F., Mathews W. G., Dobler G., Oh S. P., 2012, [The Astrophysical Journal](#), **756**, 182
- Gupta S., Nath B. B., Sharma P., Shchekinov Y., 2016, [Mon. Not. R. Astron. Soc.](#), **462**, 4532
- Hanbury Brown R., Davis R. D., Hazard C., 1960, *The Observatory*, **80**, 191

- Haslam, C. G. T.; Salter, C. J.; Stoffel, H.; Wilson W. E., 1982, *Astronomy and Astrophysics Supplement Series*, 47, 1
- Haslam C. G. T., Wilson W. E., Graham D. A., Hunt G. C., 1974, *Astronomy and Astrophysics Supplement*, 13, 359
- Heckman T. M., 2002, in ASPC. p. 254, <http://adsabs.harvard.edu/abs/2002ASPC..254..292H>
- Heckman T. M., Borthakur S., 2016, *The Astrophysical Journal*, 822, 9
- Heckman T. M., Armus L., Miley G. K., 1990, *The Astrophysical Journal Supplement Series*, 74, 833
- Heckman T. M., Lehnert M. D., Strickland D. K., Armus L., 2000, *The Astrophysical Journal Supplement Series*, 129, 493
- Heckman T. M., Alexandroff R. M., Borthakur S., Overzier R., Leitherer C., 2015, *The Astrophysical Journal*, 809, 147
- Henley D. B., Shelton R. L., 2010, *The Astrophysical Journal Supplement Series*, 187, 388
- Immer K., Schuller F., Menten K. M., 2011, in Cernicharo J., Bachiller R., eds, *IAU Symposium Vol. 280, The Molecular Universe*.
- Immer K., Menten K. M., Schuller F., Lis D. C., 2012, *Astronomy & Astrophysics*, 548, A120
- Kacprzak G. G., Muzahid S., Churchill C. W., Nielsen N. M., Charlton J. C., 2015, *The Astrophysical Journal*, 815, 22
- Karachentsev I. D., Kaisina E. I., 2013, *The Astronomical Journal*, 146, 46
- Kataoka J., et al., 2013, *The Astrophysical Journal*, 779, 57
- Kauffmann G., White S. D. M., Guiderdoni B., 1993, *Mon. Not. R. Astron. Soc.*, 264, 201
- Kennicutt, Jr. R. C., 1998, *Annual Review of Astronomy & Astrophysics*, 36, 189
- Kereš D., Katz N., Weinberg D. H., Davé R., 2005, *Mon. Not. R. Astron. Soc.*, 363, 2
- Keshet U., Gurwicz I., 2017, *The Astrophysical Journal*, 840, 7
- Kim C.-g., Ostriker E. C., Raileanu R., 2017, *The Astrophysical Journal*, 834, 1
- King A., 2003, *The Astrophysical Journal*, 596, L27
- King A. R., 2010, *Mon. Not. R. Astron. Soc.*, 402, 1516
- Koepferl C. M., Robitaille T. P., Morales E. F. E., Johnston K. G., 2015, *The Astrophysical Journal*, 799, 53

- Kompaneets A. S., 1960, *Soviet Physics Doklady*, **5**, 46
- Koyama H., Inutsuka S.-i., 2004, *The Astrophysical Journal Letters*, **602**, L25
- Lacki B. C., 2014, *Mon. Not. R. Astron. Soc.*, **444**, L39
- Lallement R., Snowden S., Kuntz K. D., Dame T. M., Koutroumpa D., Grenier I., Casandjian J. M., 2016, *Astronomy & Astrophysics*, **595**, A131
- Larson R. B., 1974, *Mon. Not. R. Astron. Soc.*, **169**, 229
- Law C. J., 2010, *The Astrophysical Journal*, **708**, 474
- Lehner N., Howk J. C., Thom C., Fox A. J., Tumlinson J., Tripp T. M., Meiring J. D., 2012, *Mon. Not. R. Astron. Soc.*, **424**, 2896
- Lehnert M. D., Heckman T. M., Weaver K. A., 1999, *The Astrophysical Journal*, **523**, 575
- Leitherer C., et al., 1999, *The Astrophysical Journal*, **123**, 3
- Li Z., Wang Q. D., 2007, *The Astrophysical Journal Letters*, **668**, L39
- Li J. T., Wang Q. D., 2013, *Monthly Notices of the Royal Astronomical Society*, **428**, 2085
- Liou M.-S., 1996, *Journal of Computational Physics*, **129**, 364
- Lockman F. J., 1984, *The Astrophysical Journal*, **283**, 90
- Lockman F. J., McClure-Griffiths N. M., 2016, *The Astrophysical Journal*, **826**, 215
- Longair M. S., 1981, *High energy astrophysics*
- Lynds C. R., Sandage A. R., 1963, *The Astrophysical Journal*, **137**, 1005
- Mac low M.-M., Ferrara A., 1999, *The Astrophysical Journal*, **513**, 142
- Macciò A. V., Dutton A. A., Van Den Bosch F. C., Moore B., Potter D., Stadel J., 2007, *Mon. Not. R. Astron. Soc.*, **378**, 55
- Maciel W. J., Costa R. D. D., 2010, in Cunha K., Spite M., Barbuy B., eds, *IAU Symposium Vol. 265, Chemical Abundances in the Universe: Connecting First Stars to Planets*. pp 317–324 ([arXiv:0911.3763](https://arxiv.org/abs/0911.3763)), doi:10.1017/S1743921310000803
- Madau P., Ferrara A., Rees M. J., 2001, *The Astrophysical Journal*, **555**, 92
- Marrone D. P., Moran J. M., Zhao J.-h., Rao R., 2006, *The Astrophysical Journal*, **640**, 308
- Martin C. L., 1999, *The Astrophysical Journal*, **513**, 156
- Martin C. L., 2005, in Braun R., ed., *Astronomical Society of the Pacific Conference Series Vol. 331, Extra-Planar Gas*. p. 305

- Mathews W. G., Baker J. C., 1971, *The Astrophysical Journal*, 170, 241
- McMillan P. J., 2011, *Mon. Not. R. Astron. Soc.*, 414, 2446
- McMillan P. J., 2017, *Mon. Not. R. Astron. Soc.*, 465, 76
- Mccourt M., Oh S. P., Leary R. M. O., Madigan A.-m., 2016, preprint ([arXiv:1610.01164v1](https://arxiv.org/abs/1610.01164v1))
- Mckee C. F., Ostriker J. P., 1977, *The Astrophysical Journal*, 218, 148
- Mertsch P., Sarkar S., 2011, *Physical Review Letters*, 107, 091101
- Mignone A., Bodo G., Massaglia S., Matsakos T., Tesileanu O., Zanni C., Ferrari A., 2007, *The Astrophysical Journal Supplement Series*, 170, 228
- Miller M. J., Bregman J. N., 2013, *The Astrophysical Journal*, 770, 118
- Miller M. J., Bregman J. N., 2015, *The Astrophysical Journal*, 800, 14
- Miller M. J., Bregman J. N., 2016, *The Astrophysical Journal*, 829, 9
- Miller M. J., Hodges-Kluck E. J., Bregman J. N., 2016, *The Astrophysical Journal*, 818, 112
- Mineo S., Gilfanov M., Sunyaev R., 2012a, *Mon. Not. R. Astron. Soc.*, 419, 2095
- Mineo S., Gilfanov M., Sunyaev R., 2012b, *Mon. Not. R. Astron. Soc.*, 426, 1870
- Mineo S., Gilfanov M., Lehmer B. D., Morrison G. E., Sunyaev R., 2014, *Mon. Not. R. Astron. Soc.*, 437, 1698
- Miyamoto M., Nagai R., 1975, *Publications of Astronomical Society of Japan*, 27, 533
- Mo H. J., Mao S., White S. D. M., 1998, *Mon. Not. R. Astron. Soc.*, 295, 319
- Mo H., van den Bosch F. C., White S., 2010, *Galaxy Formation and Evolution*
- Molinari S., et al., 2011, *The Astrophysical Journal Letters*, 735, L33
- Moster B. P., Somerville R. S., Maulbetsch C., Bosch F. C. V. D., Macci A. V., Naab T., Oser L., 2010, *The Astrophysical Journal*, 710, 903
- Mou G., Yuan F., Bu D., Sun M., Su M., 2014, *The Astrophysical Journal*, 790, 109
- Mou G., Yuan F., Gan Z., Sun M., 2015, *The Astrophysical Journal*, 811, 37
- Mukherjee D., Sharma P., Nath B. B., Yadav N., Mukherjee D., Sharma P., Nath B. B., 2017, *Mon. Not. R. Astron. Soc.*, 465, 1720
- Muno M. P., et al., 2004, *The Astrophysical Journal*, 613, 326
- Murakami H., Maeda Y., Sakano M., Koyama K., Tsujimoto M., 2000, in *American Astronomical Society Meeting Abstracts #196*. p. 766

- Murray N., Rahman M., 2010, [The Astrophysical Journal](#), 709, 424
- Murray N., Quataert E., Thompson T. A., 2005, [The Astrophysical Journal](#), 618, 569
- Narlikar J. V., Padmanabhan T., 2001, [Annual Review of Astronomy & Astrophysics](#), 39, 211
- Nath B. B., Shchekinov Y., 2013, [The Astrophysical Journal Letters](#), 777, L12
- Nath B. B., Trentham N., 1997, [Mon. Not. R. Astron. Soc.](#), 291, 505
- Navarro J. F., Frenk C. S., White S. D. M., 1996, [The Astrophysical Journal](#), 462, 563
- Navarro J. F., Frenk C. S., White S. D. M., 1997, [The Astrophysical Journal](#), 490, 493
- Nicastro F., Senatore F., Krongold Y., Mathur S., Elvis M., 2016, [The Astrophysical Journal](#), 828, 12
- O’Sullivan E., Forbes D. A., Ponman T. J., 2001, [Mon. Not. R. Astron. Soc.](#), 328, 461
- Olano C. A., 2009, [Astronomy & Astrophysics](#), 506, 1215
- Oort J. H., 1977, [Annual Review of Astronomy & Astrophysics](#), 15, 295
- Oppenheimer B. D., Davé R., 2006, [Monthly Notices of the Royal Astronomical Society](#), 373, 1265
- Oppenheimer B. D., Davé R., 2008, [Mon. Not. R. Astron. Soc.](#), 387, 577
- Oppenheimer B. D., Davé R., Kereš D., Fardal M., Katz N., Kollmeier J. A., Weinberg D. H., 2010, [Mon. Not. R. Astron. Soc.](#), 406, 2325
- Park S., Finley J. P., Snowden S. L., Dame T. M., 1997, [The Astrophysical Journal Letters](#), 476, L77
- Paumard T., et al., 2006, [The Astrophysical Journal](#), 643, 1011
- Peebles P. J. E., 2017, [Nature Astronomy](#), 1, 57
- Peek J. E. G., Putman M. E., McKee C. F., Heiles C., Stanimirović S., 2007, [The Astrophysical Journal](#), 656, 907
- Peng Y., Maiolino R., Cochrane R., 2015, [Nature letter](#), 521, 192
- Persic M., Rephaeli Y., 2015, in Rosquist K., ed., Thirteenth Marcel Grossmann Meeting: On Recent Developments in Theoretical and Experimental General Relativity, Astrophysics and Relativistic Field Theories. pp 1036–1038 ([arXiv:1405.3107](#)), [doi:10.1142/9789814623995_0075](#)
- Piddington J. H., Trent G. H., 1956, [Australian Journal of Physics](#), 9, 481
- Planck Collaboration et al., 2013, [Astronomy & Astrophysics](#), 554, A139

- Prada F., Klypin A. A., Simonneau E., Betancort Rijo J., Patiri S., Gottlober S., Sanchez Conde M. A., 2006, *The Astrophysical Journal*, 645, 1001
- Press W. H., Schechter P., 1974, *The Astrophysical Journal*, 187, 425
- Putman M. E., Saul D. R., Mets E., 2011, *Mon. Not. R. Astron. Soc.*, 418, 1575
- Quataert E., Gruzinov A., 2000, *The Astrophysical Journal*, 545, 842
- Rees M. J., Ostriker J. P., 1977, *Mon. Not. R. Astron. Soc.*, 179, 541
- Rougoor G. W., Oort J. H., 1960, in *Proceeding of National academy of science*. p. 1, [doi:10.3384/ecp15118](https://doi.org/10.3384/ecp15118), <http://www.pnas.org/content/46/1/1.full.pdf?sid=b1745c4c-3605-4134-82f2-0decc97f213e>
- Roy A., Nath B. B., Sharma P., Shchekinov Y., 2013, *Mon. Not. R. Astron. Soc.*, 434, 3572
- Roy A., Nath B. B., Sharma P., Shchekinov Y., 2016, *Mon. Not. R. Astron. Soc.*, 463, 2296
- Rubin V. C., Ford W. K. J., 1970, *The Astrophysical Journal*, 159, 379
- Rupke D. S., Veilleux S., Sanders D. B., 2002, *The Astrophysical Journal*, 570, 588
- Rupke D. S., Veilleux S., Sanders D. B., 2005, *The Astrophysical Journal*, 632, 751
- Rybicki G. B., Lightman A. P., 1979, *Radiative processes in astrophysics*
- Sarkar K. C., Nath B. B., Sharma P., Shchekinov Y., 2015a, *Mon. Not. R. Astron. Soc.*, 448, 328
- Sarkar K. C., Nath B. B., Sharma P., 2015b, *Mon. Not. R. Astron. Soc.*, 453, 3827
- Sarkar K. C., Nath B. B., Sharma P., Shchekinov Y., 2016, *The Astrophysical Journal Letters*, 818, L24
- Sarkar K. C., Nath B. B., Sharma P., 2017, *Mon. Not. R. Astron. Soc.*, 467, 3544
- Scannapieco E., 2017, *The Astrophysical Journal*, 837, 28
- Schaye J., et al., 2015, *Mon. Not. R. Astron. Soc.*, 446, 521
- Schwartz C. M., Martin C. L., 2004, *The Astrophysical Journal*, 610, 201
- Selig M., Vacca V., Oppermann N., Ensslin T. A., 2015, *Astronomy & Astrophysics*, 581, A126
- Sell P. H., et al., 2014, *Mon. Not. R. Astron. Soc.*, 441, 3417
- Sembach K. R., et al., 2003, *The Astrophysical Journal Supplement Series*, 146, 165
- Semenov V., Dyadechkin S., Punsly B., 2004, *Science*, 305, 978

- Shapiro P. R., Field G. B., 1976, [The Astrophysical Journal](#), 205, 762
- Sharma M., 2013, PhD thesis, Jawaharlal Nehru University, New Delhi
- Sharma M., Nath B. B., 2012, [The Astrophysical Journal](#), 750, 55
- Sharma M., Nath B. B., 2013, [The Astrophysical Journal](#), 763, 17
- Sharma P., McCourt M., Parrish I. J., Quataert E., 2012, [Mon. Not. R. Astron. Soc.](#), 427, 1219
- Sharma M., Nath B. B., Chattopadhyay I., Shchekinov Y., 2014a, [Mon. Not. R. Astron. Soc.](#), 441, 431
- Sharma P., Roy A., Nath B. B., Shchekinov Y., 2014b, [Mon. Not. R. Astron. Soc.](#), 443, 3463
- Shopbell P. L., Bland-Hawthorn J., 1998, [The Astrophysical Journal](#), 493, 129
- Singh P., Nath B. B., Majumdar S., Silk J., 2015, [Mon. Not. R. Astron. Soc.](#), 448, 2384
- Smith M. C., et al., 2007, [Mon. Not. R. Astron. Soc.](#), 379, 755
- Snowden S. L., et al., 1995, [The Astrophysical Journal](#), 454, 643
- Snowden S. L., et al., 1997, [The Astrophysical Journal](#), 485, 125
- Sofue Y., 1977, *Astronomy & Astrophysics*, 60, 327
- Sofue Y., 1984, *Publications of the Astronomical Society of Japan*, 36, 539
- Sofue Y., 1994, [The Astrophysical Journal](#), 431, L91
- Sofue Y., 2000, [The Astrophysical Journal](#), 540, 224
- Sofue Y., 2003, [Publications of the Astronomical Society of Japan](#), 55, 445
- Sofue Y., Handa T., 1984, *Nature letter*, 310, 568
- Sofue B., Reich B., 1979, *Astronomy and Astrophysics Supplement Series*, 38, 251
- Sofue Y., Habe A., Kataoka J., Totani T., Inoue Y., Nakashima S., Matsui H., Akita M., 2016, [Mon. Not. R. Astron. Soc.](#), 459, 108
- Somerville R. S., Primack J. R., 1999, [Mon. Not. R. Astron. Soc.](#), 310, 1087
- Songaila A., 2001, [The Astrophysical Journal](#), 561, L153
- Spitzer L., 1956, *Physics of Fully Ionized Gases*
- Springel V., Hernquist L., 2003, [Mon. Not. R. Astron. Soc.](#), 339, 289
- Springel V., et al., 2005, *Nature*, 435, 629

- Steidel C. C., Erb D. K., Shapley A. E., Pettini M., Reddy N., Bogosavljević M., Rudie G. C., Rakic O., 2010, [The Astrophysical Journal](#), 717, 289
- Stern J., Hennawi J. F., Prochaska J. X., Werk J. K., 2016, [The Astrophysical Journal](#), 830, 87
- Strickland D. K., Heckman T. M., 2007, [The Astrophysical Journal](#), 658, 258
- Strickland D. K., Heckman T. M., 2009, [The Astrophysical Journal](#), 697, 2030
- Strickland D. K., Stevens I. R., 2000, [Monthly Notices of the Royal Astronomical Society](#), 314, 511
- Strickland D. K., Heckman T. M., Weaver K. A., Hoopes C. G., Dahlem M., 2002, [The Astrophysical Journal](#), 568, 689
- Strickland D. K., Heckman T. M., Colbert E. J. M., Hoopes C. G., Weaver K. a., 2004a, [The Astrophysical Journal Supplement Series](#), 151, 193
- Strickland D. K., Heckman T. M., Colbert E. J. M., Hoopes C. G., Weaver K. A., 2004b, [The Astrophysical Journal](#), 606, 829
- Su M., Slatyer T. R., Finkbeiner D. P., 2010, [The Astrophysical Journal](#), 724, 1044
- Suchkov A. A. a., Balsara D. S. D., Heckman T. T. M., Leitherner C., 1994, [The Astrophysical Journal](#), 430, 511
- Suchkov A. A., Berman V. G., Heckman T. M., Balsara D. S., 1996, [The Astrophysical Journal](#), 463, 528
- Sutherland R. S., Dopita M. A., 1993, [The Astrophysical Journal Supplement Series](#), 88, 253
- Tchekhovskoy A., 2015, in Contopoulos I., Gabuzda D., Kylafis N., eds, *Astrophysics and Space Science Library Vol. 414, The Formation and Disruption of Black Hole Jets*. p. 45, [doi:10.1007/978-3-319-10356-3_3](https://doi.org/10.1007/978-3-319-10356-3_3)
- Tegmark M., Silk J., Evrard A., 1993, [The Astrophysical Journal](#), 417, 54
- Thompson T. A., Krumholz M. R., 2016, [Mon. Not. R. Astron. Soc.](#), 455, 334
- Thompson T. A., Quataert E., Zhang D., Weinberg D. H., 2016, [Mon. Not. R. Astron. Soc.](#), 455, 1830
- Toft S., Rasmussen J., Sommer-Larsen J., Pedersen K., 2002, [Mon. Not. R. Astron. Soc.](#), 335, 799
- Totani T., 2006, [Publications of the Astronomical Society of Japan](#), 58, 965
- Tremonti C. A., Heckman T. M., Kauffmann G., Brinchmann J., White S. D. M., Seibert M., Peng E. W., Schlegel D. J., 2004, [The Astrophysical Journal](#), 613, 898

- Tremonti C. a., Moustakas J., Diamond-Stanic A. M., 2007, [The Astrophysical Journal](#), 663, L77
- Troitsky S., 2017, [Mon. Not. R. Astron. Soc.](#), 468, 36
- Tsai A.-L., Matsushita S., Kong A. K. H., Matsumoto H., Kohno K., 2012, [The Astrophysical Journal](#), 752, 38
- Tullmann R., Breitschwerdt D., Rossa J., Pietsch W., Dettmar R.-J., 2006, [Astronomy & Astrophysics](#), 457, 779
- Tumlinson J., et al., 2011, [Science](#), 334, 948
- Uson J. M., Wilkinson D. T., 1982, [Physical Review Letters](#), 49, 1463
- Vasiliev E. O., Nath B. B., Shchekinov Y., 2015, [Mon. Not. R. Astron. Soc.](#), 446, 1703
- Veilleux S., Cecil G., Bland-Hawthorn J., 2005, [Annual Review of Astronomy & Astrophysics](#), 43, 769
- Vink J., Broersen S., Bykov A., Gabici S., 2015, [Astronomy & Astrophysics](#), 579, A13
- Vogelsberger M., Genel S., Sijacki D., Torrey P., Springel V., Hernquist L., 2013, [Mon. Not. R. Astron. Soc.](#), 436, 3031
- Walter F., Weiss A., Scoville N., 2002, [The Astrophysical Journal](#), 580, L21
- Walter F., et al., 2017, [The Astrophysical Journal](#), 835, 265
- Wang Q. D., Li J., Jiang X., Fang T., 2016, [Mon. Not. R. Astron. Soc.](#), 457, 1385
- Weaver R., McCray R., Castro J., Shapiro P., Moore R., 1977, [The Astrophysical Journal](#), 218, 377
- Weinmann S. M., Pasquali A., Oppenheimer B. D., Finlator K., Mendel J. T., Crain R. A., Macciò A. V., 2012, [Mon. Not. R. Astron. Soc.](#), 426, 2797
- Werk J. K., Prochaska J. X., Thom C., Tumlinson J., Tripp T. M., Meara J. M. O., Peeples M. S., 2013, [The Astrophysical Journal](#), 204, 17
- Werk J. K., et al., 2014, [The Astrophysical Journal](#), 792, 8
- Werk J. K., et al., 2016, [The Astrophysical Journal](#), 833, 54
- White S. D. M., Rees M. J., 1978, [Mon. Not. R. Astron. Soc.](#), 183, 341
- Willingale R., Hands A. D. P., Warwick R. S., Snowden S. L., Burrows D. N., 2003, [Mon. Not. R. Astron. Soc.](#), 343, 995
- Yang H.-Y. K., Ruszkowski M., Ricker P. M., Zweibel E., Lee D., 2012, [The Astrophysical Journal](#), 761, 185
- Yao Y., Wang Q. D., 2007, [The Astrophysical Journal](#), 666, 242

- Yuan F., Quataert E., Narayan R., 2003, [The Astrophysical Journal](#), 598, 301
- Yuan F., Quataert E., Narayan R., 2004, [The Astrophysical Journal](#), 606, 894
- Yusef-Zadeh F., et al., 2009, [The Astrophysical Journal](#), 702, 178
- Zhang D., Davis S. W., 2017, [The Astrophysical Journal](#), 839, 54
- Zhang D., Thompson T. A., 2012, [Mon. Not. R. Astron. Soc.](#), 424, 1170
- Zhang D., Thompson T. A., Murray N., Quataert E., 2014, [The Astrophysical Journal](#), 784, 93
- Zubovas K., Nayakshin S., 2012, [Mon. Not. R. Astron. Soc.](#), 424, 666
- Zubovas K., King A. R., Nayakshin S., 2011, [Mon. Not. R. Astron. Soc letters](#), 415, L21
- Zwicky F., 1937, [The Astrophysical Journal](#), 86, 217
- van Woerden H., Rougoor G. W., Oort J. H., 1957, [Comptes Rendus l'Academie des Sciences](#), 244, 1691
- van der Kruit P. C., 1970, [Astronomy & Astrophysics](#), 4, 462

